Graded Origami Honeycomb for Energy Absorption



Leo de Waal

St Catherine's College

A thesis submitted for the degree of Doctor of Philosophy in the Department of Engineering Science, University of Oxford.

Trinity Term, 2022

ABSTRACT

Graded Origami Honeycomb for Energy Absorption

Leo de Waal, St Catherine's College, Oxford
A thesis submitted for the degree of Doctor of Philosophy in the Department of Engineering Science, University of Oxford.
Trinity Term, 2022

This thesis is concerned with the design of new cellular structures whose properties can be easily tuned to optimise the management of both quasi-static and dynamic external loads. This was achieved through the application of origami techniques, which allowed the mechanical performance to be functionally graded through the adjustment of the underlying crease pattern. The body of work is segmented into four areas of focus:

Firstly, a kinematic analysis was undertaken to identify the geometric possibilities for an origami honeycomb with both crease-to-crease and face-to-face connection methods. Techniques to introduce self-locking, through the restriction of the kinematic range, in the in-plane and out-of-plane direction were then highlighted. When grading in the out-of-plane direction, the Miura-ori facet width, a, was found to be dependent on the Miura-ori angle, α, for the crease-to-cease connection method. The face-to-face connection method therefore provided greater freedom in the design of grading in the out-of-plane direction. Through this analysis a family of cellular solids, that exhibit varying kinematics and the ability to self-lock, were identified.

Secondly, the effect of the underlying crease pattern variables and out-of-plane locking on the quasi-static behaviour of the regular origami honeycomb were assessed through an experimental, numerical, and analytical study. The peak force was shown to be strongly dependant on the initial eccentricity of the horizontal creases. Additionally, with all other variables equal, α could be varied to tune the peak force and the SEA. The face-to-face connection method resulted in an increased SEA when compared to the crease-to-crease connection method. Grading α along the height of the core was shown to provide a graded stiffness. For cores with the crease-to-crease connection method, the increase in stiffness was related to the alternative deformation mode that results from the restraint provided by adjacent units within the core. In contrast, for the face-to-face connection method, the stiffness increase was strongly related to the eccentricity of the units, where similar eccentricities resulted in minimal increases in stiffness. An analytical model was then developed for the face-to-face connection method, providing an expression that can facilitate the functional grading of such a core for a given application, subject to quasi-static loading.

Thirdly, the ability to imbue honeycombs with a graded mechanical behaviour using origami techniques is investigated for dynamic loading. 2×1 representative origami honeycomb cores were manufactured using a sequential stamping technique from aluminium sheets and experimentally tested using the Direct Impact Hopkinson bar and Taylor type test setup. These results validated a numerical approach that was then extrapolated to a numerical model of a 6×6 ungraded and graded core. Similar advantages, as those found for typical grading methods, were observed for the graded origami honeycomb when subjected to dynamic loading for both connection methods. However, the graded behaviour was enhanced for the face-to-face connection method due to the ability to arbitrarily select a. These results show that origami techniques can successfully be applied to introduce a gradient in the mechanical behaviour under dynamic loading, providing an attractive alternative to standard grading methods.

Lastly, the dynamic behaviour of an ungraded core is numerically investigated to assess the applicability of certain analytical models. It was shown that the force transferred to the distal end is influenced greatly by lateral inertia effects, in some cases resulting in significantly larger force when compared to the quasi-static predictions. This increase resulted from the deformation deviating from the crease pattern. For the geometry simulated a super folding element was defined to predict this force increase. Through this analysis it was illustrated that the force increase from the quasi-static prediction could be reduced through the appropriate selection of a. Alternatively, the number of units along the height and/or minimising the lateral inertia through the adjustment of the crease pattern variables could also reduce the force increase at the distal end. The force at the proximal end was predicted through a continuum approach assuming shock wave formation. This was found to only be applicable for certain combinations of height and impact velocity. Notwithstanding it can provide reasonable estimates of the average force for certain scenarios which allows the evaluation of the energy absorption.

Keywords: graded stiffness, functional gradients, energy absorption structures, quasi-static loading, dynamic impact, origami honeycomb.

ACKNOWLEDGMENTS

Firstly, I would like to thank my supervisor Prof. Zhong You. Without his guidance and support this thesis would not have been possible and I am privileged to have learned under his supervision. I would also like to thank my co-supervisor Prof. Barbara Rossi, for her valuable guidance and generous support to enable the successful completion of this thesis.

I extend my appreciation to Prof. Guoxing Lu and Dr. Jianjun Zhang for providing the opportunity to conduct the dynamic experiments in their laboratory. Their commitment to discuss all aspects of my research and the insight I gained from this interaction was invaluable.

Furthermore I would also like to express my gratitude to Prof. Dora Karagoizava for the illuminating discussions on the application of analytical models for cellular structures. Her patience and in-depth understanding have benefited me greatly.

Within the Department of Engineering Science, I would like to thank Dr. Peter Walters and Dr. Igor Dyson for sharing their expertise on constructing and testing prototypes. In addition I would also like to thank the past and present members of the special structures group.

I am also extremely grateful for the financial support provided by St Catherine's College and Prof. You.

I would like to thank my old friends for keeping in touch with me and to the new friends I have made, making Oxford a second home. I would especially like to thank Amanda Lyons for her support.

Finally, I would like to thank my family for their phenomenal encouragement. I am extremely privileged to have had this opportunity and without their support this would not have been possible. I look forward to celebrating our achievement with them in der "Ersten Reihe".

CONTENTS

Chapter 1 INTRODUCTION 1
1.1 Background 1
1.2 Aim and layout 3
CHAPTER 2 LITERATURE REVIEW 6
2.1 Energy absorption principles and evaluation criteria 6
2.2 Energy absorption devices. 8
2.2.1 Honeycombs 9
2.3 Origami energy absorption devices 10
2.3.1 General principles. 11
2.3.2 Origami energy absorption devices 12
2.4 Analytical models for impact 14
2.4.1 Formation and travelling of stress wave in solids . . . 14
2.4.2 Analytical models for Type I structures 16
2.4.3 Analytical models for Type II structures 20
2.4.4 Analytical model summary 26
CHAPTER 3 KINEMATICS 28
3.1 Geometry and connection method 29
3.2 Generalised geometry and kinematics 30
3.3 Unit cell possibilities 32
3.3.1 Identical Miura-ori angles along each individual sheet . . . 32
3.3.1.1 Connecting identical sheets to form a cell 33
3.3.1.2 Connecting sheets with different l_2, l_3 and l_4 lengths to form a cell . 34
3.3.2 Varying the Miura-ori angles along each individual unit . . 35
3.3.3 Tessellating unit cells 36
3.4 Grading 38
3.4.1 Grading in the in-plane direction 38
3.4.1.1 Identical Miura-ori angles along each individual side . . 38
3.4.1.2 Varying the Miura-ori angles along each individual unit . . 41
3.4.2 Grading along the height 42
3.4.3 Combination of grading 44
3.4.4 Tessellating graded cells 46
3.5 Conclusions 48
CHAPTER 4 QUASI-STATIC BEHAVIOUR 50

4.1 Experiment 50
4.1.1 Geometry 50
4.1.2 Sample construction 51
4.1.3 Material testing 52
4.1.4 Experimental setup 53
4.2 Numerical simulation 53
4.2.1 Inputs 53
4.2.2 Imperfections 55
4.2.3 Effect of friction coefficient 57
4.2.4 Experimental and numerical comparison 59
4.3 Geometric analysis 60
4.3.1 Numerical simulation 60
4.3.2 Ungraded tubes 61
4.3.2.1 Geometry and numerical simulation 61
4.3.2.2 Results and discussion 61
4.3.2.3 Effect of connection method 67
4.3.2.4 Comparison to core behaviour 71
4.3.2.5 Effect of friction 74
4.3.2.6 Quasi-static analytical model 76
4.3.2.7 Comparison with numerical results 80
4.3.2.8 Comments on the analytical model 82
4.3.3 Graded 86
4.3.3.1 Geometry and numerical simulation 86
4.3.3.2 Results and discussion 87
4.3.3.3 Effect of connection method 94
4.3.3.4 Comparison to core behaviour 97
4.3.4 Analytical model for graded origami honeycomb 107
4.3.4.1 Phase 1 107
4.3.4.2 Phase 2 109
4.4 Conclusions 121
CHAPTER 5 DYNAMIC BEHAVIOUR OF GRADED CORES . . 124
5.1 Graded stiffness vs gradient in strength 124
5.2 Dynamic behaviour of core with the crease-to-crease connection method . 125
5.2.1 Geometry design 125
5.2.2 Dynamic experiments 129

5.2.2.1 Sample construction 129
5.2.2.2 Experimental setup 130
5.2.3 Numerical analysis 132
5.2.4 Experimental and numerical comparison 133
5.2.4.1 Deformation modes 133
5.2.4.2 Force histories 137
5.2.5 Numerical simulation of core behaviour 141
5.2.5.1 Deformations 142
5.2.5.2 Force history 147
5.3 Dynamic behaviour of core with the face-to-face connection method . 155
5.3.1 Geometry design 155
5.3.2 Results and discussion 157
5.3.2.1 Deformations 157
5.3.2.2 Force histories 158
5.4 Conclusions 163
CHAPTER 6 THEORETICAL MODEL 166
6.1 Geometry 166
6.2 Numerical analysis 167
6.3 Dynamic behaviour of core 168
6.3.1 Effect of the initial dihedral angle, θ_0 168
6.3.2 Effect of number of units perpendicular to the loading direction (in-plane) 173
6.3.3 Effect of α 179
6.3.4 Effect of number of units along height 184
6.4 Analytical model 187
6.4.1 Force at distal end 188
6.4.1.1 Super folding element 190
6.4.2 Force at proximal end 202
6.4.2.1 Analytical model for the force at the proximal end . . . 210
6.4.2.2 Comments 216
6.5 Conclusion 217
CHAPTER 7 CONCLUSIONS 220
7.1 Summary and main achievements 220
7.2 Future work 224
REFERENCES 226

FIGURES

Figure 2.1 Typical load displacement curve 7
Figure 2.2 Miura-ori crease pattern 11
Figure 2.3 Formation of a shock front for strain-hardening material . . 16
Figure 2.4 Equivalent mass-spring model for pre-bent plates 26
Figure 3.1 (a) Representative cell; and, (b) the unit cell 28
Figure 3.2 (a) Proposed crease pattern; (b) Miura-ori unit; and, (c) folding of half the cell 29
Figure 3.3 (a) Crease pattern for side I and II; and, (b) unit cell with the face-to-face connection method. 30
Figure 3.4 (a) Crease pattern for side I and II; and, (b) unit cell with the crease-to-crease connection method. 30
Figure 3.5 (a) Generalised crease pattern; and, (b-c) partially-folded configuration 31
Figure 3.6 Identical units with (a) $l_2 = l_4$; and, (b) $l_2 \neq l_4$. 33
Figure 3.7 Crease pattern and folding of units with $l_4^{II} \neq l_2^{I}$ 35
Figure 3.8 Folding of units from class: (a) 1; (b) 2; and, (c) 3 36
Figure 3.9 Tessellating unit cells with: identical Miura-ori angle along sheets for (a) $l_2 = l_4$; and ,(b-c) $l_2 \neq l_4$; and, varying Miura-ori angles along the sheet (d-e) class 1; and, (f) class 2 37
Figure 3.10 Unit cell with alternative a and α (a) crease pattern; (b) folded states; and, (c) self-locking behaviour 40
Figure 3.11 Crease-to-crease connected Tachi-Miura polyhedron 41
Figure 3.12 (a) Graded origami honeycomb crease pattern; (b) relationship between θ_1, θ_2 and θ_3; and, (c) folding of core from initial configuration to self-locking 42
Figure 3.13 Out-of-plane grading for class 2 cell 44
Figure 3.14 Locking in the in-plane and out-of-plane direction: (a) visualisation of locking; and, (b) normalised height and width variation with θ . . 45
Figure 3.15 Tessellating graded cells with: (a) the face-to-face connection method; and, (b-c) crease-to-crease connection method 47
Figure 3.16 Tilling of graded: (a) crease-to-crease connection cores; and, (b) combination of crease-to-crease connected Tachi-Miura polyhedron and face-to-face connection method 48
Figure 4.1 Splitting of creases to facilitate crease-to-crease connection method . 51

Figure 4.2 Stamping of tube 52
Figure 4.3 Tri-linear engineering stress-strain curve for numerical simulations . 54
Figure 4.4 (a) Mesh convergence study; and, (b) energy ratio comparison for element size of 0.5mm 55
Figure 4.5 FE simulation of manufacturing process 56
Figure 4.6 (a) Imperfection sensitivity; and, (b) friction coefficient sensitivity study 57
Figure 4.7 Deformation and plastic strain contours at nominal strains of: (a) 0.04; and, (b) 0.55 for alternative friction coefficients 58
Figure 4.8 Numerical and experimental comparison 59
Figure 4.9 Deformation comparison of S3 and FE 60
Figure 4.10 Ungraded tube normalised force vs nominal strain comparison for: (a) group A; (b) group E; (c) group B; (d) group C; and, (e) group D . 63
Figure 4.11 Comparisons of tubes with alterative a α's: (a) SEA; and, (b) initial peak force 64
Figure 4.12 Deformation of: (a) 10-60-141-3; and, (b) 10-75-141-3 . . . 64
Figure 4.13 (a) 11-60-120-3; (b); 10-60-150-3; and, (c) 10-60-160-3 . . . 65
Figure 4.14 10-60-71-4 (a) deformation; and, (b) normalised force vs nominal strain 67
Figure 4.15 6-60-141-4 deformation 67
Figure 4.16 Ungraded face-to-face tube normalised force vs nominal strain for: (a-b) comparison with the crease-to-crease connected tube; (c) group A; (d) group B; (e) group C; and, (f) group E 69
Figure 4.17 Deformation of: (a) TM10-60-141-3; (b) TM10-60-141-3-fr0; (c) TM10-75-141-3; and, (d) TM8-60-141-4 70
Figure 4.18 Deformation of: (a) TM10-60-160-3; and, (b) TM4-60-141-8 . . 71
Figure 4.19 Comparison of tube and core for: (a) 11-60-120-3; and, (b) TM11-60-120-3 71
Figure 4.20 Deformation of 11-60-120-3 6×6 core 73
Figure 4.21 Deformation of TM11-60-120-3 6×6 with: (a) friction; and (b) frictionless conditions 74
Figure 4.22 Normalised force vs nominal strain for: (a) 10-60-141-3 L0.5; and, (b) 10-60-141-*M* 75
Figure 4.23 Deformation of reduced length tube (a) frictionless; and, (b) μ = 0.25 . 75
Figure 4.24 Deformation of 10-60-141-10 76

Figure 4.25 Representative unit for the crease-to-crease connected core . . 77
Figure 4.26 Representative unit face-to-face connected core 79
Figure 4.27 Comparison of analytical model to numerical simulations for: (a) 10-60-141-3 tube with friction and frictionless contact conditions; (b) 11-60-120-3 for tube and core with friction contact conditions; (c) TM10-60-141 tube with friction and frictionless contact conditions; and, (d) TM11-60-120-3 tube and core with frictionless contact conditions. . . . 81
Figure 4.28 Deformation at $\varepsilon = 0.4$ for TM11-60-120-3 (a) tube; and, (b) 6×6 core with frictionless contact conditions 82
Figure 4.29 Horizontal offset 83
Figure 4.30 Analytical equation analysis: (a) Eq.(4.26(b)); (b) Eq.(4.26(c)); and, (c) Eq.(4.16) 85
Figure 4.31 Graded tubes with crease-to-crease connection method comparison of: (a) 10-10-10-45-50-58-82 with group A; (b) group B; (c) group C; (d) group D; and (e) group E 88
Figure 4.32 (a) Deformation and (b) plastic strain contours on undeformed geometry for 10-10-10-45-50-58-82 89
Figure 4.33 Cell angle for 10-10-10-45-50-58-82 at cross sections: (a) A-A; (b) B-B; and, (c) C-C 90
Figure 4.34 Deformation of (a) 10-10-10-45-48-51-82;(b) 10-10-10-45-50-58-82;(c) 10-10-10-45-55-74-82; and,(d) 10-10-10-45-55-65-82 . . . 91
Figure 4.35 Deformation of 8-10-14-45-50-57-81 93
Figure 4.36 Normalised force vs nominal strain for: (a) comparison to ungraded tubes; and, (b); effect of $\Delta\theta$ and variable a length 95
Figure 4.37 Deformation of TM10-10-10-45-50-58-82 96
Figure 4.38 Deformation of: (a) TM10-10-10-45-47-50-82; and, (b)TM14-10-8-45-50-57-82 96
Figure 4.39 Equivalent core behaviour for: (a) crease-to-crease connection method; and, (b) face-to-face connection method 97
Figure 4.40 Deformation of 8-10-13-45-50-58-81 6×6 core 99
Figure 4.41 Deformation and plastic strain contours for a central tube of the 8-10-13-45-50-58-81 6×6 core 100

Figure 4.42 Lateral displacement for a central tube of the 8-10-13-45-50-58-81 6×6 core at several section 100
Figure 4.43 Deformation and plastic strain contours for a central tube of the 8-10-13-45-50-58-81 6×6 core at sections: A-A, B-B; and C-C . . . 101
Figure 4.44 Deformation of TM14-10-8-45-50-57-82 6×6 core . . . 102
Figure 4.45 Deformation and plastic strain contours for a central tube of the TM14-10-8-45-50-57-82 6×6 core 103
Figure 4.46 Deformation and plastic strain contours at cross sections for a central tube of the TM13-10-8-45-50-57-82 6×6 core 103
Figure 4.47 Comparison of: (a) TM14-10-8-45-50-57-82; and, (b) TM14-10-8-45-50-57-82B, (c) TM14-10-8-60-64-70-113 104
Figure 4.48 Deformation and plastic strain contours for a central tube of the TM14-10-8-45-50-57-82 6×6 core 105
Figure 4.49 Deformation and plastic strain contours at cross sections for a central tube of the TM14-10-8-45-50-57-82B 6×6 core 106
Figure 4.50 Normalised force vs nominal strain comparison for TM14-10-8-45-50-57-82B and TM14-10-8-60-64-70-113 107
Figure 4.51 Model to study formation of hinges: (a) loading conditions; (b) constraints, RR; (c) FF constraints at top and bottom edges; (d) double thickness RR-i; (e) double thickness RR-ii; and, (f) normalised force vs nominal strain . 110
Figure 4.52 Deformation and plastic strain contours for: (a) RR; (b) FF; (c) RR-2-i; and, (d) RR-2-ii 111
Figure 4.53 Plastic strain contours for a central unit of the TM14-10-8-45-50-58-81 6×6 core at $\varepsilon = 0.84$ 113
Figure 4.54 Plastic strain contours for a central unit of the 8-10-13-45-50-58-81 6×6 core at $\varepsilon = 0.75$ 114
Figure 4.55 Hinge formation for the crease-to-crease connection method: (a) equivalent to the face-to-face connection method; (b) exclusively into l_2 lengths; and, (c) approximation from plastic strain contours . . 115
Figure 4.56 Super folding element for graded face-to-face connected cores . . 116
Figure 4.57 Graded core comparison to analytical prediction for: (a,b) TM14-10-8-45-50-58-82B 6×6 ;(c) TM14-10-8-60-64-70-82 6×6; and, (c) 8-10-13-45-50-58-82 6×6 119

Figure 5.1 Geometry of: (a) 2×1 core used in experiments; (b) 6×6 graded core; (c) 6×6 ungraded core 126
Figure 5.2(a) Force and displacement plots of each layer; (b) quasi-static strength of each layer vs strength of entire core 128
Figure 5.3 Female and male moulds used to stamp the sample; (b) sequential stamping of sheets 129
Figure 5.4 Schematic of experimental setup 131
Figure 5.5 Experimental and FE deformation comparison for positively graded specimens S1 with initial impact velocity of 31m/s . . . 134
Figure 5.6 Experimental and FE deformation comparison for positively graded specimens (a) S2 with initial impact velocity of 36m/s; and, (b) S7 with initial impact velocity of 67m/s 135
Figure 5.7 Experimental and FE deformation comparison for negatively graded specimens (a) S11 with initial impact velocity of 38m/s; and, (b) S13 with initial impact velocity of 68m/s 137
Figure 5.8 Force histories for positively graded samples with initial velocity of: (a) 36m/s; (b) 48m/s; (c) 67m/s; and, (d) 31m/s 138
Figure 5.9 Debonding sequence of S6 139
Figure 5.10 Force histories for negatively graded samples with initial velocity of: (a) 31m/s; (b) 39m/s; and, (c) 68m/s 140
Figure 5.11 Deformation of UG core for 25m/s, 50m/s, 100m/s and 150m/s . . 142
Figure 5.12 Deformation of G1-8 core for 25m/s, 50m/s, 100m/s and 150m/s . 143
Figure 5.13 Nominal strain in each layer for G1-8 at: (a) 25m/s; and, (b) 150m/s . 144
Figure 5.14 Deformation of G8-1 core for 25m/s, 50m/s, 100m/s and 150m/s . 145
Figure 5.15 Nominal strain in each layer for G8-1 at: (a) 25m/s; (b) 50m/s; (c) 100m/s; and, (d) 150m/s 146
Figure 5.16 Force at proximal and distal end for G8-1 at: (a) 25m/s; (b) 50m/s; (c) 100m/s; and, (d) 150m/s 148
Figure 5.17 Normalised stress-strain at proximal and distal ends for (a, e) 25m/s; (b, f) 50m/s; (c, g) 100m/s; and, (d, h) 150m/s 150
Figure 5.18 Normalised force vs nominal strain in layer in contact with support $\alpha = 43°$ for G8-1 $V_0 = 150$m/s 152
Figure 5.19 Face-to-face connected core 156

Figure 5.20 Analytical prediction of quasi-static behaviour of the core . . 157
Figure 5.21 Deformation of TMG1-8 face-to-face connected core for 25m/s, 50m/s, 100m/s and 150m/s 158
Figure 5.22 Deformation of TMG8-1 face-to-face connected core for 25m/s, 50m/s, 100m/s and 150m/s 158
Figure 5.23 Force at proximal and distal end for the TMG8-1 face-to-face connected core at (a) 25m/s; (b) 50m/s; (c) 100m/s; and, (d) 150m/s . . 159
Figure 5.24 Normalised force vs nominal strain at the proximal and distal ends for the face-to-face connected core at (a, e) 25m/s; (b, f) 50m/s; (c, g) 100m/s; and, (d, h) 150m/s 161
Figure 5.25 Comparison of the force at the distal end with analytical prediction for TMG8-1 for a velocity of: (a) 25m/s and 150m/s; and, (b) 25m/s. . 162
Figure 6.1 Crease pattern for: (a) side I of the unit cell; (b) side II of the unit cell . 167
Figure 6.2 Initial configuration of cores 169
Figure 6.3(a) Normalised force vs nominal strain for cores with $\theta_0 = 60°$ and $\theta_0 = 150°$; and, (b) deformation of core with $\theta_0 = 150°$ 169
Figure 6.4 Force-displacement for 6×6×3 core with $\theta_0 = 60°$ for velocity of: (a) 5m/s; (b) 10m/s; (c) 25m/s; (d) 50m/s; and, (e) 100m/s 170
Figure 6.5 Force-displacement for 6×6×3 core with $\theta_0 = 150°$ for velocity of: (a) 5m/s; (b) 10m/s; (c) 25m/s; (d) 50m/s; and, (e) 100m/s. (f) Force at distal end . 171
Figure 6.6 Deformation of representative central unit from the 6×6×3 core with $\theta_0 = 150°$ when impacted with a rigid mass with constant velocity of 10m/s 172
Figure 6.7 Normalised distal force histories for core with alternative number of units in the: (a) m direction; and, (b) *n* direction with $\theta_0 = 150°$ . . . 174
Figure 6.8 In-plane length change measurement locations of units loaded in the out-of-plane direction 174
Figure 6.9 Force-histories and length change of units for: (a) 6×4 core; (b) 6×6 core; (c) 6×12 core; and, (d) 6×18 core, with $\theta_0 = 150°$. 175
Figure 6.10 Deformation of 6×6 core with $\theta_0 = 150°$ 176
Figure 6.11 Deformation of 6×18 core with $\theta_0 = 150°$ 177
Figure 6.12 Force-histories and length change of units at the distal end for alternative *n* values when $\theta_0 = 60°$ 178

Figure 6.13 The influence of α on the rate-of-change of: (a) length and width; and, (b) absolute summation for $\theta_0 = 150°$ 181
Figure 6.14 Cores with: (a) $\alpha = 70.0°$;(b) $\alpha = 48.0°$; (c) $\alpha = 58.0°$; and (d) $\alpha = 75.5°$. (e) Analytical quasi-static prediction for the cores; and, (f) force at the distal end of the cores for impact velocity of 10m/s 183
Figure 6.15 Force at distal end of a 6×2 core with alternative number of units along the height: (a) full range response; (b) zoomed in response; and (c) cores . 185
Figure 6.16 Force at different sections for the 6×2×40 core: (a) full range response; (b) zoomed in response; and (c) section locations . . . 186
Figure 6.17 Force at distal end of a 6×6 core with alternative number of units along the height: (a) full range response; and (b) zoomed in response . . 186
Figure 6.18 Distal force-history and length change of units of the 6×6×40 core with $\theta_0 = 150°$ 187
Figure 6.19 Quasi- static force-displacement for 6×2 cores with and without lateral restraint 188
Figure 6.20: Initial deformation of a central unit of a 6×2×3-LR core under quasi-static loading 189
Figure 6.21 Deformation of a representative unit for the development of the super folding element 190
Figure 6.22: Assumed super folding element: (a) folding of super folding element; (b) top view in semi-folded state; (c) top view in locked state; (d) crease pattern of side I of a single cell; and, (e) unfolded super folding element for side I in locked state 191
Figure 6.23 Horizontal hinge line definition for the super folding element . . 192
Figure 6.24 Effect of increasing l_1, l_3 on the location of the hinges . . . 193
Figure 6.25 Travelling hinge formation and propagation 194
Figure 6.26 Angle swept by travelling hinge 195
Figure 6.27 Stretching deformation for super folding element . . . 196
Figure 6.28 Location where hinges form 199
Figure 6.29 Super folding element average force comparison with FE simulation . 199
Figure 6.30 Alternative deformation mode depending on location of double thickness 200
Figure 6.31 6×2×3 core with a=3mm 201

Figure 6.32 (a) Force; and, (b-d) nominal strain history for a 6×2×40 core with impactor velocity of 100m/s 203
Figure 6.33 Displacement of units close to the support for 100m/s . . . 204
Figure 6.34 Force history at distal end of selected units for 100m/s . . . 205
Figure 6.35 Unit 3 deformation for 100m/s 206
Figure 6.36 Unit 7 deformation for 100m/s 207
Figure 6.37 Force and nominal strain history for a 6×2×40 core with impactor velocity of 150m/s 207
Figure 6.38 Force and nominal strain history for a 6×2×40 core with impactor velocity of 200m/s 208
Figure 6.39 Force history at distal end of selected units for 150m/s . . . 209
Figure 6.40 Force and nominal strain history for a 6×2×40 core with impactor velocity of 75m/s 209
Figure 6.41 Nominal strain in units when unit 21 has densified (b) unit 31 has densified 210
Figure 6.42 Densification strain vs impactor velocity 212
Figure 6.43 Comparison of analytical mode with FE simulation . . . 213
Figure 6.44 Deformation of unit 1 for a 200m/s 214
Figure 6.45 Force at a cross section 2.76mm below the top of the core. . . 215
Figure 6.46 Assumed stubbing deformation mode for core at high velocities . 216

TABLES

Table 4.1 Dimensions of tube for experiments 51
Table 4.2 Aluminium foil material properties 53
Table 4.3 Geometry and results for ungraded crease-to-crease connected tubes . 62
Table 4.4 Geometry and results for ungraded face-to-face connected tubes . . 68
Table 4.5 Geometry and results for graded crease-to-crease connected tubes . 86
Table 4.6 Dihedral angle comparison between theoretical and FE . . . 92
Table 4.7 Geometry and results for graded face-to-face connected tubes . . 95
Table 4.8 Effect of α on locking behaviour for the face-to-face connection method 107
Table 5.1 Geometry of samples 127
Table 5.2 Experimental matrix 132
Table 5.3 SEA of cores 153
Table 5.4 Geometry of face-to-face connected core 156
Table 5.5 SEA comparison of face-to-face connected cores 160
Table 6.1 Crease pattern variables 167
Table 6.2 Dimensions of a single unit 182
Table 6.3 Comparison of hinge location 199

NOTATION

A	Area swept by travelling hinges
A_0	Area enclosed by the cross section of the core
C	Boolean set equal to 1 or 0
E	Elastic modulus
E_A	Energy consumed by rotating about angled hinge
E_c	Energy absorbed by travelling hinges for the angled hinges
E_f	Energy absorption efficiency
E_h	Energy absorbed by horizontal hinges
E_s	Energy consumed by stretching
E_t	Energy absorbed by toroidal surface for angled hinges
F	Axial force
F_0	Force at distal end
$F_{0,I}$	Average force from super folding element
$F_{0,II}$	Initial quasi-static peak force
$F_{avglock}$	Average force due to locking
F_{core}	Initial strength of entire core
F_d	Force at proximal end
F_{layer}	Initial strength of a single layer
F_m	Mean crushing force
F_{norm}	Normalised force
F_{squash}	Squash load
G	Impactor mass
H	Height of specimen
I_1	Numerical integral
L	Length of core
L_s	Total side length of crease pattern
L_{cr}	Critical buckling wave-length
L_h	Length term accounting for double thickness
M	Number of units in the out-of-plane direction
M_p	Plastic moment per unit length
SA	Surface area
V_0	Impact velocity

V_s	Minimum velocity for shock wave propagation
W	Width of cell
a	Miura-ori width
a_{SF} , $a_{SF,c}$, $a_{SF,f}$	Location of horizontal hinge formation for super-folding element
c_0	Longitudinal elastic wave speed
c_p	Longitudinal plastic wave speed
h	Height of single unit
l_1, l_2, l_3, l_4, l_5	Lengths of cease pattern
l_1^{min}, l_3^{min}	Minimum crease pattern lengths for side I and side II
l_{1c}^{min}, l_{3c}^{min}	Minimum crease pattern central lengths for side I and side II
m, n	Number of units in the in-plane directions
m_e	Mass/equivalent mass
r	Radius travelling hinge is bent and unbent around
s	Width of connection facets
t	Thickness
t	Time
v_0	Particle velocity
v_y	Velocity at which plastic waves are generated
α	Miura-ori angle
α_0	Initial Miura-ori angle
α_L, α_W, α_{LW}	α solutions for maximising lateral displacements
α_{SF}	α of super folding element
β	Folding angle of angled creases
β_0	Initial folding angle of angled creases
γ	Cell angle
γ_0	Cell angle in initial configuration
γ_1, γ_2, γ_3, γ_4	Cell angles at vertices
γ_A, γ_B, γ_C, γ_D	Cell angles at vertices with respect to the x-axis
γ_{max}	Maximum cell angle of crease pattern
$\Delta\alpha$	Angles swept for super folding element
$\Delta\theta$	Difference in θ between units in the out-of-plane direction
$\Delta\varphi$	Stretching angle for super folding element
δ	Vertical displacement

δ_{max}	Maximum vertical displacement
δ_p, δ_d	Vertical displacement at proximal and distal end of a unit
ε	Nominal strain
ε_D	Densification strain
θ	Dihedral angle
θ_0	Dihedral angle in initial configuration
μ	Coefficient of friction
ρ	Density
$\overline{\rho}$	Relative Density
$\overline{\rho}_{eqv}$	Equivalent relative density of core
ρ_s	Density of sheet material
σ	Stress
σ_0	Elastic stress wave
σ_d	Dynamic crushing stress
σ_m	Maximum stress experienced up until ε
σ_p	Quasi-static plateau stress
σ_{peak}	Dynamic stress associated with plastic wave propagation
σ_y	Yield stress
ϕ	Folding angle of horizontal creases = $(\pi - \theta)/2$
ϕ_0	Initial folding angle of horizontal creases

CHAPTER 1

INTRODUCTION

1.1 Background

In recent decades, energy usage resulting from the life-cycle of materials that provide structural support are estimated to contribute to over 14% of the global energy usage (Cullen and Allwood, 2010). The demand of these materials is likely to increase with the acceleration of construction in developing countries, and the replacement and rebuilding of structures within developed countries.

Reducing the embodied energy of engineering structures is key to increasing the sustainability of our built environment. One avenue of reducing the energy requirements is increasing the efficiency of the material processing and fabrication. Increasing the efficiency of these processes has the potential to reduce energy consumption, however these are not enough to offset the growing global economies (IEA, 2009). Another avenue is to reduce the material consumption through intelligent engineering designs. Architected structures show great potential in addressing both of these areas. With advances in planar manufacturing paired with origami techniques, new structural designs are possible, which not only increase the efficiency but also reduce the complexity of the manufacturing process. Structural efficiency is a key in minimizing resource consumption and reducing the embodied energy. Understanding the behaviour of these structures deserves much research attention, as this will ultimately allow their application in industry, increasing sustainability within the field.

Honeycomb structures are widely used in engineering because of their superb strength to weight ratio. These qualities proliferate the use of honeycomb structures to applications that would ideally require vastly different mechanical performance such as energy absorbing structures. Energy absorption devices are used widely in the: automotive; aviation; and.

aerospace industry, where they are implemented to dissipate kinetic energy in a collision so that a structure or person is protected. Honeycombs are not suitable for such application as they exhibit a large initial peak load followed by a significant load drop, reducing the amount of energy that can be absorbed. Additionally, they have very few design parameters, making them less ideal to meet their mechanical performance targets.

Graded structures, in which the mechanical properties vary from layer to layer, have the ability to overcome this problem. Placing graded structures around a main frame could enable sudden impact loading to be transmitted to the main frame over a prolonged period with reduced magnitude through unrecoverable plastic deformation experienced by the graded structure. As a result, the damage to the main frame is alleviated. Previous studies have achieved this gradient by varying parameters such as wall thickness, diameter, density and yield stress. The results from these studies show that the gradient can have a significant influence on the failure mode and thus energy absorption. However, fabricating structures that are graded in this manner is difficult, preventing their successful application.

A far more elegant solution is proposed in this thesis, where the grading is achieved through origami techniques and the variation of simple geometric parameters. In recent years, origami has received much interest from the engineering community. The ability to create 3D structures from a 2D sheet has seen the creation of many new novel structures. These origami structures are typically constructed out of identical repeating units resulting in a structure with uniform stiffness. Few studies have been carried out exploring how the geometry of an origami structure can be altered to achieve a graded stiffness, especially for dynamic impact events. Compared to grading structures through a change in density or thickness, achieving grading by varying the geometry of the crease pattern allows the structure to be manufactured from a flat sheet alleviating many of the manufacturing difficulties as well as providing a structure that is optimised for its application.

1.2 Aim and layout

The aim of this thesis is to facilitate the efficient design of cellular structures by optimising the management of external forces for both quasi-static and dynamic loading scenarios. To facilitate the functional grading of these structures, origami techniques will be pursued. The grading will be realised through origami inspired units that can be geometrically varied to achieve a desired graded stiffness, specifically in the field of energy absorption structures. The topics covered in this thesis are summarised as follows.

Chapter 2 presents an extensive literature review on the topics relevant to this thesis. Firstly, the general principles of energy absorptions devices are defined including 'ideal' energy absorption device as well as evaluation criteria. Following this, current literature detailing the behaviour of functionally graded materials, FGMs, under quasi-static and dynamic loading scenarios as well as limitations of manufacturing these standard FGMs is examined. Focus is then drawn to the behaviour of honeycombs in the in-plane and out-of-plane direction. Thirdly, origami principles will be reviewed with focus on the application of origami techniques used in the design of energy absorption structures. Finally, analytical models used to predict the dynamic behaviour of cellular structures are examined.

In chapter 3 origami techniques are applied to create an origami honeycomb with two alternative connection methods. The chapter then explores the different geometric possibilities for an origami honeycomb cellular structure through a kinematic study. Following this, techniques to grade the structures and introduce self-locking in both the in-plane and out-of-plane direction are highlighted. This chapter results in the identification of a number of unique cellular solids that exhibit varying kinematics as well as the ability to design self-locking behaviour.

Chapter 4 explored the effect that the out-of-plane self-locking has on the quasi-static behaviour numerically. The numerical model is validated using the experimental results.

Initially the numerical study focuses on the analysis of ungraded tubes (1×1 core) and 6×6 cores with both connection methods. These studies investigate the effect of the parameters used to parameterise the crease pattern. Following this, a numerical analysis of the graded cores is completed, highlighting the ability to grade the stiffness at defined points. Analytical equations are then derived for the initial force-displacement following the kinematics of the crease pattern and the subsequent behaviour due to self-locking. The analytical models are validated against the numerical models and provide insights on how the force can be altered with the underlying crease pattern. Compared to standard honeycombs, the origami honeycomb provides greater opportunity to grade the stiffness through the variation of the underlying crease pattern.

In chapter 5 the dynamic behaviour of the graded core is numerically investigated for both connection methods to assess if similar behaviour to standard FGMs can be achieved with the origami honeycomb. Initially, numerical simulations are validated through impact experiments of a 2×1 core and covers the: material testing; manufacturing; experimental setup; and experimental and numerical comparison. Following this, the validated numerical technique is used to investigate the effect of grading on a 6×6 core under constant velocity. This provides insight into how the grading influences the failure mode and therefore the energy absorption mechanisms of the device under dynamic loading. The numerical investigation showed that the grading could be used to increase the specific energy absorption or limit the force transferred to the structure for both connection methods.

In chapter 6 the dynamic behaviour of the origami honeycomb will be examined to assess the applicability of certain analytical models. To form an analytical model, the behaviour of the origami honeycomb is examined initially. As opposed to the previous chapters, which illustrated the ability to grade the stiffness of the origami honeycomb under quasi-static and dynamic loading, this chapter will focus on understanding the dynamic behaviour of ungraded cores with alternative geometries. This understanding of the underlying cells will enable the

development of analytical models that incorporate grading in the future. Ultimately an analytical model is suggested for the ungraded core.

Finally, chapter 7 provides a summary of the work in addition to future research avenues that the thesis uncovers.

CHAPTER 2

LITERATURE REVIEW

This chapter is split into four main sections. Initially the general energy absorption principles are defined. Following this, typical energy absorption devices found in literature are summarised including the concept of functionally grading these structures. Then, within this section, the focus is directed towards the behaviour of ungraded and graded honeycombs in the in-plane and out-of-plane directions. In the third section an overview of origami principles and the design of energy absorption devices using origami techniques is provided. Finally, an extensive review of analytical models for the impact of cellular structure is provided.

2.1 Energy absorption principles and evaluation criteria

Energy absorption devices play an integral part in many industries including automotive, ships and aerospace. Unlike conventional engineering structures, which are typically designed so they only undergo elastic deformation, energy absorption devices are designed for various impact scenarios resulting in vastly different analysis requirements that consider the associated large deformations and strain rate effects (Lu and Yu, 2003). Lu and Yu (2003) define the general principles for an effective energy absorption device as; irreversible energy conversion; restricted and constant reactive force; long stroke; stable and repeatable deformation mode; light weight and high specific energy absorption; and, low cost and easy installation.

During impact energy absorption devices should ideally dissipate the kinetic energy through irreversible means. Kinetic energy that is converted into elastic deformations is stored and then converted back into kinetic energy causing an elastic snapback that can result in additional damage to the structure or persons the energy absorption device is protecting. The mode of irreversible energy conversion is related to the material behaviour and geometrical

parameters. Generally ductile materials that exhibit a high strain capacity (i.e. metals) convert the energy through irreversible plastic deformations, whereas, brittle materials with low strain capacity (i.e. fibre reinforced composites) convert the energy through a variety of fracture mechanisms (Kindervater and Georgi, 1993).

An efficient energy absorption device will ideally exhibit a low peak force, $F_{0,II}$, such that the main structure does not experience a large reaction force, and a high and constant mean crushing force, F_m, such that the kinetic energy dissipated is high and the force fluctuations are minimal (Figure 2.1). Crush force efficiency is defined as the ratio of the mean crushing force to the peak force and provides an evaluation of the ability of the energy absorbing device to restrict and produce a constant reaction force. A value of 1 indicates an absorber with a rectangular force deflection curve. Values of less than 1 generally represent absorbers with a high initial peak force followed by a load drop as deformations continue (Kindervater and Georgi, 1993).

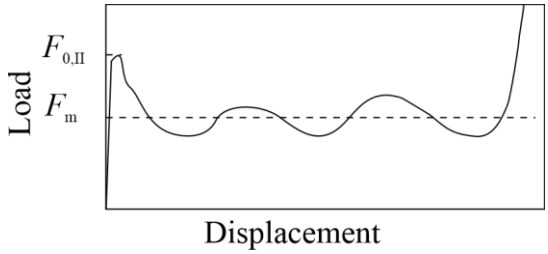


Figure 2.1 Typical load displacement curve

Another important factor is the stroke, the distance that the absorber is crushed. For the same stroke length, reducing $F_{0,II}$ reduces the energy absorbed by the structure. To absorb an equivalent amount of energy the stroke has to increase. This leads to the requirement for energy absorbers to have a long stroke. Stroke efficiency is defined as the ratio between the stroke when it is fully crushed to the initial length of the absorber, with larger ratios providing an indication of efficient material usage (Kindervater and Georgi, 1993).

Impact loads acting on structures have a high uncertainty. The ability of an energy absorbing device to produce a repeatable deformation mode is therefore required to ensure the designed level of energy absorption will match the in service energy absorption.

Additionally, the strain-rate sensitivity of the deformation mode can result in vastly different forces being transferred to the protected structure. Low dependency of the performance with the loading rate is therefore also a desirable characteristic.

The specific energy absorption, SEA, is defined as the energy absorbed per unit mass. Significant benefits (fuel economy, gas emissions, structural integrity, safety) can be derived from improving the energy absorption capacity and weight of these devices (Xu *et al.*, 2018). Large SEA values improve the effectiveness of the energy absorption device.

Due to the irreversible deformations, energy absorption devices are typically single use. Thus, to ensure their uptake, the ease and cost of manufacturing and installing the energy absorption device is an important requirement.

2.2 Energy absorption devices

Thin-walled structures are commonly used for energy absorbing purposes. A plethora of research has been conducted into metal tubes made out of common geometries (i.e. circular, square) leading to an in-depth understanding of the energy absorbing mechanism. The post-buckling behaviour is of most interest as this is where the majority of the energy absorption occurs. The wall thickness influences the failure mode of the tube greatly, with circular tubes crushing in axis-symmetric concertina mode, non-symmetric diamond mode or a mixture of both and square tubes typically crushing in non-compact mode or symmetric mode (Lu and Yu, 2003). In these failure modes the energy is dissipated through the formation of plastic hinges and material stretching. The plastic hinges come in two forms; stationary and travelling. Travelling plastic hinges sweep across a surface as crushing occurs, whereas stationary hinges do not. Wierzbicki and Abramowicz (1983) developed a super folding element which

accurately predicted the folding mechanism of selected metal structures. Whilst the energy absorption mechanism is understood well, these standard structures provide few parameters that can be adjusted to tune their mechanical behaviour.

Efforts to improve the structural efficiency have led to the introduction of a gradient in the mechanical properties of some cellular materials. These so called functionally graded materials, FGMs, have been manufactured by varying the material properties (density, strength, material type) or geometric parameters (diameter, width, wall thickness) (Xu *et al.*, 2018). Studies on these structures have shown that the gradient can have a significant influence on the failure mode and thus energy absorption (Zeng *et al.*, 2010; Liu *et al.*, 2012, 2013; Fan *et al.*, 2013; Zhang *et al.*, 2014). Additionally, under dynamic loading, FGMs show great potential in limiting the force transferred to the structure being protected, which is an important design feature for mitigating damage or injury. Whilst these structures exhibit enhanced performance when compared to their homogenous counterparts, the cost and difficulties associated with the manufacturing process generally prevent them from being widely applied (Chen and Goto, 2003; G Li *et al.*, 2015; Guangyao Li *et al.*, 2015; Ma *et al.*, 2018; Xu *et al.*, 2018). Origami has received much interest from the engineering community in recent years and shows great potential in overcoming these issues.

2.2.1 Honeycombs

Honeycombs and re-entrant honeycombs have also been applied widely as energy absorption devices due to their high strength-to-weight ratio (Wierzbicki, 1983; Gibson and Ashby, 1997; Zhao and Gary, 1998; Hu and Yu, 2010). When loaded in the in-plane direction their load-displacement response is a relatively ‘flat-topped’ curve typical of a Type I structure (Calladine and English, 1984; Gibson and Ashby, 1997). In contrast with quasi-static loading, where failure initiates in a single row of cells (Papka and Kyriakides, 1994), under dynamic loading,

three different failure modes are observed, dependant on the impact velocity for homogenous honeycombs (Ruan *et al.*, 2003).

The effect of in-plane grading has been investigated numerically in a number of studies (Ali *et al.*, 2008; Ajdari *et al.*, 2011; Shen *et al.*, 2013). In these studies, the grading is realised through the adjustment of the cell wall thickness or material properties. Generally, in these studies, positive gradients were shown to increase the energy absorption when compared to homogenous counterparts, whereas negative gradients were shown to limit the force transferred to the support. Whilst grading can be achieved in this manner it requires the structure to be manufactured from multiple sheets that have alternative thickness and/or properties to one another, greatly increasing the manufacturing complexity. The ability to grade a structure using sheets of identical thickness and properties would provide a more elegant solution.

When loaded in the out-of-plane direction honeycombs exhibit a high initial stiffness and peak force followed by softening behaviour as progressive failure occurs. This behaviour is typical of a Type II structure, whose behaviour is influenced greatly by lateral inertia effects under dynamic loading (Calladine and English, 1984; Zhao and Gary, 1998). Under dynamic loading, when compared to foams or honeycombs loaded in the in-plane direction, honeycombs loaded in the out-of-plane direction show some advantages in terms of SEA (Karagiozova and Alves, 2017). However, the large force transmitted to the supported end is a disadvantage and the post peak behaviour provides little opportunity to tune the stiffness. Again, origami techniques show promise in addressing these shortcomings.

2.3 Origami energy absorption devices

Origami provides the ability to create 3D structures from a 2D sheet. Various engineering structures have been developed using origami techniques, including energy absorption devices (Song *et al.*, 2012; Ma and You, 2014; Ma *et al.*, 2016; Xiang *et al.*, 2020).

2.3.1 General principles

The transformation from a 2D flat sheet to a 3D structure is realised through the assignment of a crease pattern. Figure 2.2 shows the widely used Miura-ori crease pattern. The crease pattern is made up of mountain and valley fold lines. In origami, developability refers to the ability to fold the 3D pattern from a flat sheet. A crease pattern is developable if the sum of the angles between crease lines around a vertex equals 2π (Tachi, 2009). Developability is an important characteristic as it allows the structure to be folded from a flat sheet. Flat-foldability refers to the ability of a crease pattern to be folded flat (Hull, 1994). For a crease pattern to be flat foldable, the difference between the number of mountain creases and valley creases meeting at a vertex must be ± 2 (Maekawa's Theorem); the summation of alternative sector angles about a vertex must be π (Kawasaki's Theorem); and, the paper is not able to intersect itself (the Big-Little-Big Angle Theorem) (Hull, 1994). In Figure 2.2 the crease pattern of a single Miura-ori unit this shown. At the vertex there are three valley folds and one mountain fold, $\alpha_1 + \alpha_3 = \alpha_2 + \alpha_4 = \pi$ and the paper does not self-intersect resulting in a crease pattern that abides by all three of these theorems. Crease patterns that do not abide by Kawasaki's theorem exhibit locking behaviour, which can be harnessed to lock a structure into a predetermined configuration.

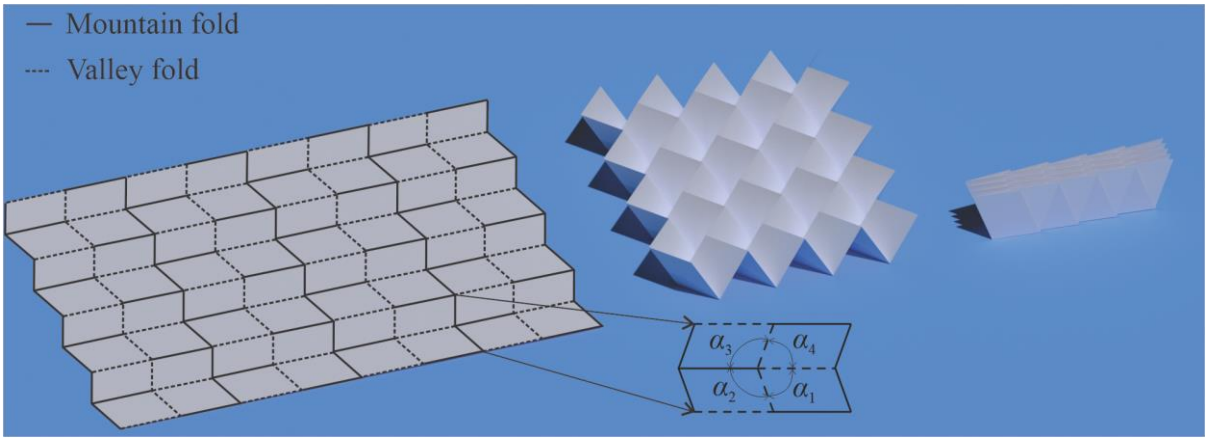


Figure 2.2 Miura-ori crease pattern

A subset of origami, rigid origami, is particularly important for engineering application. In rigid origami the facets do not stretch or bend during folding (i.e. they are ridged) and all deformations are localised at crease locations. This allows structures to be manufactured from a series of rigid sheets that are made from standard engineering materials. A crease pattern with this characteristic resembles a mechanism and therefore the kinematics of rigid origami can be modelled using mechanism theories such as the matrix method.

2.3.2 Origami energy absorption devices

Origami patterns have previously been introduced into thin-walled structures to control the buckling and post-buckling behaviour. By applying origami patterns to a square hollow section, Ma and You (2014) showed that the failure mode could be controlled such that the energy absorption increased and the peak force reduced. Similar results were also found for the kite-shaped pattern (Ma *et al.*, 2016) and the Tachi-Miura polyhedron (Yang *et al.*, 2016). Aside from the origami crash box, the crease pattern implemented in these structures are generally rigidly foldable. Therefore, during the deformation process the plastic strains are predominately localised at the crease locations and the plastic hinges are stationary i.e. they do not travel. As stated previously, for energy absorption purposes, travelling plastic hinges are desirable as they contribute a large portion of the total energy that is absorbed.

The majority of origami inspired structures are constructed from identical repeating units, and thus exhibit uniform stiffness along the length. A recent study used the Miura-ori unit as the base pattern to create a graded energy absorption device (Ma *et al.*, 2018). In the study, the device was loaded quasi-statically in the in-plane direction (perpendicular to the prismatic cells). By varying the geometric parameters over the volume, an increase in the energy absorption was achieved. Additionally, it was shown that the geometric parameters can be varied to tune the stiffness throughout the loading. This tuning was achieved by activating plastic strains in the facets through locking behaviour. This study solely focused on grading in

one direction, perpendicular to the prismatic cells. Additionally, each individual layer is developable, but the structure itself cannot be folded from a flat sheet as the locking behaviour relies on each layer folding into a flat sheet at different stages in the crushing process. When manufacturing the structure each individual layer therefore has to be folded separately and then subsequently stacked. Whilst promising results were achieved, there is great opportunity to extend this further using other crease patterns that allow the structure to be folded from a series of stacked sheets, and additionally explore grading in the other two directions. Specifically, in the direction parallel to the prismatic cells, the orientation typically used for energy absorption devices.

Fang *et al*. (2016) introduced self-locking to grade the stiffness of the structure in the direction parallel to the prismatic cells. This was achieved by connecting two Miura-ori units with varying internal sector angles, α, providing a single step in the stiffness. Whilst promising results were achieved, there is great opportunity to extend this further to include multiple units with varying α, providing multiple stiffness jumps. Additionally, the origami structures proposed in these studies are asymmetric, this may be undesirable for a number of applications as the response of the structure will also be asymmetric.

The studies mentioned above also only considered quasi-static loading conditions. Under dynamic loading conditions, the response of origami inspired structures become more localised, resulting in layer by layer collapse (Karagiozova *et al.*, 2019; Harris and McShane, 2021). This localisation reduces the auxeticity of the structure as the crushing deviates from the rigid folding mode (Harris and McShane, 2021). Additionally, under quasi-static conditions the stiffness increase observed by Fang *et al*. (2016) and Ma *et al*. (2018) occurs due to the origami structure reaching the end of its kinematic range, this behaviour is a feature of the quasi-static response of the origami pattern as a whole rather than the strength of the individual units that make up the structure. To functionally grade the structure for an impact event, the

strength of the individual cell in their initial configuration may also be an important characteristic.

2.4 Analytical models for impact

Before going into the details of analytical models for cellular structures, it is useful to briefly discuss the travelling of stress waves through solids. Following this, analytical models that have been applied to Type I and Type II structures will be summarised.

2.4.1 Formation and travelling of stress wave in solids

Detailed explanations on the stress wave propagation in solids can be found in most textbooks concerning impact, only salient details will be provided here.

Stress waves are formed in deformable bodies when subjected to a disturbance. When a disturbance is applied there is a finite time required for the disturbance to propagate through the body. For cellular solids subject to an impact event, elastic and plastic stress waves are typically formed (Johnson, 1972; Guo *et al.*, 2010). In a homogenous slender rod, the longitudinal elastic wave speed, c_0, is provided below (Johnson, 1972), where: E is the elastic modulus of the material; and, ρ is the density. This equation neglect Poisson's effects.

$$c_0 = \sqrt{\frac{E}{\rho}} \tag{2.1}$$

Typically, when the disturbance is not that large the solid deforms elastically. In the case of a rod which is impacted by a rigid impactor, the magnitude of the elastic stress wave, σ_0, is proportional to the impact velocity, elastic wave speed and density as follows.

$$\sigma_0 = \rho c_0 v_0 \tag{2.2}$$

In the equation, v_0 is the particle velocity and ρc_0 is commonly referred to as the acoustic impedance. When a stress wave encounters a boundary with a different mechanical impedance reflection and transmission of the wave occur. By adjusting the difference in mechanical

impedance between the rods, the stress wave magnitude that is transmitted and reflected can be altered (Johnson, 1972).

Two special boundary conditions that exist are when the stress wave encounters a free or fixed end. When reflecting from the free end the stress has the same magnitude but a phase change of π i.e. a compressive wave reflects as tensile wave and visa-versa. When reflecting from a fixed end the phase of the stress wave remains the same resulting in a doubling of the total stress magnitude (Yu and Qiu, 2018).

Another important boundary can be in the form of a bend. When an elastic longitudinal stress-wave reaches a bend, longitudinal and flexural waves are reflected and transmitted. The bend angle has a large influence on the magnitude of these stresses, with larger bends resulting in smaller axial stress transmission (Guo *et al.*, 2010). For larger bends, when a compressive axial stress reaches the bend, it may even result in the transmission of a tensile stress wave.

For materials that exhibit elastic-plastic behaviour, in addition to the elastic precursor wave, a plastic wave may also be generated on impact or on reflection of the elastic precursor wave. The velocity at which a plastic wave is generated, v_y, can be estimated by setting the magnitude of the stress wave equal to the yield stress, σ_y, in Eq.(2.2) and rearranging.

$$v_y = \frac{\sigma_y}{\rho c_0} \tag{2.3}$$

If the velocity of the rigid impactor is larger than v_y a plastic wave will be generated. Alternatively, if the elastic stress wave is larger than or equal to $0.5\sigma_y$, on reflecting off a fixed boundary a plastic stress wave will also be generated. The plastic wave speed, c_p, for a homogenous slender rod is given in the equation below (Johnson, 1972).

$$c_p = \sqrt{\frac{1}{\rho}\frac{d\sigma}{d\varepsilon}} \tag{2.4}$$

Whilst the elastic wave speed is typically constant, the plastic wave speed is dependent on the slope of the materials constitutive behaviour. For materials that exhibit stress-strain

behaviour that is concave to the strain axis, the tangential modulus reduces, resulting in scattering of the plastic waves. In contrast, for materials that exhibits stress-strain behaviour that is convex to the strain axis, the tangential modulus increases, resulting in the convergence of the plastic waves. This results in the formation of a shock front (Figure 2.3), where there is a strong discontinuity in the particle velocity and stress (Lu and Yu, 2003; Yu and Qiu, 2018). In the case of a shock front, rather than the absorbed energy being proportional to the area below the stress-strain curve between the initial (point A) and final state (point B), the absorbed energy is instead proportional to the area below the Rayleigh line that connects the initial (A) and final states (B) shown in the figure below. A shock wave therefore results in a larger change in internal energy than the quasi-static scenario (Lu and Yu, 2003).

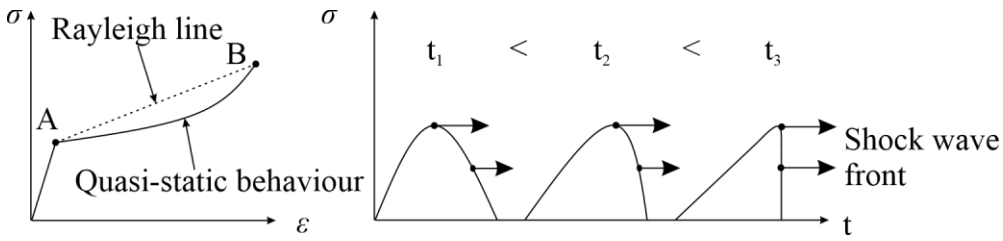


Figure 2.3 Formation of a shock front for strain-hardening material (Lu and Yu, 2003)

For a semi-infinite length bar made from elastic-plastic linear strain hardening material, the dynamic stress associated with the plastic wave propagation, when impacted at a velocity $V_0 \geq v_y$, can be determined with the below expression (Yu and Qiu, 2018).

$$\sigma_{peak} = \sigma_y + \rho c_p \left(V_0 - \frac{\sigma_y}{\rho c_o} \right) \tag{2.5}$$

2.4.2 Analytical models for Type I structures

A continuum approach utilising shock theory has successfully been applied to analytical model the behaviour of cellular structures that exhibit Type I behaviour (Reid *et al.*, 1983; Reid and Peng, 1997). In these continuum models the cellular structures behaviour is represented as rigid-perfectly plastic-locking (R-P-P-L). On impact it assumed the stress in front of the shock

wave instantly rises to the quasi-static plateau stress, σ_p, and the shock wave travels form the proximal end towards the distal end. Applying the conservation of mass and momentum across the shock front, the dynamic crushing strength, σ_d, of the cellular structure that is rate-independent can be found using the equation provided below. In this equation the second term represents the axial inertia where ε_D is the densification strain.

$$\sigma_d = \sigma_p + \frac{\rho}{\varepsilon_D} V_0^2 \tag{2.6}$$

In reality, on impact, rather than the stress ahead of the shock front instantly increasing to σ_p, an elastic precursor wave would travel along the cellular structure raising the stress as it travels towards the distal end (Reid *et al.*, 1983). Once the elastic stress wave reaches the support it is reflected. Harrigan *et al.* (2005) assumed this reflection resulted in a second shock front forming from the distal end, and used an elastic-plastic-hardening model that captured this behaviour. Notwithstanding, the R-P-P-L matched experimental and numerical work quite well.

In Eq.(2.6) the magnitude of the second term generally becomes dominant under high velocity impact. The selection of the densification strain therefore can manipulate the magnitude of the dynamic stress greatly. The R-P-P-L model is therefore only appropriate for materials with a well-defined densification strain. Zou *et al.* (2009) studied the in-plane crushing of honeycombs and found that the densification increased with velocity towards an asymptote 15% larger than the value associated with quasi-static loading. Rather than use the quasi-static densification strain, they therefore used a densification strain that is a function of the velocity in Eq.(2.6).

To predict the minimum velocity where shock wave propagation can be expected, V_s, Tan *et al.* (2005) proposed a kinematic existence condition for aluminium foam as follows.

$$V_s \geq \sqrt{\frac{2\sigma_p \varepsilon_D}{\rho}} \tag{2.7}$$

As described above, Harrigan *et al.* (2005) assumed that a shock wave develops at the distal end of the core on the reflection of the elastic stress wave. While a shock wave could eventually develop, initially the compaction begins under zero velocity at the distal end, and therefore it is below the critical velocity (Eq.(2.7)) required for shock propagation. The double shock mode provides a convenient and simple approach; however, it is not capturing the physical behaviour correctly.

Shock wave theory has also been applied to derive analytical models that predict the behaviour of a graded cellular rod subjected to a rigid mass with an initial velocity (Shen *et al.*, 2013; Shen *et al.*, 2014). In these models the continuum is modelled as R-P-P-L. Similar to the homogenous continuum R-P-P-L model described above, for positive gradients the shock wave exclusively travels from the proximal end to the distal end. In contrast, for negative gradients the model assumes that both forward and backward shock waves form on impact. As described above, this is a simplification, however, it is not physically and mathematically correct, as a shock wave will not form at sub critical velocities. However, these models showed reasonable agreement with FE analysis. Further modifications using a rigid-power-law material model, instead of a rigid-perfectly-plastic-rigid model, further improved the accuracy (Shen *et al.*, 2016).

Hu and Yu (2010) found a consistent equation for the dynamic crushing strength of a honeycomb loaded in the in-plane direction utilising a structural approach of the collapse mode rather than a continuum approach. A similar method was also applied to derive the dynamic crushing strength for a re-entrant honeycomb that exhibits a negative Poisson's ratio (Hu *et al.*, 2018). However, in this paper, when calculating the linear momentum for each cell, the assumed initial state of the cell at the crushing front has a non-zero velocity, where the proximal

end has an equivalent velocity to the crushing front and the distal end is stationary. Once this cell is crushed it imparts the same velocity profile to its neighbouring unit that is now at the crushing front, assuming constant impactor velocity. The change in momentum of the neighbouring cell to the assumed initial velocity profile at the end of the crushing of the cell is not accounted for in the momentum balance by Hu *et al.* (2018), resulting in a lower axial inertial term than that found using a continuum approach. This results in an underestimation of the dynamic crushing strength.

Karagiozova *et al.* (2019) also applied the conservation of momentum approach for the dynamic in-plane compression of a Miura-ori metamaterial. The model assumes that crushing of the core occurs layer by layer in a sequential manner from the proximal end to the distal end. Additionally, the crushing of each cell is assumed to follow the deformation mode prescribed by the crease pattern, resulting in the force at the distal end of each unit being associated with the quasi-static collapse mode. The cells at the crushing front are then assumed to accelerate from rest to the velocity of the impactor. Applying the conservation of moment where the force at the distal end of the unit is equal to the quasi-static initial peak force, they found an equation for the average dynamic force consistent with Eq.(2.6), which was derived assuming a shock wave formation. The energy absorption is also taken as the area underneath the Rayleigh line in the paper. Miura-ori units with relatively small dihedral angles (i.e. 60° - 100°) have quasi-static behaviour typical of a Type I structure. For large velocities, the analytical model provided close agreement with FE simulations. However, as the dihedral angle increases, it would be expected that the wave front becomes more diffuse, at which point the applicability of shock wave theory will be questionable.

Mass spring models have also been implemented to predict the behaviour of cellular structures with Type I behaviour (Li and Meng, 2002; Gao and Yu, 2006). However, as outlined by Harrigan *et al.* (2010), mass-spring model assume a loading path that follows the quasi-

static behaviour. In the case where shock waves form in cellular materials, mass-spring models are unable to capture the strong discontinuity in the stress and particle velocity. As detailed in section 2.4.1, the energy absorbed due to shock wave propagation is the area underneath the Rayleigh line, as opposed to the area underneath the quasi-static loading path. Therefore mass-spring models will tend to underpredict the energy absorbed as velocity increase.

2.4.3 Analytical models for Type II structures

Early work on structures that exhibited Type II behaviour was focused on the behaviour of a pair of pre-bent plates impacted with a rigid projectile. Zhang and Yu (1989) created an analytical model for a pair of pre-bent plates subjected to an impacting mass. In this theoretical model the initial impact is assumed to be inelastic between two rigid bodies, resulting in an instantaneous energy loss. After this initial impact the top of the specimen and impactor are assumed to have a common velocity. Following this, the remaining energy absorption is captured by a one degree of freedom model, consisting of four rigid links connected with hinges. The energy absorbed during phase I was found to be a function of the mass ratio (m_e/G) and the initial cell geometry and did not depend on the initial impact velocity or the material properties. When compared to experiments, Zhang and Yu (1989) predicted a greater effect of the initial cell angle than found in experiments conducted by Tam and Calladine (1991).

Rather than treating the initial interaction as an instantaneous loss of energy, Tam and Calladine (1991) assumed the initial impact between the striker and the top of the specimen occurs over a finite time period. In the analysis, in comparison to Zhang and Yu (1989), they replace the rigid links with axially deformable ones. These axially deformable bars are assumed to be rigid until yielding, at which point the plates cross-section support the full squash load, resulting in the axial shortening of the plates. The velocity attenuation of the striker can be simply found by applying Newton's second law, where the force decelerating the striker is equal to the squash load. The velocity of the striker can also be found by differentiating the

longitudinal displacement taken at the top of the specimen with respect to time. The longitudinal displacement of the specimen is the summation of the axial shortening and the longitudinal displacement associated with the inextensional collapse mode of the bars. This initial axial shortening phase ends once the bars have accelerated laterally to an extent where the longitudinal velocity associated with the inextentional deformation mode is equivalent to the velocity of the striker. The remaining energy is then absorbed through the rotation of the plastic hinge. Unlike Zhang and Yu (1989) models, Tam and Calladine (1991) model accounts for the change in geometry during the first phase of the response. This allows the model to account for the change in the equivalent mass associated with the change in the internal angle of the plates as the structure collapses. Additionally, the energy absorbed in Phase I is a function of the initial impact velocity and the material properties.

In both the models described above the elastic behaviour of the pre-bent plates was not accounted for. Su *et al.* (1995) addressed this by representing the pre-bent plates with four elastic-plastic deformable bars connected with elastic-plastic hinges. Zou *et al.* (2007) studied a chain of these pre-bent plates also using an elastic-plastic bar-hinge model which additionally accounted for self-contact during the collapse mode. Interestingly, Zou *et al.* (2007) showed that increasing the number of pre-bent plates in a chain results in a reduction of its overall inertia sensitivity. This is because the energy absorbed in the initial axial compression phase becomes proportionally smaller to the energy consumed by rotation of hinges as the number of pre-bent plates in the chain increases.

In the models described above, the deformation is assumed to occur through uniform axial compression in the bars and rotation about the hinges. These models are therefore only applicable for impact velocities and slenderness ranges where this assumed deformation mode occurs. As velocity increases or the slenderness of the members decreases, it is expected that the deformation of the pre-bent plates becomes more localised, resulting in alternative

deformation modes. For these scenarios the models described above will not be able to capture the behaviour of the structure.

The models above also assume that the propagation of the axial wave can be decoupled from the buckling of the member. In reality, under high velocity impacts that induce axial plastic stress waves, plastic buckling of the member will occur during the waves propagation, leading to the creation of bucklewaves (Vaughn and Hutchinson, 2006). Plastic stress waves occur when the impactor velocity is greater than the velocity found using Eq.(2.3). This results in the formation of two stress waves, an initial elastic stress wave, travelling at c_0, raising the stress to σ_y, followed by a plastic stress wave, travelling at c_p. For linear strain hardening materials, a uniform stress state is assumed to form within the region behind the plastic stress wave with magnitude found using Eq.(2.5). In the region behind the plastic wave, short wave buckles occur, however, due to lateral inertia effects this section will absorb the majority of the energy through axial straining. Vaughn and Hutchinson (2006) introduced a bucklewave model to predict the critical length, L_{cr}, at which buckling will occur, resulting in the end of this initial phase. The critical length is calculated assuming a beam with clamped ends is subjected to a uniform compressive stress equal to the stress found using Eq.(2.5) assuming that $V_0 >> v_y$. This quasi-static analogy is assumed to be reasonable as the stress, strain and particle velocity are uniform within the region behind the plastic wave front. Clamped conditions at the location of the plastic wave front are assumed reasonable as the stress and strain ahead of the plastic region was found to reduce substantially and the lateral deformation was small. When calculating L_{cr}, it was found that the first mode solution did not accurately capture the observed deflection bucklewaves (Vaughn and Hutchinson, 2006). This was because, instead of the peak deformation occurring at the centre of the clamped beam, local peaks formed and remained in the same location during the progression of the plastic waves. The lateral inertia stabilisation

results in higher modes, meaning that plastic wave can traverse far greater distances along the beam than the L_{cr} found assuming the first buckling mode.

Several studies on the behaviour of prismatic cores (Ferri *et al.*, 2006, 2010; Radford *et al.*, 2007) found that the initial phase, associated with the axial straining, would end once the plastic wave reaches the distal end of the core. From these results Ferri *et al*. (2010) created a continuum model assuming shock wave propagation for a double layer prismatic core that exhibits Type II behaviour under quasi-static conditions. The homogenised properties in the model consisted of a dynamic dual-level stress-time model. The initial stress was taken as the dynamic stress associated with the plastic-wave propagation (Eq.(2.5)). The initial phase ends once the plastic stress wave reaches the distal end of the specimen (H/c_{p}), resulting in a stress drop to a steady state value, calibrated from FE simulations. The results showed reasonable agreement for high velocities. Discrepancies were due the effects associated with the elastic-wave propagation, which was not considered in the model. Additionally at lower velocities the assumption of the formation of a shock front may become invalid.

In contrast, Li *et al.* (2019), found that the end of the initial phase was captured by calculating the L_{cr} using the first mode for a honeycomb loaded in the out-of-plane direction. A dual-level stress behaviour was then applied, where the initial stress is calculated in the same manner as Ferri *et al*. (2010) described above. In the second phase, where the progressive buckling of the cell walls occurs, the stress is calculated by assuming that the folding begins only once an adjacent fold has completely collapsed. For linear-strain hardening materials, once the neighbouring cell collapses, a plastic-wave is formed at the proximal end of the cell, resulting in an increase in the stress state (Eq.(2.5)). The plateau stress for the honeycomb is then calculated using this σ_{peak} for the material rather than σ_{y}. Using this plateau stress as the force at the distal end of the fold, Li *et al.* (2019) then apply the conservation of momentum to

calculate the dynamic force at the location of the folding front. Again, the energy absorbed for this approach represents the area underneath the Rayleigh line.

The model used by Li *et al.* (2019) was based partly off the phenomenological model described by Karagiozova and Alves (2017). However, this model was only used by Li *et al.* (2019) to calculate the plateau stress of the honeycomb that accounts for the stress increase caused by the propagation of a plastic-wave in linear strain-hardening material. In contrast to the continuum approaches assuming shock wave formation, Karagiozova and Alves (2017) developed an analytical model for honeycomb loaded in the out-of-plane direction applying the conservation of energy for a load path defined by the dynamic collapse curve of the honeycomb. This approach was pursued as the significant softening behaviour results in strain localisation which always occurs within a single fold, regardless of the impact velocity. The dynamic deformation mode was therefore known and it was possible to separate the stages of deformation. The collapse of the honeycomb was assumed to occur in two stages. Initially buckling occurs (formation and development of folds), corresponding to the dynamic plateau stress of the honeycomb, followed by flattening, which absorbs additional energy due to the development of larger deformations. The initial peak force is not captured by the model as only the dynamic plateau stress during the buckling phase is considered. Notwithstanding, the length of the cores simulated were large enough that this initial peak force had minimal effect and the model was therefore able to capture the velocity attenuation of the honeycomb loaded in the out-of-plane direction well. The formation of a shock wave is not assumed here and therefore the absorbed energy is the area underneath the stress-strain curve of the honeycomb rather than the energy below the Rayleigh line.

Harrigan *et al.* (2005) applied a continuum approach assuming shock wave formation for wood loaded along the grain at high velocities. Wood loaded along the grain has behaviour consistent with Type II structures. That is, the wood is sensitive to inertia effects, resulting in

the suppression of the quasi-static deformation mode in favour of an initial higher energy deformation mode when subjected to an impact. In order to account for this stiffness increase due to inertia effects, rather than applying the quasi-static load displacement behaviour for the wood in the continuum model, Harrigan *et al.* (2005) used a dynamic load-displacement behaviour for the wood that was proposed from the results of Split Hopkinson Pressure Bar experiments. It is not clear how well defined the dynamic densification strain is from the wood from experiments, as discussed earlier, the selection of the densifications strain can vary the analytical predictions greatly. The dynamic load-displacement curve of the wood was concave to the displacement axis, and therefore Harrigan *et al.* (2005) approximated it as a Type I structure and applied the continuum approach assuming the formation of a shock wave as described previously. At high velocities the analytical model matched the experiments well. However, at lower velocities the results deviated. This is due to the analytical analysis assuming the deformation follows the higher energy mode for the entire crushing process of the specimen.

Mass-spring models have also been applied to predict the behaviour of pre-bent plates subjected to an impacting mass with an initial velocity. Gao *et al.* (2005a, 2005b) mass-spring model incorporated two types of spring (Figure 2.4). The first spring, representing the contact, is a constant force spring between the impacting mass and the lumped mass at the top of the specimen. This lumped mass, for the pre-bent plates, is a variable equivalent mass that accounts for the lateral inertia during the folding process. The constant force of the spring is set to the squash load of the pre-bent plates. The second spring, a non-linear spring, representing the quasi-static behaviour of the pre-bent plates, connects the lumped mass to the neighbouring lumped mass or support. The mass-spring model therefore explicitly defines a deformation path which the model must follow, and therefore it is only applicable for velocities and slenderness ranges where the assumed deformation mode occurs.

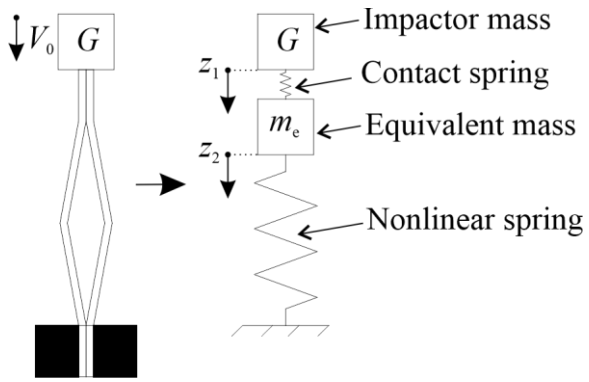


Figure 2.4 Equivalent mass-spring model for pre-bent plates (Gao *et al.*, 2005a)

Setting the second spring to the quasi-static behaviour of the pre-bent plates is also problematic. Due to inertia effects, Type II structures exhibit higher energy modes initially. In the case of the pre-bent plates (Tam, 1990; Tam and Calladine, 1991), the initial phase was dominated by axial compression. Therefore, by setting the spring to the quasi-static behaviour, the force transferred through the plates in the initial phase is not captured correctly. However, in Gao *et al.* (2005a, 2005b) the spring representing the quasi-static behaviour of the plates included an initial peak equal to the squash-load. This is significantly higher than the peak found from the quasi-static simulations (Gao *et al.*, 2005a) and therefore does not represent the quasi-static behaviour correctly for the pre-bent plates analysed in this study.

2.4.4 Analytical model summary

A variety of analytical models have been applied to structures that exhibit both Type I and Type II behaviour in the literature. The application of shock wave propagation in cellular materials assumes that the cells are sufficiently small and the characteristic wave thickness of the shock wave is comparable with the cell size (Tan *et al.*, 2005). For cellular solids, the application of shock theory assumes that the single cell attains a fully densified state within a very short time, disregarding the stress-strain history. The majority of studies that apply shock wave theory are on structures that exhibit Type I behaviour. These structures have minimal lateral inertia effects, the plastic wave front is predominately confined within a single cell and

the force at the distal end of the cell is equal to the quasi-static force. However, as pointed out by Tan *et al.* (2005), the shock wave approach is only applicable for velocities where a plane plastic wave front develops. In sub-critical velocity regimes, increases in the dynamic force may instead be due to micro-inertial effects of the cell.

Generally, for Type II structures the wave front becomes more dispersed and therefore the application of shock theory becomes more questionable. Continuum models have nonetheless been pursued for these types of structures where rather than using the quasi-static load displacement behaviour, dynamic (Harrigan *et al.*, 2005) or dual level behaviour (Ferri *et al.*, 2010; Li *et al.*, 2019) are implemented.

Where the formation of shock fronts is not expected, both mass-spring models (Li and Meng, 2002; Gao and Yu, 2006) and a phenomenological (Karagiozova and Alves, 2017) provide reasonable agreement for Type I and Type II structures respectively. However, these models will underpredict the energy absorbed when shock waves occur. Additionally, the phenomenological model does not predict the maximum peak force at both the proximal and distal ends. These however have been predicted for Type II structures assuming that lateral inertia allows the squash load to develop in the structure and the dynamic initial stress is associated with plastic-wave propagation (Ferri *et al.*, 2010; Li *et al.*, 2019).

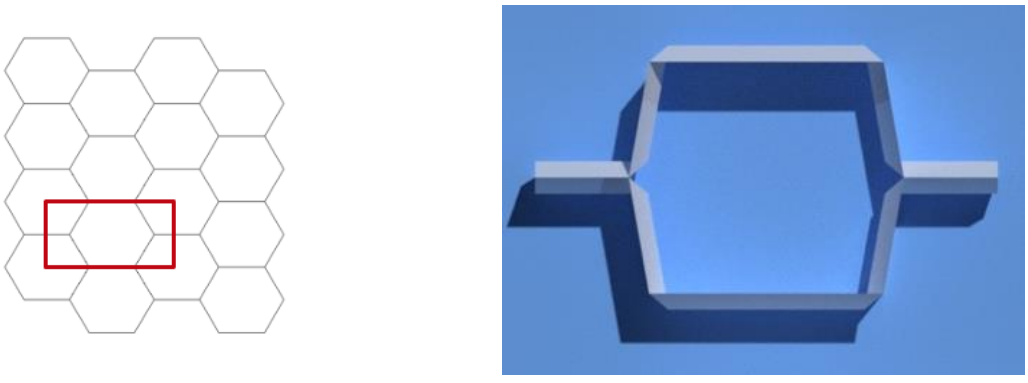
Mass-spring models for Type II structures have been less successful at describing the behaviour. This is due to the lateral inertia effects, which prevents the units from crushing in the quasi-static manner during the initial period. If this period is significantly long in comparison to the total collapse time of the structure, the mass-spring model will not provide a good representation of the behaviour. However, for sufficiently large structures, this initial phase is relatively short in comparison to the second phase and the mass-spring model may therefore be more applicable, assuming the deformation mode follows the quasi-static one.

CHAPTER 3

KINEMATICS

Honeycombs are used widely in engineering applications, however their mechanical performance is not ideal for certain applications, with few design variables available to tune their response. Origami techniques can be implemented to form arbitrary 3D shapes, including honeycombs. An origami honeycomb may alleviate this issue by allowing the design of honeycombs with greater functionality through the simple adjustment of the underlying crease pattern. To this end, the following chapter explores the different geometric possibilities for an origami cellular structure derived from a honeycomb.

A representative cell from a honeycomb will be used to study the kinematics (Figure 3.1). Initially the general kinematics for one sheet (one half of a cell, Figure 3.2(c)) will be derived. The geometric space for a unit cell will then be traversed by exploring the possibilities in which two sheets can be attached to form a cell. These alternative geometries will be separated based on their ability to fold through their kinematic range and through their ability to tessellate and form a cellular structure. Using this family of cellular structures, the ability to grade the core in the in-plane and out-of-plane direction will be explored



(a) (b)

Figure 3.1 (a) Representative cell; and, (b) the unit cell

3.1 Geometry and connection method

Recently a novel crease pattern was proposed (Wang *et al.*, 2020) that exhibits both negative in-plane and out-of-plane Poisson's ratio (Figure 3.2(a)). In the figure, solid lines represent mountain creases and dashed lines represent valley creases. The crease pattern is formed by a repetition of a Miura-ori unit (Figure 3.2(b)). The Miura-ori unit has one degree of freedom as four creases meet at each vertex. When this crease pattern is folded, the edges will either form a honeycomb or re-entrant honeycomb cross section (Figure 3.2(c)), depending on the internal angle, α, and the dihedral angle, θ, selected.

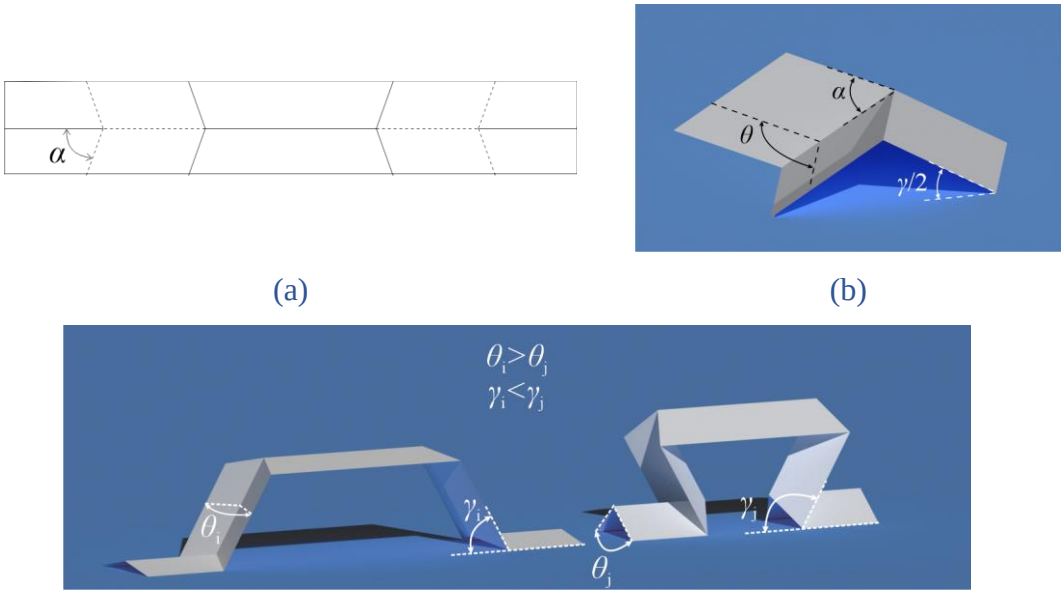
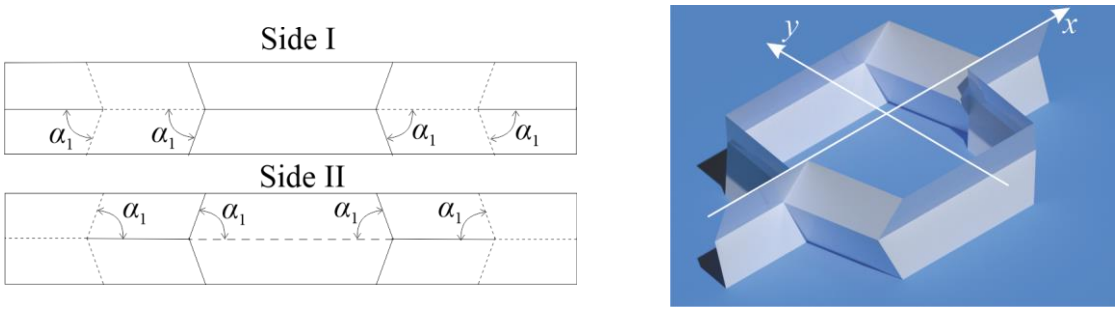


Figure 3.2 (a) Proposed crease pattern; (b) Miura-ori unit; and, (c) folding of half the cell

Two methods of joining the sheets to form a unit cell are defined as the face-to-face and crease-to-crease connection methods. The former method involves the connection of two separate crease patterns (side I and side II) that have identical geometric parameters but are mirrored about each Miura-ori vertex. The sheets can then be attached along the facets (Figure 3.3(b)), producing the so called Tachi-Miura polyhedron (Miura and Tachi, 2010). Connecting sheets in this manner results in the loss of symmetry in the *x*-*x* plane (Figure 3.3(b)). This may be undesirable for a number of applications as the response of the structure will not be

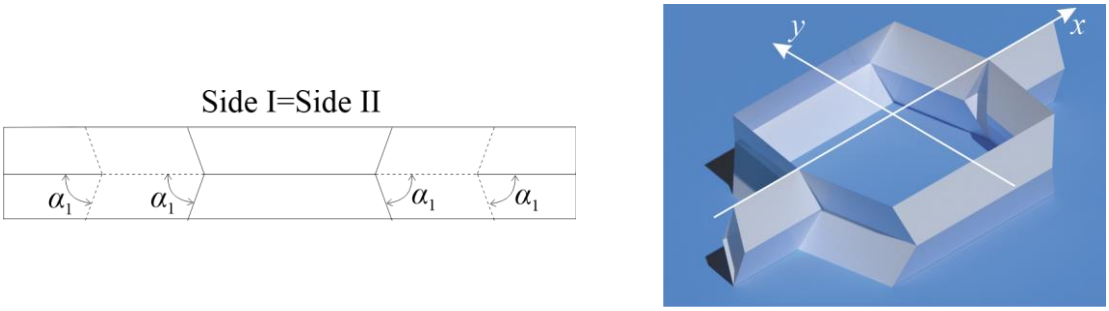
symmetric. Additionally, the resulting structure does not provide open cells in the in-plane directions, trapping moisture that can proliferate the degradation process (Heimbs, 2013).



(a) (b)

Figure 3.3 (a) Crease pattern for side I and II; and, (b) unit cell with the face-to-face connection method

A second method, the crease-to-crease connection method, preserves symmetry in both the *x*-*x* and *y*-*y* plane by connecting the crease patterns along the crease lines (Figure 3.4(b)). This results in the two sheets that make up the unit cell being equivalent (i.e. side I = side II). The underlying crease pattern for the unit cell is developable and rigidly foldable.



(a) (b)

Figure 3.4 (a) Crease pattern for side I and II; and, (b) unit cell with the crease-to-crease connection method

3.2 Generalised geometry and kinematics

A generalised geometric analysis will be completed to investigate the alternative configurations that can be achieved. The generalised crease pattern is shown in Figure 3.5(a) and is made up

of a four Miura-ori units. The below expression is derived from the Miura-ori unit ((Figure 3.2(b)) and relates the cell angle, γ, to θ and α.

$$\cos\frac{\theta}{2} = \frac{\tan\frac{\gamma}{2}}{\tan\alpha} \tag{3.1}$$

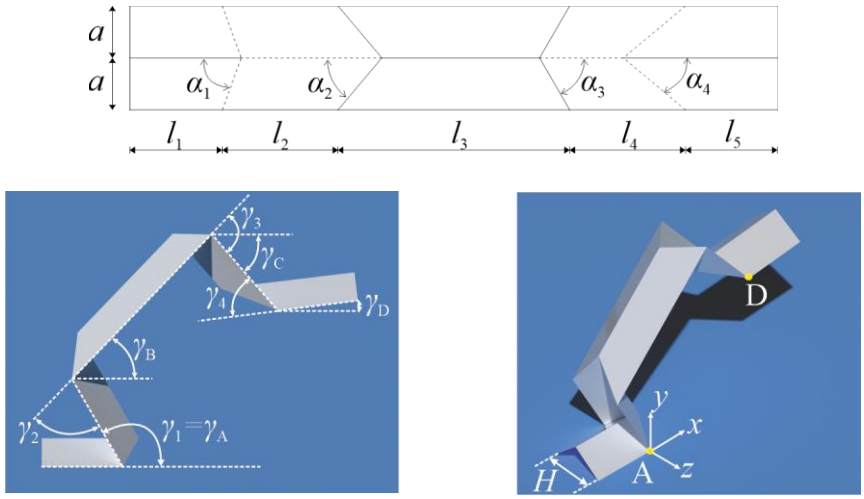


Figure 3.5 (a) Generalised crease pattern; and, (b-c) partially-folded configuration

To connect two sheets to form a unit cell, the connection facets of side I and II must be coincident. To assess this, the angles that the connection facets make with respect to the *x*-axis and the location of a points A and D on the connection facet can be found using the following equations.

$$\gamma_A = \gamma_1 \tag{3.2}$$

$$\gamma_B = \gamma_1 - \gamma_2 \tag{3.3}$$

$$\gamma_C = \gamma_B - \gamma_3 = \gamma_1 - \gamma_2 - \gamma_3 \tag{3.4}$$

$$\gamma_D = \gamma_4 + \gamma_C = \gamma_4 + \gamma_1 - \gamma_2 - \gamma_3 \tag{3.5}$$

$$A(x, y, z) = [0, 0, 0] \tag{3.6}$$

$$D(x, y, z) = [l_2 \cos\gamma_A + l_3 \cos\gamma_B + l_4 \cos\gamma_C, l_2 \sin\gamma_A + l_3 \sin\gamma_B + l_4 \sin\gamma_C, 0] \tag{3.7}$$

The height of the single unit can be calculated as follows.

$$H = 2a \sin\frac{\theta}{2} \tag{3.8}$$

3.3 Unit cell possibilities

Now that the generalised geometry and kinematics are defined, the geometric space will be traversed by first examining how α affects the geometry. Specifically, how it can be varied whilst preserving the ability to attach two sheets (side I and side II) to form a unit cell. Any restraint on the kinematic range that the connection provides will also be assessed. To connect two sheets, three conditions must be satisfied for both connection methods:

1. Point D for both side I and II are coincident;
2. H is equivalent; and,
3. $\gamma_D^I = -\gamma_D^{II}$.

Additionally, for the face-to-face connection method θ^I must equal θ^{II} to allow the entire face to be connected. Unless otherwise stated, the below findings are applicable for both the crease-to-crease and face-to-face connection methods.

3.3.1 Identical Miura-ori angles along each individual sheet

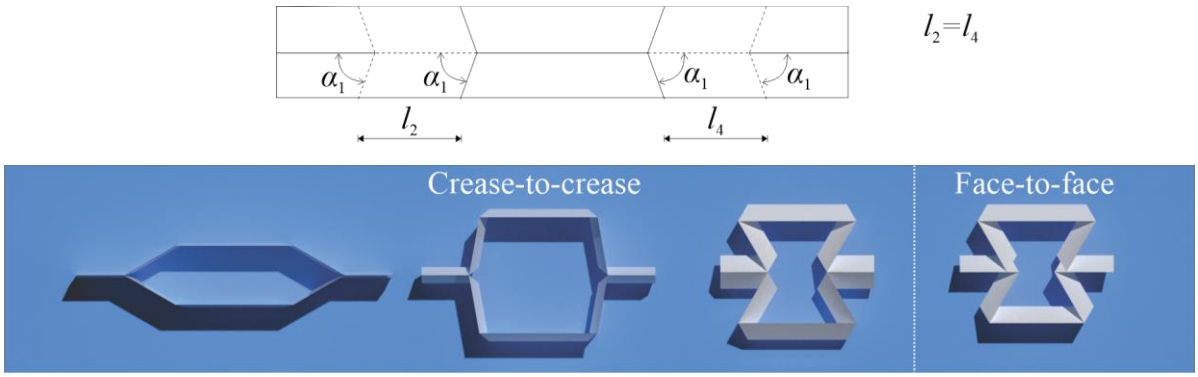
The simplest configuration is when the Miura-ori angles are identical for each Miura-ori unit along the sheet ($\alpha_1 = \alpha_2 = \alpha_3 = \alpha_4 = \alpha$). In this case, $\gamma_1 = \gamma_2 = \gamma_3 = \gamma_4 = \gamma$ and therefore the connection facets remain parallel throughout the kinematic range as $\gamma_B = \gamma_D = 0$ (Figure 3.6).

Additionally, the equation for point D simplifies to the equation below and condition 3 defined in section 3.3 is automatically met.

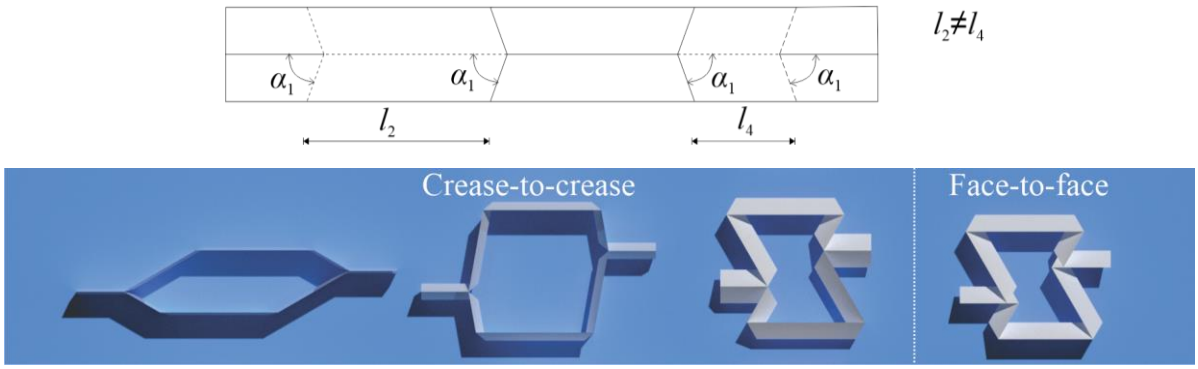
$$\mathrm{D}(x, y, z) = [l_2 \cos\gamma + l_3 + l_4 \cos\gamma, l_2 \sin\gamma - l_4 \sin\gamma, 0] \tag{3.9}$$

3.3.1.1 Connecting identical sheets to form a cell

When identical sheets are connected to form a unit cell (i.e. side I = side II) the only non-trivial changes that can be made are the lengths l_2 and l_4. When $l_2 = l_4$, two identical sheets can be connected to form a regular symmetrical cell whose kinematic range is not restricted. If $l_2 \neq l_4$, two identical sheets form a non-symmetric unit cell whose kinematic range is also not restricted (Figure 3.6). For brevity separate folding states are only shown for the crease-to-crease connection method in Figure 3.6, with only one folded state shown for the face-to-face connection method.



(a)



(b)

Figure 3.6 Identical units with (a) $l_2 = l_4$; and, (b) $l_2 \neq l_4$

3.3.1.2 Connecting sheets with different l_2, l_3 and l_4 lengths to form a cell

Two sides with the same α and a length but different l_2, l_3 and l_4 lengths can also be connected as long as point D for both sides I and II are coincident. From Eq.(3.8), when the a length of both units is identical, θ must also be identical for H to remain equal. Then from Eq.(3.1), γ must also be identical. Equating point D at both x and y locations for sides I and II, the following equations can be formed.

$$D_x^{\mathrm{I}} = D_x^{\mathrm{II}}$$

$$\left(l_2^{\mathrm{I}} + l_4^{\mathrm{I}}\right)\cos\gamma + l_3^{\mathrm{I}} = \left(l_2^{\mathrm{II}} + l_4^{\mathrm{II}}\right)\cos\gamma + l_3^{\mathrm{II}} \tag{3.10}$$

$$D_y^{\mathrm{I}} = D_y^{\mathrm{II}}$$

$$l_2^{\mathrm{I}} - l_4^{\mathrm{I}} = -l_2^{\mathrm{II}} + l_4^{\mathrm{II}} \tag{3.11}$$

Substituting Eq.(3.11) into Eq.(3.10) and rearranging to give the expression below, it can be seen that by defining the lengths of side I and one of the lengths of side II, the remaining lengths of side II can be calculated.

$$l_3^{\mathrm{I}} + 2l_4^{\mathrm{I}}\cos\gamma = l_3^{\mathrm{II}} + 2l_4^{\mathrm{II}}\cos\gamma \tag{3.12}$$

Now, to determine if the lengths of side II can be chosen so that the kinematic range of the unit cell is preserved, consider two separate folded states γ_{i} and γ_{j}. As previously stated, γ for both sides must be identical if α and H are equal. Substituting γ_{i} and γ_{j} into Eq.(3.12) and subtracting these equations from one another we find that the l_4^{II} must equal l_2^{I} to ensure that the kinematic range is preserved. Substituting this back into Eq.(3.10) and (3.11) it can be easily shown that $l_2^{\mathrm{II}} = l_4^{\mathrm{I}}$ and $l_3^{\mathrm{II}} = l_3^{\mathrm{I}}$. This would result in sides I and II being identical. If the sides are not identical the kinematic range of the unit cell will be restricted to the designed configurations. An example of a unit cell where $l_4^{\mathrm{II}} \neq l_2^{\mathrm{I}}$ is shown in Figure 3.7, which clearly shows that the lengths of the two sides do not remain equal during the folding process.

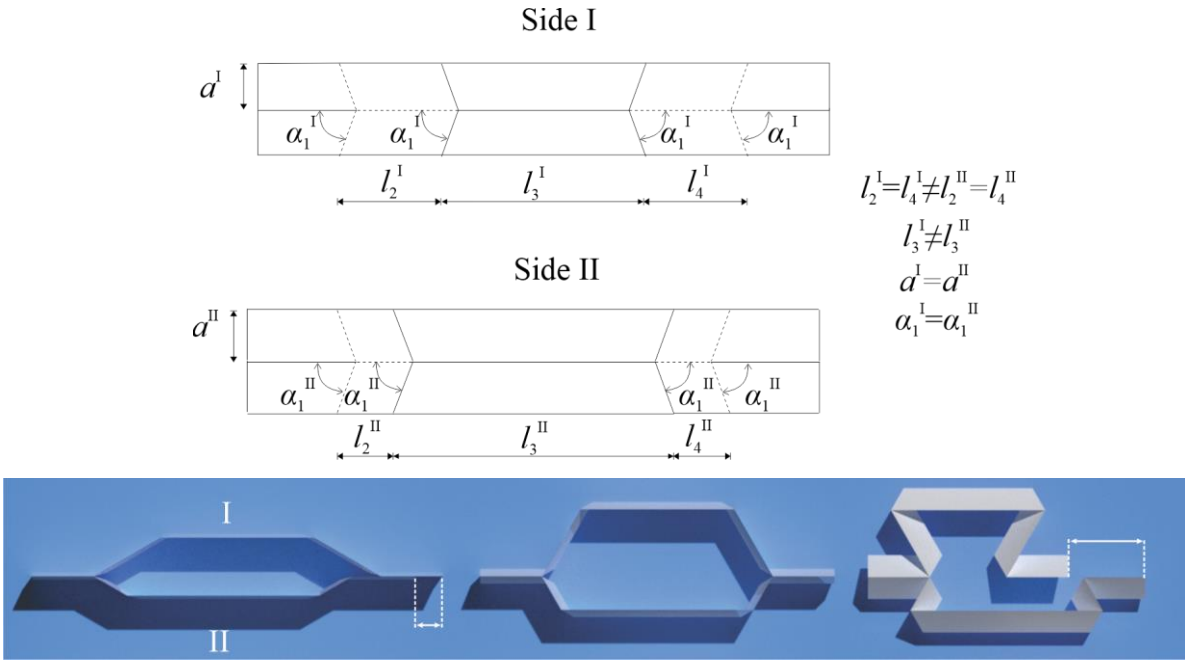


Figure 3.7 Crease pattern and folding of units with $l_4^{II} \neq l_2^{I}$

3.3.2 Varying the Miura-ori angles along each individual unit

The Miura-ori angle can also be varied along the length of the sheet ($\alpha_1 \neq \alpha_2 \neq \alpha_3 \neq \alpha_4$). In this case θ remains constant along the side, however, $\gamma_1 \neq \gamma_2 \neq \gamma_3 \neq \gamma_4$. One method to connect identical sides is to ensure the connection facets remain parallel (i.e. $\gamma_D = 0$) Substituting this into Eq.(3.5) gives the following expression.

$$\gamma_2 + \gamma_3 = \gamma_4 + \gamma_1 \tag{3.13}$$

There are three classes of unit cells which can be formed to achieve this. The first class is achieved by setting $\gamma_1 = \gamma_2$ and $\gamma_4 = \gamma_3$ resulting in $\alpha_1 = \alpha_2$ and $\alpha_4 = \alpha_3$. This produces a cell where the l_1, l_3 and l_5 lengths remain parallel ($\gamma_B = \gamma_D = 0$) throughout the folding process (Figure 3.8(a)). The second class is achieved by setting $\gamma_1 = \gamma_3$ and $\gamma_4 = \gamma_2$ meaning that $\alpha_1 = \alpha_3$ and $\alpha_4 = \alpha_2$. For this class, the l_3 length does not remain parallel with l_1 and l_5 ($\gamma_B \neq 0$) during the folding process (Figure 3.8(b)). The final class is achieved by setting $\gamma_1 \neq \gamma_2 \neq \gamma_3$. In this case, only in the designed configuration will the l_1 and l_5 lengths be parallel (Figure 3.8(c)).

When two identical sides are attached to form a unit cell only class 1 and 2 will have their full kinematic range. Additionally, the finding in section 3.3.1.1 are equally applicable for these classes. That is, l_2 and l_4 do not need to be identical. Similar to section 3.3.1.2, varying the l_2, l_3 and l_4 for side I and II for all classes will result in the kinematic range being restricted. Class 3 will however be locked in the initial configuration it was designed for (Figure 3.8(c)).

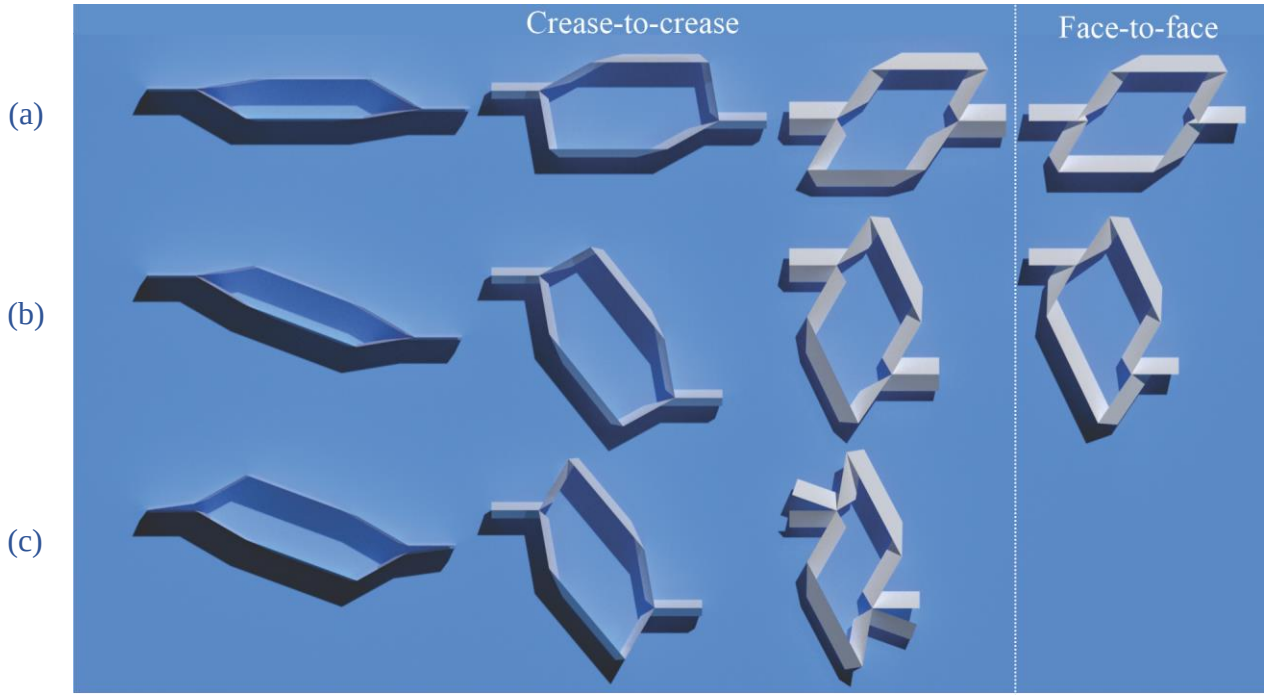


Figure 3.8 Folding of units from class: (a) 1; (b) 2; and, (c) 3

3.3.3 Tessellating unit cells

All the unit cells whose kinematic range is not restricted can also be tessellated into cores that have their full kinematic range. This is the case for both the crease-to-crease and face-to-face connection methods. For brevity only examples of the crease-to-crease connection method will be provided below.

In section 3.3.1 two units were identified with an unrestricted kinematic range. When $l_2 = l_4$, there is only one possibility for tessellating the unit cell (Figure 3.9(a)). In contrast, when $l_2 \neq l_4$ two distinct cores can be tiled by either translating or mirroring the unit cell (Figure 3.9(b,c)). When tessellated, these units always form either a honeycomb or re-entrant

honeycomb cross-sections (Figure 3.9(a-c)). When tessellating the unit cell with $l_2 \neq l_4$ by translations, identical skewed honeycombs make up the cross section (Figure 3.9(b)). However, when tessellating this unit cell by mirroring, larger and smaller regular honeycombs as well as skewed honeycombs can be observed within the cross section.

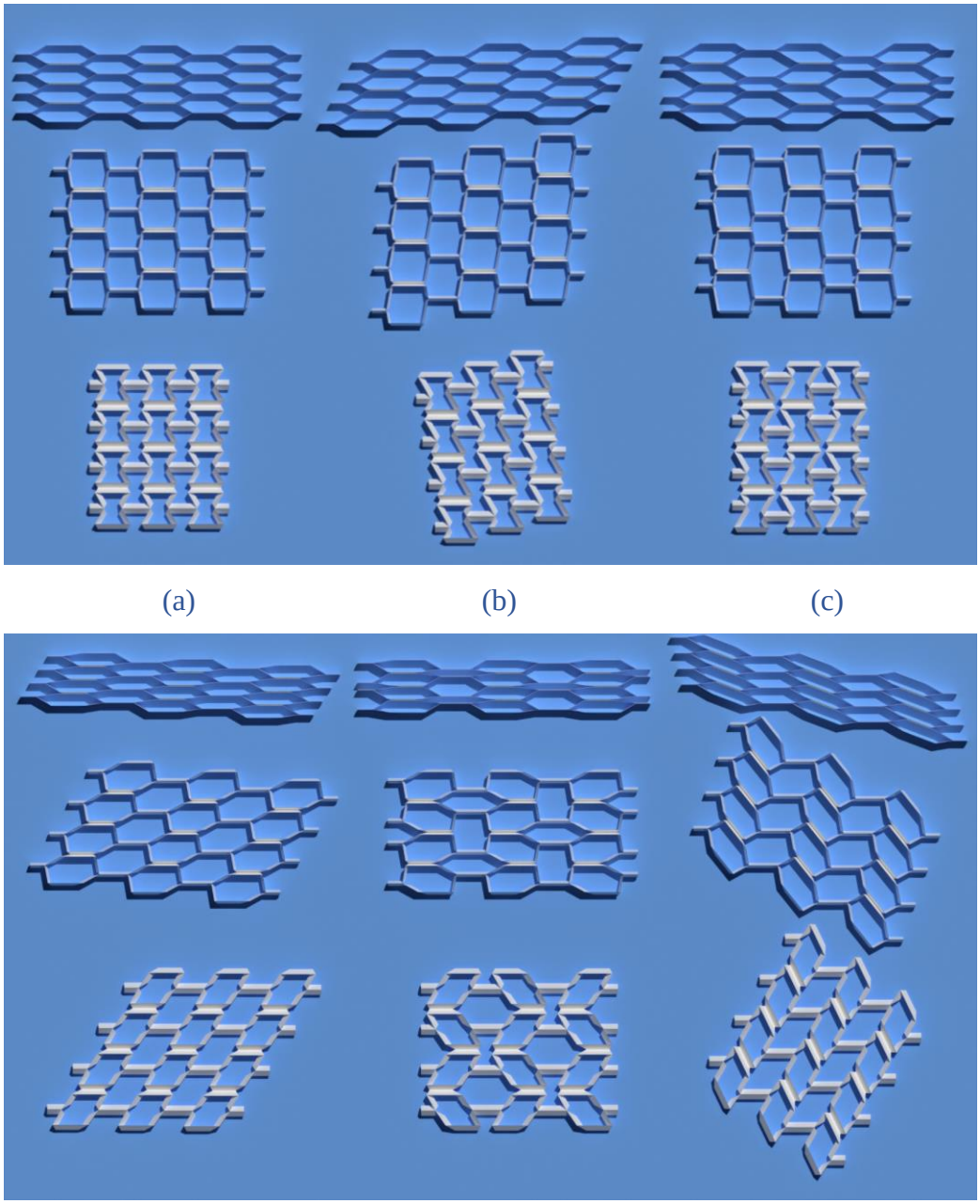


Figure 3.9 Tessellating unit cells with: identical Miura-ori angle along sheets for (a) $l_2 = l_4$; and ,(b-c) $l_2 \neq l_4$; and, varying Miura-ori angles along the sheet (d-e) class 1; and, (f) class 2

Similarly, for the unit cells with variable α along the length of the sheet, case 1 can be tessellated into a core by translating or mirroring the unit cell (Figure 3.9(d, e)), whereas, case 2 can only be tessellated by translating the unit cell (Figure 3.9(f)). When translating case 1 (Figure 3.9(d)), the cross section of the core is made up of skewed honeycombs. In contrast, when mirroring (Figure 3.9(e)), regular honeycomb with different γ's and skewed honeycombs make up the cross section. Interestingly, both honeycombs and re-entrant honeycombs may form in this cross section depending on the fold angle. The tessellated class 2 unit also exhibits some unique behaviour, where a change in the length is translated into a rotation.

3.4 Grading

Grading here is defined as the ability to change the underlying crease pattern of sides I and II to invoke in-plane grading and/or along the height of the individual sides to invoke out-of-plane grading. Of particular interest is a variation that results in self-locking as this shows potential in grading the stiffness of the structures under loading.

3.4.1 Grading in the in-plane direction

3.4.1.1 Identical Miura-ori angles along each individual side

Consider that sides I and II, that make up the unit cell, have different a and α values. Equating point D for both sides gives the following two equations respectively.

$$D_x^{\mathrm{I}} = D_x^{\mathrm{II}}$$

$$\left(l_2^{\mathrm{I}} + l_4^{\mathrm{I}}\right)\cos\gamma^{\mathrm{I}} + l_3^{\mathrm{I}} = \left(l_2^{\mathrm{II}} + l_4^{\mathrm{II}}\right)\cos\gamma^{\mathrm{II}} + l_3^{\mathrm{II}} \tag{3.14}$$

$$D_y^{\mathrm{I}} = D_y^{\mathrm{II}}$$

$$\left(l_2^{\mathrm{I}} - l_4^{\mathrm{I}}\right)\sin\gamma^{\mathrm{I}} = \left(l_2^{\mathrm{II}} - l_4^{\mathrm{II}}\right)\sin\gamma^{\mathrm{II}} \tag{3.15}$$

Substituting these into one another and rearranging gives the following expression.

$$l_3^{\mathrm{I}}+\left(l_2^{\mathrm{I}}+l_4^{\mathrm{I}}\right)\cos\gamma^{\mathrm{I}}-\left(l_2^{\mathrm{I}}-l_4^{\mathrm{I}}\right)\frac{\sin\gamma^{\mathrm{I}}}{\tan\gamma^{\mathrm{II}}}=l_3^{\mathrm{II}}+2l_4^{\mathrm{II}}\cos\gamma^{\mathrm{II}} \tag{3.16}$$

Again, consider two separate folded states γ_i and γ_j to determine if the lengths of side II can be chosen so that the kinematic range of the individual units is preserved. Substituting these two states into Eq.(3.16) and subtracting them from one another results in the following relationship

$$l_4^{\mathrm{II}}=\frac{\left(l_2^{\mathrm{I}}+l_4^{\mathrm{I}}\right)\left(\cos\gamma_{\mathrm{i}}^{\mathrm{I}}-\cos\gamma_{\mathrm{j}}^{\mathrm{I}}\right)-\left(l_2^{\mathrm{I}}-l_4^{\mathrm{I}}\right)\left(\frac{\sin\gamma_{\mathrm{i}}^{\mathrm{I}}}{\tan\gamma_{\mathrm{i}}^{\mathrm{II}}}-\frac{\sin\gamma_{\mathrm{j}}^{\mathrm{I}}}{\tan\gamma_{\mathrm{j}}^{\mathrm{II}}}\right)}{2\left(\cos\gamma_{\mathrm{i}}^{\mathrm{II}}-\cos\gamma_{\mathrm{j}}^{\mathrm{II}}\right)} \tag{3.17}$$

As the height of both units must be equivalent, an equation relating γ^{II} to γ^{I} can be derived by substituting Eq.(3.1) into Eq.(3.8) and then equating this for the two units.

$$\gamma^{\mathrm{II}}=2\arctan\left(\sqrt{\tan^2\alpha^{\mathrm{II}}-\left[\frac{a^{\mathrm{I}}\tan\alpha^{\mathrm{II}}}{a^{\mathrm{II}}\tan\alpha^{\mathrm{I}}}\sqrt{\tan^2\alpha^{\mathrm{I}}-\tan\frac{\gamma^{\mathrm{I}}}{2}}\right]^2}\right) \tag{3.18}$$

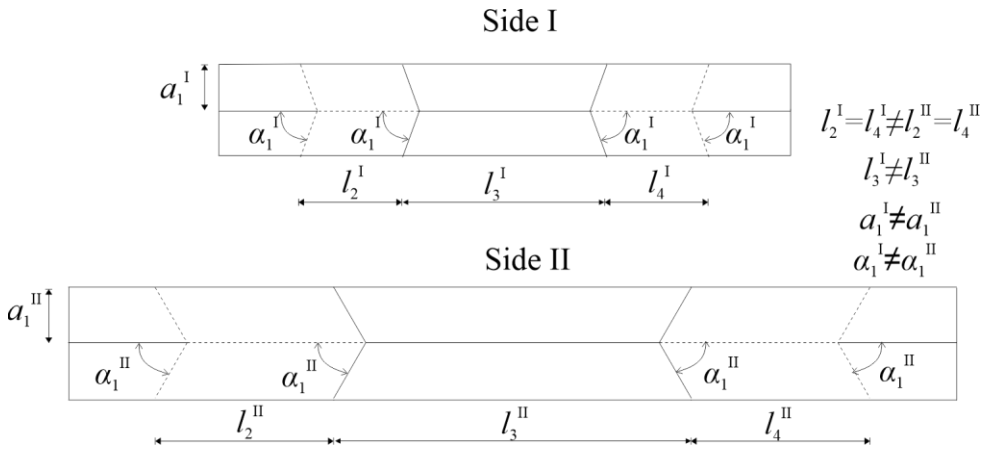
By defining all variables for side I and a^{II}, α^{II} for side II, the remaining variable of side II can be calculated using Eq.(3.14, 3.15, 3.17, 3.18). Interestingly, while the unit cell can be attached for the designed γ_i and γ_j, the kinematic range may still be locked at these two locations. Only when a^{II} is set using the below equation does the kinematic range remain unrestrained, although the side with the smaller a will lock the kinematic range of the other side when unfolded flat.

$$a^{\mathrm{II}}=a^{\mathrm{I}}\frac{\sin\alpha^{\mathrm{II}}}{\sin\alpha^{\mathrm{I}}} \tag{3.19}$$

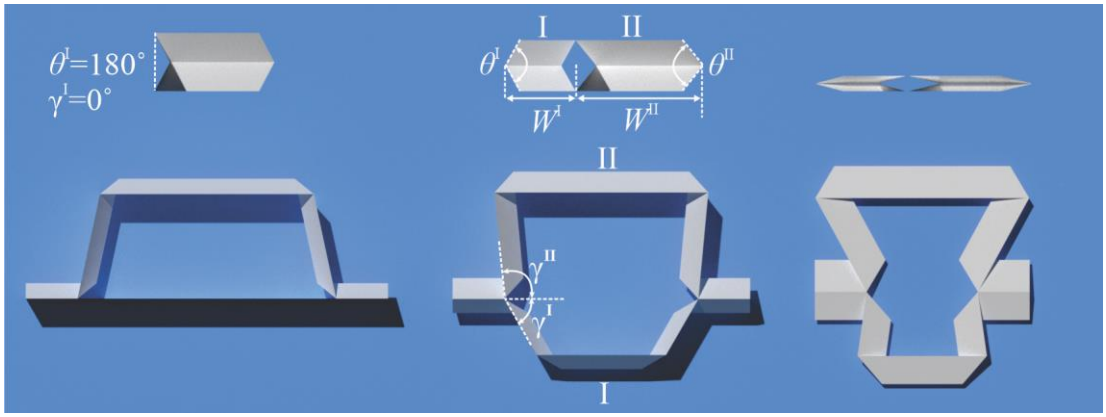
This self-locking effect is illustrated in Figure 3.10 for the unit cell with $\alpha_1^{\mathrm{I}} = 50°$, $a_1^{\mathrm{I}} = 4.5$mm and $\alpha_1^{\mathrm{II}} = 60°$.$a_1^{\mathrm{II}}$ is set equal to Eq.(3.19). Locking occurs when $\theta_1 = 180°$ for side I in this scenario (Figure 3.10(b-c)). While side I is a perfectly flat sheet, side II of the cell has $\theta_1 < 180°$, resulting in a residual width. Both θ_1^{I} and θ_1^{II} are plotted against θ_1^{I} in Figure 3.10(c)

to show this. Additionally, the width of each half of the cell (Eq.(3.20)) is normalized against the largest l_2 value for the cell and plotted against θ_1^{I} in Figure 3.10(c).

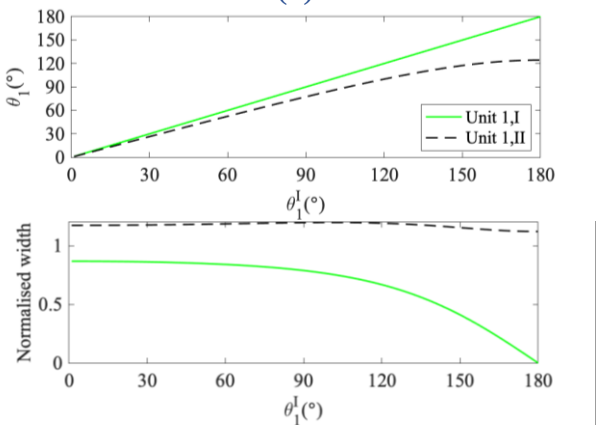
$$W = a\cos\frac{\theta}{2} + l_2\sin\gamma \tag{3.20}$$



(a)



(b)



(c)

Figure 3.10 Unit cell with alternative *a* and *α* (a) crease pattern; (b) folded states; and, (c) self-locking behaviour

This grading methodology is only applicable for the case where $l_2 = l_4$ (section 3.3.1.1). When $l_2 \neq l_4$, the connection facets do not remain on the same plane (Figure 3.6) and therefore it is not possible for one side of the cell to be completely unfolded ($\theta = 180°$) whilst the other has $\theta < 180°$.

Creating a unit cell in this manner results in $\theta^{I} \neq \theta^{II}$ which precludes the formation of the cell with face-to-face connection method. However, it is still possible for side I and II to be attached for the Tachi-Miura polyhedron. Rather than the entire face being connected, only the creases are connected. This results in prismatic cells running in the in-plane direction (Figure 3.11).

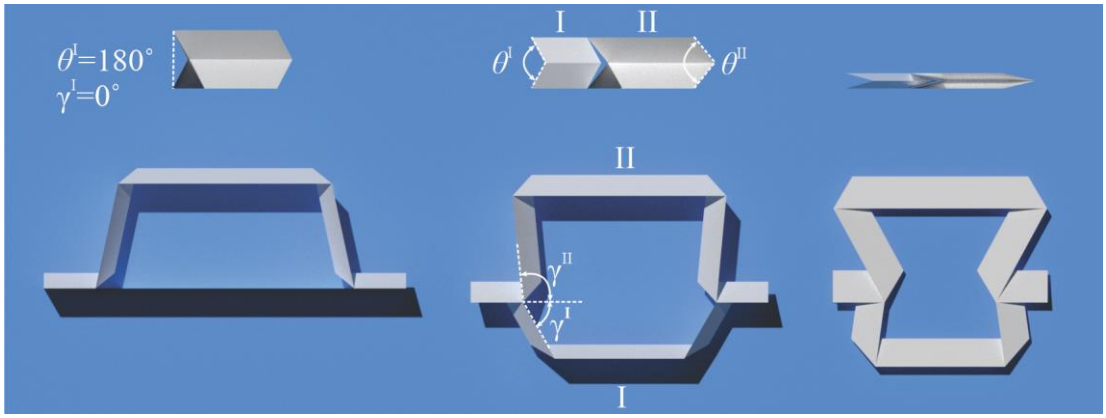


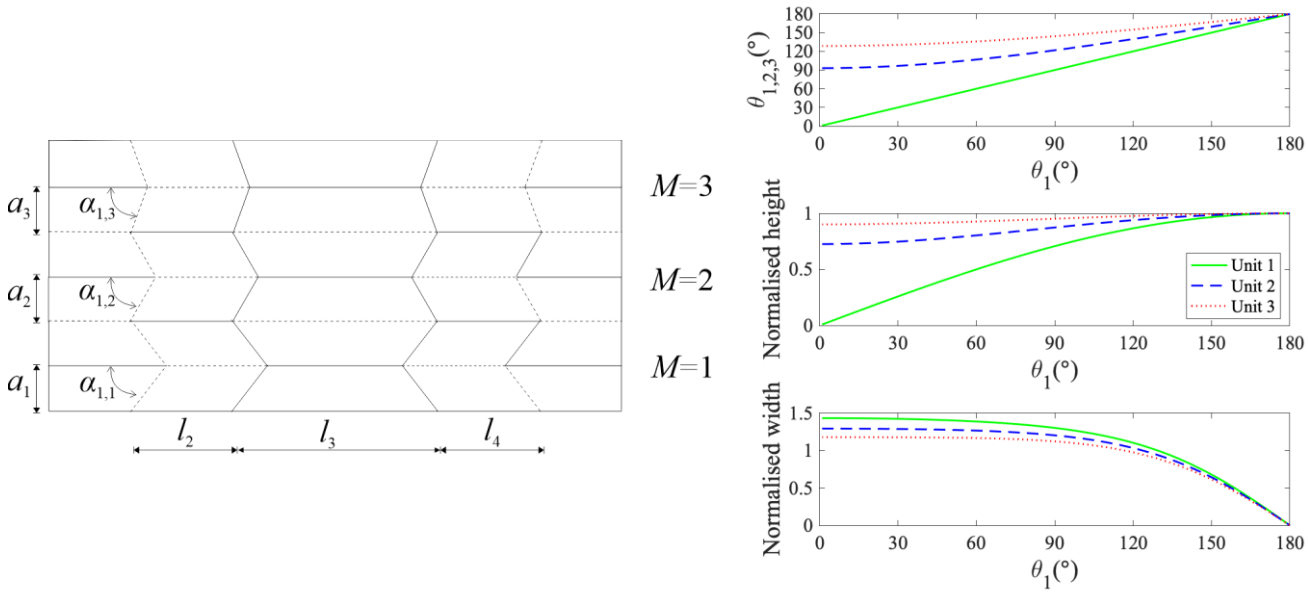
Figure 3.11 Crease-to-crease connected Tachi-Miura polyhedron

3.4.1.2 Varying the Miura-ori angles along each individual unit

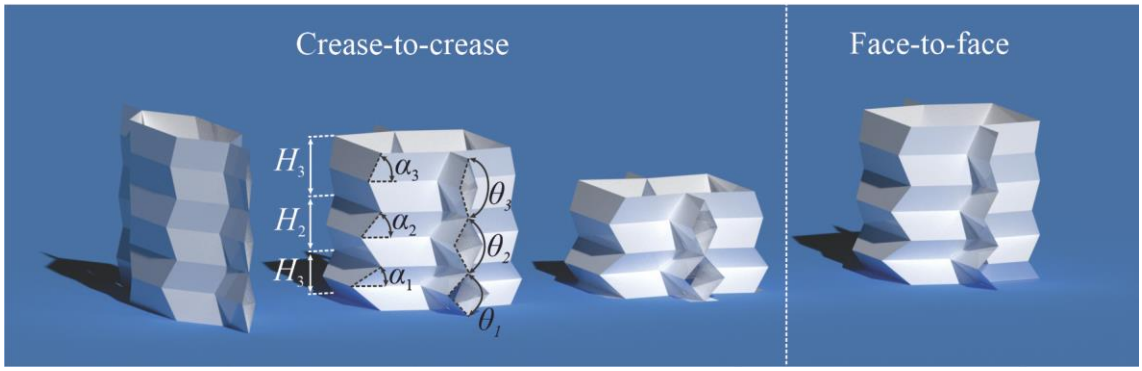
The method outlined in section 3.4.1.1 cannot be applied to grade class 1 and 2 unit cells defined in section 3.3.2. As discussed above, varying *a* between the sides that make up the cell results in one half of the cell returning to a flat sheet whilst the other still has $\theta < 180°$ (Figure 3.10). As point A and D do not remain on the same plane for class 1 and 2 cells it is impossible for one side of the unit cell to have $\theta = 180°$ when the other does not.

3.4.2 Grading along the height

When α is varied across the height of the cell, kinematically, each M unit will exhibit a different θ as the tube folds (Figure 3.12(b-c)). For this crease pattern to be rigidly foldable the γ for each M unit must be identical. By defining γ for the core the θ for each unit M can be determined. The relationship between θ_1 and $\theta_{1,2,3}$ for $\alpha_1 = 50°$, $\alpha_2 = 60°$, $\alpha_3 = 70°$ is provided in Figure 3.12(b). Locking occurs when one of the fold angles reaches $\theta = 0°$ (Figure 3.12(b-c)). This will occur for the unit with the smallest α.



(a) (b)



(c)

Figure 3.12 (a) Graded origami honeycomb crease pattern; (b) relationship between θ_1, θ_2 and θ_3; and, (c) folding of core from initial configuration to self-locking

The total height of the tube can be calculated using the equation below and is the summation of the height of each *M* unit. The vertical height of each *M* unit is normalized against the initial vertical height for the side of the cell with the minimum *a* value (min($2a^{I}$, $2a^{II}$)) and plotted against θ_1 in Figure 3.12 (b). The figure also provides the width (defined in section 3.4.1.1) of each unit and shows that they are not necessarily equal along the height. This will be of interest when attempting to tesselate the unit cell for the crease-to-crease connection method.

$$H = \sum_{i=1}^{M} \left(2a_i \sin \frac{\theta_i}{2} \right) \tag{3.21}$$

Unlike the in-plane grading described in section 3.4.1, the out-of-plane grading is equally applicable for cases where $l_2 \neq l_4$ defined in section 3.3.1.1 and class 1 and 2 unit cells defined in section 3.3.2.

For class 1 and 2 unit cells (section 3.3.2) the α for each vertex j along the unit i must be selected to ensure $\gamma_{i,j}$ is equal along the height of the core. Firstly the α at each vertex for one side must be defined. Assuming this is for unit at $M = 1$, then $\gamma_{1,j}$ can be calculated at each vertex for a given θ_1 using Eq.(3.1). Noting that $\gamma_{1,j}$ is equivalent in each unit along the height ($\gamma_{1,j} = \gamma_{i,j}$, Figure 3.13) and defining one α value at vertex j for the adjacent unit, θ_i for this unit i may be calculated as follows.

$$\theta_i = 2 \arccos \left(\frac{\tan \frac{\gamma_{1,j}}{2}}{\tan \alpha_{i,j}} \right) \tag{3.22}$$

$$\alpha_{i,j} = 2 \arctan \left(\frac{\tan \frac{\gamma_{1,j}}{2}}{\cos \frac{\theta_i}{2}} \right) \tag{3.23}$$

With θ_i and $\gamma_{1,j}$ defined the three remaining α can be calculated using Eq.(3.23). An example of the out-of-plane grading for class 2 is provided in Figure 3.13.

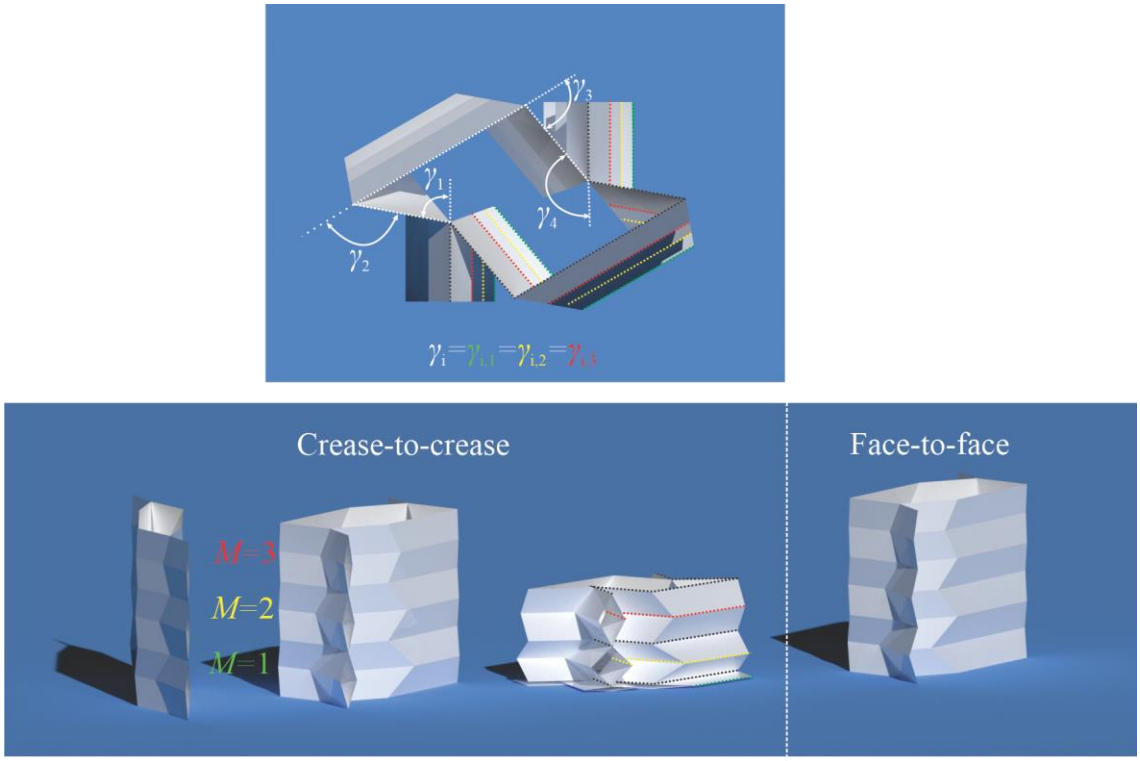
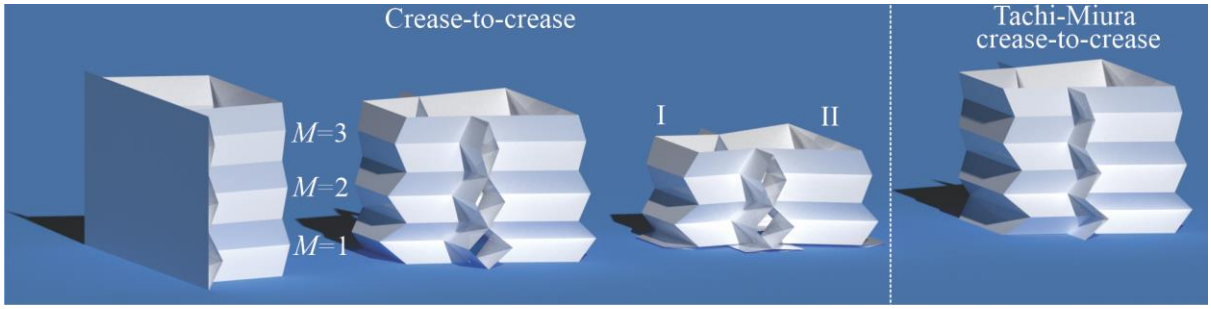


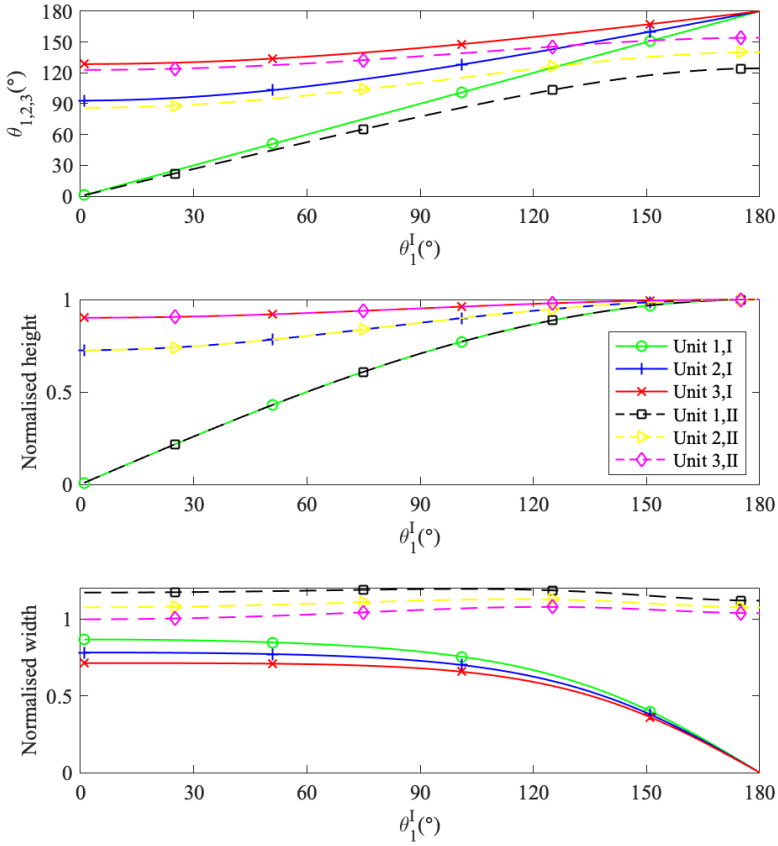
Figure 3.13 Out-of-plane grading for class 2 cell

3.4.3 Combination of grading

Combining the in-plane and out-of-plane grading technique is also possible for the unit cell with identical α's along each individual sheet where $l_2 = l_4$. This creates a cell that can be locked at either end of the kinematic range (Figure 3.14). Figure 3.14(b) compares θ, the normalised height and normalised width of each M unit (1,2,3) for both sides (I and II) with respect to θ_1^{I}. In this scenario $\alpha_1^{\mathrm{I}} = 50°$, $\alpha_2^{\mathrm{I}} = 60°$, $\alpha_3^{\mathrm{I}} = 70°$, $a^{\mathrm{I}} = 4.5$mm and $\alpha_1^{\mathrm{II}} = 60°$. a_1^{II} is set equal to Eq.(3.19). The remaining α^{II} values can be calculated using Eq.(3.18) and Eq.(3.19) for each M unit along the height. Figure 3.14(b) shows that while the height for each M layer for sides I and II remains equivalent, θ and the width do not. Additionally, θ and the width for each side also varies for each unit along the height.



(a)



(b)

Figure 3.14 Locking in the in-plane and out-of-plane direction: (a) visualisation of locking; and, (b) normalised height and width variation with θ

While the combined in-plane and out-of-plane grading is not possible for the face-to-face connection method as discussed in section 3.4.1.1, the two sides of the Tachi-Miura polyhedron

can still be attached using a crease-to-crease connection method. Again, this results in prismatic cells running in the in-plane direction.

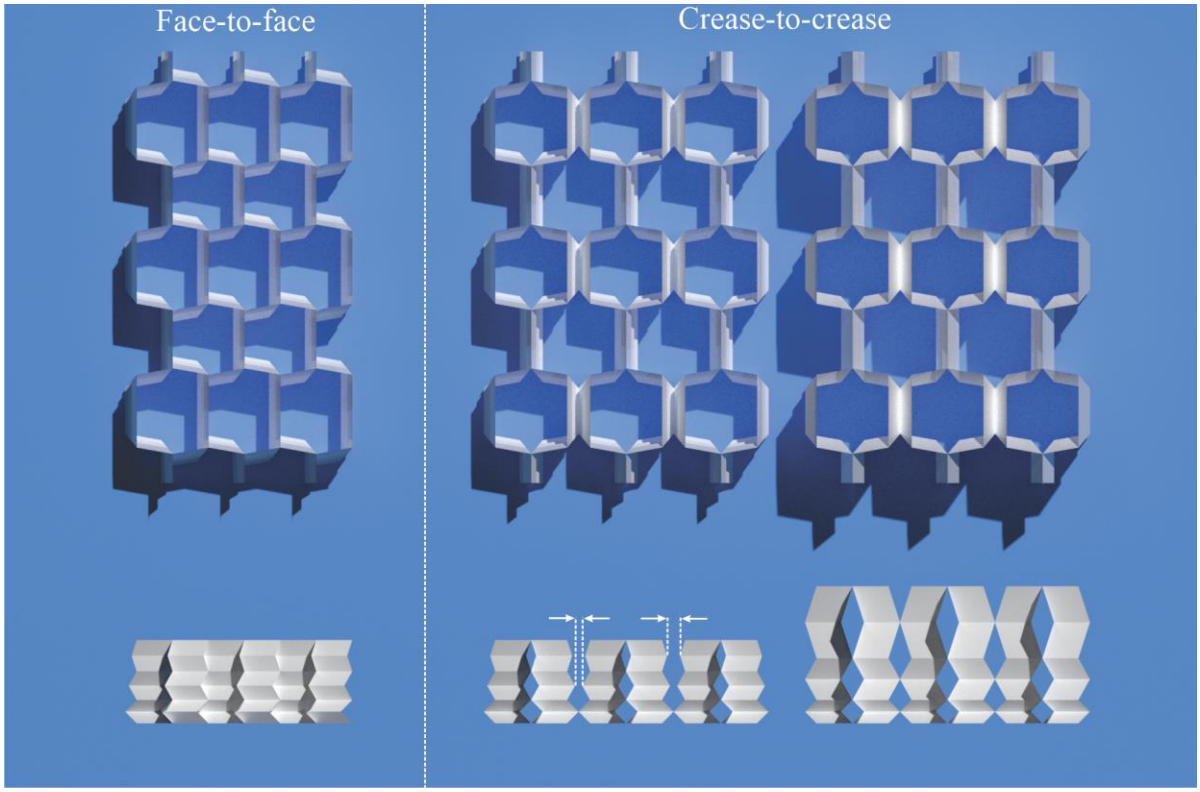
3.4.4 Tessellating graded cells

For the face-to-face connection method, it is possible to tessellate the graded geometries without any further design constraints in the same manner as described in section 3.3.3. For brevity only one example of the graded face-to-face connection method is provided in Figure 3.15(a).

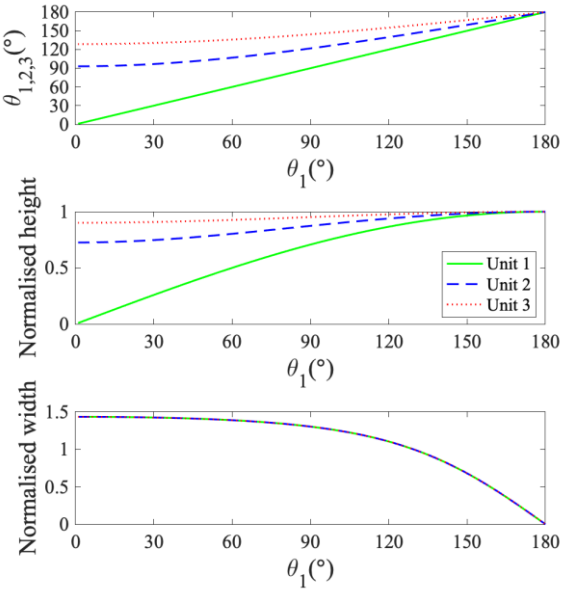
For the crease-to-crease connection method, the width of the units along the height are not necessarily equal (Figure 3.12(b)) resulting in adjacent cells not being connected at the crease location's (Figure 3.15(b)). Therefore, tessellating cells with the crease-to-crease connection method requires the selection of a such that the connection creases remain on the same plane as one another throughout the kinematic range (Figure 3.15(c)). This can be achieved by selecting a for each M units along the height using the expression provided below.

$$a_{\mathrm{j}} = a_{\mathrm{i}} \frac{\tan \alpha_{\mathrm{j}}}{\tan \alpha_{\mathrm{i}}} \tag{3.24}$$

Figure 3.15(d) is for the identical geometry as Figure 3.12(b) except a is varied along the height following Eq.(3.24). Comparing the two figures it can be clearly seen that this results in the width of the units along the height remaining equivalent. With this added constraint the crease-to-crease connection method may also be tessellated into a core with its kinematic range intact.



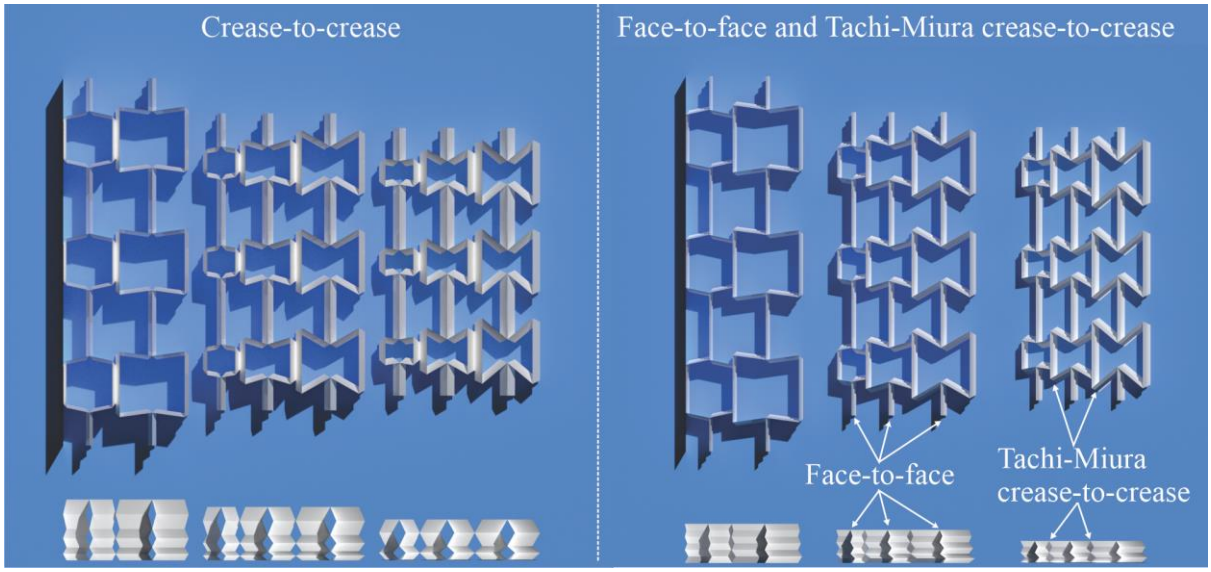
(a) (b) (c)



(d)

Figure 3.15 Tessellating graded cells with: (a) the face-to-face connection method; and, (b-c) crease-to-crease connection method

Using this constraint, a core with grading in both directions can also be formed for the crease-to-crease connection method. Figure 3.16(a) provides an example of this, where each layer of the core is graded in both the in-plane and out-of-plane direction.



(a) (b)

Figure 3.16 Tilling of graded: (a) crease-to-crease connection cores; and, (b) combination of crease-to-crease connected Tachi-Miura polyhedron and face-to-face connection method

The face-to-face connection method (Figure 3.15(a)) can also be combined with the crease-to-crease connected Tachi-Miura polyhedron (Figure 3.14**)** to provide a core with grading in both directions (Figure 3.16(b)). In this case *a* can be chosen arbitrarily rather than with Eq.(3.24).

3.5 Conclusions

In this chapter the different geometric possibilities for an origami honeycomb cellular structure were explored. Initially the general kinematics for one sheet was derived and the geometric space for a unit cell was explored, forming several derivatives that can be tessellated to form a cellular structure. Using this family of cellular structures, methods to grade the crease pattern along the in-plane direction, out-of-plane direction, or a combination of the two was shown.

The various derivatives and possible grading schemes illustrate a diverse range of honeycombs that can be formed which exhibit different behaviour. This provides much greater versatility in the design of honeycombs when compared to a standard honeycomb core and is the first step towards enabling more functional and therefore efficient designs.

The individual behaviour of each of these derivatives when subjected to a load is yet to be explored. In the next chapter the effect of grading the cells in the out-of-plane direction will be examined towards this end.

CHAPTER 4

QUASI-STATIC BEHAVIOUR

In the previous chapter the kinematics of the origami honeycomb were investigated, forming a family of derivatives and methodologies to design honeycomb cores whose kinematic range can be locked at defined points. In this chapter the ability of this locking to grade the stiffness of the origami honeycomb in the out-of-plane direction is investigated.

Initially an experiment of an ungraded tube with the crease-to-crease connection method will be used to validate a numerical model. The behaviour of the ungraded tube for both connection methods will then be numerically investigated. This will be expanded to study the behaviour of a 6×6 core numerically. Subsequently an analytical model to predict the force displacement behaviour will be derived. Finally, the effect of changing the Miura-ori angle along the height of the tube and core, introducing the locking effect, will be sought numerically and analytically for both connection methods.

4.1 Experiment

4.1.1 Geometry

To validate the numerical model an ungraded tube with the crease-to-crease connection method was manufactured and experimentally tested. Whilst the face-to-face connection method is not experimentally tested, it is assumed that the validated numerical method is equally applicable.

Practically, to facilitate the crease-to-crease connection method, the creases along the length are split into two, providing a facet where the two sheets can be glued together. These facets, with width s, are highlighted in orange in Figure 4.1. The addition of these facets results in a residual height when $\theta = 0°$, as the vertices no longer fulfil Kawasaki's criteria (Hull, 1994) (Figure 4.1).

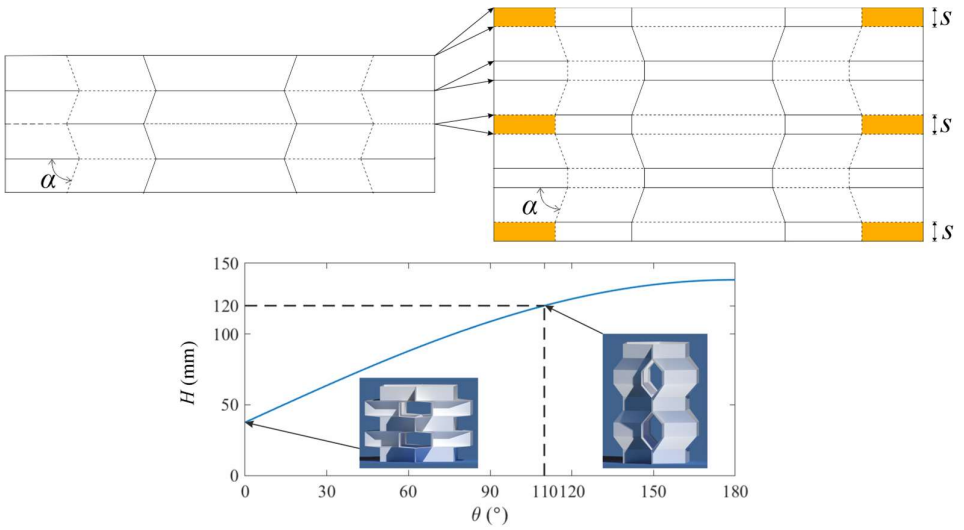


Figure 4.1 Splitting of creases to facilitate crease-to-crease connection method

The dimensions of the underlying crease pattern that make up the tube are provided in Table 4.1. The initial cell angle was set to 60°, equivalent to a standard honeycomb. The height of the core can be calculated as follows.

$$H = 2aM \sin\frac{\theta}{2} + (2M+1)s \tag{4.1}$$

Table 4.1 Dimensions of tube for experiments

a [mm]	α [°]	l_1 [mm]	l_2 [mm]	l_3 [mm]	$\overline{\rho}$ [-]	M [-]	s [mm]	θ_0 [°]	γ_0 [°]	H [mm]
10	60	20	20	50	0.0119	3	5	141.1	60	91.57

4.1.2 Sample construction

Three origami honeycomb tubes were constructed by stamping sheets of aluminium 1200 H14 foil with 0.2mm thickness. A single mould was used to stamp the core from the flat sheet to the initial configuration (Figure 4.2). The mould was 3D printed from ABS material with bead size of 0.15mm.

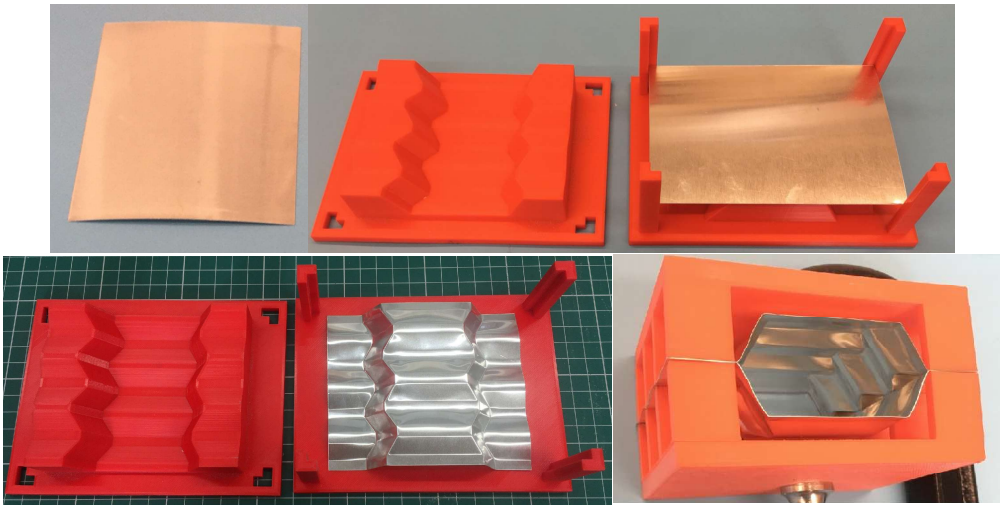


Figure 4.2 Stamping of tube

Once stamped, two sheets were connected at the connection facets using adhesive. Before applying the adhesive, the connection facets were washed with acetone, mechanically abraded by hand with sandpaper and subsequently cleaned with air. The adhesive used to bond the sheets together was commercially available Permabond ET538 Honeycomb Bonding Epoxy Adhesive. After applying the adhesive, pressure was applied to the bonded area and the samples were left to cure for a minimum of 72hrs at 23°C. It should be noted that the epoxy was placed only on the connection facets, which, if the kinematics of the crease pattern is followed, do not deform significantly before locking. This paired with the lower strength of the adhesive compared to the aluminium parent material result in the adhesive having minimal effect on the ungraded tubes performance.

4.1.3 Material testing

Tensile coupons were cut from the aluminium sheet following ASTM E345 (ASTM International, 2016). Shear fracture occurred in all coupons soon after the ultimate stress was reached. This strain localisation at the onset of necking meant that the ultimate strain could not be captured using the extensometer readings across the gauge length (Fu and Chan, 2011; Yu

et al., 2014). Instead, the ultimate strain was taken from the material data sheet provided by the manufacturer. The averaged mechanical properties are provided in Table 4.2.

Table 4.2 Aluminium foil material properties

Yield stress [MPa]	Tensile strength [MPa]	Elastic Modulus (E) [GPa]	Ultimate strain [%]	Density [kg/m^3]
123	140	45.6	8.6%	2700

4.1.4 Experimental setup

The quasi-static experiments were conducted on a INSTRON Universal Testing machine. The samples were placed between two rigid steel plates and the top plate was used to compress the sample under a loading rate of 10mm/min. The final crush distance was set to 70mm which is approximately 76% of the initial height.

4.2 Numerical simulation

4.2.1 Inputs

The crushing process was modelled with ABAQUS Explicit. The tube was placed between two rigid plates. All DOF of the plates were restrained, aside from the vertical translation degree of freedom for the loading plate, which was assigned a displacement of 0.76 H. The inbuilt smooth amplitude definition was implemented to control the loading rate such that the change in acceleration between increments remained small. When assembling the sheets in ABAQUS, an offset of 0.2mm was applied between the connection facets to account for the sheet thickness. To simplify the model, a perfect bond between the two sides of the tube was assumed and implemented with tie constraints. Debonding was not observed in the experiments, so this assumption was assumed to be valid. A general contact definition was assigned to the model with hard-contact in the normal direction and a friction coefficient of 0.13. The friction coefficient was selected from a sensitivity study detailed in section 4.2.3. The material behaviour was modelled as isotropic with an elastic modulus and Poisson's ratio of 45.6GPa

and 0.33 respectively. The nonlinear behaviour was modelled with a tri-linear stress-strain curve that was fitted to the data found in section 4.1.3.

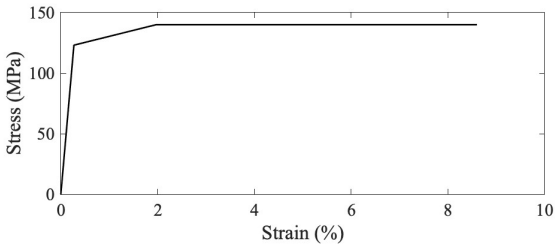


Figure 4.3 Tri-linear engineering stress-strain curve for numerical simulations

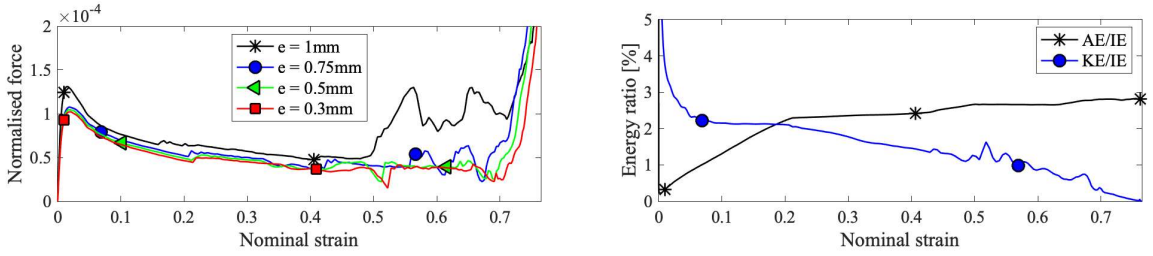
Four-node linear reduced integration shell elements (S4R) were used to mesh the majority of the tube. Additionally, a few three-node elements were included (S3) to prevent distortion. A global element size of 0.5mm was selected from a convergence study. This level of discretisation provided negligible difference in the normalised force vs nominal strain when compared to a global element size of 0.3mm (Figure 4.4(a)). In the figure the force is normalised as follows.

$$F_{\text{norm}} = \frac{F}{SA \times \sigma_{\text{y}}} \tag{4.2}$$

Where F is the force output at the support; SA is the surface area of the tube; and, σ_{y} is the yield stress of the parent material. This will allow the comparison of alternative tubes in section 4.3.The nominal strain, ε, is defined as follows, where δ is the vertical displacement.

$$\varepsilon = \frac{\delta}{H} \tag{4.3}$$

For each model the ratio of the kinetic energy to internal energy, KE/IE, and the ratio of artificial strain energy to internal energy, AE/IE, was kept below 5% to ensure that the dynamic and hourglass effects were negligible (ABAQUS, 2004). An analysis time of 0.05s was found to meet these requirements (Figure 4.4(b)).



(a) (b)

Figure 4.4 (a) Mesh convergence study; and, (b) energy ratio comparison for element size of 0.5mm

4.2.2 Imperfections

Schenk *et al.* (2014) noted that the Miura-ori core loaded in the out-of-plane direction was less geometric imperfection sensitive as the dominant deformation mode follows that prescribed by the crease pattern, rather than buckling. To investigate if this is also the case for the origami honeycomb core, imperfections were added to the simulation.

Initially, a static buckling analysis of the core loaded in the out-of-plane direction was completed. Unlike in the crushing analysis, at the proximal and distal ends the deformation and rotation about the in-plane axis were restrained. This limited the number of free edge buckling modes, ensuring that the imperfections were distributed through the core rather than the ends. A linear combination of the first ten buckling modes was then superimposed onto the undeformed geometry for the crushing analysis. The displacement assigned to each mode was set equal to the 3D printer bead size (Gattas and You, 2015) of 0.15mm.

In addition to geometric imperfections, the residual stresses and hardening due to the manufacturing process may also affect the behaviour of the core. The forming process of the core was simulated in ABAQUS to evaluate its effect. Unless stated otherwise, identical material properties and numerical inputs as outlined in section 4.2 were implemented. The flat sheet was partitioned at the location of the crease lines (Figure 4.5(a)). The sheets were then positioned between two rigid moulds. The outer rigid moulds were then displaced until they

were 0.2mm away from the inner moulds (equivalent to the thickness of the sheet) (Figure 4.5(c-f)). Following this the outer moulds were lifted away to allow any spring back effects to occur (Figure 4.5(g)). In each of these steps a smooth step amplitude was applied and KE/IE was limited to below 5% following the onset of plastic strains developing in the sheet. The deformed geometry and initial stress state were then imported into a new model; tie-constraints were applied; and, the core was crushed.

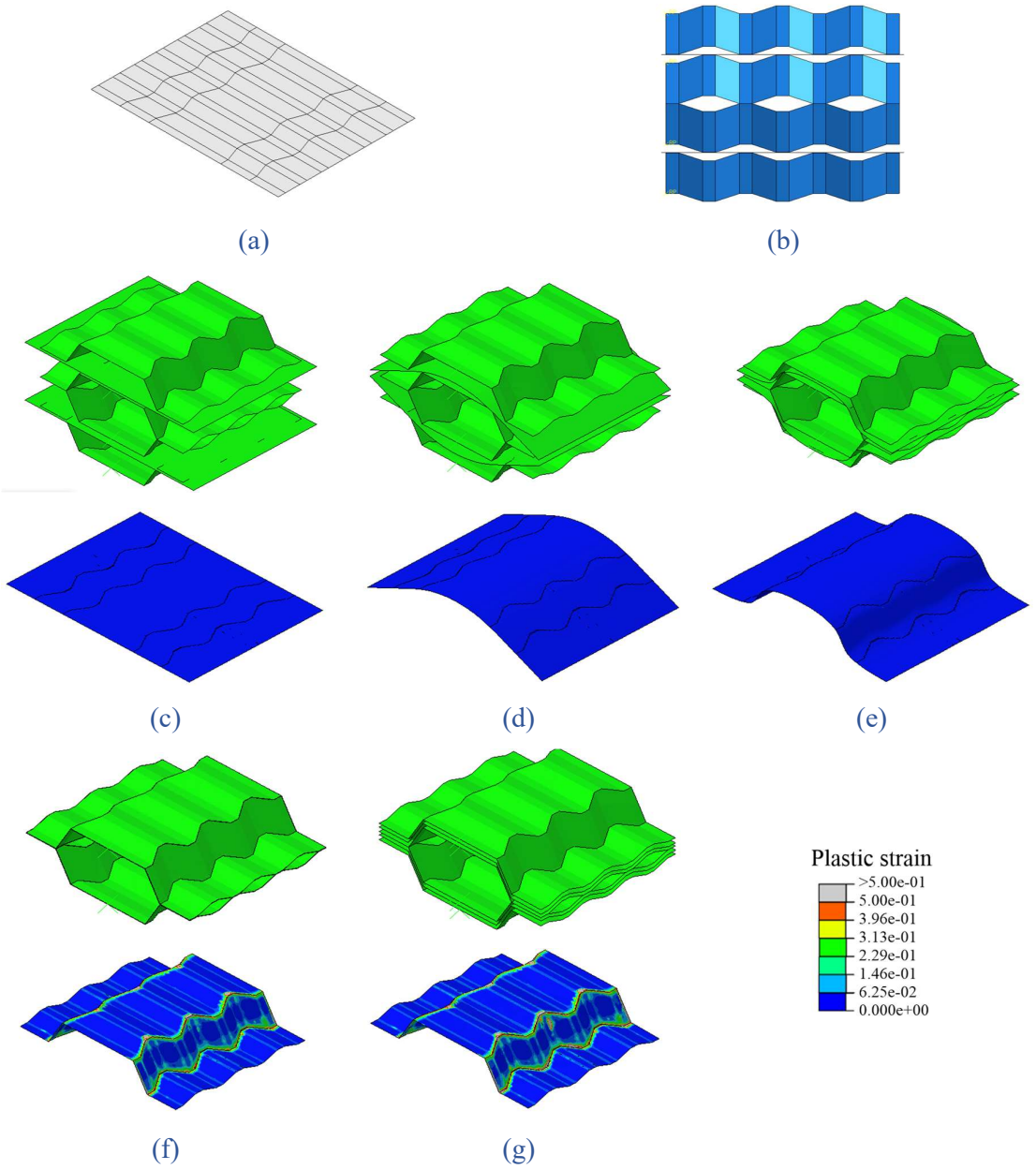
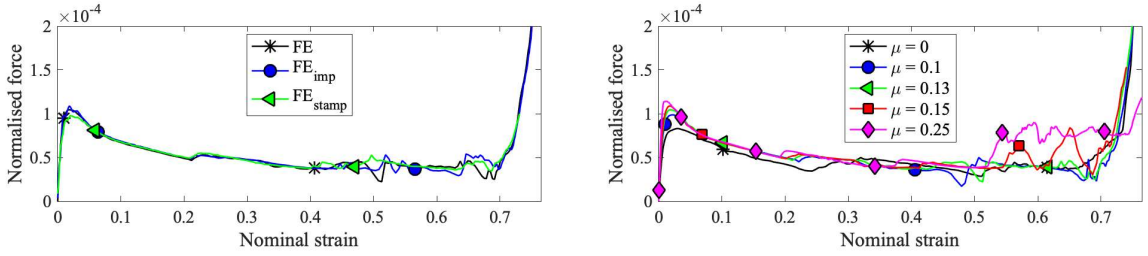


Figure 4.5 FE simulation of manufacturing process

Figure 4.6(a) compares the unbuckled geometry, FE, with the model that has superimposed buckling modes, FE_{imp}, and the model mimicking the manufacturing process, FE_{stamp}. The initial peak force for FE and FE_{imp} are approximately equivalent whilst FE_{stamp} has a reduced initial peak magnitude. Notwithstanding, the remaining behaviour for all three is approximately equivalent, indicating that the effect of initial imperfections and stress state does not influence the overall behaviour greatly. For simplicity all the simulations will therefore not include initial geometric imperfections or an initial stress state.



(a) (b)

Figure 4.6 (a) Imperfection sensitivity; and, (b) friction coefficient sensitivity study

4.2.3 Effect of friction coefficient

Due to the kinematics of the crease pattern, the origami honeycomb exhibits lateral deformation during the crushing of the tube. Penalty friction was applied in the simulations which provides some restraint to this movement. To investigate the effect of friction and select an appropriate value for comparison with experiments, a sensitivity study was completed with friction values, μ, of 0, 0.1, 0.13, 0.15 and 0.25. The results are provided in Figure 4.6(b).

In general, for all cases with $\mu > 0$ an increased response was observed when compared to $\mu = 0$. For $\mu > 0$, the magnitude of the force is approximately equivalent except in the initial and final stages of the deformation. In the initial stages the peak force magnitude increases with increasing μ. Figure 4.7(a) shows the deformation and plastic strain contours on the deformed and undeformed geometry at $\varepsilon = 0.04$ respectively. It is clearly seen that the increase in friction reduces the lateral movement at the supports resulting in an increased hourglass

shape. When compared to $\mu = 0$, where the plastic strains are quite uniformly distributed at the hinges for all units along the height, as the friction increases the plastic strains develop non-uniformly with the largest strains developing in the middle unit. Additionally, these plastic strains deviate slightly from the crease pattern. This deviation from the crease pattern, due to the restraint provided by the friction, results in a higher initial peak force.

For $\mu = 0.13$ and 0.25 the force increases significantly at around $\varepsilon = 0.55$. Figure 4.7(b) shows that for $\mu = 0.25$ the side l_1 length of the top and bottom units bend inwards and meet. This results in the increased force in the later stages of the deformation. As the friction reduces (refer to $\mu = 0.13$ in Figure 4.7(b)), the bending inwards of these lengths becomes less severe and they do not contact one another. Ultimately $\mu = 0.13$ was chosen for comparison with experiments as the observed deformation from experiments matched closely.

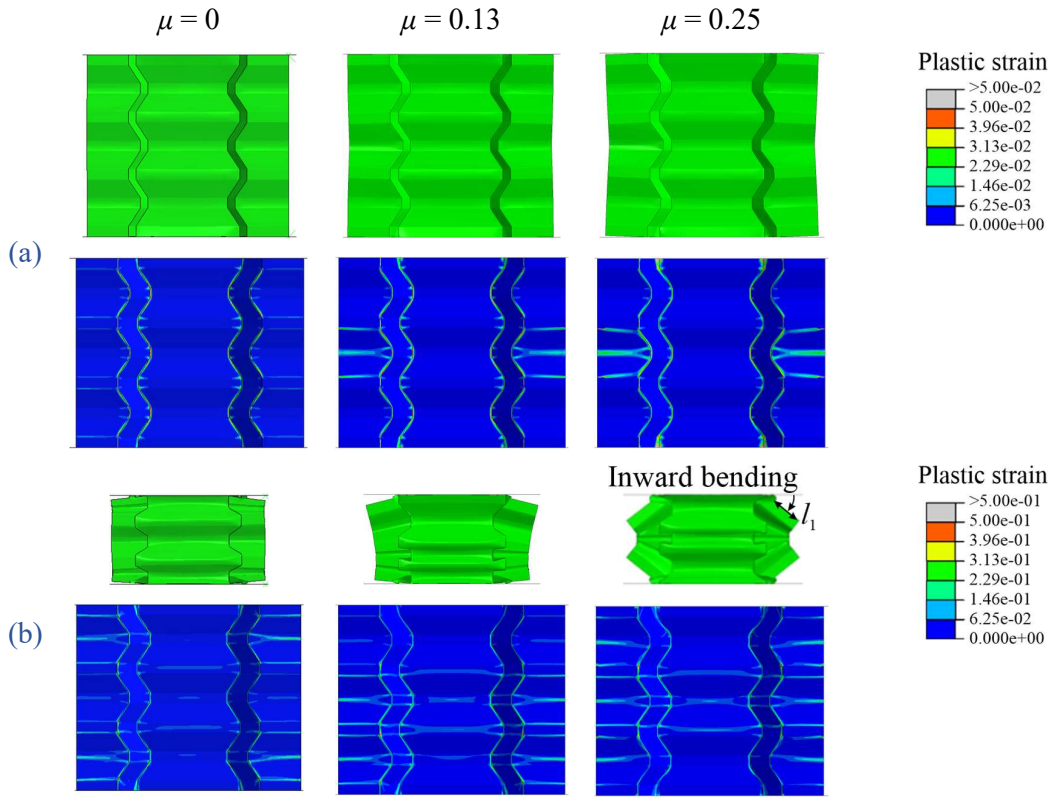


Figure 4.7 Deformation and plastic strain contours at nominal strains of: (a) 0.04; and, (b) 0.55 for alternative friction coefficients

4.2.4 Experimental and numerical comparison

Figure 4.8 compares the experiments, S1-3, with the numerical simulation, FE. The initial peak of S1 and S2 is approximately equivalent with FE, while S3 has an initial peak of larger magnitude. Following the initial peak S1-3 return to a similar value. In section 4.2.3 it was shown that friction can influence the initial peak before the behaviours generally return to a similar level. The increase in the initial peak of S3 could potentially be due to increased friction resulting from the surface roughness at the edges.

In the samples, following the initial peak, softening occurs followed by an increase in force at $\varepsilon = 0.19$. Softening then continues with another less defined increase in force at around $\varepsilon = 0.38$. Finally, the force plateau's and varying degrees of stiffening occur before locking. When compared to FE, the softening after the initial peak is slightly larger and the force oscillations are more pronounced for S1-3. Additionally, the stiffening and increase in force as the nominal strain increases past $\varepsilon = 0.55$ is less pronounced for FE.

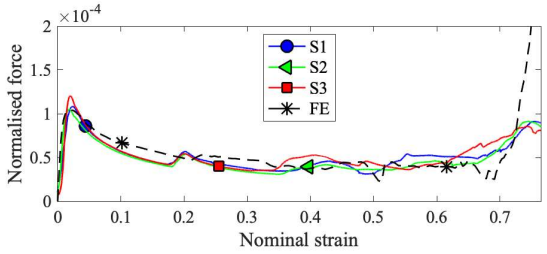


Figure 4.8 Numerical and experimental comparison

The deformation of S3 and FE is compared in Figure 4.9. The deformation of both is roughly similar with the deformation initially forming in the central unit, followed by the sequential folding of the bottom unit and then finally the folding of the top unit. One major difference is the deformation of the *s* length in contact with the bottom support. For S3, between $\varepsilon = 0.26$ - 0.34 the *s* length (refer to Figure 4.1 and 4.9) at the support folds flat whereas for FE it remains vertical. Additionally, between $\varepsilon = 0.56$ - 0.73 the degree of inward folding appears to be larger and less symmetric for S3 when compared to FE. This may be due to a larger

friction in the experiments restricting the lateral displacement of the unit. The friction sensitivity study in section 4.2.3 illustrated that an increase in force in the later stages of deformation was due to the inward bending of the l_1 lengths. Notwithstanding, the behaviour and deformation matches relatively well with the experiments.

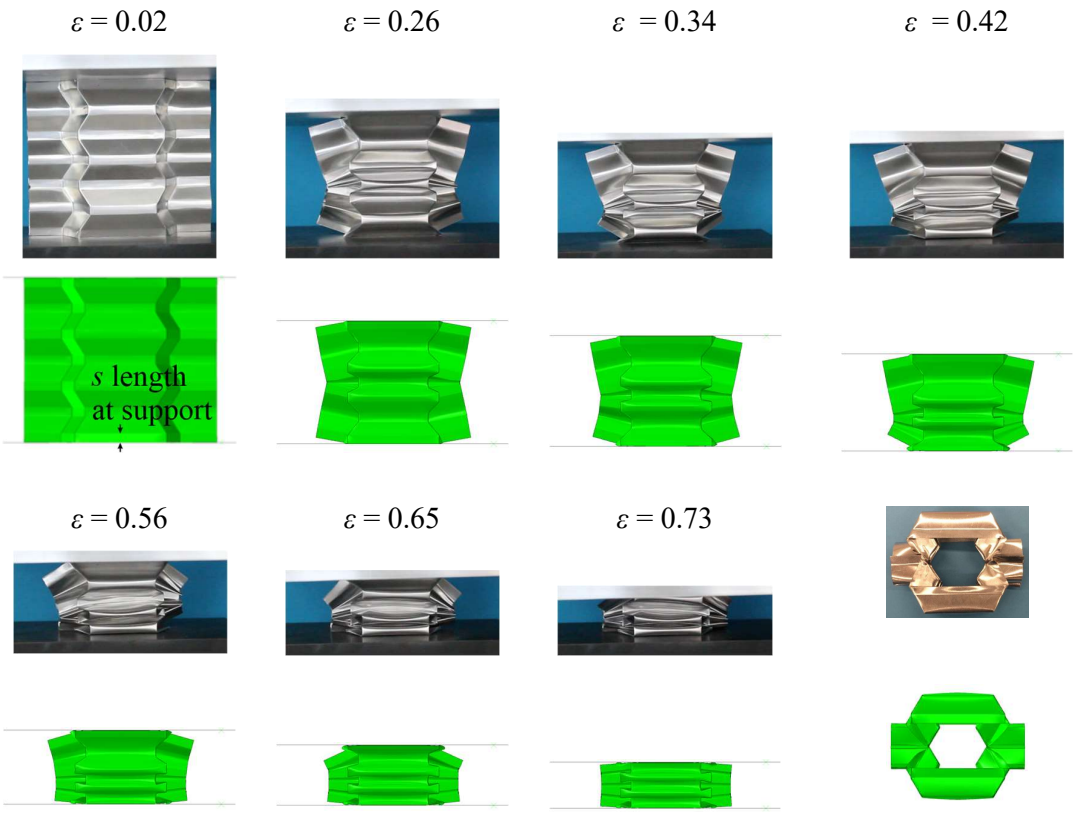


Figure 4.9 Deformation comparison of S3 and FE

4.3 Geometric analysis

In the following section a parametric study will be pursued to determine the effect of the variables that make up the underlying crease pattern and initial configuration.

4.3.1 Numerical simulation

The numerical modelling technique was shown to provide accurate representation of the behaviour in section 4.2, with the small differences predominately attributed to the effect of

friction. The numerical method for the parametric studies was identical to that outlined in section 4.2.

4.3.2 Ungraded tubes

4.3.2.1 Geometry and numerical simulation

In the parametric study l_1, l_2 and l_3 remain equivalent for all tubes. H also remains constant for all tubes except tubes in group E. Variables a, α, θ_0 and M are varied systematically to determine their effect. The dimensions of all the tubes are provided in Table 4.3. The model's name notation adopted is a-α-θ_0-M. In group A the α is varied. In group B, θ_0 is varied and a is also adjusted to ensure H remains equivalent. Similarly in group C and D, M is varied and θ_0 and a are adjusted respectively to ensure H remains constant. Group E is equivalent to a except the θ_0 is varied resulting in a smaller H.

4.3.2.2 Results and discussion

Due to the variation in a and M the weights of the tubes are not constant. The energy per unit mass, specific energy absorption, SEA, determined with the equation below (Lu and Yu, 2003), is therefore used to compare the energy absorption capacity of the tubes.

$$SEA = \int_0^{\varepsilon_D} \sigma d\varepsilon \tag{4.4}$$

where ε_D is the densification strain of the core. Tan et al. (2002) provided a standardised method for determining the densification strain in foams numerically by maximising the energy absorption efficiency, E_f.

$$\left[\frac{dE_f}{d\varepsilon}\right]_{\varepsilon=\varepsilon_D} = 0 \tag{4.5}$$

The energy absorption efficiency for structures that exhibit structural softening or hardening is provided as follows (Harris *et al.*, 2017), where σ_m is the maximum stress experienced up until ε.

$$E_f = \frac{1}{\sigma_m}\int_0^{\varepsilon} \sigma d\varepsilon \tag{4.6}$$

The initial peak force, $F_{0,II}$, and SEA were extracted from the analysis results and are presented in Table 4.3. $F_{0,II}$ is normalised using Eq.(4.2).

Table 4.3 Geometry and results for ungraded crease-to-crease connected tubes

Group	Name	a	α	$\bar{\rho}$	θ_0	γ_0	M	H	Mass	ε_D	SEA	$F_{0,II}$
	a-α-θ_0-M	[mm]	[°]	[-]	[°]	[°]	[-]	[mm]	[g]	[-]	[J/g]	[-]
	10-60-141-3	10	60	0.0119	141.06	60	3	91.57	13.34	0.73	0.76	1.05e-4
A	10-40-141-3	10	40	0.0159	141.06	31.25	3	91.57	13.34	0.73	0.79	9.3e-5
	10-45-141-3	10	45	0.0144	141.06	36.87	3	91.57	13.34	0.73	0.80	9.8e-5
	10-75-141-3	10	75	0.0145	141.06	102.41	3	91.57	13.34	0.73	0.75	1.07e-4
	10-80-141-3	10	80	0.0202	141.06	124.24	3	91.57	13.34	0.75	0.60	8.6e-5
B	19-60-60-3	18.86	60	0.0193	60	112.62	3	91.57	20.80	0.73	0.25	1.3e-5
	11-60-120-3	10.89	60	0.0119	120	81.79	3	91.57	14.08	0.71	0.52	5.1e-5
	10-60-150-3	9.76	60	0.0131	150	48.29	3	91.57	13.14	0.76	1.22	1.63e-4
	10-60-160-3	9.57	60	0.0168	160	33.48	3	91.57	12.98	0.77	1.79	2.51e-4
C	10-60-71-4	10	60	0.0174	71.20	109.25	4	91.57	17.55	0.69	0.49	2.5e-5
	10-60-43-5	10	60	0.0229	42.90	116.38	5	91.57	21.76	0.63	0.45	2.0e-5
D	18-60-141-2	17.65	60	0.0107	141.06	60.00	2	91.57	13.42	0.76	0.46	6.4e-5
	6-60-141-4	6.17	60	0.0126	141.06	60.00	4	91.57	13.25	0.68	1.31	1.67e-4
	4-60-141-5	3.88	60	0.0130	141.06	60.00	5	91.57	13.17	0.69	2.00	2.34e-4
E	10-60-120-3	10	60	0.0120	120	81.79	3	86.96	13.34	0.70	0.55	5.9e-5
	10-40-120-3	10	40	0.0126	120	45.52	3	86.96	13.34	0.71	0.63	6.6e-5
	10-45-120-3	10	45	0.0119	120	53.13	3	86.96	13.34	0.70	0.61	6.3e-5
	10-75-120-3	10	75	0.0194	120	123.63	3	86.96	13.34	0.68	0.46	5.0e-5
	10-80-120-3	10	80	0.0276	120	141.15	3	86.96	13.34	0.70	0.46	4.4e-5

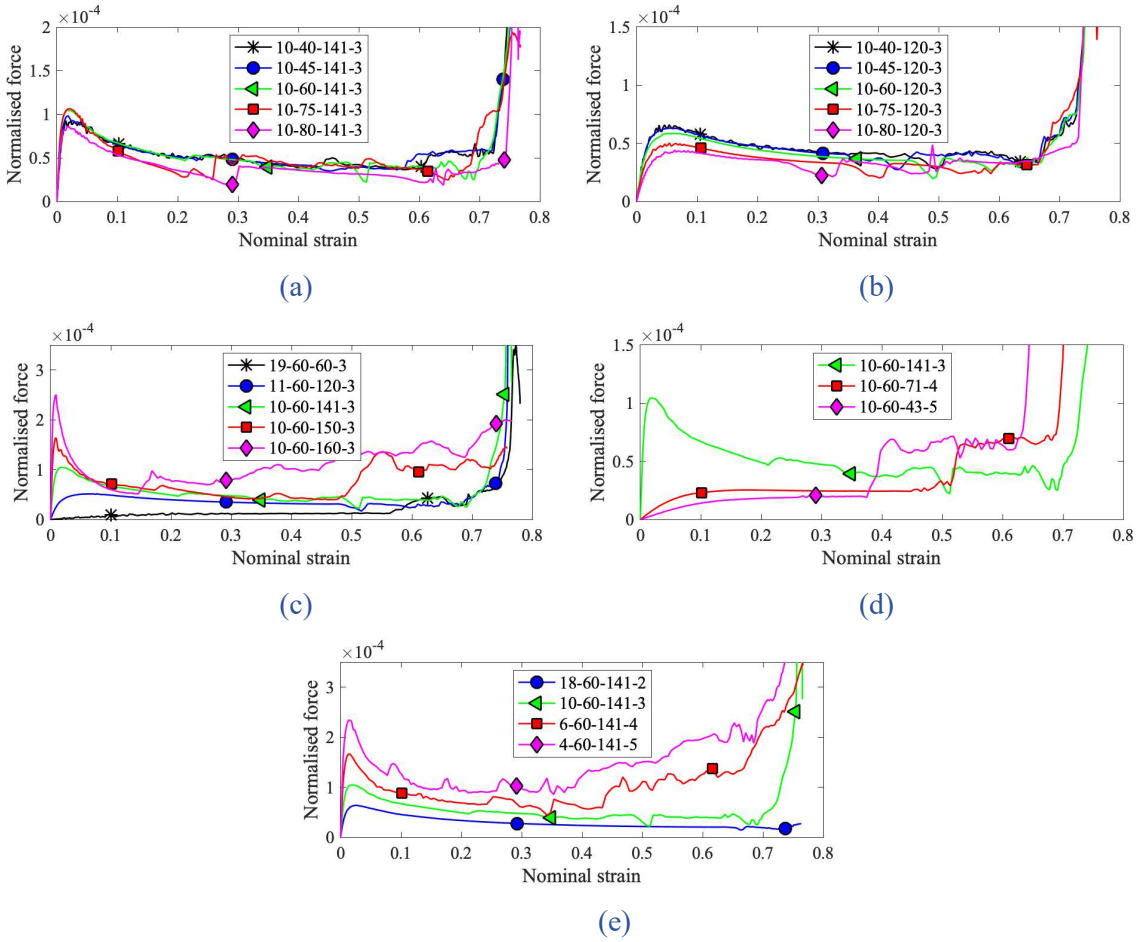
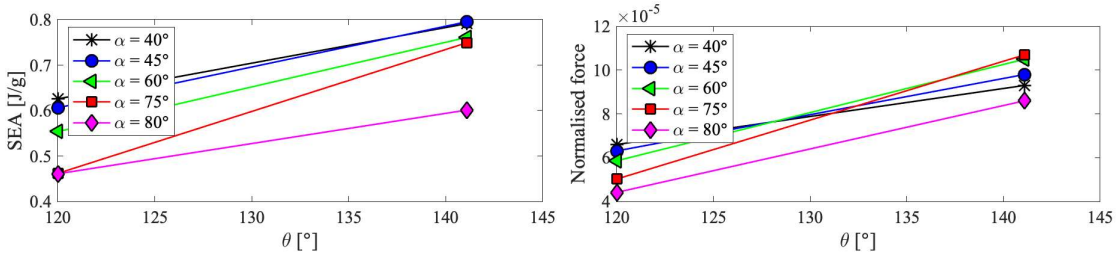


Figure 4.10 Ungraded tube normalised force vs nominal strain comparison for: (a) group A; (b) group E; (c) group B; (d) group C; and, (e) group D

Figure 4.10(a, b) show that tubes with alterative α's, but otherwise identical parameters, can exhibit different behaviour. Figure 4.11 provides the SEA and the initial peak normalised force magnitude for cores with different α's at the two θ_0's. The SEA appears to generally increase as α decreases, with $\alpha = 80°$ having the smallest SEA for both initial θ_0's and $\alpha = 40°$ and $\alpha = 45°$ having the largest SEA at $\theta_0 = 120°$ and 141.1° respectively. In contrast, the effect of α on the initial normalised peak force is varied, with $\alpha = 75°$ having the second smallest and largest initial normalised peak force for $\theta_0 = 120°$ and 141.1° respectively. With all other variables equivalent, α influences both the initial peak force and the SEA for the tubes. Additionally, reducing θ_0 results in a reduction in both the SEA and initial peak force.



(a) (b)

Figure 4.11 Comparisons of tubes with alterative a α's: (a) SEA; and, (b) initial peak force

The order at which the units in the tubes collapse also varies depending on the initial α. Figure 4.12(a, b) shows the collapse of 10-60-141-3 and 10-75-141-3 respectively. While the central unit collapses first for 10-60-141-3, the unit closest to the loading plate collapses first for 10-75-141-3. Notwithstanding the initial peak force for both is quite similar.

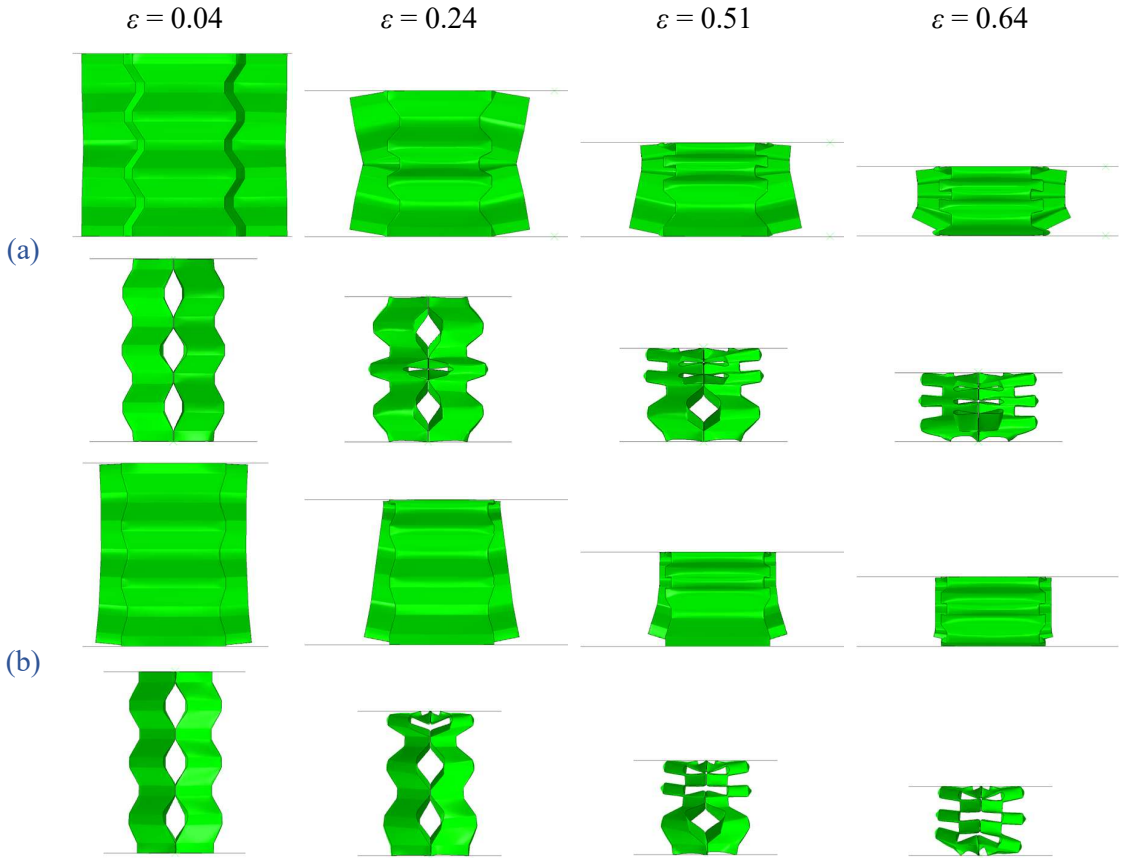


Figure 4.12 Deformation of: (a) 10-60-141-3; and, (b) 10-75-141-3

The normalised force vs nominal strain for tubes from group B are provided in Figure 4.10(c). Reducing a and increasing θ_0 results in an increase in the peak force and SEA. However, there appears to be a limit at which point the deformation significantly deviates from the crease pattern. This is observed in Figure 4.13, where the deformation follows the crease pattern and the plastic strains are localised at these locations for 11-60-120-3. However, for 10-60-160-3, even in the early stages of loading, significant deformation occurs away from the crease lines. Rather than undergoing softening as the loading continues, hardening behaviour is observed for 10-60-160-3 (Figure 4.10(c)). Tube 10-60-150-3 exhibits softening until a load jump at $\varepsilon = 0.50$. This is attributed to significant inward bending of the l_1 length of the top and bottom units (Figure 4.13(b)). This results in the behaviour deviating from the crease pattern, albeit initially it does follow the crease pattern.

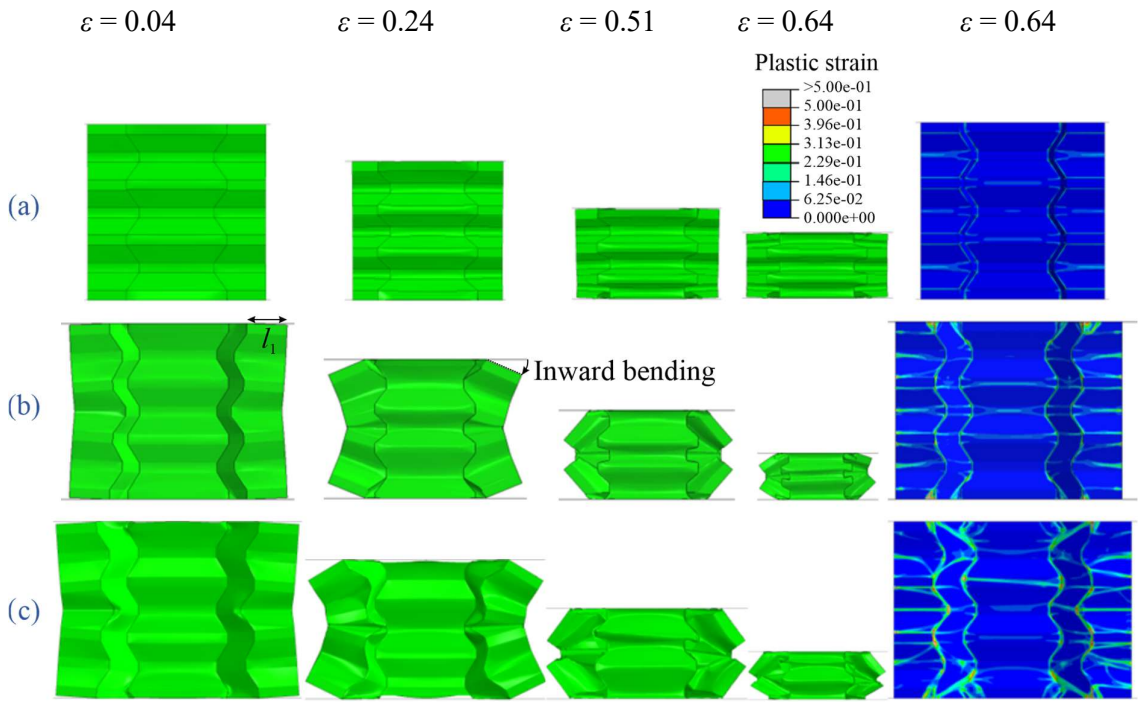


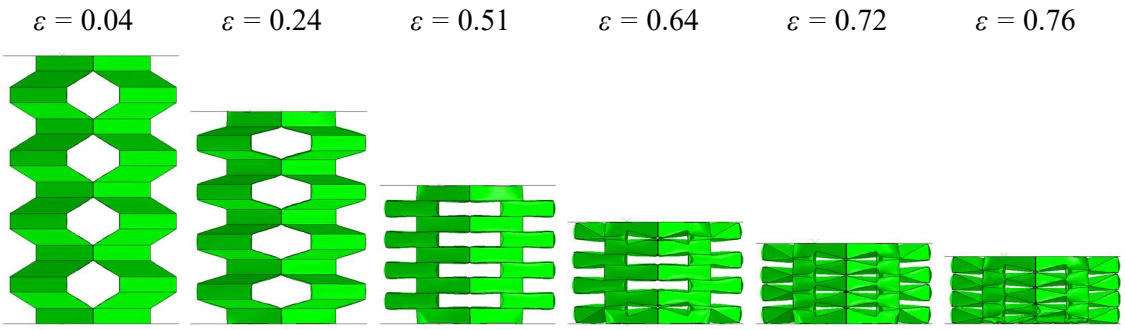
Figure 4.13 (a) 11-60-120-3; (b); 10-60-150-3; and, (c) 10-60-160-3

Similarly, as observed in group B, for group C the reduction of θ_0 results in the deformation of the tube following the crease pattern more closely with a reduction in the initial

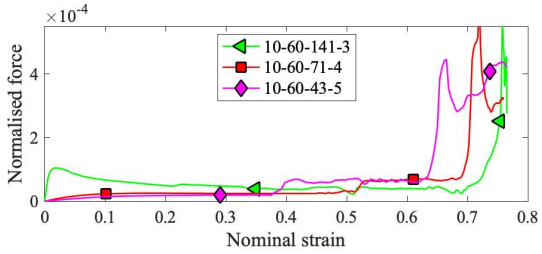
peak force and SEA. Figure 4.14(a) shows that all units for 10-60-71-4 fold simultaneously until locking at approximately $\varepsilon = 0.51$. At this point the load jumps to larger magnitude and oscillates about this value until a further increase in the force. During this period, the dominant deformation mechanism is the collapse of the prismatic voids that run in the in-plane direction ($\varepsilon = 0.51$ to $\varepsilon = 0.72$). In the final stages of deformation, the connection facets buckle ($\varepsilon = 0.76$). For clarity the range of the normalised force in Figure 4.11 was reduced to show the initial peaks closely. However, Figure 4.14(b) shows the complete behaviour. From this figure, 10-60-71-4 is shown to have roughly three stages, corresponding to the deformation mechanisms described above.

For tubes where the deformation does not occur simultaneously, see Figure 4.12(a), the second plateau does not occur or is less pronounced as the prismatic voids that run in the in-plane direction have already collapsed/deformed. However, Figure 4.14(b) shows that 10-60-141-3 also exhibits the third stage associated with the buckling of the connection facets. While the collapse of the voids and buckling of connection facets provides an increase in the stiffness, for this thesis, the effect of grading the origami crease pattern is of primary interest. Therefore, the buckling of the connection facets it taken as the onset of densification. For group C, as the connection facets width s remained constant, increasing M results in an early onset of densification (Figure 4.11(d, e)).

Similarly to group B, reducing a resulted in an increase in the initial peak force for group D. However, in contrast to group C, where an increase in θ_0 and reduction in M resulted in an increase in the peak force, the increase observed in group D occurred with an increase in M. This highlights that a and θ_0 may be more dominant variables than M. Additionally, reducing a and increasing M resulted in larger amounts of inward bending of the l_1 length (Figure 4.15).



(a)



(b)

Figure 4.14 10-60-71-4 (a) deformation; and, (b) normalised force vs nominal strain

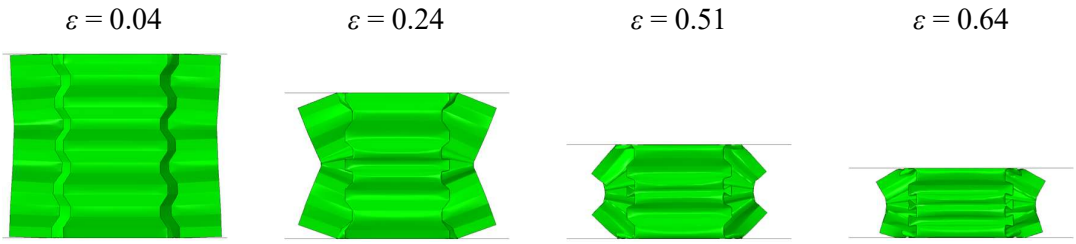


Figure 4.15 6-60-141-4 deformation

4.3.2.3 Effect of connection method

To compare the crease-to-crease connection method with the face-to-face connection method identical tubes from each group in Table 4.3, except with no s length, were simulated with the face-to face connection method. This results in tubes with an initial height of 56.57mm. The lengths for side I of the crease pattern were identical to the values found in Table 4.1. For side II, l_1^{II}, l_2^{II} and l_3^{II} were set to 25mm, 20mmm and 40mm respectively. The tubes are labelled in the same manner except with a TM is inserted in front of a-α-θ_0-M. Table 4.4 provides a summary of the geometry and the results from the simulations.

Table 4.4 Geometry and results for ungraded face-to-face connected tubes

Group	Name	a	α	$\bar{\rho}$	θ_0	γ_0	M	H	Mass	ε_D	SEA	$F_{0,II}$
	TMa-α-θ₀-M	[mm]	[°]	[-]	[°]	[°]	[-]	[mm]	[g]	[-]	[J/g]	[-]
	TM10-60-141-3	10	60	0.0132	141.06	60	3	56.57	8.42	0.87	1.31	2.37e-4
A	TM10-40-141-3	10	40	0.0184	141.06	31.25	3	56.57	8.42	0.86	1.34	1.95e-4
	TM10-45-141-3	10	45	0.0165	141.06	36.87	3	56.57	8.42	0.86	1.35	2.04e-4
	TM10-75-141-3	10	75	0.0160	141.06	102.41	3	56.57	8.42	0.87	1.16	2.22e-4
	TM10-80-141-3	10	80	0.0225	141.06	124.24	3	56.57	8.42	0.84	1.01	1.93e-4
B	TM11-60-120-3	10.89	60	0.0139	120	81.79	3	56.57	9.17	0.88	0.80	9.4e-5
	TM10-60-150-3	9.76	60	0.0143	150	48.29	3	56.57	8.22	0.84	2.00	3.39e-4
	TM10-60-160-3	9.57	60	0.0180	160	33.48	3	56.57	8.06	0.78	2.61	4.52e-4
C	TM10-60-69-5	10	60	0.0263	68.90	110.01	5	56.57	14.04	0.81	0.35	3.9e-5
D	TM8-60-141-4	7.50	60	0.035	141.06	60.00	4	56.57	8.42	0.87	1.85	2.95e-4
	TM4-60-141-8	3.75	60	0.0140	141.06	60.00	8	56.57	8.42	0.66	3.03	4.43e-4

Figure 4.16(a) provides a comparison of the normalised force and nominal strain for 10-60-141-3 and TM10-60-141-3 for μ = 0 and 0.13. While the peak normalised force increases for both connection methods, the face-to-face connection method appears to be more sensitive to the μ, exhibiting a far larger increase. Like the crease-to-crease connection method (section 4.2.3), following the initial peak the magnitude of the force returns to a similar magnitude for frictionless and friction conditions.

The face-to-face connection method provides a significant increase in the normalised peak force and SEA when compared to the crease-to-crease connection method. The difference cannot be purely associated with the reduced surface area of TM10-60-141-3. Figure 4.16(b) provides the force and displacement behaviour, which is not normalised, illustrating that the face-to-face connection results in a larger force throughout the crushing process. Additionally, TM10-60-141-3 has a larger nominal strain at densification. This is due to the additional

connection facets of width s that increase the height for the crease-to-crease connection method and result in a residual height when the units have reached the end of their kinematic range. The same conclusions can be drawn by comparing the SEA, normalised peak force, and nominal densification strain for the other equivalent tubes in Table 4.3 and Table 4.4.

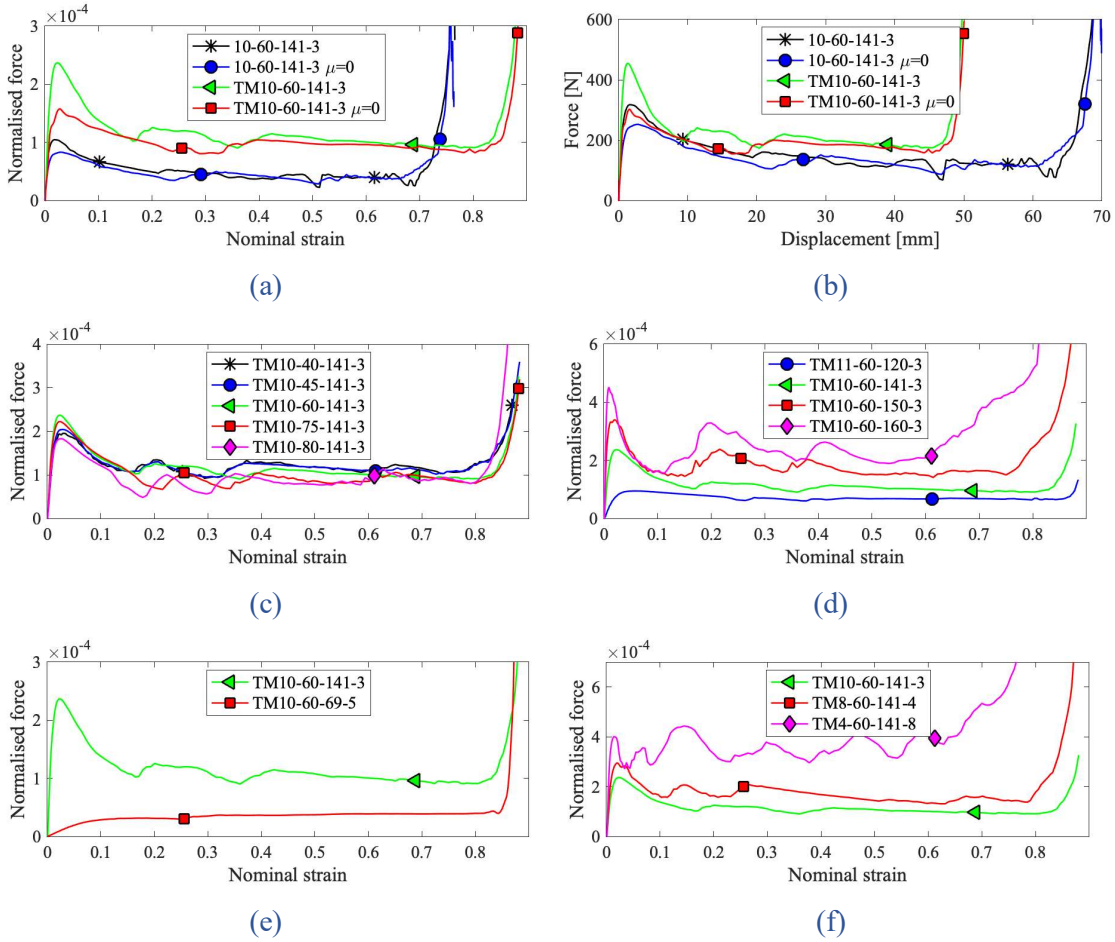


Figure 4.16 Ungraded face-to-face tube normalised force vs nominal strain for: (a-b) comparison with the crease-to-crease connected tube; (c) group A; (d) group B; (e) group C; and, (f) group E

Like the crease-to-crease connection method, α alters both the initial peak force and the SEA when all other variables are held constant (Figure 4.16(c)), though, the order from minimum to maximum changes.

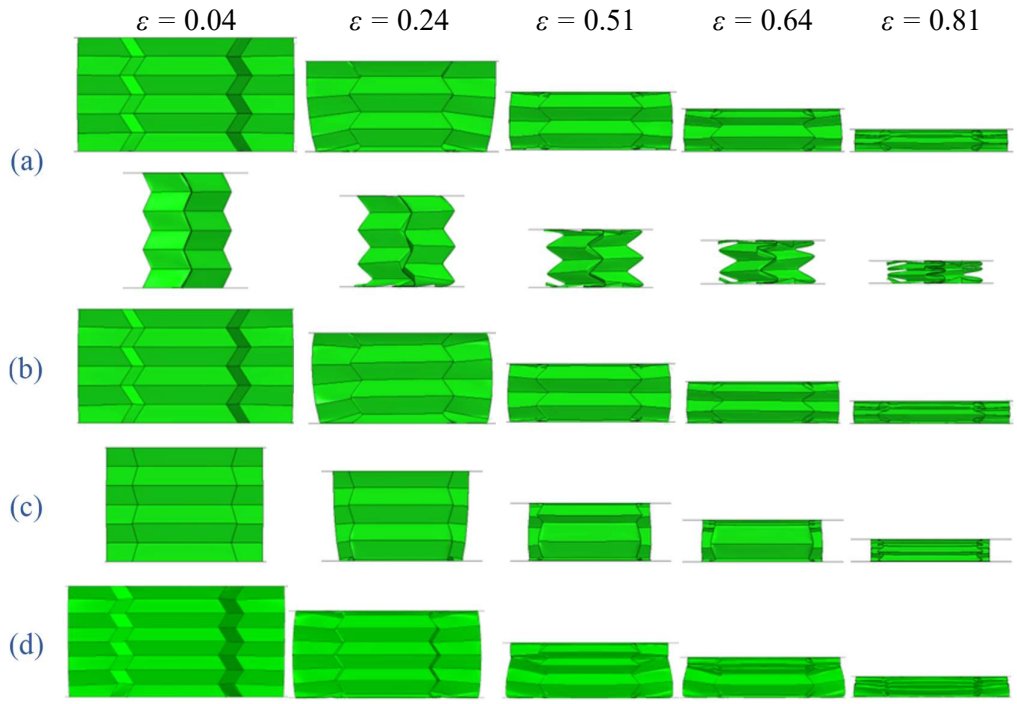


Figure 4.17 Deformation of: (a) TM10-60-141-3; (b) TM10-60-141-3-fr0; (c) TM10-75-141-3; and, (d) TM8-60-141-4

A difference in the deformation mode is also observed for the face-to-face connection method. Rather than the central unit collapsing first, half of the unit in contact with the support initially folds (Figure 4.17 (a), $\varepsilon = 0.24$), followed by half the unit at the other support folding. Subsequently the unfolded portions of the tube fold. This deformation process is observed for most of the tubes simulated (Figure 4.17(a, c-d)). However, like the findings from the crease-to-crease connection method, there appears to be a limit on the maximum θ_0 and minimum a after which point the deformation deviates significantly from the crease pattern. This is clearly observed in Figure 4.18 for TM10-60-160-3 and TM4-60-141-8.

The face-to-face connection method increases both the SEA and initial peak force when compared to the crease-to-crease connection method. Notwithstanding the general behaviour is quite consistent and similar trends were found from the parametric studies.

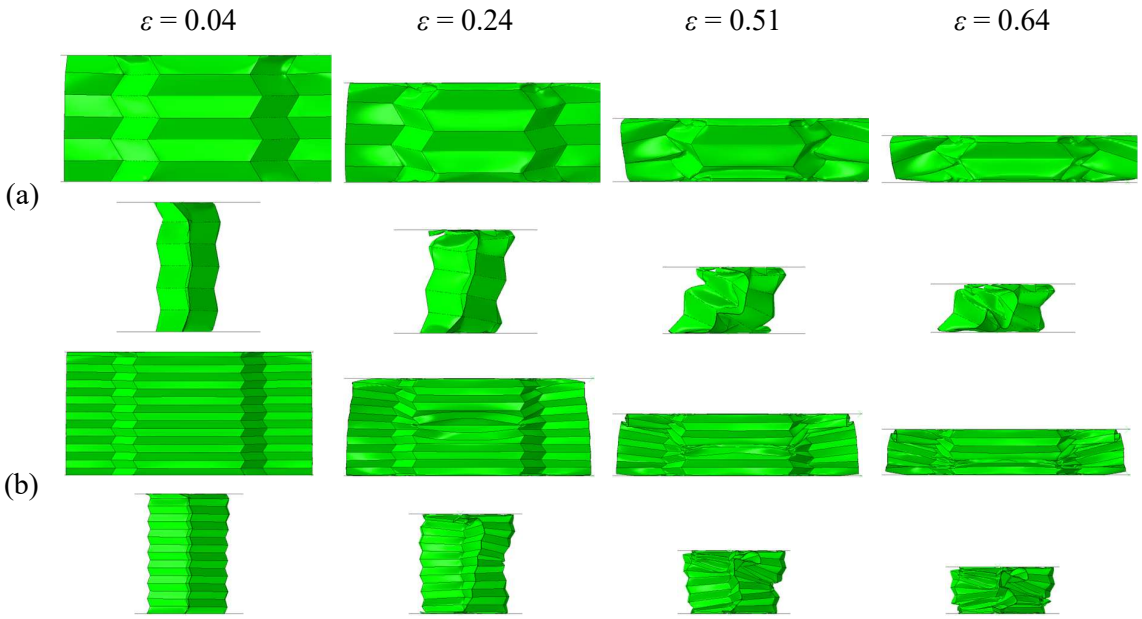


Figure 4.18 Deformation of: (a) TM10-60-160-3; and, (b) TM4-60-141-8

4.3.2.4 Comparison to core behaviour

In the previous section the behaviour of the origami honeycomb was only sought with respect to a representative tube. When implementing the origami honeycomb as a core the constraints provided by adjacent cells will influence the behaviour. To investigate the influence of these edge effects both face-to-face and crease-to-crease cores were simulated for the 11-60-120-3 tubes.

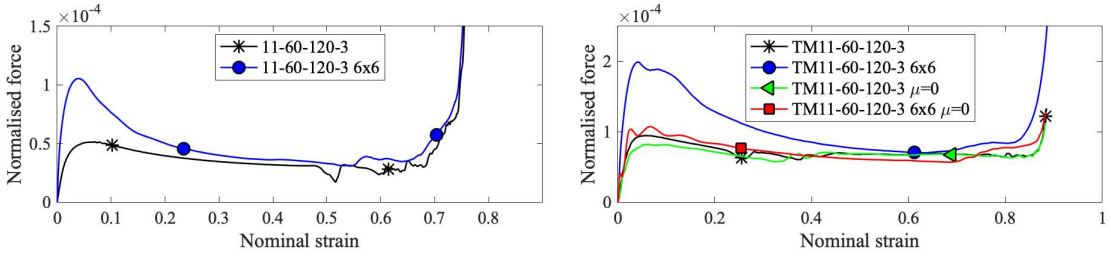


Figure 4.19 Comparison of tube and core for: (a) 11-60-120-3; and, (b) TM11-60-120-3

In both cases the normalised initial peak force is significantly larger for the 6×6 core when compared to the tube (1×1 core) (Figure 4.19). Figure 4.20 provides the deformation of

the 6x6 core while the deformation of the tube can be found in Figure 4.10(a). It is clear from the figures that the deformation of each singular tube that makes up the 6×6 core varies. In the *m* direction, the tubes at the centre deform a larger amount at the middle unit along the height ($M = 2$), whereas at the edges, the top ($M = 3$) and bottom ($M = 1$) units deform a larger amount initially. Initially larger changes in γ are also observed at the edges in the *n* direction. However, towards the end of the crushing ($\varepsilon = 0.75$) the deformation throughout the core becomes more uniform. Similar behaviour is also observed for the face-to-face connection method (Figure 4.21(a)).

The increase in the force is associated with this alternative and nonuniform deformation mode which is caused by the friction at the top and bottom faces of the core. The TM11-60-120-3 tube and 6×6 core were additionally simulated with frictionless conditions. The normalised force and nominal strain for these simulations are also provided in Figure 4.19(b). When frictionless conditions are applied the deformation becomes uniform (Figure 4.21(b)) and the behaviour of the core and tube therefore become similar. It should however be noted that the core still has a larger initial peak force when compared to the tube. This may be due to the additional creases that have double the thickness for the face-to-face connection method. This will be examined further in section 4.3.2.6.

As the number of cells increase in both the *m* and *n* direction the friction effects increase, resulting in deformations that deviates from the crease pattern and therefore significantly larger forces.

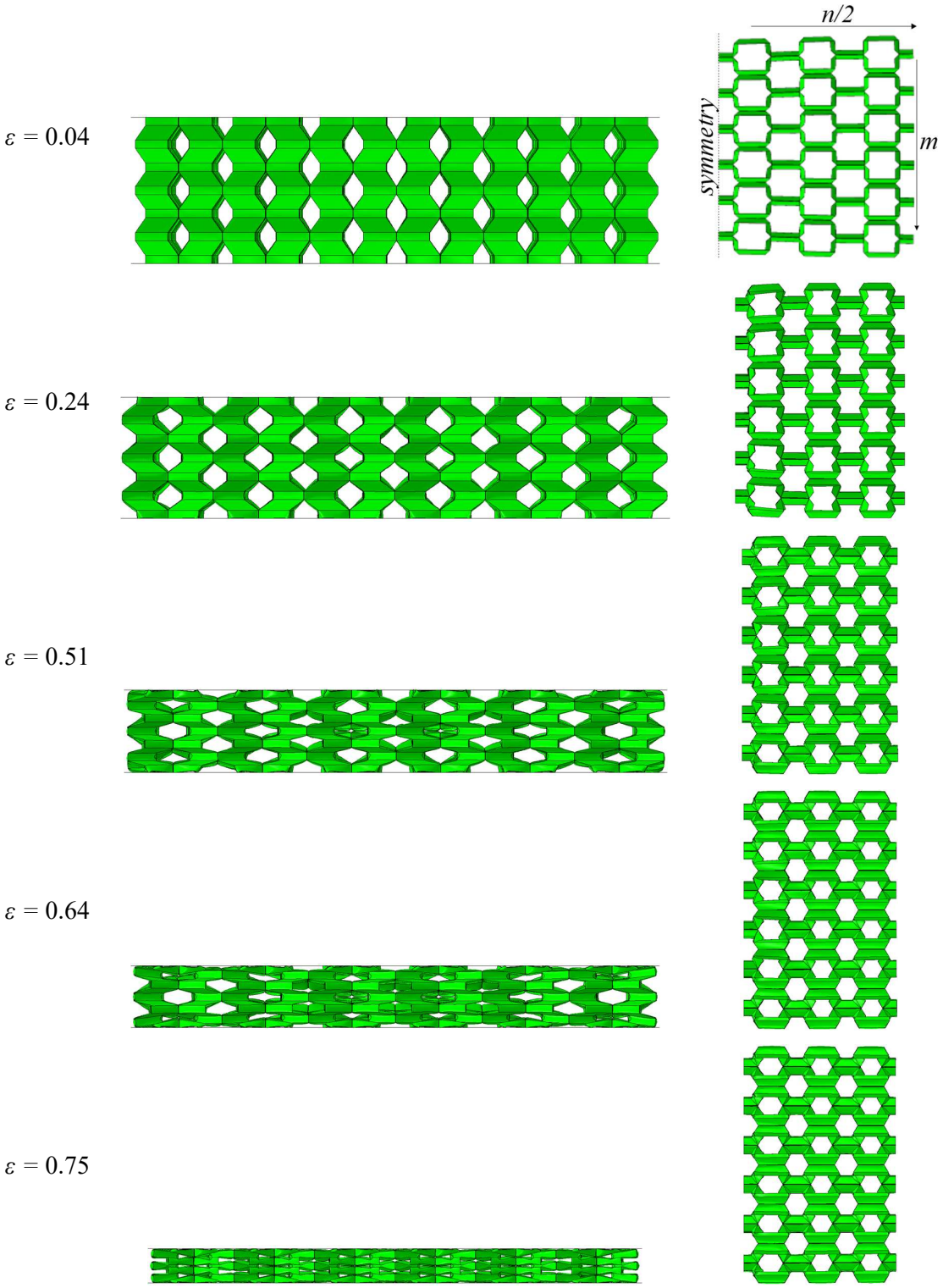


Figure 4.20 Deformation of 11-60-120-3 6×6 core

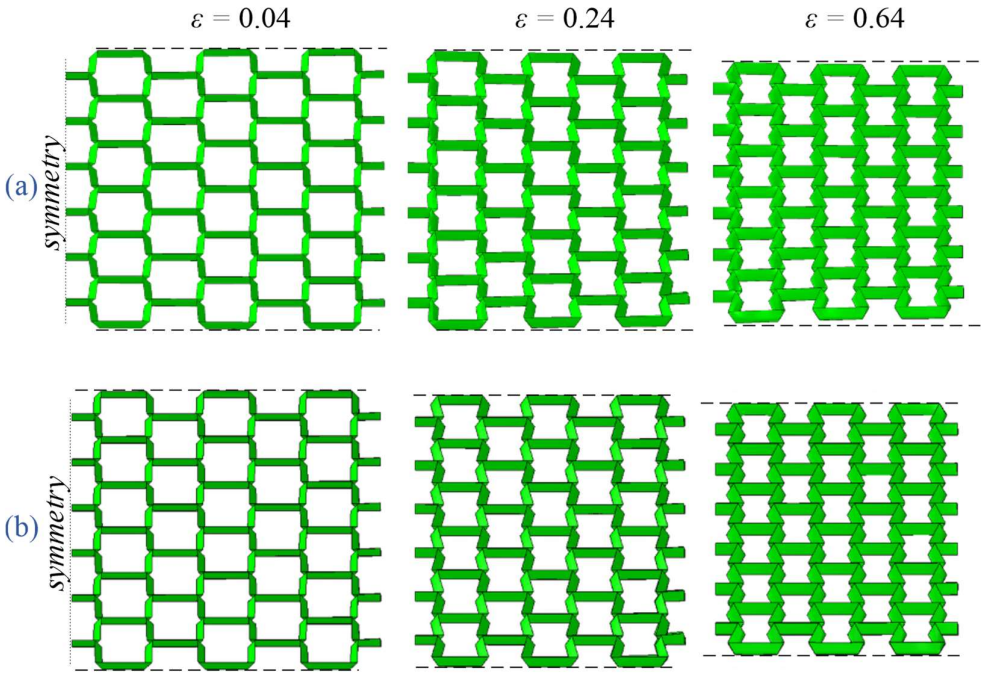
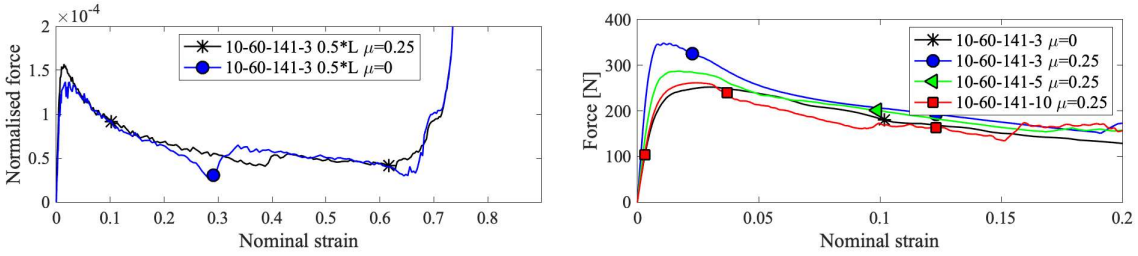


Figure 4.21 Deformation of TM11-60-120-3 6×6 with: (a) friction; and (b) frictionless conditions

4.3.2.5 Effect of friction

In the previous section it has been shown that the selection of μ has a large effect on the behaviour for the geometry simulated, especially in the initial stages where the peak force may increase significantly when compared to the frictionless scenario. This increase occurs due to the restraint provided by friction at the support. In all cases simulated the l_1, l_2 and l_3 length remained equivalent. In this section the effect of these lengths will be briefly touched on. Additionally, increasing the number of equivalent units along the height, to reduce these edge effects, is examined. These effects are investigated by simulating the tubes with a $\mu = 0.25$ and $\mu = 0$. $\mu = 0.25$ was selected as opposed to $\mu = 0.13$ to increase the observed effect of the friction.



(a) (b)

Figure 4.22 Normalised force vs nominal strain for: (a) 10-60-141-3 L0.5; and, (b) 10-60-141-*M*

Reducing l_1, l_2 and l_3 results in a reduction in the magnitude of the in-plane length change. A tube with identical parameters as outlines in Table 4.1 except half the l_1, l_2 and l_3 lengths (10mm,10mm,25mm) was simulated to examine the friction sensitivity. When compared to the original length tube, the reduced length tubes behaviour is less sensitive to μ (Figure 4.22(a)). This is also clearly observed in the deformation and plastic strain contours where minimal inward bending of l_1 length occurs for the reduced length tube (Figure 4.23) when compared to the original tube (Figure 4.7).

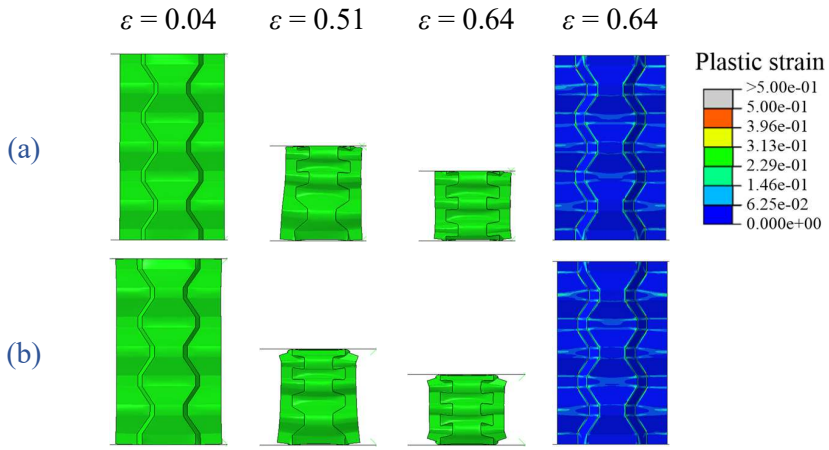


Figure 4.23 Deformation of reduced length tube (a) frictionless; and, (b) μ = 0.25.

Increasing the number of units in the *M* direction also reduces the friction sensitivity (Figure 4.22(b)), with 10-60-141-10 only having a marginally larger initial peak force. Due to the friction at the ends, the deformation occurs at the centre of the tube (Figure 4.24). The

increase in the number of units in the *M* direction increases the distance from the ends and therefore reduces the constraint to the central units.

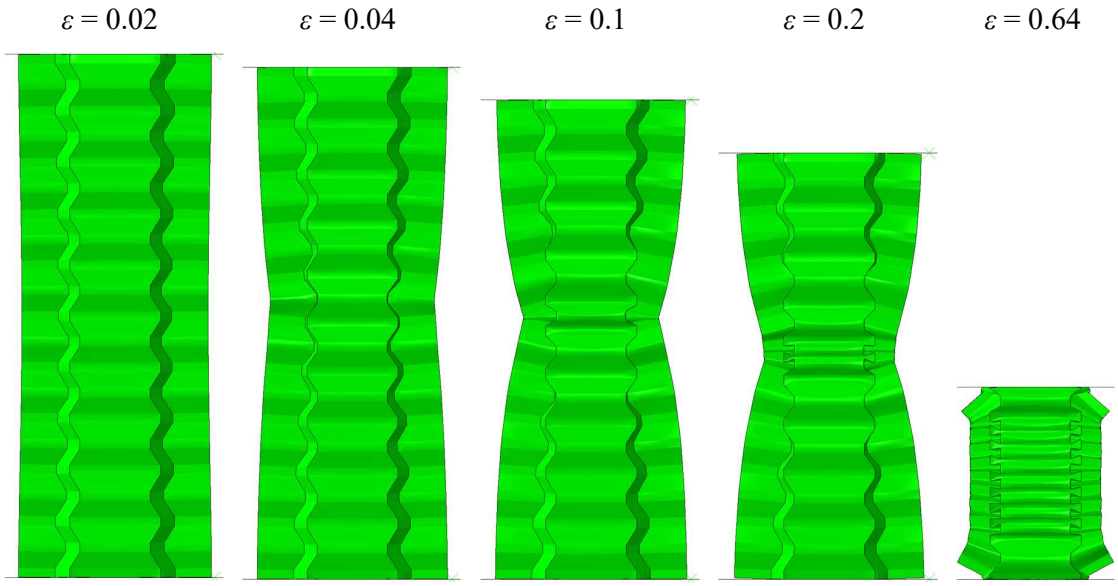


Figure 4.24 Deformation of 10-60-141-10

4.3.2.6 Quasi-static analytical model

An analytical prediction of the force displacement behaviour for the origami honeycomb can be formed assuming that all the deformation occurs following the kinematics imposed by the underlying crease pattern. In this case, the relationship can be found by equating the external work to the internal energy consumed by the rotation about the creases. The origami honeycomb is a single degree-of-freedom structure and therefore the angles that the creases must rotate through for a given change in height is known from Eq.(3.8). The rotation about the creases is large and therefore the analysis assumes fully plastic condition. M_p, should be calculated with respect to plane strain conditions as follows (Alexander, 1960; Johnson *et al.*, 1977; Meng *et al.*, 1983). In this case σ_y is taken as 140MPa (refer to Figure 4.3).

$$M_p = \frac{\sigma_y t^2}{2\sqrt{3}} \tag{4.7}$$

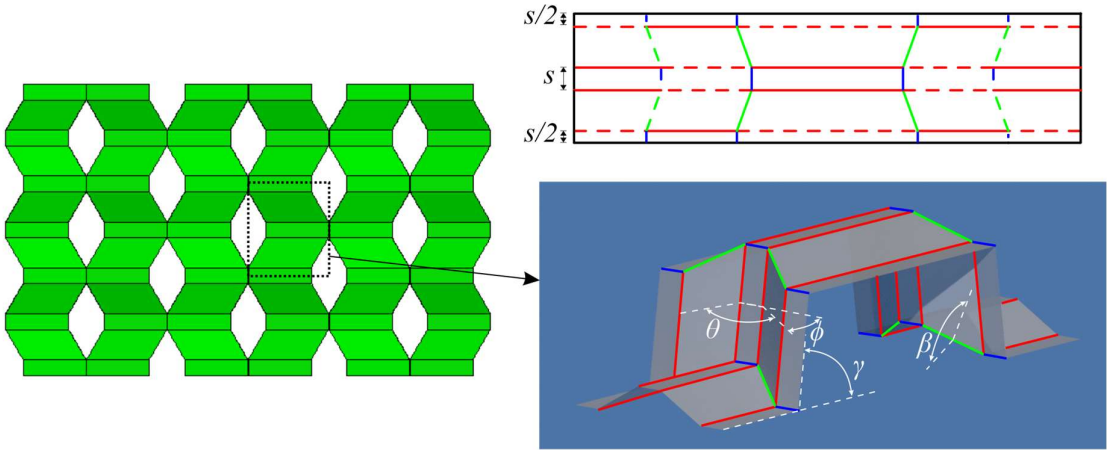


Figure 4.25 Representative unit for the crease-to-crease connected core

Taking a representative unit highlighted in Figure 4.25 for a core with the crease-to-crease connection method and equating external work to internal energy, the following expression is formed.

$$Fd\delta = 8M_{\mathrm{p}}L_{\mathrm{s}}d\phi + 16M_{\mathrm{p}}sd\gamma + 16M_{\mathrm{p}}\frac{a}{\sin\alpha}d\beta \tag{4.8}$$

where:

$$\delta = 2a\left(\sin\frac{\theta}{2} - \sin\frac{\theta_0}{2}\right) \tag{4.9}$$

$$\phi = \frac{\pi - \theta}{2} \tag{4.10}$$

$$\sin\phi = \frac{\tan\frac{\gamma}{2}}{\tan\alpha} \tag{4.11}$$

$$\tan\beta = \frac{\tan\phi}{\cos\alpha} \tag{4.12}$$

$$L_{\mathrm{s}} = 2l_1 + 2l_2 + l_3 \tag{4.13}$$

Using ϕ as the governing variable and rearranging Eq.(4.8) gives the following relationship.

$$F\frac{d\delta}{d\phi}d\phi = 8M_{\mathrm{p}}\left(L_{\mathrm{s}} + 2s\frac{d\gamma}{d\phi} + \frac{2a}{\sin\alpha}\frac{d\beta}{d\phi}\right)d\phi \tag{4.14}$$

Using the relationships provided in Eq.(4.9, 4.11-12), the quasi-static force can be found explicitly in terms of α and θ as follows.

$$F = \frac{4M_{\mathrm{p}}}{a\cos\frac{\theta}{2}}\left(L_{\mathrm{s}} + \frac{4s\tan\alpha\sin\frac{\theta}{2}}{1+\tan^2\alpha\cos^2\frac{\theta}{2}} + \frac{4a}{\tan\alpha\left(\cos^2\frac{\theta}{2}+\sin^2\frac{\theta}{2}\cos^2\alpha\right)}\right) \tag{4.15}$$

At the ends of the tube there is an extra half s length. Taking these extra lengths into consideration and multiplying by $m \times n$ to account for the entire core, the force displacement relationship is provided below for a core with M units along the height.

$$F = \frac{4mnM_{\mathrm{p}}}{a\cos\frac{\theta}{2}}\left(L_{\mathrm{s}} + \frac{s\tan\alpha\sin\frac{\theta}{2}\left(4+\frac{2}{M}\right)}{1+\tan^2\alpha\cos^2\frac{\theta}{2}} + \frac{4a}{\tan\alpha\left(\cos^2\frac{\theta}{2}+\sin^2\frac{\theta}{2}\cos^2\alpha\right)}\right) \tag{4.16}$$

$$\delta = 2aM\left(\sin\frac{\theta}{2} - \sin\frac{\theta_0}{2}\right) \tag{4.17}$$

The same process can be followed for the core with a face-to-face connection method, taking into consideration the creases with double thickness (Figure 4.26). In this case the force displacement relationship is defined below.

$$F = \frac{4mnM_{\mathrm{p}}}{a\cos\frac{\theta}{2}}\left(\begin{array}{l}\frac{1}{2}\left(\begin{array}{l}2L_{\mathrm{s}} + 2l_1^{\min} + l_3^{\min} - \frac{L_{\mathrm{s}} + 2l_1^{\min} + l_3^{\min}}{M} - \frac{l_3^{\min}}{m} + \frac{l_3^{\min}}{Mm} \\ +2l_{1c}^{\min} + l_{3c}^{\min} - \frac{l_{3c}^{\min}}{m}\end{array}\right) \\ +\frac{4a}{\tan\alpha\left(\cos^2\frac{\theta}{2}+\sin^2\frac{\theta}{2}\cos^2\alpha\right)}\end{array}\right) \tag{4.18}$$

where:

$$l_1^{\min} = \min\left(l_1^{\mathrm{I}}, l_1^{\mathrm{II}}\right) \tag{4.19}$$

$$l_3^{\min} = \min\left(l_3^{\mathrm{I}}, l_3^{\mathrm{II}}\right) \tag{4.20}$$

$$l_{1c}^{\min} = \min\left(l_1^{\mathrm{I}} + \frac{a}{\tan\alpha}, l_1^{\mathrm{II}} - \frac{a}{\tan\alpha}\right) \tag{4.21}$$

$$l_{3c}^{\min} = \min\left(l_3^{\mathrm{I}} - \frac{2a}{\tan\alpha}, l_3^{\mathrm{II}} + \frac{2a}{\tan\alpha}\right) \tag{4.22}$$

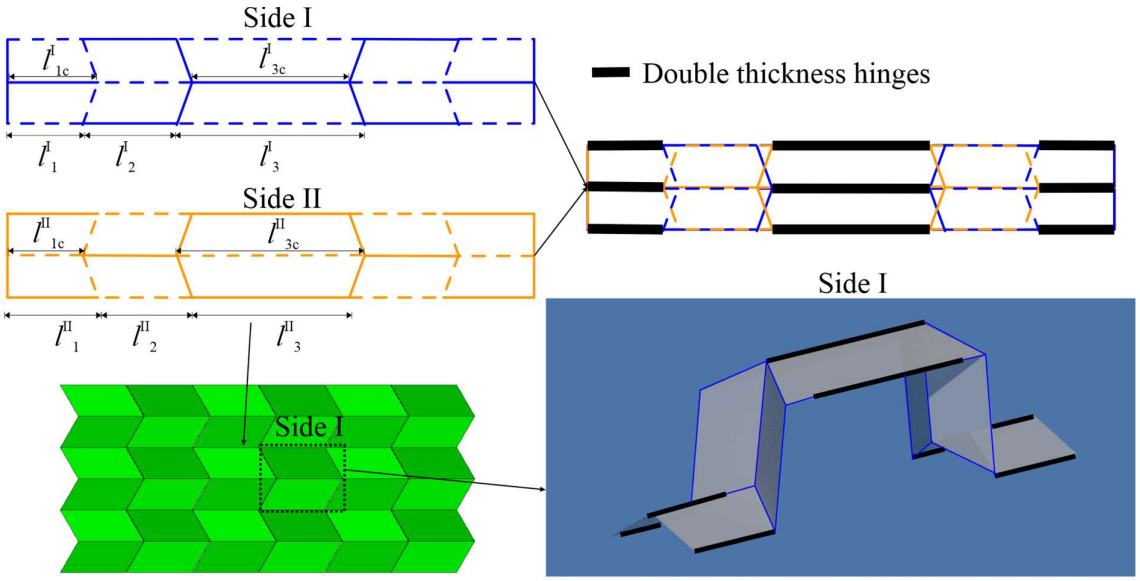


Figure 4.26 Representative unit face-to-face connected core

An estimation of the nominal densification strain is found using the equations below for the crease-to-crease and face-to-face connection method respectively. These equations are formed by assuming that densification occurs once $\theta = 0°$ and accounting for the thickness of the folded facets along the centre of two sheets.

$$\varepsilon_{\mathrm{D}} = \frac{2a\sin\frac{\theta_0}{2} - 4t}{2a\sin\frac{\theta_0}{2} + \left(2 + \frac{1}{M}\right)s} \tag{4.23}$$

$$\varepsilon_D = 1 - \frac{4t}{a \sin \frac{\theta_0}{2}} \tag{4.24}$$

4.3.2.7 Comparison with numerical results

As shown in previous sections, the origami honeycomb may show sensitivity to friction. The change in behaviour is most prevalent in the initial stages of deformation and depends on the initial geometry with: larger l_1, l_2 and l_3 lengths; larger $m \times n$ core; and, reduced M resulting in a larger sensitivity to friction and therefore initial peak force. In this section the analytical models Eq.(4.16-18) will be compared to both tubes and cores with friction and frictionless cases to validate their applicability. The analytical forces are normalised using Eq.(4.2).

Figure 4.27(a) compares Eq.(4.16-17) to the 10-60-141-3 tube with friction and frictionless contact conditions. The analytical predictions provide a good fit to the numerical model, except it overpredicts the initial peak for both the friction and frictionless end conditions. This is to be expected as the analytical model assumes fully plastic conditions and does not account for the initial elastic deformation. As the response is largely well predicted by the fully plastic conditions, the analytical model provides a reasonable estimation of the force displacement behaviour. While Eq.(4.16-17) also predicts the response for the 11-60-120-3 tube with friction well, it underestimates the response for the 6x6 core with friction contact conditions (Figure 4.27(b)). As discussed previously, this is due to the constraints provided by friction at the top and bottom faces, resulting in the deformation mode deviating from that prescribed by the crease pattern. In the cases where the friction provides a significant restraint, the analytical model will underestimate the force displacement behaviour.

The nominal strain at which densification occurs is also underpredicted by the analytical model. For 10-60-141-3 and 11-60-120-3 ε_D from the numerical simulation was found to be 0.73 and 0.71 respectively. In contrast, the analytical model predicts $\varepsilon_D = 0.59$ for both. This results in approximately 12.5mm and 10.5mm extra crushing distance before

densification for 10-60-141-3 and 11-60-120-3 respectively. The extra height due to the connection facets with width s is 35mm. However, as observed in Figure 4.12(a), some of these connection facets also experience significant deformation before $\theta_0 = 0°$ for all units in the tube. This results in the underprediction in the densification strain from analytical model for the crease-to-crease connection method.

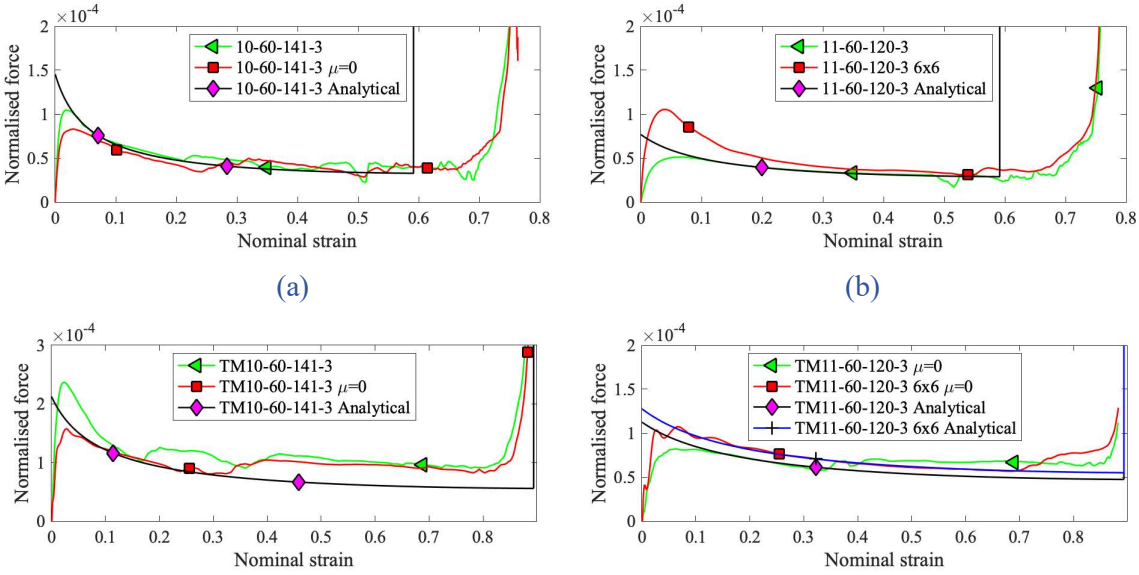
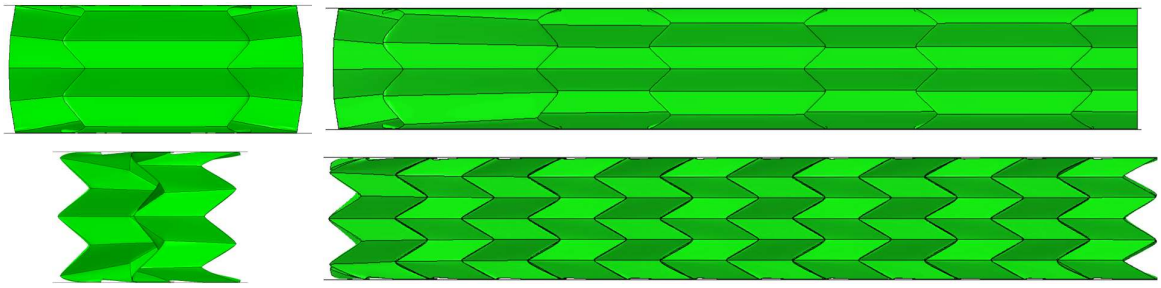


Figure 4.27 Comparison of analytical model to numerical simulations for: (a) 10-60-141-3 tube with friction and frictionless contact conditions; (b) 11-60-120-3 for tube and core with friction contact conditions; (c) TM10-60-141 tube with friction and frictionless contact conditions; and, (d) TM11-60-120-3 tube and core with frictionless contact conditions

Similarly to the finding for the crease-to-crease connection method, friction results in the underprediction of the force using Eq.(4.17-18) (Figure 4.27(c)). Additionally, the analytical model for the face-to-face connection method provides a less accurate fit for the tube (Figure 4.27 (c-d)). However, it accurately predicts the response of the core when friction does not affect the behaviour. For the tubes with frictionless contact conditions, the analytical model provides a reasonable prediction until $\varepsilon = 0.4$. After this point, the force from the numerical model increases and remains larger than that predicted by the analytical model. Comparing the

deformation of the tube and core in Figure 4.28 at this point, the deformation of the tube deviates a larger amount from the crease pattern. As opposed to the crease-to-crease connection method, where symmetry is maintained, the face-to-face connection method is not symmetric about the x - z plane. This imbalance results in the tendency of the tube to deviate further from the crease pattern. For the core, this is less of an issue as the restraint provided by neighbouring units prevent the core from deviating significantly from the crease pattern.



(a) (b)

Figure 4.28 Deformation at $\varepsilon = 0.4$ for TM11-60-120-3 (a) tube; and, (b) 6×6 core with frictionless contact conditions

When comparing the analytical models for the tube and core for TM11-60-120-3 (Figure 4.27 (d)), the core has a larger force then the tube. This is due to the extra double thickness lengths present in the core.

In contrast to the crease-to-crease connection method, the analytical model for the face-to-face connection method overpredicts the densification strain. The densification strain found using Eq.(4.24) does not consider the radius about which the hinges occur. In reality, the hinge locations are more diffuse and therefore it can be expected that the densification strain is lower than that predicted by Eq.(4.24).

4.3.2.8 Comments on the analytical model

The analytical models provide reasonable predictions of the behaviour, provided that the friction does not influence the behaviour greatly. The degree to which friction effects the

response is related to the: kinematics of the cell; geometry; and, number of units in the *m* and *n* direction. Care should be taken when applying the analytical model as for certain cores the friction effects may result in a significant increase in the force transferred than that predicted by the analytical model.

In this section Eq.(4.16), for the crease-to-crease connection method, will be examined closely to determine the effect of the underlying crease pattern. In the equations the variables associated with the underlying crease pattern are α, θ_0, a, s, L_s and M. Eq.(4.18), for the face-to-face connection, is quite similar and therefore the findings are equally applicable for this connection method.

The multiplier for both Eq.(4.16) and Eq.(4.18) is equivalent and is provided only in terms of the variable from the underlying crease pattern below. This term provides the horizontal offset (eccentricity) of the creases which are separated by the facets with width a (Figure 4.29). This is equivalent to the term that is found in the denominator for the force of a pair of pre-bent plates from a perfectly plastic analysis (Gao *et al.*, 2005). From this equation it can be seen that the multiplier is inversely proportional to this eccentricity. The force can therefore be increased by reducing this eccentricity (i.e. reducing a or increasing θ_0).

$$\frac{1}{a\cos\frac{\theta}{2}} \tag{4.25}$$

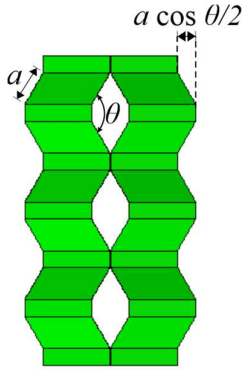


Figure 4.29 Horizontal offset

The first, second and third term within the parenthesis in Eq.(4.16) are associated with the horizontal, vertical and angled hinges respectively. These terms are provided below. The contribution to the force for each hinge can be increased by increasing the respective length of that hinge (i.e. L_s, s and a).

$$L_s \quad \text{(a)}$$

$$\frac{s\tan\alpha\sin\frac{\theta}{2}\left(4+\frac{2}{M}\right)}{1+\tan^2\alpha\cos^2\frac{\theta}{2}} \quad \text{(b)} \qquad \text{(4.26(a-c))}$$

$$\frac{4a}{\tan\alpha\left(\cos^2\frac{\theta}{2}+\sin^2\frac{\theta}{2}\cos^2\alpha\right)} \quad \text{(c)}$$

Eq.(4.26(b)) is plotted for several α's for the geometry specified in Table 4.1 with respect to θ in Figure 4.30(a). For each α, the magnitude of Eq.(4.26(b)) is the largest in the unfolded state ($\theta_0 = 180°$) and reduces to 0 at the fully folded state ($\theta_0 = 0°$). The figure also shows that as θ increases the variation between the α's increases. Additionally, the α that results in the largest magnitude of Eq.(4.26(b)) varies, where above $\theta_0 = 160°$ the largest α results in the largest magnitude and smallest α results in the smallest magnitude. Below $\theta_0 = 120°$ the difference becomes less significant, however, as θ_0 decreases further, the magnitude is larger for smaller α's.

A similar trend is observed (Figure 4.30(b)) for the angled hinges (Eq.(4.26(c))), albeit in the fully folded state the magnitude of Eq.(4.26(c)) does not tend to 0 and as θ_0 decreases there is a larger difference between α's. From the figure it is observed that for a given θ_0, the magnitude of Eq.(4.26(c)) is largest for the smallest α when $\theta_0 < 145°$. The force associated with the angled hinges is therefore predominately responsible for the observed increase in SEA

with decreases in α for θ_0 = 120° and 141° in Figure 4.11(a), as when folding from θ_0 = 145° to θ_0 = 0°, the area beneath the curves in Figure 4.30(b) is largest for the smallest α.

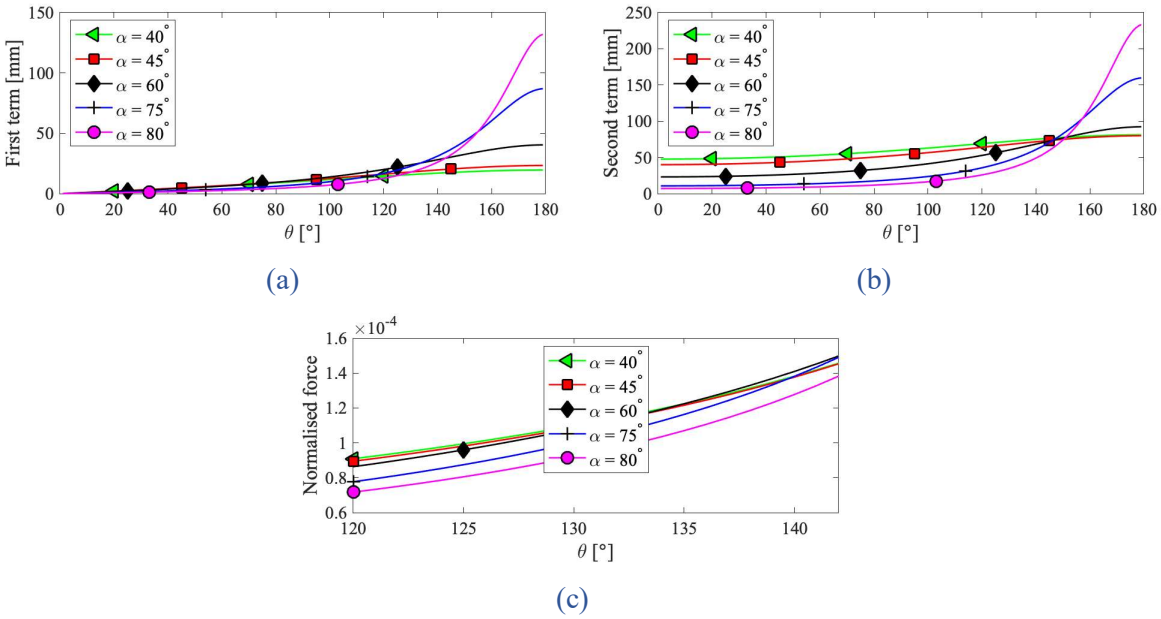


Figure 4.30 Analytical equation analysis: (a) Eq.(4.26(b)); (b) Eq.(4.26(c)); and, (c) Eq.(4.16) normalised with Eq.(4.2)

The difference in the peak force magnitude observed in Figure 4.11(b) is related to both the angled and vertical hinges. When θ_0 = 120° the results from the simulations showed that the magnitude of the force increased with decreasing α. However, when θ_0 =141° the opposite was the case, except for 10-80-141-3 which had the smallest overall magnitude. While the initial peak force magnitude is not captured by the analytical model due to friction and initial elastic deformations, this general trend is still predicted well by the analytical model (Figure 4.30(c)). Similar conclusions may also be drawn from the analytical model for the face-to-face connection method, except that the vertical hinges are not present.

4.3.3 Graded

4.3.3.1 Geometry and numerical simulation

Similar to the analysis of the ungraded geometry, the l_1, l_2 and l_3 will remain constant for the parametric study of the graded geometry. M will also be kept constant at 3. H of the graded tubes will however not remain constant. As shown form the analytical equations (section 4.3.2.8) both a and θ_0 significantly influence the force. Rather than altering both these variables to ensure H remains constant, for groups B-D only θ_0 is varied for each unit along the height. Group E varies both a and θ_0 to allow the connection of the facets, where a is calculated using Eq.(3.24). θ_0 is varied by adjusting α of each unit along the height. A series of ungraded tubes are also simulated (group A) for comparison purposes. A summary of the geometries is provided in Table 4.5. The naming convention is a_1-a_2-a_3-α_1-α_2-α_3-γ_0 where subscript 1,2,3 correspond to units along the height of the core (M = 1, 2, 3).

Table 4.5 Geometry and results for graded crease-to-crease connected tubes

Group	Name	a_1	a_2	a_3	α_1	α_2	α_3	γ_0	θ_1	θ_2	θ_3	M	H	Mass
	a_1-a_2-a_3-α_1-α_2-α_3-γ_0	[mm]			[°]	[°]	[°]	[°]	[°]	[°]	[°]	[-]	[mm]	[g]
	10-10-10-45-45-45-82	10			45.00	45.00	45.00	81.79	60.00	60.00	60.00	3	65.00	13.34
A	10-10-10-50-50-50-82	10			50.00	50.00	50.00	81.79	86.78	86.78	86.78	3	76.22	13.34
	10-10-10-58-58-58-82	10			57.68	57.68	57.68	81.79	113.56	113.56	113.56	3	85.20	13.34
	10-10-10-45-48-51-82	10			45.00	47.50	50.75	81.79	60.00	74.96	89.92	3	71.30	13.34
B	10-10-10-45-50-58-82	10			45.00	50.00	57.68	81.79	60.00	86.78	113.56	3	75.47	13.34
	10-10-10-45-55-74-82	10			45.00	55.00	73.71	81.79	60.00	105.34	150.68	3	80.25	13.34
C	10-10-10-45-55-65-82	10			45.00	55.00	65.00	81.79	60.00	105.34	132.36	3	79.20	13.34
	10-10-10-45-55-65-86	10			45.00	55.00	65.00	86.44	40.00	97.71	128.02	3	74.88	13.34
D	10-10-10-45-55-65-75	10			45.00	55.00	65.00	74.91	80.00	115.12	138.14	3	83.42	13.34
	10-10-10-45-55-65-65	10			45.00	55.00	65.00	65.46	100.00	126.50	145.12	3	87.26	13.34
E	8-10-13-45-50-58-82	8.39	10	13.26	45.00	50.00	57.68	81.79	60.00	86.78	113.56	3	79.33	13.80

The numerical simulation for the parametric study of the graded tube was identical to that outlined in section 4.2 except that the analysis time was increased. Unlike the ungraded tubes, locking occurs for the graded tubes during the analysis resulting in a jump in the force. To minimise any dynamic effects at these points the analysis time was increased. For 10-10-10-45-48-51-82 the analysis time was 0.1s. The analysis time was adjusted proportionally with the heights of the other tubes.

4.3.3.2 Results and discussion

Figure 4.31(a) compares 10-10-10-45-50-58-82 with three ungraded tubes (group A) constructed from each individual layer of the graded tube. Compared with the ungraded tubes, 10-10-10-45-58-58-82 undergoes three well defined load oscillations with increasing magnitude before densification. The initial peak force of 10-10-10-45-50-58-82 is of a similar magnitude to 10-10-10-45-45-45-82. However, the peak magnitudes of the subsequent load oscillations are larger than the equivalent ungraded tubes. This highlights the ability of the locking to grade the stiffness.

While the magnitude at the peak of these oscillation increases, the load returns to a similar value before the next oscillation begins. The first oscillations, approximately between $0.14 < \varepsilon < 0.3$, initiates once the tube has reached the end of its kinematic range (i.e. $\theta_1 = 0°$). At this point locking occurs, preventing the other units from folding further. Figure 4.32 provides the deformation and plastic strain contours on the undeformed geometry for 10-10-10-45-50-58-82. When the tube locks at $\varepsilon = 0.14$, γ at selected cross-sections along the height of the tube are approximately constant and equal to 90° (Figure 4.33). This is equivalent to γ_{max} of the underlying crease pattern.

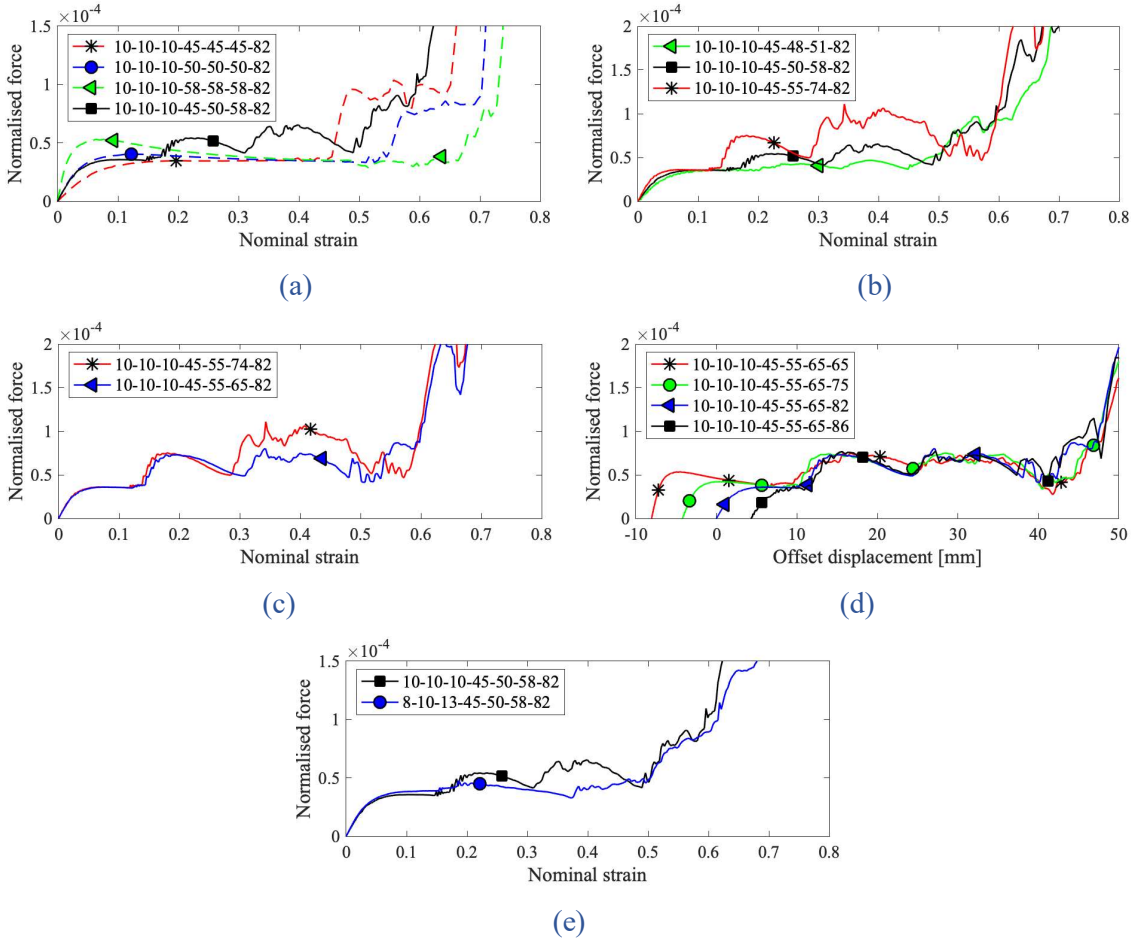


Figure 4.31 Graded tubes with crease-to-crease connection method comparison of: (a) 10-10-10-45-50-58-82 with group A; (b) group B; (c) group C; (d) group D; and (e) group E

To continue the crushing, the next unit must overcome the locking, resulting in a deformation mode that deviates from the crease pattern of the unit. The plastic strains that form away from the crease lines highlight this deviation. During the crushing of the second unit ($\varepsilon = 0.14 - 0.37$) these plastic strains, that form away from the crease lines, appear to be predominately located around the angled creases (Figure 4.32). While the second unit folds flat, the third unit also continues deforming simultaneously. However, the deformation appears to be largely concentrated at the crease locations, suggesting that it does not deviate significantly from the crease pattern as the second unit folds.

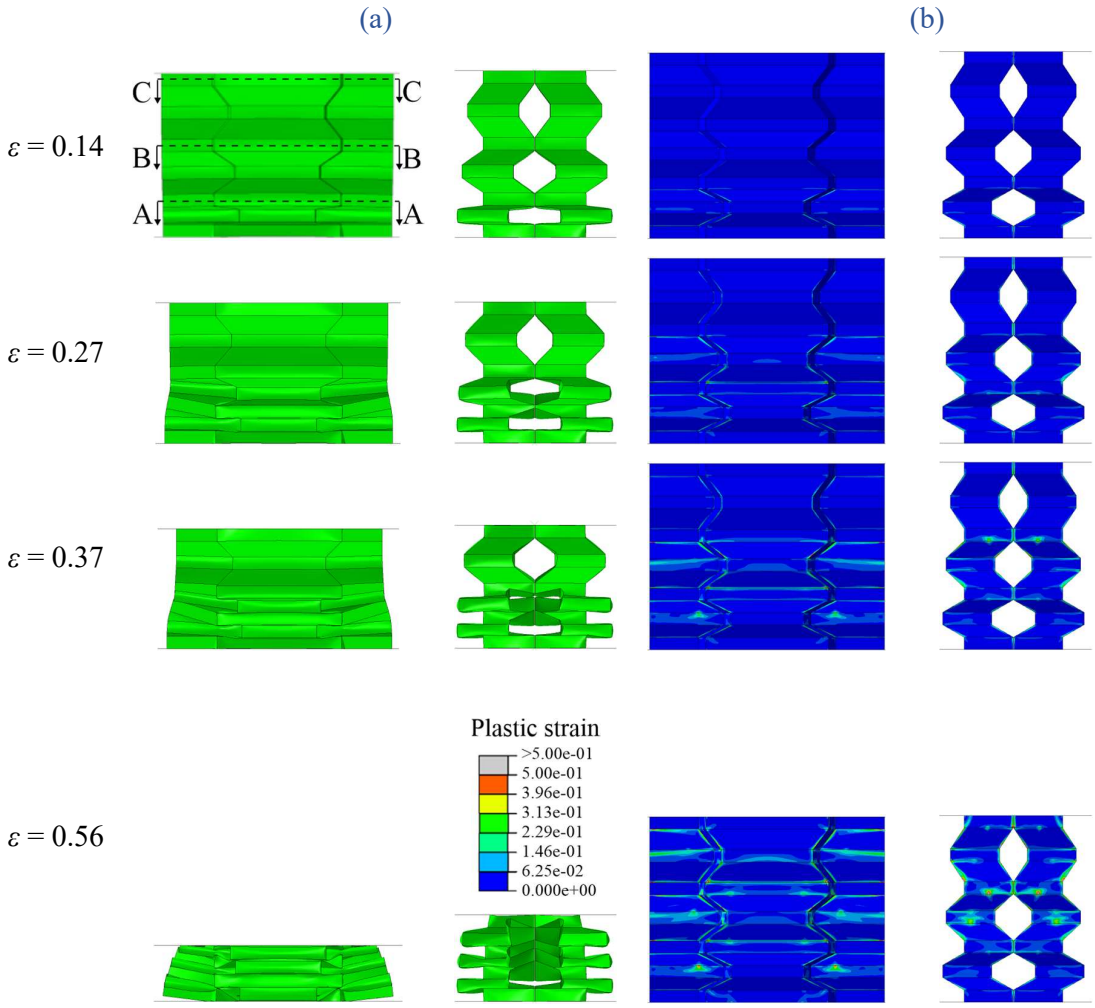


Figure 4.32 (a) Deformation and (b) plastic strain contours on undeformed geometry for 10-10-10-45-50-58-82

The first load oscillations end once $\theta_2 = 0°$ ($\varepsilon = 0.37$ in Figure 4.32), initiating the collapse of the third unit and the second load oscillation. When the third unit folds, plastic strains form around the angled crease locations in a similar manner as described above for the second unit. The units fold flat in an order of ascending θ_0 corresponding to ascending α.

When the second unit has folded flat ($\varepsilon = 0.37$), γ's at the selected cross-sections along the height of the tube have increased to 96°, 100° and 102° for sections A-A, B-B and C-C respectively (Figure 4.33). The increase in the γ at section A-A indicates that although the first unit has locked, the constraint provided by the first unit is not a fully fixed condition. At section

B-B, γ is again equal to γ_{max} for an equivalent unit with α = 50°, suggesting that although the tube locks, each individual unit still attempt to fold towards γ_{max} of the equivalent ungraded unit. Similar trends are also observed when the third unit has folded (ε = 0.56), where γ at sections A-A, B-B and C-C is approximately 98°, 105° and 114° respectively.

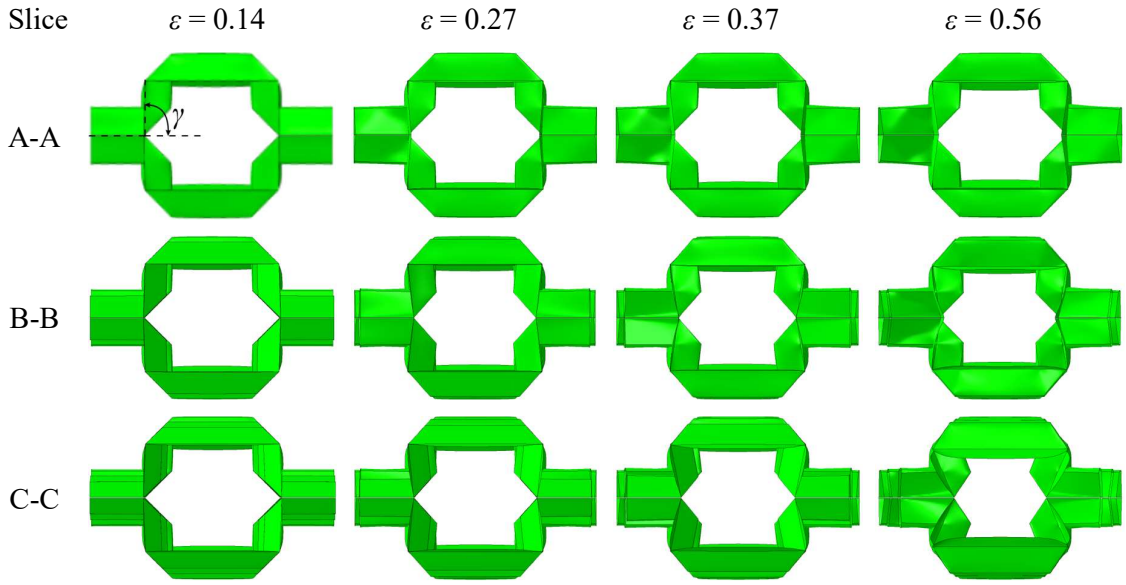


Figure 4.33 Cell angle for 10-10-10-45-50-58-82 at cross sections: (a) A-A; (b) B-B; and, (c) C-C

The tendency for each unit to fold towards γ_{max} of the equivalent ungraded unit results in the difference in curvature along the sides of the tube observed in Figure 4.34. From the kinematics of the crease pattern for an ungraded unit, increasing γ results in a length reduction. In the graded tube, once the first unit locks, the increased length reduction of the second unit results in a curvature developing. The degree of curvature is therefore related to the relative length change of adjacent unit which is governed by the α's of the adjacent units. This is observed when comparing 10-10-10-45-48-51-82, 10-10-10-45-50-58-82 and 10-10-10-45-55-74-82 in Figure 4.34(a-c), where the curvature along the edges increases with the difference in α's between adjacent units.

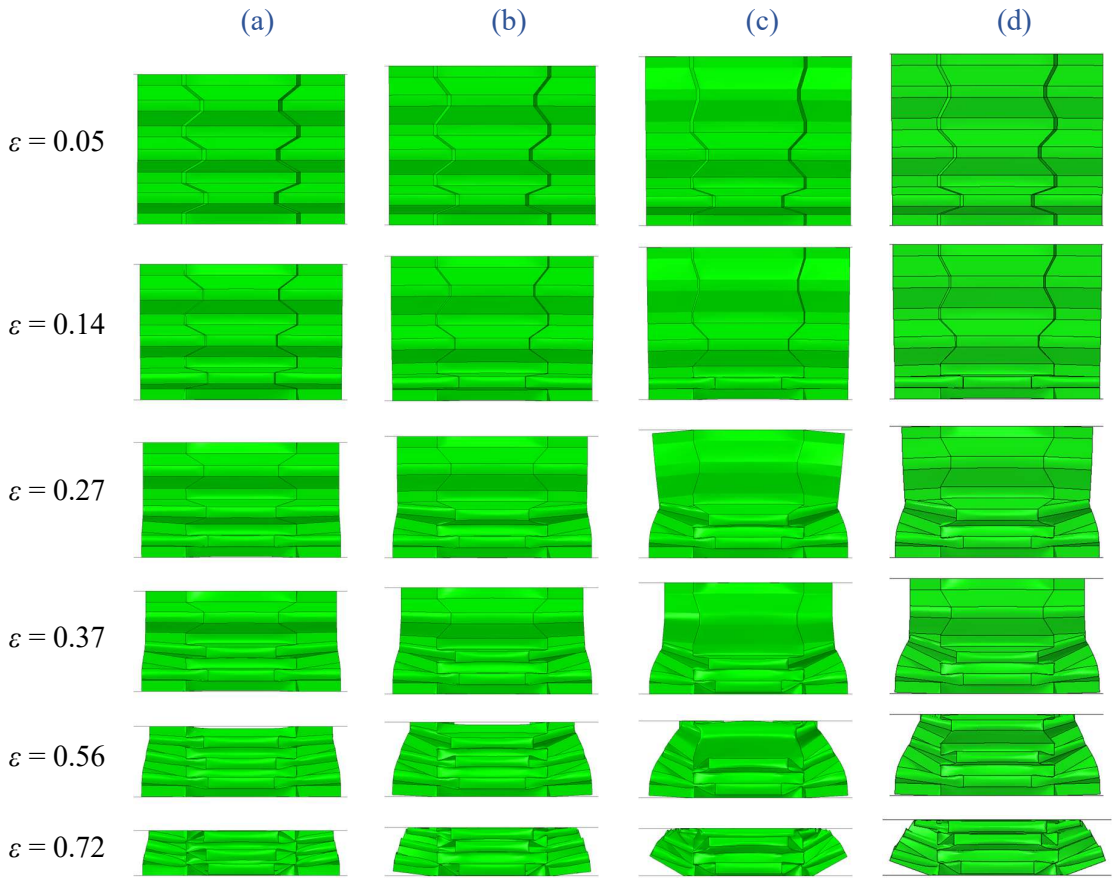


Figure 4.34 Deformation of (a) 10-10-10-45-48-51-82;(b) 10-10-10-45-50-58-82;(c) 10-10-10-45-55-74-82; and,(d) 10-10-10-45-55-65-82

Tubes with identical θ_1 but varying θ_2 and θ_3 are compared in Figure 4.31(b). The difference between θ's ($\Delta\theta=\theta_{i+1} - \theta_i$) is kept constant for the initial configuration of each tube in group B through the appropriate selection of α. Increasing $\Delta\theta$ between units results in an increase in the peak force during the load oscillations. As previously discussed, the units initially fold following the crease pattern. The theorical values of θ_2 and θ_3 when $\theta_2 = 0°$ and θ_3 when $\theta_2=0°$ can then be calculated for the tubes and compared to the angles measured directly from the FE simulations (Table 4.6). The theoretical values provide a reasonable approximation of θ albeit, they generally slightly underpredict the value. For 10-10-10-45-48-51-82, when $\theta_1 = 0°$, $\theta_2 = 47°$, which is less than the θ_1 value in the initial configuration ($\theta_{1,0} = 60°$). From the analytical model in section 4.3.2.8 for an ungraded tube, it was shown

that the force reduces with an increase in the eccentricity of the tube (i.e. increasing a or reducing θ_0). Additionally, for the geometry analysed, below $\theta_0 = 120°$ an increase in α results in a decrease in the force (Figure 4.30(a,b)). An ungraded unit with $\alpha = 47.5°$ and $\theta_0 = 47°$ would be expected to have a lower force than an ungraded unit with $\alpha = 45°$ and $\theta_0 = 60°$. The increase in the force observed for 10-10-10-45-48-51-82 is therefore expected to be due to the locking effect. For 10-10-10-45-50-58-82 and 10-10-10-45-55-74-82 the magnitude of the oscillations (Figure 4.31(b)) are thought to be much larger due to the combination of the locking effect and θ_2 being greater than $\theta_{1,0} = 60°$. The comparison between the second peak oscillation of 10-10-10-45-55-74-82 and 10-10-10-45-55-65-82 also suggests this is the case. When $\theta_1 = 0°$, θ_2 was measured as 94° and 92° from the FE simulation. This results in an approximately equivalent load oscillation for both tubes during the collapse of the second unit (Figure 4.31(c)). However, once $\theta_2 = 0°$, θ_3 was measured as 132° and 94° for 10-10-10-45-55-74-82 and 10-10-10-45-55-65-82 respectively. For 10-10-10-45-55-65-82, this is almost equivalent to θ_2 when $\theta_1 = 0°$ and results in an almost equivalent magnitude load oscillation during the collapse of both the second and third units. In contrast, θ_3 is much larger at the initiation of the third units collapse ($\theta_2 = 0°$) when compared to θ_2 when the second units collapses ($\theta_1 = 0°$) for 10-10-10-45-55-74-82. This, in combination with the locking effect, is believed to cause the larger magnitude load oscillation during the collapse of the third unit when compared to the second unit.

Table 4.6 Dihedral angle comparison between theoretical and FE

Name	Theoretical			FE		
	$\theta_1 = 0°$		$\theta_2 = 0°$	$\theta_1 = 0°$		$\theta_2 = 0°$
	θ_2	θ_3	θ_3	θ_3	θ_2	θ_3
10-10-10-45-48-51-82	47°	70°	54°	50°	74°	56°
10-10-10-45-50-58-82	66°	102°	82°	68°	104°	76°
10-10-10-45-55-74-82	91°	146°	131°	94°	148°	132°
10-10-10-45-55-65-82	91°	124°	96°	92°	128°	94°

The initial peak force can be increased by adjusting γ_0 so that the initial θ_0 for each unit increases. This is observed in Figure 4.31(d) where the response of identical tubes with varying initial γ_0 is provided. Rather than plotting the response with respect to the nominal strain, the displacement of each tube is offset by the difference in height of the tube with the height of tube 10-10-10-45-55-65-82 (i.e. for 10-10-10-45-55-65-65 the offset is $79.20 - 87.26 =$ 8.06mm from Table 4.5). This results in the end of the kinematic range ($\theta_1 = 0°$) theoretically converging to one point. Following locking, the tubes continue to follow a similar response, which is expected if the topology at the point of locking for each tube is equivalent. Therefore, provided that the kinematics of the crease pattern result in the units folding simultaneously, the initial peak force can be controlled without significantly affecting the subsequent load oscillations caused by locking.

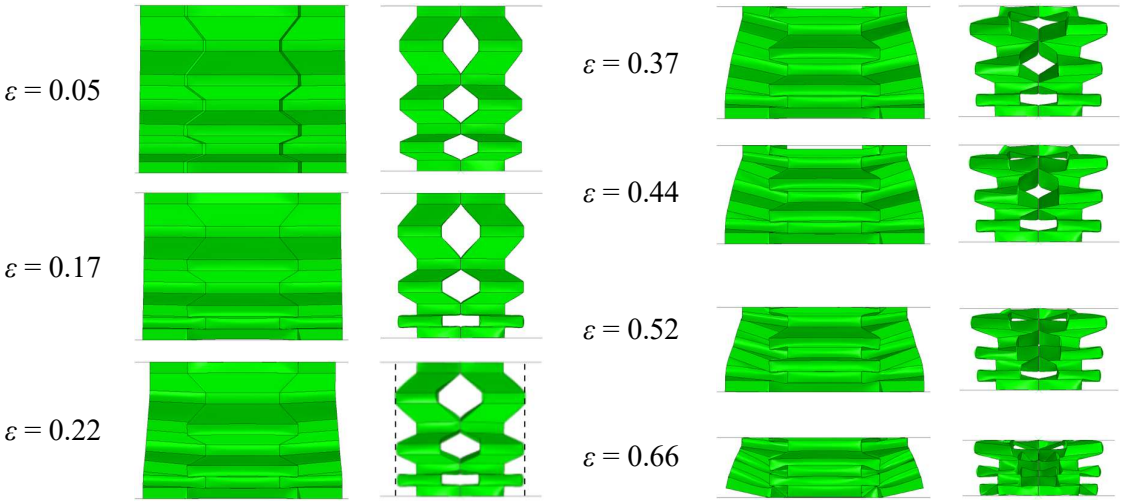


Figure 4.35 Deformation of 8-10-14-45-50-57-81

In group E a is adjusted to allow the connection of the facets when creating a core. Kinematically this results in the eccentricity of each unit being equivalent until the point of locking ($\theta_1 = 0°$). This is observed in Figure 4.35 from $\varepsilon = 0.05$ - 0.17, where the connection facets on each side remain on the same plane. While a small increase in the force is initially observed at the point of locking, generally 8-10-14-45-50-57-81 exhibits plateau/softening

behaviour as loading continue (Figure 4.31(e)). As previously discussed, the plastic strains that develop away from the crease lines after locking appear to form around the angled crease lines (Figure 4.32). The remaining plastic strains, however, continue to develop about the crease lines rather than in the facets. Like the ungraded tube, the force associated with the continued plastic straining at the crease locations is expected to be inversely proportional to the eccentricity of the facets (Eq.(4.25)). This may be the reason why the increase in force for 8-10-14-45-50-57-81 is not significant when locking occurs, as the equal eccentricity of the units minimises the effect of the larger θ of the second and third units. In contrast, when a is equal for all units (10-10-10-45-50-57-81), the larger θ for the second and third unit results in a reduction in the eccentricity when compared to the first unit.

4.3.3.3 Effect of connection method

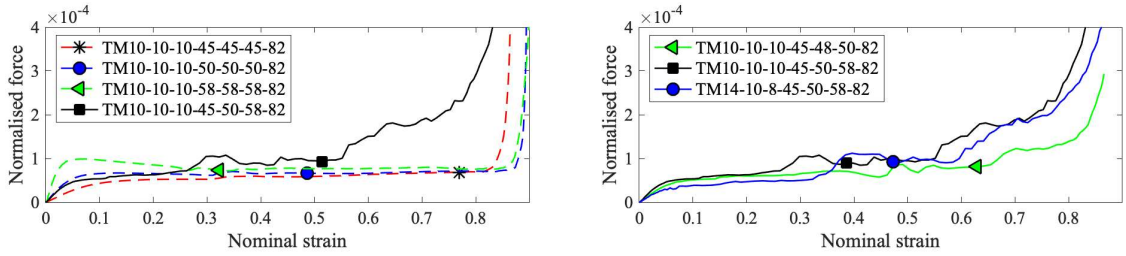
To allow the connection of the tubes into a core for the crease-to-crease connection method, the a value must be selected using Eq.(3.24). In contrast, a is an independent variable for the face-to-face connection method i.e. the selection of a does not affect the ability to stack the tubes into a core. This provides greater versatility in the design of cores using the face-to-face connection method. In this section several graded tubes with face-to-face connection method will be simulated to observed if similar conclusions drawn from the crease-to-crease connection tubes are applicable. a will remain constant except for TM14-10-8-45-50-58-82, where a is adjusted so the height of each individual unit is equivalent in the initial configuration. Several ungraded tubes are also simulated for comparison purposes. A summary of the tubes is provided in Table 4.7.

Figure 4.36(a) compares TM10-10-10-45-50-58-82 with equivalent ungraded tubes. The initial peak force is approximately equal to TM10-10-10-45-45-45-82, however two increases in the force occur at $\varepsilon = 0.25$ and $\varepsilon = 0.55$. At $\varepsilon = 0.25$ the increase occurs due to locking ($\theta_1 = 0°$) (Figure 4.37). Unlike tubes with the crease-to-crease connection method, the

second increase in force at $\varepsilon = 0.55$ is less defined for the face-to-face connection method. For TM10-10-10-45-50-58-82, following locking of the first unit, ε at which the second unit locks is not clear from the deformation provided in Figure 4.37. Instead, only the upper half (the facets bordering the third unit with $\alpha = 58°$) appears to completely flatten, with additionally folding occurring on the upper left side of third unit. Indeed, similar unsymmetric deformation modes are observed for the other tubes simulated (Figure 4.38). This unsymmetric deformation may result from the lack of symmetry of the face-to-face connection method when compared to the crease-to-crease connection method. Nonetheless, two load increases occur for TM10-10-10-45-50-58-82 with magnitudes larger than the equivalent ungraded tube indicating similar locking effects to the crease-to-crease tubes.

Table 4.7 Geometry and results for graded face-to-face connected tubes

Group	Name	a_1	a_2	a_3	α_1	α_2	α_3	γ_0	θ_1	θ_2	θ_3	M	H	Mass
	a_1-a_2-a_3-α_1-α_2-α_3-γ_0	[mm]	[mm]	[mm]	[°]	[°]	[°]	[°]	[°]	[°]	[°]	[-]	[mm]	[g]
A	TM10-10-10-45-45-45-82	10	10	10	45.00	45.00	45.00	81.79	60.00	60.00	60.00	3	30.00	8.42
	TM10-10-10-50-50-50-82	10	10	10	50.00	50.00	50.00	81.79	86.78	86.78	86.78	3	41.22	8.42
	TM10-10-10-58-58-58-82	10	10	10	57.68	57.68	57.68	81.79	113.56	113.56	113.56	3	50.20	8.42
B	TM10-10-10-45-48-50-82	10	10	10	45.00	47.50	50.00	81.79	60.00	74.96	89.92	3	35.91	8.42
	TM10-10-10-45-50-58-82	10	10	10	45.00	50.00	57.68	81.79	60.00	86.78	113.56	3	40.47	8.42
	TM14-10-8-45-50-58-82	13.74	10	8.21	45.00	50.00	57.68	81.79	60.00	86.78	113.56	3	41.22	8.97



(a) (b)

Figure 4.36 Normalised force vs nominal strain for: (a) comparison to ungraded tubes; and, (b); effect of $\Delta\theta$ and variable a length

Similar to the findings from the crease-to-crease connection method, increasing $\Delta\theta$ between units results in an increase in the load jumps (Figure 4.36(b)). This is clearly observed when comparing TM10-10-10-45-50-58-82 with TM10-10-10-45-48-50-82.

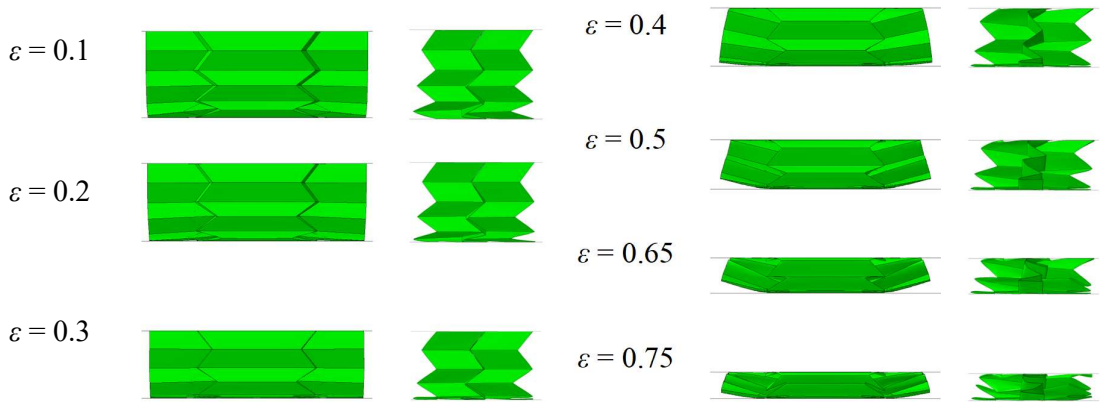


Figure 4.37 Deformation of TM10-10-10-45-50-58-82

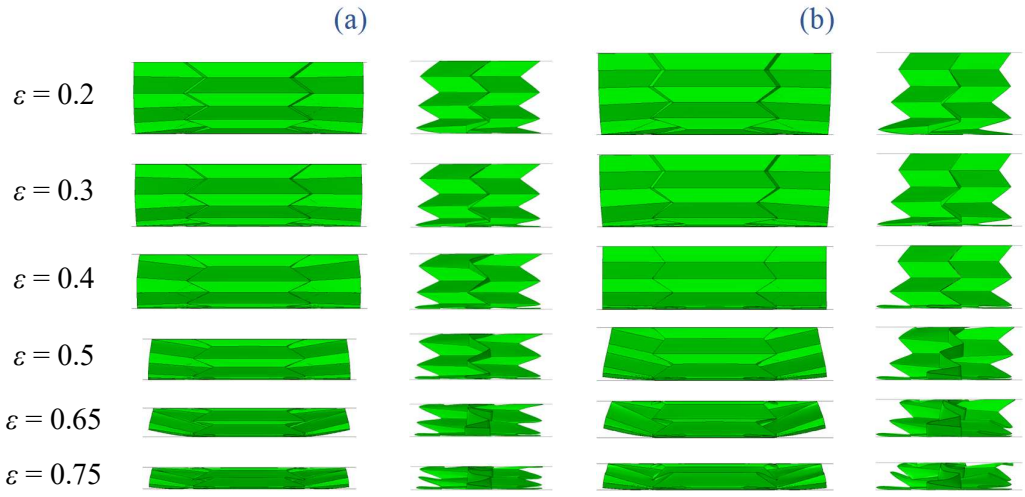


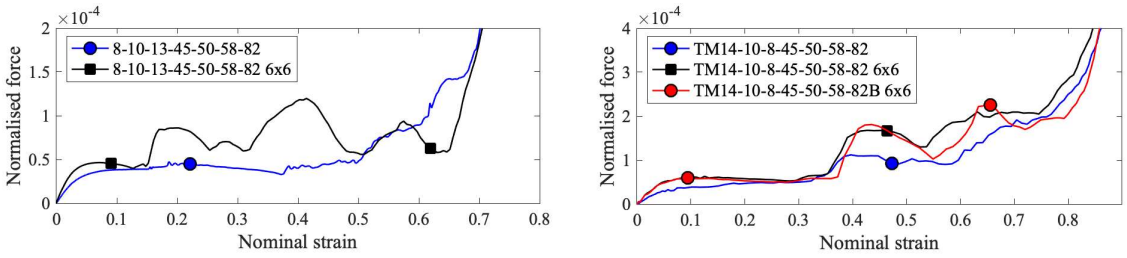
Figure 4.38 Deformation of: (a) TM10-10-10-45-47-50-82; and, (b)TM14-10-8-45-50-57-82

For the crease-to-crease connection method two tubes with identical parameters for their first two units resulted in an almost equivalent load oscillation (Figure 4.31(c)). When comparing TM10-10-10-45-50-58-82 and TM14-10-8-45-50-58-82 in Figure 4.36(b), the first load oscillation for each tube is also approximately equivalent in magnitude, albeit that for the later it occurs at a larger nominal strain due to the increase a length of the first unit. The increase in this length also results in a reduction in the initial peak force when compared to TM10-10-

10-45-50-58-82. The variation in a therefore shows potential as an additional way to vary the stiffness increase during the crushing of the tube. This is not possible for the crease-to-crease connection method when implemented as a core.

4.3.3.4 Comparison to core behaviour

The behaviour of the ungraded tubes and cores was generally similar when friction effects were negligible. For both the face-to-face and crease-to-crease connection method the added constraint provided by neighbouring unit, especially once locking occurs, may influence the deformation mode and therefore the behaviour when compared to the single tubes. In this section the behaviour of selected tubes will be compared with an equivalent 6x6 core. Again, like the ungraded core analysis, a 6×3 core with symmetry conditions will be simulated with other inputs identical to the equivalent graded tube.



(a) (b)

Figure 4.39 Equivalent core behaviour for: (a) crease-to-crease connection method; and, (b) face-to-face connection method

In contrast with the ungraded cores (Figure 4.19, section 4.3.2.4), increasing the number of units in the *m* and *n* direction does not significantly increase the initial peak force. This is attributed to the reduced kinematic range of the core before locking occurs. For TM14-10-8-45-50-58-82 (Figure 4.39(b)) and TM11-60-120-3 (Figure 4.19(b)) the initial cell angle is 82°. However, kinematically γ_{max} is 90° and 120° for each core respectively. Therefore TM14-10-8-45-50-58-82 kinematic range is less than TM11-60-120-3, resulting in less sensitivity to

friction. However, it should be noted that further increasing the number of units in the m and n direction may result in greater sensitivity.

Comparisons of the normalised force vs nominal strain for both connection methods are provided in Figure 4.39. For 8-10-13-45-50-58-81 (Figure 4.39(a))), the effect of locking is much greater for the core, with two large oscillations occurring before densification at $\varepsilon = 0.2$ and 0.4. However two distinct smaller load oscillations occur following these peaks at $\varepsilon = 0.3$ and 0.55. The smaller peaks are likely associated with the nonuniform folding of each individual unit. This is clearly observed in Figure 4.40 for the third unit at $\varepsilon = 0.5$, where at the centre of the core, only the bottom half of the third unit has folded.

Figure 4.40 shows that when joining tubes to create a core, the constraint provided by adjacent units once locking occurs influence the deformation mode for the crease-to-crease connection method. The deformations and plastic strain contours for a central tube are provided in Figure 4.41 to observe this closely. Comparing the deformation to the equivalent tube in Figure 4.35, the outer connection facets for the core remain approximately on the same plane, this is not the case for the tube.

Additionally, the length change along the height of the central tube significantly reduces once locking occurs for the core. The lateral displacement at the sections illustrated in Figure 4.41 are provided in Figure 4.42. This shows that minimal lateral displacement occurs following locking ($\varepsilon = 0.15$). Views of the sections provided in Figure 4.43 also illustrates this phenomenon, as γ for each section along the height does not vary significantly. This also suggests that following locking friction effects may become more negligible as minimal in-plane deformations occur subsequently.

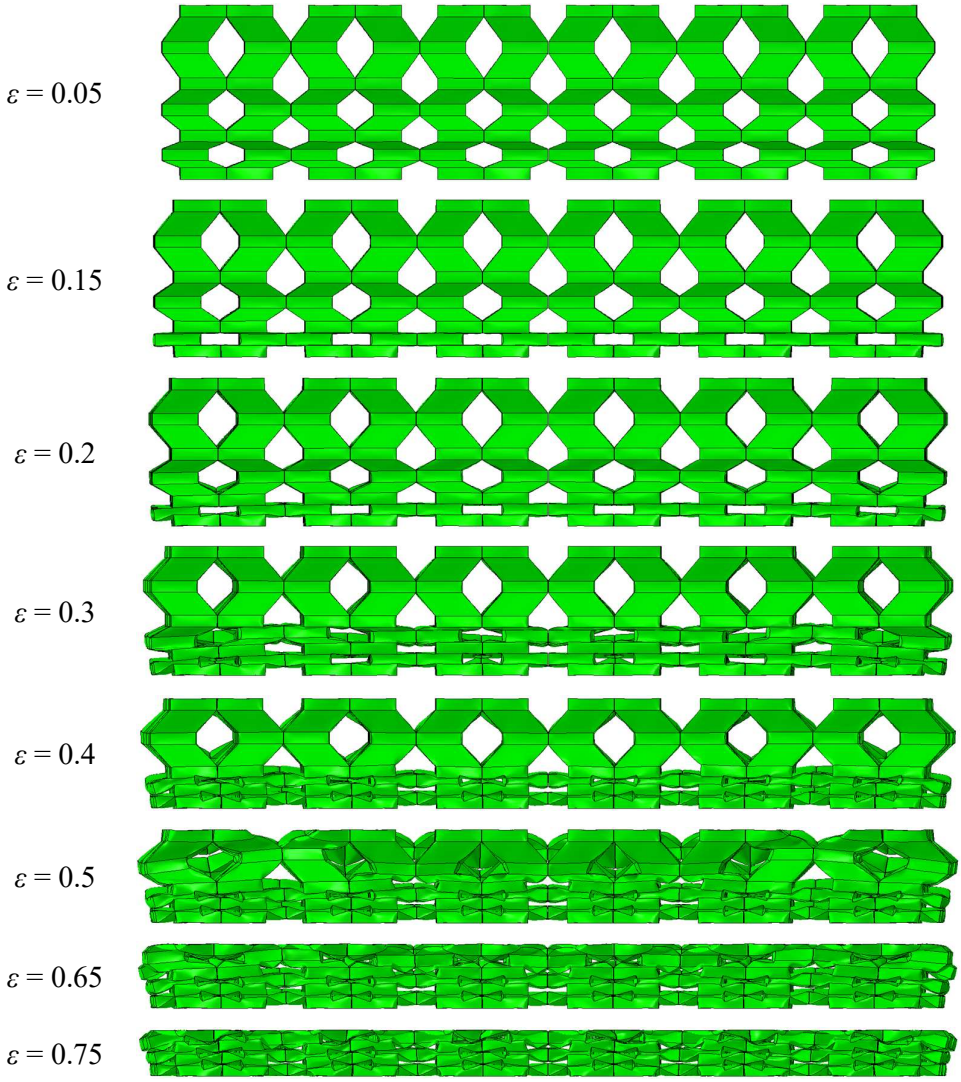


Figure 4.40 Deformation of 8-10-13-45-50-58-81 6×6 core

The constraint provided by neighbouring tubes in the core significantly alters the deformation mode. Comparing the plastic strain contours for the core in Figure 4.41 to the tube in Figure 4.32, the alternative deformation mode results in an increase in the development of plastic strains, especially within the l_2 facets close to the angled creases.

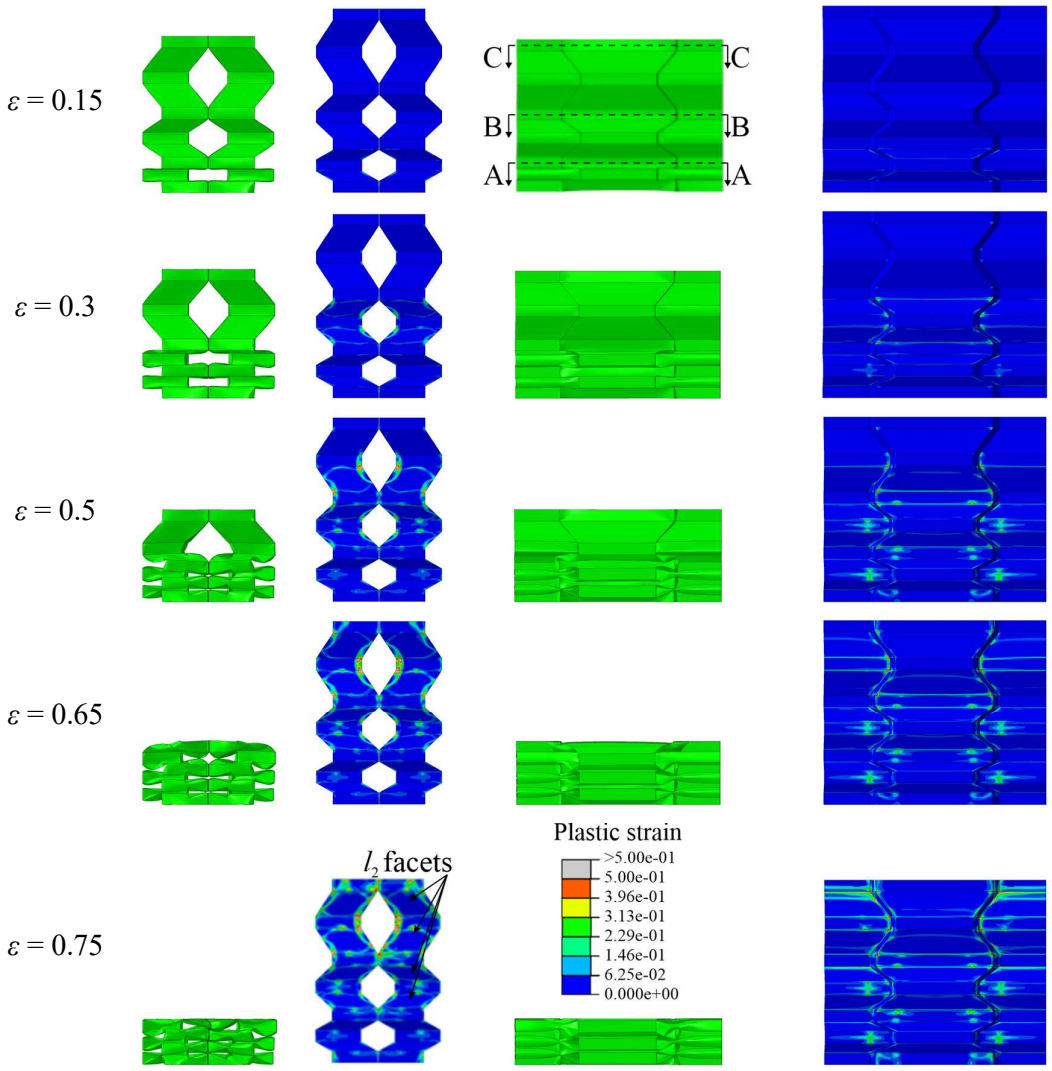


Figure 4.41 Deformation and plastic strain contours for a central tube of the 8-10-13-45-50-58-81 6×6 core

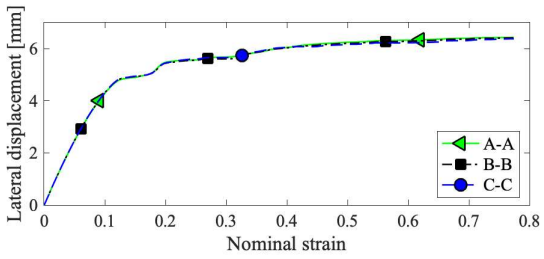


Figure 4.42 Lateral displacement for a central tube of the 8-10-13-45-50-58-81 6×6 core at several section

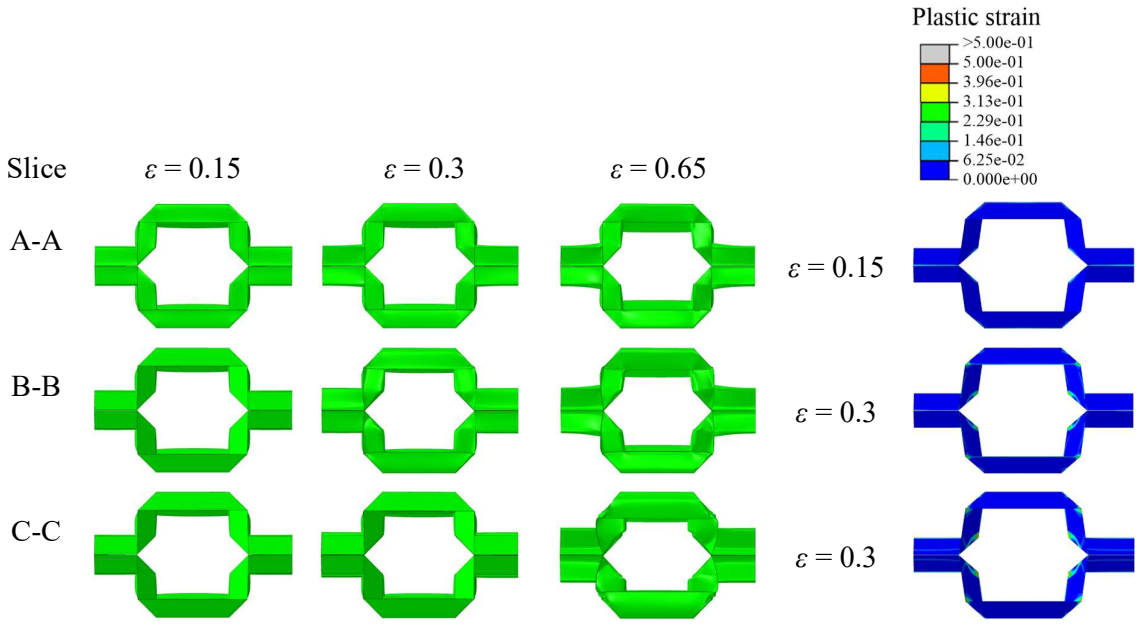


Figure 4.43 Deformation and plastic strain contours for a central tube of the 8-10-13-45-50-58-81 6×6 core at sections: A-A, B-B; and C-C.

While a graded single tube does not provide significant gradients in the stiffness for the crease-to-crease connection method, when implemented as a core, the locking provides an additional lateral constraint to the continued deformation, resulting in a significant change in the deformation mechanisms when compared to the tube. This results in an increased performance and shows potential in grading the strength of the core.

While the general behaviour of the face-to-face connection method remains similar for the core, larger magnitude and more distinct load steps are observed when compared to the single tube (Figure 4.39(b)). When comparing the deformation of the core in Figure 4.44 to a single tube in Figure 4.38(b), less simultaneous folding of the second and third unit results in a reduction in the skewness of the deformation mode. The restraint provided when implemented as a core ameliorates the effect of the asymmetry of the face-to-face connection method and is believed to be one of the reasons for the observed enhancement of the locking effect.

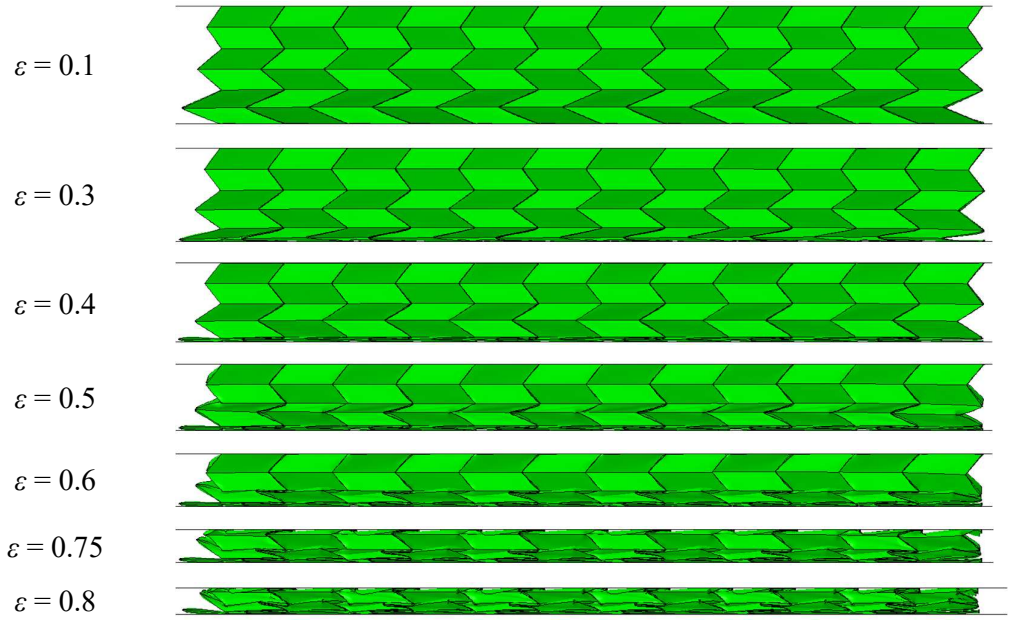


Figure 4.44 Deformation of TM14-10-8-45-50-57-82 6×6 core

The deformation and plastic strain contours for a central tube are provided in Figure 4.45 for the TM14-10-8-45-50-57-82 6×6 core. Only half of side A and B views are provided as the plastic strain contours are relatively symmetric for each side. Following locking, the most severe plastic strains that occur away from the crease lines are around the angled creases. Lower magnitude plastic strains are also observed to the sides of the horizontal crease lines about the l_2 lengths.

Again, as is the case for the crease-to-crease connection method (Figure 4.43), minimal variation in the length or γ for each section along the height of the core is observed for the face-to-face connection method (Figure 4.46).

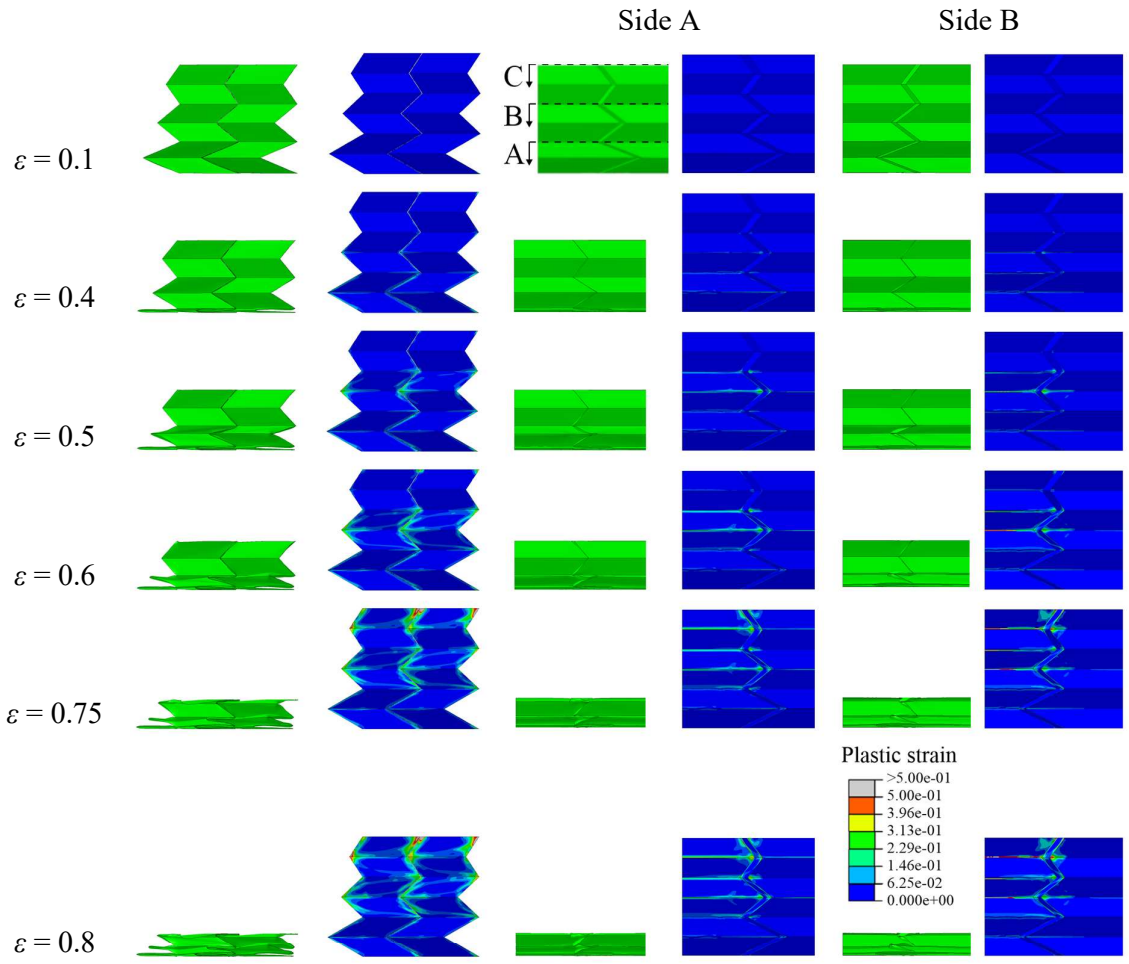


Figure 4.45 Deformation and plastic strain contours for a central tube of the TM14-10-8-45-50-57-82 6×6 core

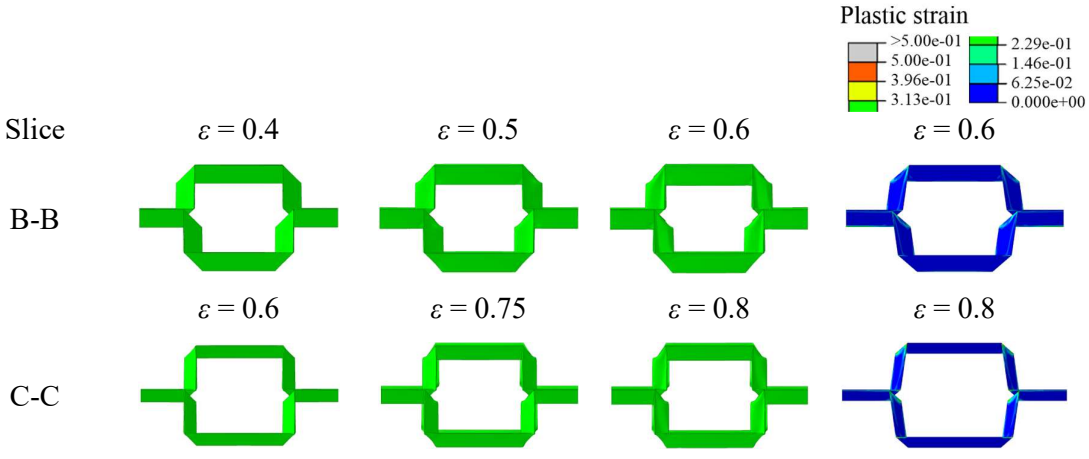
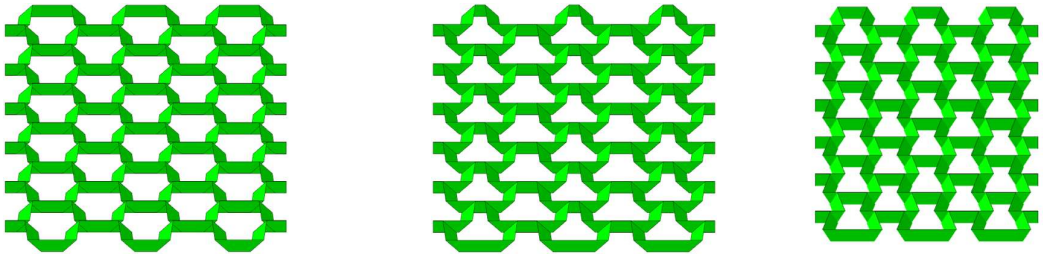


Figure 4.46 Deformation and plastic strain contours at cross sections for a central tube of the TM14-10-8-45-50-57-82 6×6 core.

The face-to-face connection method results in portions of the l_1 and l_3 facets having double thickness. The locations of the double thickness can be adjusted through the variation of l_1^{I}, l_3^{I} and l_1^{II}, l_3^{II} while ensuring that the total summation of each side length ($2l_1^{I}+2l_2^{I}+l_3^{I}=2l_1^{II}+2l_2^{II}+l_3^{II}$) remains equal. Therefore there is the opportunity to adjust the locations of double thickness, especially at the location of the angled creases, which may alter the deformation mode once locking occurs. Another core, labelled TM14-10-8-45-50-57-82B, was simulated that had all parameters identical to TM14-10-8-45-50-57-82 except: l_1^{I}=10mm; l_3^{I}=70mm; l_1^{II}=40mm; and, l_3^{II}=10mm. These lengths were chosen in an attempt to 'force' the deformation about the angled creases into either the l_1/l_3 lengths or the l_2 lengths (refer to section 4.3.4.2a)). In contrast, for TM14-10-8-45-50-57-82, the plastic strains occurred in both the l_1/l_3 and the l_2 lengths about each of the angled creases (see Figure 4.45 at ε = 0.8). Figure 4.47(a, b) compares the cross section of both cores.



(a) (b) (c)

Figure 4.47 Comparison of: (a) TM14-10-8-45-50-57-82; and, (b) TM14-10-8-45-50-57-82B, (c) TM14-10-8-60-64-70-113

Figure 4.39(b) includes the normalised force vs nominal strain for the TM14-10-8-45-50-57-82B 6×6 core. The initial response, before locking, is equivalent to the TM14-10-8-45-50-57-82 6×6 core. This is expected as the total crease lengths and other parameters remain equal for the two cores. The behaviour once locking occurs also remains relatively similar, although TM14-10-8-45-50-57-82B experiences slightly larger peak force magnitudes from locking and the force drops to a slightly lower magnitude after these peaks.

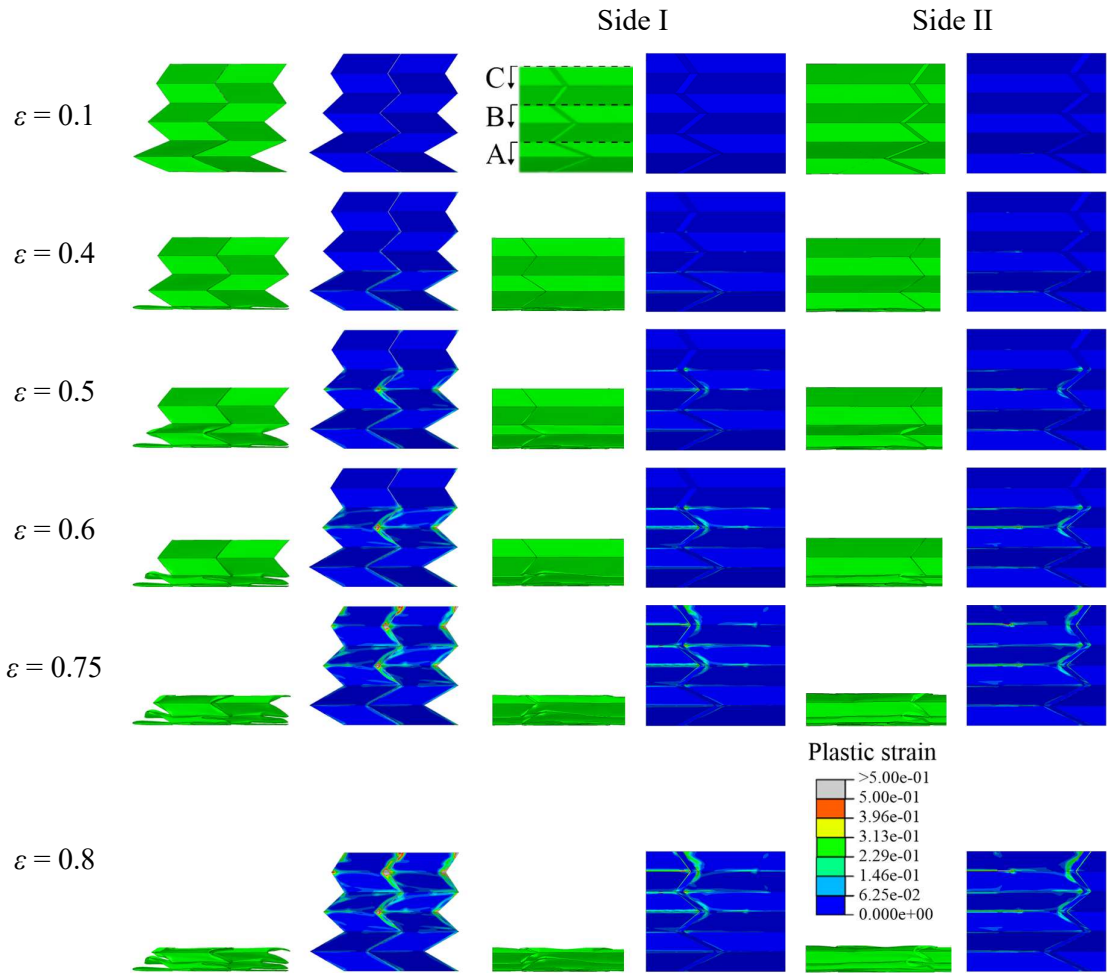


Figure 4.48 Deformation and plastic strain contours for a central tube of the TM14-10-8-45-50-57-82 6×6 core

The nominal densification strain also increases marginally for the TM14-10-8-45-50-57-82B 6×6 core when compared to the TM14-10-8-45-50-57-82 6×6 core. This is attributed to the change in deformation mode. Figure 4.48 and Figure 4.49 provide the deformation and plastic strain contours for the TM14-10-8-45-50-57-82B 6×6 core. In contrast to the TM14-10-8-45-50-57-82 6×6 core (Figure 4.45 and Figure 4.46) the plastic strains tend to favour sweeping out from the angled creases either into the l_1/l_3 lengths or the l_2 lengths rather than a combination of both. Additionally, less significant plastic strains were observed towards the centre of the l_2 facets.

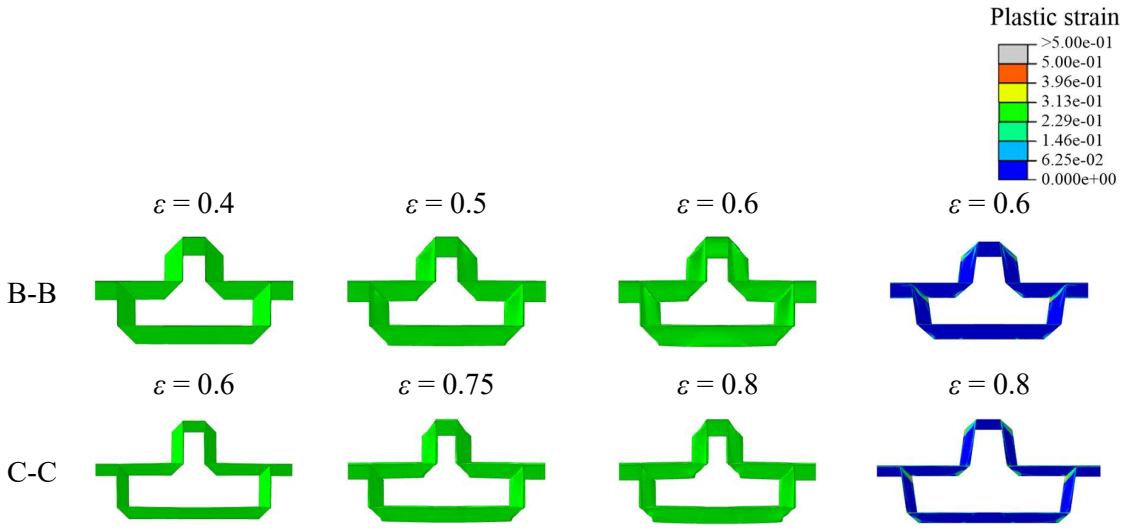


Figure 4.49 Deformation and plastic strain contours at cross sections for a central tube of the TM14-10-8-45-50-57-82B 6×6 core

To investigate the effect that α has on the locking behaviour, another 6x6 core, TM14-10-8-60-64-70-113, was simulated (Figure 4.47(c)). The input variables of this core were identical to TM14-10-8-45-50-58-82B except the α's and the lengths l_1, l_2, and l_3 are varied. The dimensions of a single tube from these cores are provided in Table 4.8. α_2 and α_3 are selected so that θ_2 and θ_3 for TM14-10-8-60-64-70-113 were identical to θ_2 and θ_3 for TM14-10-8-45-50-58-82B. This also results in the theoretical values of θ_2 and θ_3 at locking being equivalent. The l_1, l_2 and l_3 lengths were varied to ensure that the majority of the plastic strains developed to one side of the Miura-ori vertices.

Figure 4.50 provides a comparison of the normalised force vs nominal strain for the two cores. The general behaviour of both cores is quite similar. However, with most other variables equal, it is interesting to note that an increase in α results in a reduction in the force associated with the locking of both units 2 and 3. This will be explored further in the analytical model but shows that even when θ_0 and a are set there is the ability to alter the behaviour through the selection of α.

Table 4.8 Effect of α on locking behaviour for the face-to-face connection method

Name	a_1	a_2	a_3	α_1	α_2	α_3	γ_0	θ_1	θ_2	θ_3	H	Mass
TMa_1-a_2-a_3-α_1-α_2-α_3-γ_0	[mm]	[mm]	[mm]	[°]	[°]	[°]	[°]	[°]	[°]	[°]	[mm]	[g]
TM14-10-8-45-50-58-82B	13.7	10	8.21	45.00	50.00	57.68	81.79	60.00	86.78	113.56	41.22	8.97
TM14-10-8-60-64-70-113	13.7	10	8.21	60.00	64.15	69.94	112.62	60.00	86.78	113.56	41.22	8.97

							Theoretical values		
							θ_1=0°		θ_2=0°
Name	l_1^{I}	l_2^{I}	l_3^{I}	l_1^{II}	l_2^{II}	l_3^{II}	θ_2	θ_3	θ_3
TMa_1-a_2-a_3-α_1-α_2-α_3-γ_0	[mm]	[mm]	[mm]	[mm]	[mm]	[mm]	[°]	[°]	[°]
TM14-10-8-45-50-58-82B	10	20	70	40	20	10	65.91	101.52	82.15
TM14-10-8-60-64-70-113	15	20	60	30	20	30	65.91	101.52	82.15

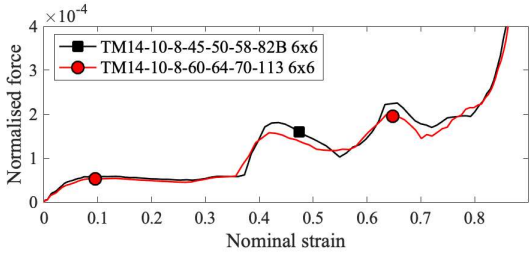


Figure 4.50 Normalised force vs nominal strain comparison for TM14-10-8-45-50-57-82B and TM14-10-8-60-64-70-113

4.3.4 Analytical model for graded origami honeycomb

The analytical model for the graded cores is divided into two phases. The first phase is before locking occurs, where the deformation follows the kinematics prescribed by the crease pattern. This phase ends once locking occurs, at which point the second phase begins and the units fold in a manner that deviates from the crease pattern.

4.3.4.1 Phase 1

The derivation of the force displacement behaviour in the first phase mirrors that outlined in section 4.3.2.6, except, that the energy absorbed and deformation of each layer is variable. During this phase, while ϕ varies for each unit along the height, γ remains equal. Taking ϕ_1 as

the reference variable and considering the summation of the components from each layer, rather than Eq.(4.14) we have the equation below for the crease-to-crease connection method.

$$F\frac{d\delta}{d\phi_1}d\phi_1 = 8M_p\left((2M+1)s\frac{d\gamma}{d\phi_1}+\sum_1^{i=M}\left(L_s\frac{d\phi_i}{d\phi_1}+\frac{2a_i}{\sin\alpha_i}\frac{d\beta_i}{d\phi_1}\right)\right)d\phi_1 \tag{4.27}$$

Substituting in the geometric relationships found previously, an equation for the force and displacement for a graded origami honeycomb with the crease-to-crease connection method can be found as follows.

$$F = \frac{4mnM_p}{\sin\phi_1\tan\alpha_1\sum_1^{i=M}\left(\dfrac{a_i}{\tan^2\alpha_i\sqrt{1-\dfrac{\tan^2\alpha_1}{\tan^2\alpha_i}\sin^2\phi_1}}\right)}\left(\begin{array}{l}\dfrac{(4M+2)s}{1+\tan^2\alpha_1\sin^2\phi_1}\\ +\sum_1^{i=M}\left(\begin{array}{l}\dfrac{L_s}{\tan\alpha_i\sqrt{1-\dfrac{\tan^2\alpha_1}{\tan^2\alpha_i}\sin^2\phi_1}}\\ +\dfrac{4a_i\cos^2\alpha_1}{\tan\alpha_1\cos\phi_1\sin\phi_1\left(\sin\phi_1\tan\phi_1+\cos\phi_1\cos^2\alpha_1\right)}\\ \times\dfrac{1}{\sin\alpha_i\sqrt{\dfrac{\sin^2\alpha_i}{\sin^2\phi_1\tan^2\phi_1}-\cos^2\alpha_i}}\end{array}\right)\end{array}\right) \tag{4.28}$$

$$\begin{aligned}\delta &= \sum_1^{i=M}\left(2a_i\left(\cos\phi_i-\cos\phi_{i,o}\right)\right) \\ &= \sum_1^{i=M}\left(2a_i\left(\sqrt{1-\frac{\tan^2\alpha_1}{\tan^2\alpha_i}\sin^2\phi_1}-\sqrt{1-\frac{\tan^2\alpha_1}{\tan^2\alpha_i}\sin^2\phi_{1,0}}\right)\right)\end{aligned} \tag{4.29}$$

The same approach is taken for the face-to-face connection method with the consideration of the hinges where double thickness is applicable and is provided as follows.

$$F=\frac{4mnM_p}{\sin\phi_1\tan\alpha_1\sum_1^{i=M}\left(\frac{a_i}{\tan^2\alpha_i\sqrt{1-\frac{\tan^2\alpha_1}{\tan^2\alpha_i}\sin^2\phi_1}}\right)}\left(\frac{\frac{l_{M,3}^{\min}}{m}-L_s-2l_{M,1}^{\min}-l_{M,3}^{\min}}{4\tan\alpha_M\sqrt{1-\frac{\tan^2\alpha_1}{\tan^2\alpha_M}\sin^2\phi_1}}+\frac{\frac{l_{1,3}^{\min}}{m}-L_s-2l_{1,1}^{\min}-l_{1,3}^{\min}}{4\tan\alpha_1\sin\phi_1}\right.$$
$$\left.+\sum_1^{i=M}\left(\frac{\frac{2L_s+2l_{i,1}^{\min}+l_{i,3}^{\min}-\frac{l_{i,3}^{\min}}{m}+2l_{i,1c}^{\min}+l_{i,3c}^{\min}-\frac{l_{i,3c}^{\min}}{m}}{2\tan\alpha_i\sqrt{1-\frac{\tan^2\alpha_1}{\tan^2\alpha_i}\sin^2\phi_1}}+\frac{4a_i\cos^2\alpha_1}{\tan\alpha_1\cos\phi_1\sin\phi_1\left(\sin\phi_1\tan\phi_1+\cos\phi_1\cos^2\alpha_1\right)}\right.\right.$$
$$\left.\left.\times\frac{1}{\sin\alpha_i\sqrt{\frac{\sin^2\alpha_i}{\sin^2\phi_1\tan^2\phi_1}-\cos^2\alpha_i}}\right)\right) \tag{4.30}$$

The locking displacement for the graded core occurs once the unit with the smallest α locks. The densification strain for this unit can be estimated using Eq.(4.23) and Eq.(4.24) for the crease-to-crease and face-to-face connection method respectively.

4.3.4.2 Phase 2

a) General effect of locking

Before attempting to derive equations for the locking of the core it is useful to discuss the formation and propagation of plastic hinges on a simplified model subject to certain constraints. The simplified mode is made from a single Miura-ori unit with square ends where α = 70°, a = 10mm and both edge lengths are 20mm. The initial cell angle, γ_0, was set to 90° and symmetry conditions were applied to the unit along the edges to enforce this throughout folding (Figure 4.51(b)). The unit is placed between two rigid loading plates shown in Figure 4.51(a) and is then crushed under quasi-static loading conditions. Two sets of boundary conditions were simulated: (1) no constraints applied at the top and bottom edges (RR - Figure 4.51(b)); and, (2) fixed in-plane translations (FF-Figure 4.51(c)). Additionally, the thickness was varied for two more simulations with RR constraints, where in turn each side of the Miura-ori vertex was assigned twice the thickness. These were labelled RR-i and RR-ii and are shown in Figure 4.51(d,e) respectively. In the figures the thickness is scaled by 10 for clarity.

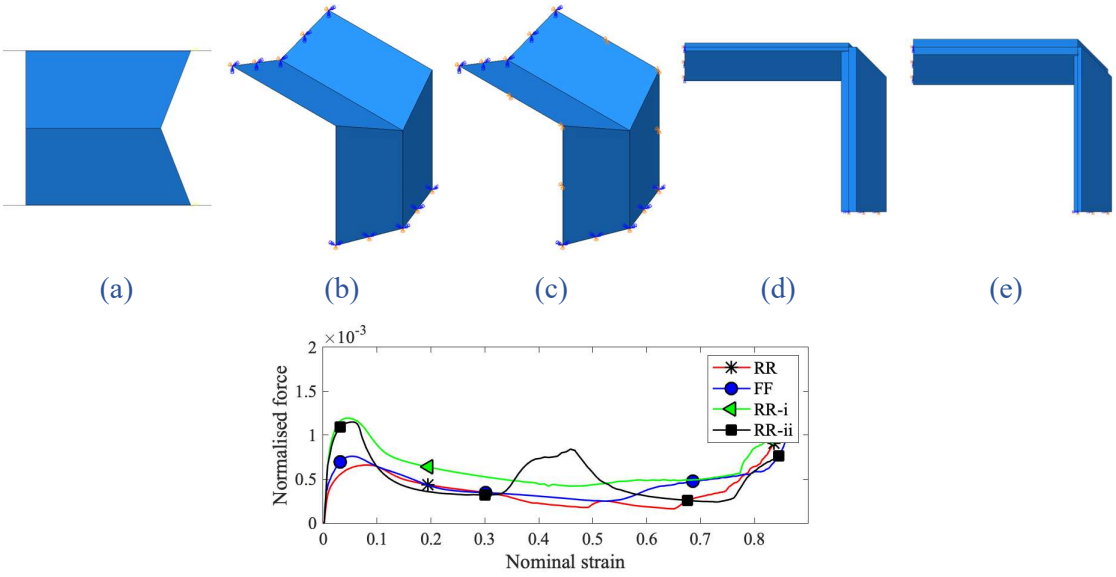


Figure 4.51 Model to study formation of hinges: (a) loading conditions; (b) constraints, RR; (c) FF constraints at top and bottom edges; (d) double thickness RR-i; (e) double thickness RR-ii; and, (f) normalised force vs nominal strain

Figure 4.51(f) shows the force displacement behaviour from the simulations. FF has an approximately 17% increase when compared to RR. When observing the propagation of hinges in Figure 4.52(a), RR shows the propagation of hinges on both sides of the Miura-ori vertex. These hinges appear to travel towards an angle of approximately $\alpha = 45°$ about the centre of the angled creases. Kinematically, $\alpha = 45°$ is required for the unit to fold flat ($\theta = 0°$) whilst maintaining $\gamma = 90°$ and is consistent with the propagation of hinges for the crushing of square tubes (Meng *et al.*, 1983; Wierzbicki and Abramowicz, 1983).

Rather than a travelling hinge forming about the centre of the angled unit, the hinges form about to one end of the angled creases for FF. This results in the hinges sweeping out to only one side of the vertex (Figure 4.52(b)). The angle that is swept by the hinges for FF is slightly smaller with $\alpha = 51°$. It can be easily shown that the change in the propagation results in a larger swept area by the plastic hinges for FF (theoretically by a factor of 2) and this is the likely reason for the larger force observed in the initial stages for FF.

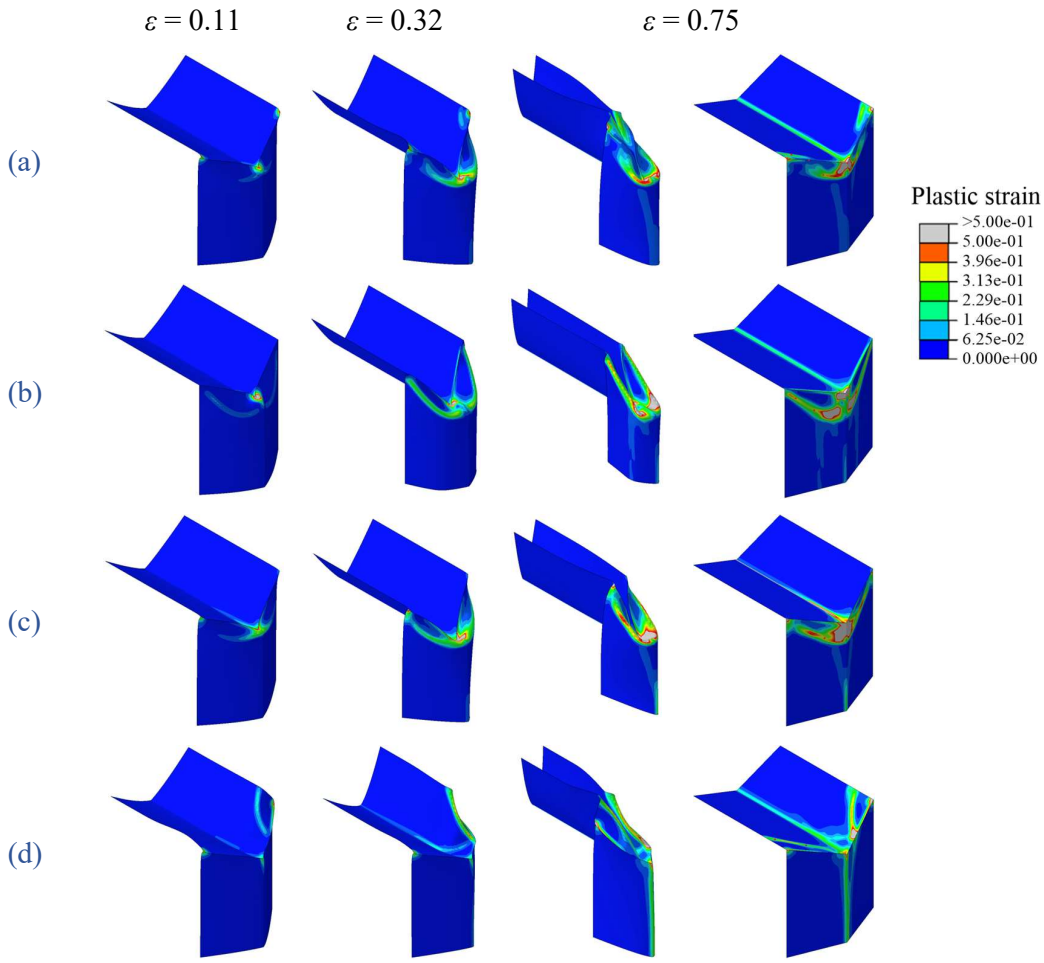


Figure 4.52 Deformation and plastic strain contours for: (a) RR; (b) FF; (c) RR-2-i; and, (d) RR-2-ii

The magnitude of the peak force for RR-i and RR-ii is larger when compared to RR and FF due to the increased thickness of the selected facets. In both cases the angle swept by the travelling hinges ($\alpha = 54°$) is slightly smaller than FF($\alpha = 51°$). The travelling hinges for both RR-i and RR-ii predominately occur to one side of the Miura-ori vertex, favouring the facets with the smaller thickness. Assuming fully plastic conditions, the energy required to bend a double thickness sheet increases by a factor of 4 when compared to a single thickness sheet. Therefore, while the area swept is larger, the minimum energy path is for the hinges to travel exclusively through the facets with the original thickness, rather than the facets with double

thickness. This illustrates that not only can the boundary conditions be used to influence the deformation mode but so can the location of increased thicknesses. This is particularly salient for the face-to-face connection method, where, the location of double thickness facets can be varied by the selection of l_1, l_2 and l_3 for sides I and II. The dimensions for TM14-10-8-45-50-57-82B were selected in this manner so that each individual Miura-ori unit was similar to the scenario in RR-i.

b) Origami honeycomb

- *General observations of hinge formation*

While the findings in the previous section are for a simplified model, several of the points can be transferred/extrapolated to the origami honeycomb. Firstly, when γ is locked there is a tendency for the angled hinges to travel/form towards that of an equivalent unit where $\theta = 0°$ for that given γ. For the graded origami honeycomb, the units fold simultaneously until one of the units lock ($\theta_1 = 0°$). At this point the locked unit acts as a constraint, almost completely preventing the increase in γ for the other units (refer to Figure 4.43 for the crease-to-crease connection method and Figure 4.46 and Figure 4.49 for the face-to-face connection method). For the 6×6 cores, γ is approximately 90° at locking which is equivalent to $\gamma_{max}=2\alpha_1$. The α angle that the plastic strains tend towards in the l_2 or l_1/l_3 facet for the second and third unit of TM14-10-8-45-50-57-82B are 53° and 50° respectively (Figure 4.53). Like the simplified model, while this is slightly larger than the value required kinematically, the locking appears to result in the plastic strains tending towards the theoretical value of $\alpha = 45°$.

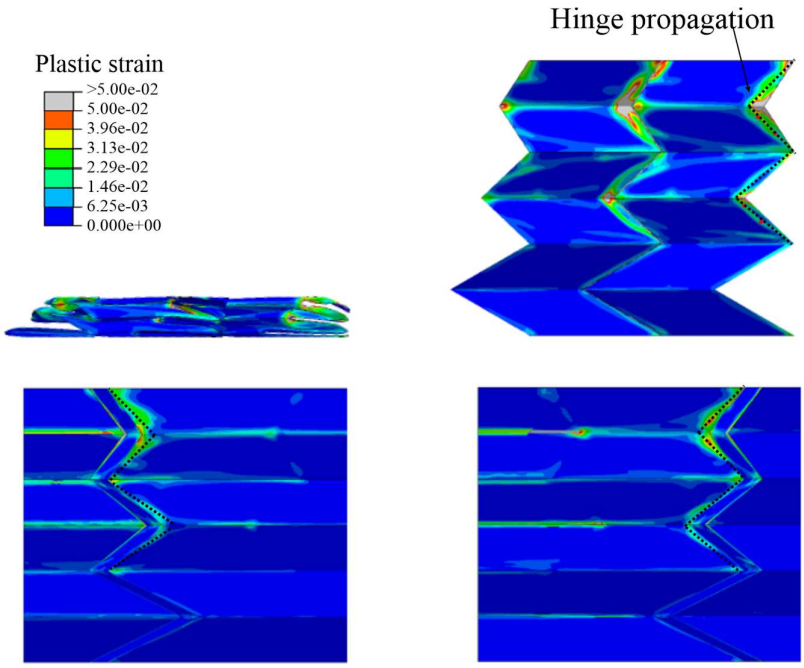


Figure 4.53 Plastic strain contours for a central unit of the TM14-10-8-45-50-58-81B 6×6 core at $\varepsilon = 0.84$

Secondly, the travelling hinges ideally will rotate about the centre of the angled hinges as this is the lowest energy path (smallest swept area). However, restraints provided at the top and bottom edges or through increased thickness of the facets result in the travelling hinges rotating about different locations along the angled hinges. The effect of the locations of double thickness on the formation of plastic strains can be observed when comparing the TM14-10-8-45-50-57-82 and TM14-10-8-45-50-57-82B 6×6 cores in Figure 4.45 and Figure 4.48 respectively. As previously discussed, the location of double thickness was adjusted in TM14-10-8-45-50-57-82B to encourage the plastic hinges to form to one side of each of the Miura-ori vertex. When compared to TM14-10-8-45-50-57-82 this tendency can be clearly observed and may be a reason for the slightly higher magnitude load oscillations for TM14-10-8-45-50-57-82B (Figure 4.39(b))). The formation and propagation of the plastic hinges for TM14-10-8-45-50-57-82 is however not well defined and therefore it is not clear if they are associated with the rotation about the centre of the angled creases. Therefore, the small increase in force

for TM14-10-8-45-50-57-82B may instead be associated with an alternative deformation mode for TM14-10-8-45-50-57-82 rather than an increase in the swept area of the travelling hinges. An analytical model for TM14-10-8-45-50-57-82 will not be pursued as the propagation of deformation is not clearly distinguishable. Instead, an analytical model for TM14-10-8-45-50-57-82B will be formulated as the propagation of plastic strains are defined clearly and the overall response does not differ significantly from TM14-10-8-45-50-57-82.

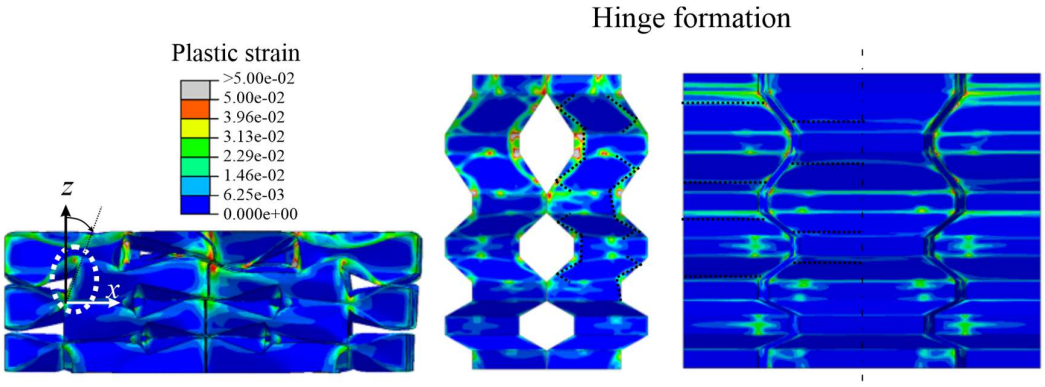


Figure 4.54 Plastic strain contours for a central unit of the 8-10-13-45-50-58-81 6×6 core at $\varepsilon = 0.75$

The location about which the plastic hinges form and travel for the crease-to-crease connection method is more complex due to the restraint provided by neighbouring units. From Figure 4.54 the travelling hinges appear to form exclusively in the l_2 facets. Additionally, while it appears that these travelling hinges form at the corners, there are areas between the hinge and the angled crease line that do not show significant plastic straining, suggesting that the hinge does not travel through these locations.

The two travelling plastic hinges that form on either side of the l_2 facet rotate about points that are not on the same *x*-*y* plane. Without restraint provided by the neighbouring tube in the core, it could be expected that the hinges travel in a similar manner to the face-to-face connection method (Figure 4.55(a)). However, due to the restrain provided by the connection facets, the hinges cannot sweep into the l_3 lengths. Instead, they must sweep into the l_2 lengths about the opposite end of the angled crease lines (Figure 4.55(b)). Herein lies a geometrical

inconsistency, sweeping inwards into the l_2 lengths from the opposite vertex results in travelling hinges in neighbouring units being offset in the *y*-*z* plane when meeting the horizontal hinges that are associated with the connection facets. Inspecting the deformation of these lengths in Figure 4.54 and Figure 4.41 it is clearly observed that the horizontal hinges associated with the connection facets do not remain on the *y*-*z* plane but instead rotate inwards about the x axis. This is consistent with Figure 4.55(b).

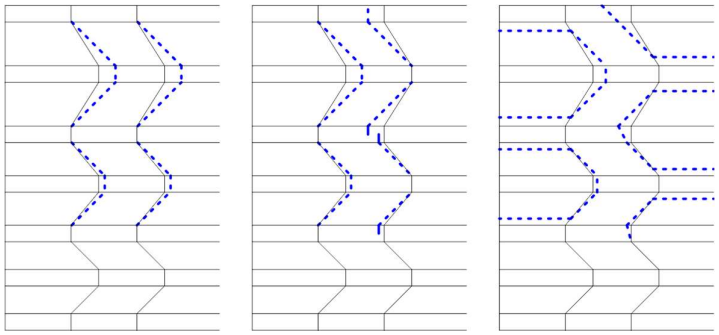


Figure 4.55 Hinge formation for the crease-to-crease connection method: (a) equivalent to the face-to-face connection method; (b) exclusively into l_2 lengths; and, (c) approximation from plastic strain contours

From the plastic strain contours in Figure 4.54, it is clear the plastic hinges do not rotate about the ends of the angled creases, instead they appear to be offset by some small distance. This results in stationary plastic hinges forming in the l_1 and l_3 lengths in addition to several other hinges in the l_2 lengths. The offset distance of these hinges is different for both the second and third unit and analytically predicting the distance that these horizontal hinges form away from the crease pattern is complicated.

The majority of the identifiable plastic hinges are shown in Figure 4.55(c) apart from several additional plastic hinges that appear in the l_2 facets. Therefore, due to the complexity of this deformation mode, it is equally complex to form a super folding element that is kinematically admissible. Therefore, an analytical model for the locking of the crease-to-crease connection method will not be pursued further at this stage.

- *Analytical model for the face-to-face connection method*

As discussed above, when locking occurs for the face-to-face connection method, the unfolded units will develop travelling plastic hinges that rotate about the vertices and tend towards the α of the locked unit. The remaining hinges are assumed to be stationary and are located at the crease locations. This crease pattern for this progression is provided in Figure 4.56, where the hinges are separated into two types: (1) stationary horizontal hinges; and (2) travelling angled hinges. The energy consumed by these respective hinges is calculated here with respect to an incremental change in ϕ.

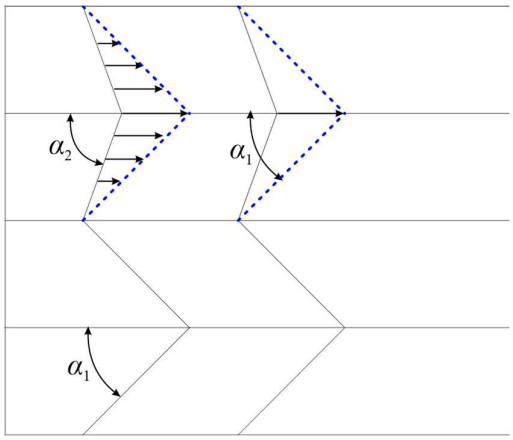


Figure 4.56 Super folding element for graded face-to-face connected cores

i. Horizontal hinges

Accounting for the double thickness at some sections, the energy absorbed by rotating about the horizontal hinges, E_h, by an angle $\Delta\phi$ can be calculated as follows.

$$E_h = 4mnM_p \begin{pmatrix} 2L_s + 2l_1^{min} + l_3^{min} - \frac{C}{2}\left(L_s + 2l_1^{min} + l_3^{min}\right) \\ -\frac{l_3^{min}}{m} + \frac{Cl_3^{min}}{2m} + 2l_{1c}^{min} + 2l_{3c}^{min} - \frac{l_{3c}^{min}}{m} \end{pmatrix} \Delta\phi = mnM_p\left(L_h\right)\Delta\phi \qquad (4.31)$$

where C is set to 1 when the unit has one free edge and 0 when it is between two units.

ii. Angled hinges

The energy consumed about the angled hinges can be calculated following the approach set out by Wierzbicki and Abramowicz (1983). Two distinct areas are associated with the travelling hinges: (1) two inclined conical elements; separated by, (2) a toroidal surface.

The energy consumed by the inclined conical elements can be calculated by considering the area swept by the hinges, A. Assuming that γ remains constant due to locking, the energy for one conical element can be calculated as follows, where r is the radius the travelling hinge is bent and unbent around.

$$E_c = \frac{2M_p A}{r} = \frac{2M_p}{r}\frac{a^2}{\tan\frac{\gamma}{2}}\sin\frac{\Delta\phi}{2}\cos\left(\phi_0 + \frac{\Delta\phi}{2}\right) \tag{4.32}$$

The energy consumed by the toroidal surface is calcaulted as follows.

$$E_t = \frac{16M_p ra}{t} I_1 \tag{4.33}$$

$$I_1\left(\frac{\gamma}{2}\right) = \frac{\pi}{(\pi-\gamma)\tan\frac{\gamma}{2}}\int_{\phi_0}^{\phi_0+\Delta\phi}\left(\cos\phi\left(\cos\frac{\gamma}{2} - \cos\left(\frac{\gamma}{2} + \frac{\pi-\gamma}{\pi}\arctan\left(\frac{\tan\phi}{\sin\frac{\gamma}{2}}\right)\right)\right)\right)d\phi \tag{4.34}$$

iii. Force

Assuming the deformation is localised within unit i following locking, the external work and internal energy for the entire super folding element can be equated as follows. The equation to calculate the displacement increment is also provided below.

$$F_m \Delta\delta_i = mn\left(E_h + 16E_c + 8E_t\right) \tag{4.35}$$

$$\Delta\delta_i = 2a_i\left(\cos\left(\phi_{i,0} + \Delta\phi\right) - \cos\left(\phi_{i,0}\right)\right) \tag{4.36}$$

Solving explicitly for the force displacement relationship is not simple. Instead, the average force, F_m, over an increment is calculated. In each increment r is found by minimising

the force with respect to r (Eq.(4.37)). Assuming that the increment is sufficiently small, the average force over this increment of deformation will provide a reasonable approximation of the actual force, F, at this point.

$$\frac{dF_{\mathrm{m}}}{dr} = 0 \tag{4.37}$$

In the following increment the process is repeated, taking the initial position of this increment as the final position from the previous increment. This process is repeated until the densification strain is reached for that unit which can be calculated with Eq.(4.24). In this way the complete force displacement curves can be generated rather than the mean over the entire crushing of the unit.

The densification strain for the entire graded core with M layers is provided in the expression below using the same assumptions used to derive Eq.(6.24).

$$\varepsilon_D = 1 - \frac{4tM}{\sum_{i=1}^{M} a_i \sin\left(\frac{\theta_{i,0}}{2}\right)} \tag{4.38}$$

- *Comparison of analytical model with FE simulation for a graded core*

The normalised force and nominal strain are compared with the normalised analytical model in Figure 4.57(a) for the TM14-10-8-45-50-58-82B 6×6 core. The average force during the collapse of the second and third unit is also provided from the analytical model. In the initial phase, before locking, the analytical model captures the behaviour well. However, similar to the discussion provided in section 4.3.2.8, it should be noted that the friction effects may increase significantly for alternative geometries and core sizes, resulting in an underestimation of the initial response of the core by the analytical model.

Following locking, the first load jump is overpredicted by the analytical mode (Figure 4.57(a)). This overprediction appears to increase for the second load jump, which occurs once the second unit has been crushed fully. This inconsistency is most likely related to the

idealisation of the deformation which assumes that γ remains constant once locking occurs. For the crease-to-crease connection method it was shown that the length does change slightly once locking occurs (Figure 4.42). Kinematically this is equivalent to a small increase γ or α of the locking unit, which would result in a reduction in the energy absorbed by the travelling hinges. The observed increase in the overprediction for the second load jump suggests that γ continues to increase following the locking of the second unit. In Figure 4.57(b) the force due to the locking of the first and second units is calculated assuming an increase in γ by 2° and 4° respectively. This reduces the difference in the peak force when compared to the simulations.

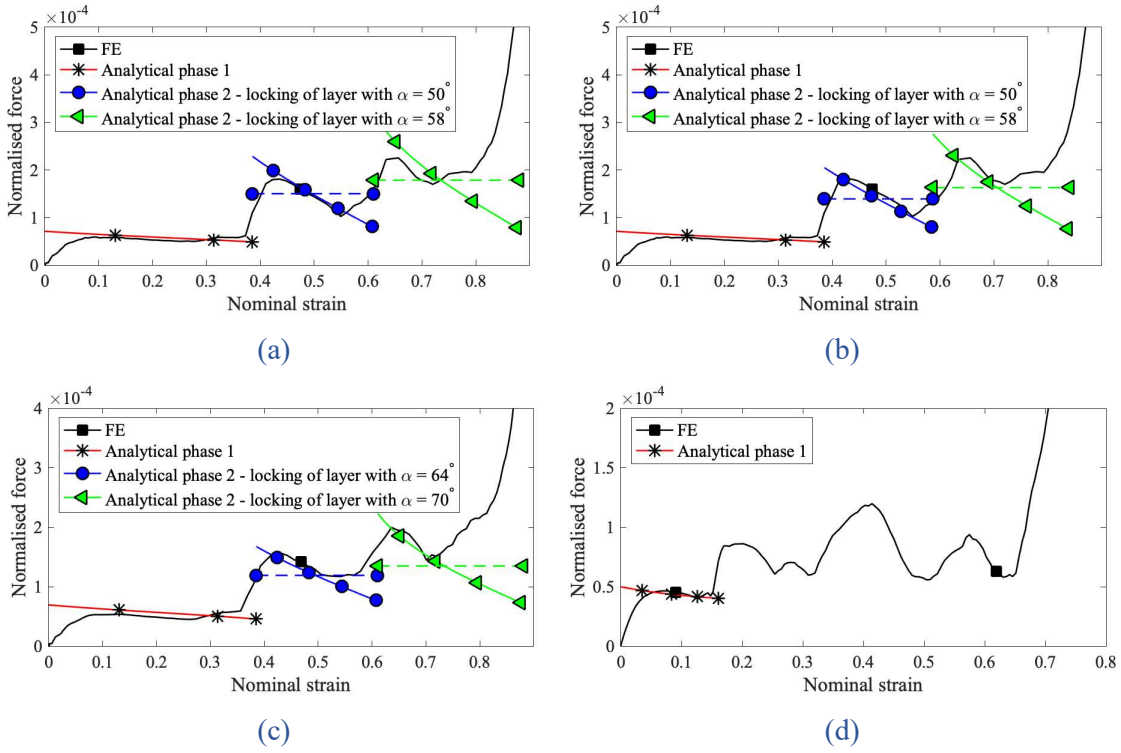


Figure 4.57 Graded core comparison to analytical prediction for: (a ,b) TM14-10-8-45-50-58-82B 6x6; (c) TM14-10-8-60-64-70-113 6×6; and, (d) 8-10-13-45-50-58-82 6×6

The numerical simulations show a force jump at $\varepsilon = 0.7$ during the collapse of the third unit. In contrast, the analytical model predicts continued softening behaviour. Although not presently demonstrated, the reason for this difference may be related to a deviation from the

assumed super folding element. Notwithstanding, in the initial stages of the collapse of the third unit, the analytical model provides reasonable agreement.

The densification point of the first unit is also overpredicted by the analytical model. This is again attributed to the idealised deformation mode which among other simplifications does not consider the radius about which the hinges bend.

Similar trends are also observed when comparing the analytical model to the TM14-10-8-60-64-70-113 6×6 core. The analytical model provides more accurate predictions of the force jumps due to locking of this core, however, the average force is underpredicted. This most likely results from the overestimation of the densification strain and/or the deviation from the super folding element in the later stages of crushing.

In general, the analytical model appears to provide a reasonable prediction of the force increase due to locking.

- *Comments on the analytical model*

To provide insights into how each variable affects the response an equation for the mean force for the complete collapse of the unit can be found by setting $\Delta\phi = \pi/2-\phi_0$. Substituting Eq.(4.31-33) and Eq.(4.36) into Eq.(4.35); inputting the limiting value of $\Delta\phi$ and, rearranging, gives the following expression.

$$F_{\mathrm{m}} = \frac{2mnM_{\mathrm{p}}}{a\cos\phi_0}\left(L_h\left(\frac{\pi}{2}-\phi_0\right)+\frac{4a^2}{r\tan\alpha}\left(\frac{1}{\sin\phi_0}-1\right)+\frac{32ra}{t}I_1\right) \tag{4.39}$$

Eq.(4.39) can be minimised with respect to r (Eq.(4.37)) resulting in the following relationship.

$$r = \sqrt{\frac{ta\left(\frac{1}{\sin\phi_0}-1\right)}{8I_1\tan\alpha}} \tag{4.40}$$

Substituting Eq(4.40) and Eq(4.7) back into Eq.(4.39) and using the relationship provided in Eq.(4.10) an equation for the mean force can be found and is provided below.

$$F_m = \frac{mn\sigma_y}{\sqrt{3}}\left(\frac{L_h\left(\frac{\theta_0}{2}\right)t^2}{a\sin\frac{\theta_0}{2}} + \frac{32a^{\frac{1}{2}}I_1^{\frac{1}{2}}t^{\frac{3}{2}}}{\sqrt{2\tan\alpha}\sin\frac{\theta_0}{2}}\sqrt{\left(\frac{1}{\cos\frac{\theta_0}{2}}-1\right)}\right) \tag{4.41}$$

It should be noted that Eq.(4.41) assumes that the unit that collapses is able to fold completely flat (i.e. $\varepsilon_D = 1$). In reality this is not the case and therefore the mean force calculated with this equation will underestimate the force when compared to the prediction in Figure 4.57(a), which calculated the nominal densification strain of the unit with Eq.(4.24). Nonetheless, Eq.(4.41) provides insights into the effect that the variable of the underlying crease pattern and initial topology have on the force increase when locking occurs.

The first term within the brackets increases with the length L_h (Eq.(4.31)), θ_0 and t but reduces with an increase in a. Similarly, the second term also increases with θ_0 and t, however in contrast with the first term, it also increases with a. Additionally the second term increases with I_1 and reduces with an increase in α.

From this it can be deduced that increasing θ_0 in the locking phase increases the force. Additionally, while an increase in a does result in a larger swept area, it also results in a reduction in the energy associated with the stationary horizontal hinges. Interestingly, the energy associated with the travelling hinges reduces with increasing α which was also observed from the FE simulations (Figure 4.50).

4.4 Conclusions

This chapter has presented a systematic experimental, numerical and analytical study aimed at identifying the effects that the variables of the underlying crease pattern and initial topology have on the behaviour of an origami honeycomb that is graded in the out-of-plane direction.

Initially an experimental study was used to validate a numerical method. Following this a numerical and analytical study was undertaken for ungraded tubes and cores for both the crease-to-crease and face-to-face connection methods. This study showed that the eccentricity of the horizonal creases influences the peak force greatly. α was also found to influence the peak force and SEA when all other variables were kept equal. Additionally, the increase in thickness for the face-to-face connection method resulted in an increased SEA when compared to the crease-to-crease connection method.

A numerical study was then undertaken to investigate the effect of grading α along the height of tubes. The locking showed potential in providing graded stiffness, however, if the eccentricity of the units is equal at locking this effect was diminished. When implemented as a core, even though the crease-to-crease connection method resulted in equal eccentricity at locking, a graded response was observed. This was due to the restraint provided by adjacent tubes in the core, resulting in a vastly different deformation mode when compared to the tube. While similar trends were observed for both the tube and the core with the face-to-face connection method, the response was more defined for the core due to the reduced effect that the asymmetry has on the deformation.

An analytical model was then formed to predict the increase in force when locking occurs for the face-to-face connection method. This was however not applicable to the crease-to-crease connection method due to the complexity of the deformation mode. The analytical model illustrated how the variables of the underlying crease pattern can be altered to vary the increase in stiffness under quasi-static loading.

When implemented as cores, both the face-to-face and the crease-to-crease connection method provided a graded response. Furthermore, for the face-to-face connection method the variables that can adjust the stiffness were well defined through an analytical model, providing the opportunity to functionally grade the stiffness of such core for a given application. These

findings are however only applicable to quasi-static loading conditions. In reality energy absorption devices are often implemented in dynamic loading scenarios. The behaviour of these cores when subject to an impact velocity is therefore essential for their application. Understanding the behaviour of these cores under dynamic conditions will therefore be the focus of Chapters 5 and 6.

CHAPTER 5

DYNAMIC BEHAVIOUR OF GRADED CORES

In the previous chapter the quasi-static behaviour of the origami honeycomb was investigated for two connection methods, crease-to-crease and face-to-face. For both, it was shown that the peak force can be controlled by altering simple geometric parameters and that self-locking can be used to grade the stiffness. The benefits of providing a strength gradient in cellular structures for impact events have been shown widely in existing literature (Ali *et al.*, 2008; Zeng *et al.*, 2010; Ajdari *et al.*, 2011; Liu *et al.*, 2012, 2013; Fan *et al.*, 2013; Shen *et al.*, 2013; Shen *et al.*, 2013; Shen *et al.*, 2014; Yang *et al.*, 2017; Zhang *et al.*, 2019). In this chapter, the dynamic behaviour of the graded origami honeycomb is explored experimentally and numerically. The purpose is to examine if similar benefits, as those found for existing graded cellular structures, are observed for this novel grading scheme when loaded dynamically.

In this chapter the behaviour of a core with the crease-to-crease connection method will be analysed first. This entails an experimental study using both the direct impact Hopkinson pressure bar (DIHPB) and Taylor type impact conducted on a 2×1 graded honeycomb core. To extend the study beyond the experimental geometric limitations, a numerical model is then built and verified against the experimental results. This numerical model is then built on to investigate the behaviour of a 6×6 graded origami honeycomb core with the crease-to-crease connection method. Using the same numerical method, the response of a 6×6 graded origami core with the face-to-face connection method will also be examined.

5.1 Graded stiffness vs gradient in strength

Before continuing it is important here to differentiate between a strength gradient and a graded stiffness. To grade the stiffness of the origami honeycomb, a variation in α is introduced along

the height of the core. Kinematically this variation introduces self-locking to the core which is the mechanism that provides the graded stiffness under quasi-static conditions (Chapter 4). This is a function of the entire core's behaviour rather than a gradient in the strength along the individual units of the core. That is, before locking the origami honeycomb is a 1DOF structure, therefore, the strength before locking is related to the entire core's behaviour rather than the strength of a single unit within it.

Under dynamic conditions the behaviour is more complex as the core may not necessarily be in equilibrium. Rather than the units of the core folding simultaneously, the response will generally become more localised, potentially resulting in a layer by layer collapse. In this case, the strength of the individual units within the core may dominate and determine the force that can be transferred to the neighbouring unit and therefore the strength gradient.

The force-displacement relationship for a core was derived in Chapter 4. Eq.(4.28-30) provide expressions for the force and displacement in relation to the initial cell angle of the core for the crease-to-crease and face-to-face connection method and can equally be applied to calculated the strength of a single unit. Of course, when units are connected to form a core, the constraint provided by the neighbouring unit will prevent it from following this kinematic path exactly. However, it is useful to provide an estimate of the initial strength of each layer in this manner.

5.2 Dynamic behaviour of core with the crease-to-crease connection method

5.2.1 Geometry design

The crease pattern for this study was designed with the consideration of the geometric constraints imposed by the dynamic experiment detailed in section 5.2.2. While the experimental program is carried out on a 2×1 representative core, the constraints provided by adjacent units were found to influence the mechanical behaviour greatly in section 4.3.2.4 of Chapter 4. The experimental investigation is predominately used to validate the numerical

approach. The behaviour is then interpreted through a purely numerical study on a 6x6 core (Figure 5.1(b)). The core consists of eight units ($M = 8$) along the height of the core with the α graded linearly in this direction from 43° - 64°. a is varied accordingly to allow the connection of the facets along the height (Eq.(3.24)). The initial design γ_0 is set to 60°, equivalent to that of a standard honeycomb. The other geometric parameters are provided in Table 5.1 and were set so that two representative units of the core could fit in series within the rectangular casing fitted inside the barrel of the gas gun (Figure 5.1(a)).

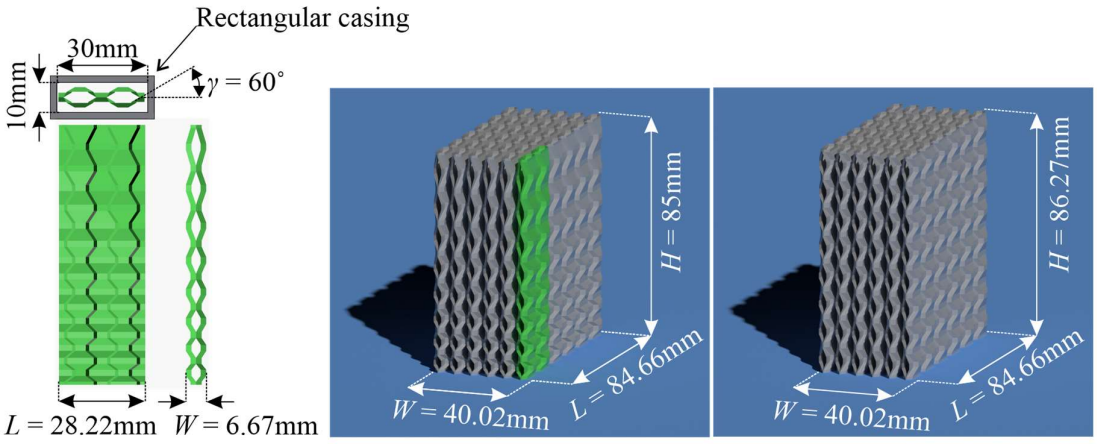


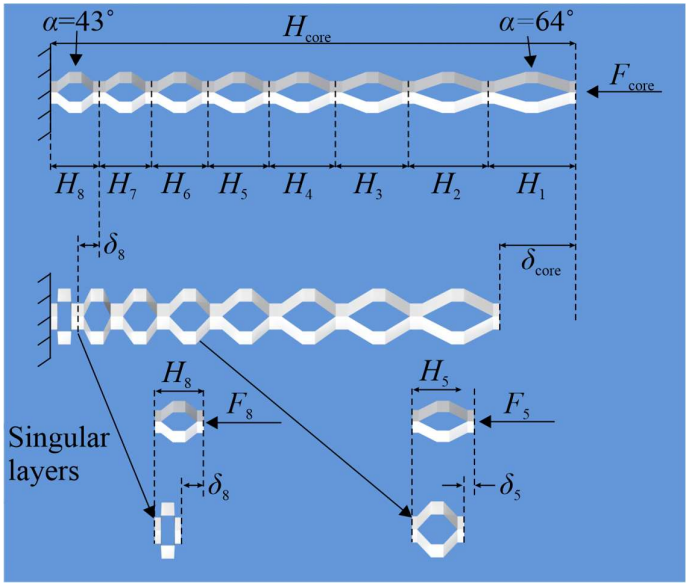
Figure 5.1 Geometry of: (a) 2×1 core used in experiments; (b) 6×6 graded core; (c) 6×6 ungraded core

Table 5.1 also provides the relative density and the prediction of the initial strength of the entire core, F_{core}, and of each singular layer, F_{layer}, from Eq.(4.28). The force in a single layer is calculated by considering the core is exclusively made up of that layer (Figure 5.2 (a)). The layer with the smallest α corresponds with the weakest initial strength and the unit with the largest α corresponds to the highest initial strength.

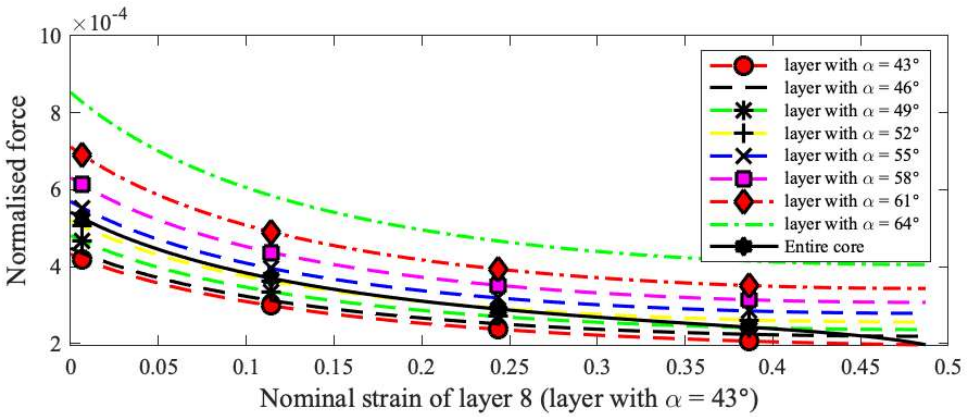
Table 5.1 Geometry of samples

α [°]	t [mm]	s [mm]	a [mm]	l_1 [mm]	l_2 [mm]	l_3 [mm]	$\bar{\rho}$ [-]	$F_{layer}/(m \times n)$ [N]	$F_{core}/(m \times n)$ [N]
43	0.2	2.00	2.42	1.68	2.12	8.63	0.0782	156.50	195.92
46			2.69				0.0764	161.87	
49			2.99				0.0750	173.81	
52			3.32				0.0739	188.20	
55			3.71				0.0730	205.93	
58			4.16				0.0723	228.27	
61			4.68				0.0716	257.18	
64			5.32				0.0711	308.48	

The differences between the theoretical quasi-static strength of the individual layers compared with the entire core from Eq.(4.28-29) are shown in Figure 5.2(b). The forces are normalised with Eq.(4.2) using the surface area of the entire core rather than the individual layers. The force of each layer is also only calculated to the displacement corresponding to the locking of the layer with $\alpha = 43°$ (i.e. for layer 5 the force is only provided until a displacement of δ_5, Figure 5.2 (a)). The normalised forces are provided with respect to the nominal strain in layer 8 (δ_8/H_8, Figure 5.2 (a)). From this the difference between the strength gradient and graded stiffness can be elucidated further. When treating the individual layers separately the force of each layer is different. However, when implementing these layers as a core, the initial quasi-static strength is a weighted average of each layer. In the initial configuration there is a more equal contribution from each layer, however, as folding continues towards locking, the cores force tends towards the unit with $\alpha = 43°$. In the numerical simulations the force at the distal end will be compared to both the quasi-static strength of the individual layer in contact with the support and the quasi-static strength of the entire core to observe how the core behaves in front of the crushing front.



(a)



(b)

Figure 5.2(a) Force and displacement plots of each layer; (b) quasi-static strength of each layer vs strength of entire core

The experiments were carried out for both positive and negative gradients of α. Here we define a positive grading when the core is orientated so that the smallest α is located at the loading (proximal) end. Conversely, when the core is orientated with the largest α at the proximal end and the smallest α at the support (distal) end the core is said to be negatively graded.

In the numerical study of the 6×6 core (Figure 5.1(b)), the response of the graded core is compared with an ungraded core (Figure 5.1(c)) that is constructed entirely from the unit with α = 55° in the graded specimen. The ungraded core was designed with the same number of units along the height as the graded core. α = 55° was selected so the height and relative density of the ungraded core was similar to that of the graded core. The uniform core has a relative density of 0.0730 and height of 86.3mm. The equivalent relative density of the graded core, $\overline{\rho}_{\text{eqv}}$, can be calculated using Eq.(5.1) and is equal to 0.0735. Where $\overline{\rho}_{\text{i}}$ and h_{i} are the relative density and height of unit i. The height of the graded core was 85 mm.

$$\overline{\rho}_{\text{eqv}} = \frac{\sum_{\text{i=1}}^{M} \overline{\rho}_{\text{i}} h_{\text{i}}}{H} \tag{5.1}$$

5.2.2 Dynamic experiments

5.2.2.1 Sample construction

The samples were made from the identical aluminium foil outlined in Chapter 4, using a sequential stamping technique (Gattas and You, 2015; Ma *et al.*, 2018). Seven female and male moulds were 3D printed from ABS material and used to fold the flat aluminium sheet to the design configuration (Figure 5.3). The number of moulds was chosen in order to minimise the material stretching during the stamping process.



(a) (b)

Figure 5.3 Female and male moulds used to stamp the sample; (b) sequential stamping of sheets

To create the core, two sheets are connected together at the connection facets using adhesive. To reduce the risk of adhesion failure, the connections surfaces were prepared with solvent cleaning, mechanical abrasion and chemical treatment. Initially the connection facets were washed with acetone and then water. The surface was then mechanically abraded by hand with sand paper and cleaned with air. Finally, the sheets were immersed in a bath of sulphuric acid for 20 minutes, rinsed off with water and dried before being bonded together with Araldite 420 A/B adhesive. The samples were then compressed together and left to cure in an oven for 2hrs at 70°C. The average mass of the 2×1 cores was 3.29 grams.

5.2.2.2 Experimental setup

Both the Direct Impact Hopkinson pressure bar (DIHPB) and Taylor type impact configurations were employed in this study (Figure 5.4). The DIHPB configuration (configuration A) was used to extract the force at the distal end (supported end) of the sample. In this configuration the sample was attached to the Hopkinson bar and a polycarbonate block with flat ends was launched at the sample. In the Taylor type impact configuration (configuration B), the samples were attached to the polycarbonate block and were then launched at the Hopkinson bar to provide the force at the proximal end (impacted end) of the sample. The polycarbonate block had dimensions of 30mm×10mm×65mm with an average mass of 23.14g. The experiments were carried out for samples with positive (S1-8) and negative (S9-14) gradients.

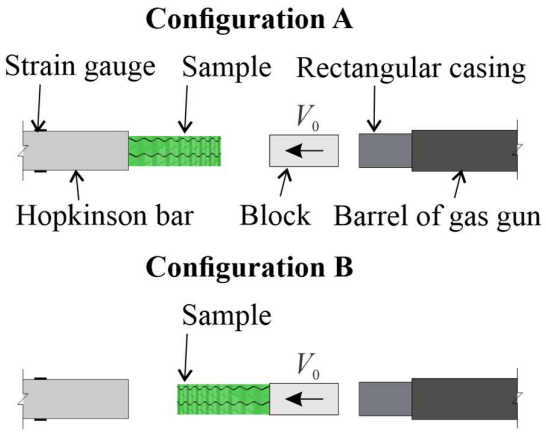


Figure 5.4 Schematic of experimental setup

During the experimental program difficulty arose when attaching the samples to the Hopkinson bar and aligning the barrel with the specimen in configuration A. This resulted in the block not directly impacting several samples. The majority of the samples were therefore tested in configuration B. Only experiments where direct impact was achieved are included in the test matrix provided in Table 5.2.

The same test setup as Xu *et al.* (2015) was used. The Hopkinson bar implemented was made out of aluminium with a Young's modulus of 70GPa, density of 2700kg/m^3, length of 4m and diameter of 37mm. The aluminium bar was chosen to match with the impedance of the sample and can be considered as a rigid wall when compared to the core's strength. To ensure the straight impact of the samples, the barrel of the gas gun was modified by inserting an aluminium rectangular casing. To provide a snug fit, the rectangular casing was sandwiched between two circular wooden segments that matched the internal diameter of the barrel (37mm).

To measure the force in the bar, two semi-conductive strain gauges were placed diametrically opposite one another at a distance of 400mm from the proximal end. This provided approximately 1.4ms before the reflected wave interfered with the signal readings. Data collected after 1.4ms was discarded for this reason. A half Wheatstone bridge was

implemented and the signal was amplified before being recorded by an oscilloscope. A Phantom V2512 high-speed camera was implemented to evaluate the initial velocity of impact and record the crushing behaviour. The initial impact velocities for all samples are provided in Table 5.2. High frequencies were removed from the signals through a method of Fast Fourier Transform (FFT). A cut-off frequency of 90kHz was implemented. Frequencies higher than this were found to have a negligible effect on the shape of the force-time curves. All experimental results provided in section 5.2.4.2 have been smoothed in this manner.

Table 5.2 Experimental matrix

Sample	Grading	Configuration	Loading velocity [m/s]
S1	+ve	A	30.90
S2	+ve	B	36.81
S3	+ve	B	35.76
S4	+ve	B	47.10
S5	+ve	B	48.82
S6	+ve	B	66.78
S7	+ve	B	67.00
S8	+ve	B	67.54
S9	-ve	B	31.20
S10	-ve	B	31.20*
S11	-ve	B	38.15
S12	-ve	B	39.25
S13	-ve	B	67.95
S14	-ve	B	68.13

*The video for this sample was not recorded. The velocity is assumed to be similar to S9 which used the same pressure to launch the sample at the Hopkinson bar.

5.2.3 Numerical analysis

ABAQUS Explicit was used to model the crushing process of the core. Two rigid plates were employed to model the support and the impinging block. An initial velocity, as determined from the experiment, was applied to the rigid loading plate to simulate the impact of the block. The loading plate was assigned a mass equivalent to the block. Both in-plane degrees of freedom and all degrees of freedom were constrained for the loading plate and base plate respectively. Tie constraints were used to model the connection between the two sheets that

make up the core. This constraint assumes a perfect bond. The core was predominantly meshed with four-node linear reduced integration shell elements (S4R). To prevent excessive distortion, a small number of three-node elements were also included (S3). A convergence study found an element size of 0.3mm provided accurate results. Hard-contact was defined in the normal direction and a friction coefficient of 0.3 was assigned for the tangential with the general contact definition provided in ABAQUS. The behaviour of the core showed little sensitivity to the friction in section 5.2.4.2. This reduced sensitivity to friction when compared to the cores simulated in Chapter 4 is most likely due to a combination of: the reduced length; larger number of units along the height; and, reduction in θ for the unit with the smallest α. Refer to section 4.3.2.5 in Chapter 4 for the discussion relating to the effect of each of these components. Additionally, glue was used to attach the samples to either the polycarbonate block or the Hopkinson bar, which, if perfectly bonded, would alter the boundary conditions. The effect of this end constraint will be discussed further in section 5.2.4.

The material behaviour was identical to that outlined in section 4.2 of Chapter 4. Strain-rate effects and failure of the aluminium were not considered in the material model, as this study focuses on the effect of the gradient achieved through origami techniques on the overall behaviour. The numerical and experimental results matched reasonably closely indicating that the strain-rate effects are not significant below 70m/s. At higher velocities this may not be the case. Similarly, while fracture was not observed in the experiments, this assumption may not be valid for larger velocities.

5.2.4 Experimental and numerical comparison

5.2.4.1 Deformation modes

The deformations at selected time steps for experiments and FE analysis are provided in Figure 5.5 -Figure 5.7. Figure 5.5 shows the deformations for a positively graded sample tested in configuration A with an initial impact velocity of 31m/s. In the experiment, the impinging block

appears to be slightly skewed, resulting in the impact of the bottom edge of the core before the top edge. This is seen at t = 0ms, the time of initial impact. Nevertheless, no significant asymmetry can be observed and the units fold sequentially from the proximal end towards the distal end. At t = 2.32ms the velocity of the polycarbonate block has approximately reduced to 0m/s. At this point, the energy of the impact has been completely absorbed. The deformation observed in the FE analysis matches closely with the experiment. A small difference is observed in the densification of each layer. In the experiments, contact is observed between the central lengths of each unit. This is highlighted in Figure 5.5 at t = 0.62ms. A gap remains between these lengths in the FE analysis. At larger velocities, contact between the layers is also observed in the FE analysis (Figure 5.7).

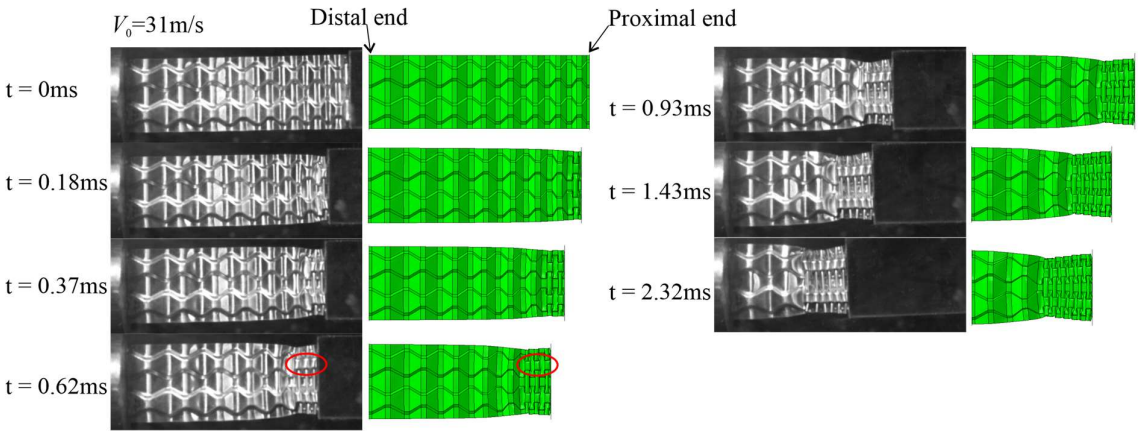


Figure 5.5 Experimental and FE deformation comparison for positively graded specimens S1 with initial impact velocity of 31m/s

The deformation of two positively graded samples loaded in configuration B at velocities of 36m/s and 67m/s are shown in Figure 5.6(a, b). For both samples the deformation initiates at the impinged end and propagates towards the distal end in a sequential folding manner. This deformation mode appears similar to those described for positively graded cellular blocks (Shen *et al.*, 2014; Yang *et al.*, 2017) and Miura-ori cellular material (Karagiozova *et al.*, 2019). In the final two time steps shown in Figure 5.6(a), S2 deforms laterally outwards. This is not

observed in the FE analysis and is most likely due to a small misalignment of the specimen as it impacts the Hopkinson bar and/or geometric errors caused by the manufacturing method. A slight difference in the final deformation (t = 1.14ms) is also observed in S7. In the FE analysis the top and bottom sides of the core have a negative and positive slope respectively. In the experiment, although the initial seven units follow this trend, the last unit length appears larger. The glue used to attach the core to the block provides some restraint to the end unit, preventing it from folding.

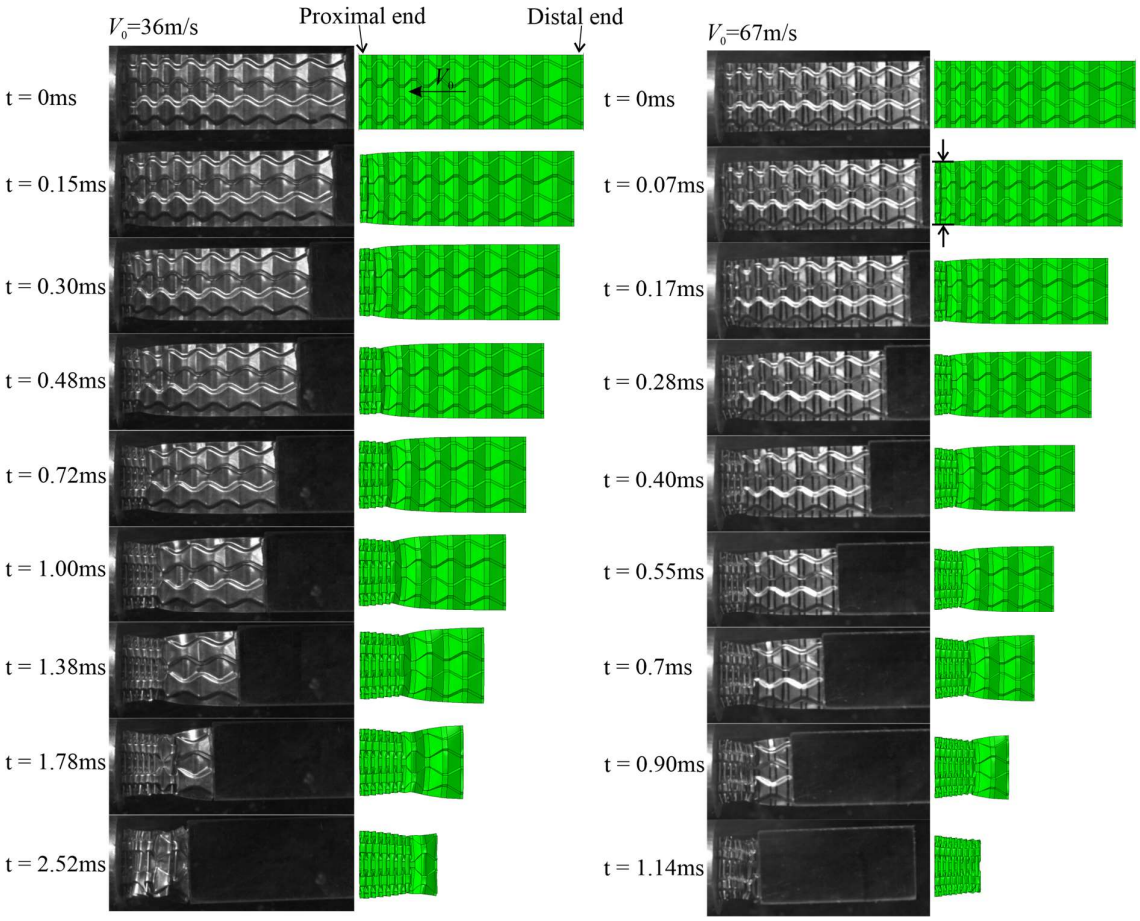


Figure 5.6 Experimental and FE deformation comparison for positively graded specimens (a) S2 with initial impact velocity of 36m/s; and, (b) S7 with initial impact velocity of 67m/s

FE analyses conducted for negatively graded units resulted in three alternative deformation modes. These deformation modes are consistent with those found in other

negatively graded cellular structures (Shen *et al.*, 2014; Yang *et al.*, 2017; Karagiozova *et al.*, 2019). At low velocities, aside from small initial localised deformations of the impinged unit, the units sequentially fold from the distal end to the proximal end (i.e. similar to quasi-static failure mode). Under high initial velocities the inverse is observed, units sequentially fold from the proximal end to the distal end. Between these deformation modes, where the folding only occurs from one end, there is a range of velocities where the folding occurs from both ends. This failure mode was observed in the FE simulations for S11 and S13 (Figure 5.7). Initially the deformation is localised at the proximal end. After some time period the unit at the distal end begins to fold, resulting in the sequential folding from both ends towards one another. The initial impact velocity appears to determine the number of units that sequentially fold from the distal end. For the initial impact velocity of 38m/s three units fold from the distal end, whereas only two units fold for 68m/s. These numerical findings were not readily observed in the experiments. The unit at the distal end did not undergo any visible crushing, instead, the folding propagated from the proximal end with only minor partial folding observed in the second and third unit from the distal end. The partial folding is most clearly seen at t = 0.65ms and t = 0.95ms in Figure 5.7(a). White guide lines are introduced to represent the initial length of the core. At these time points, the top and bottom side length are slightly convex and concave respectively, illustrating that the second and third unit from the distal end have reduced in length. The difference in the deformation is due to the constraints provided by the glue that attaches the sample to the polycarbonate block. This prevents the unit at the distal end from folding in a manner that follows the crease pattern, increasing the strength of the unit. Another FE analysis was run which included pinned restraints along the distal edge of the core. The deformation of this model matched the experiments closely.

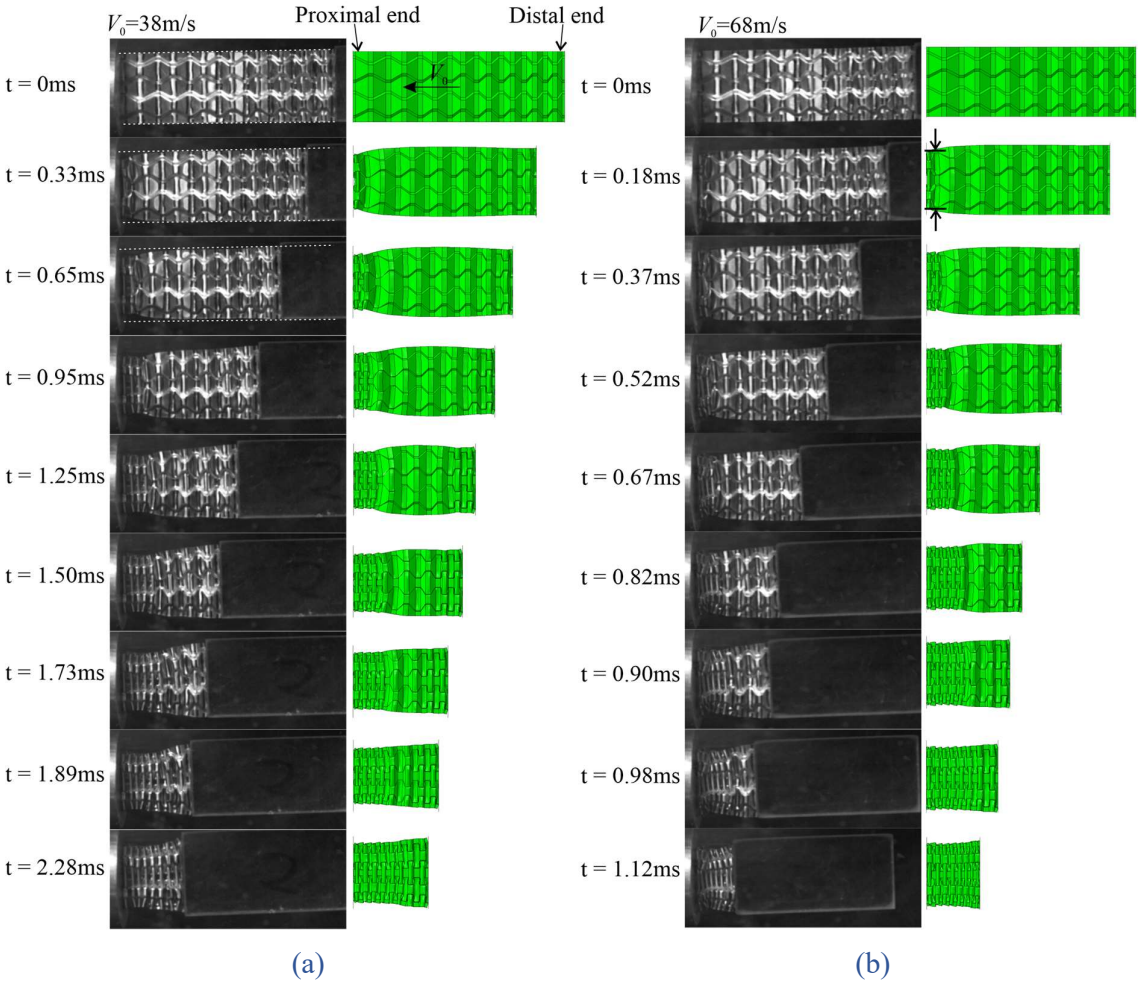


Figure 5.7 Experimental and FE deformation comparison for negatively graded specimens (a) S11 with initial impact velocity of 38m/s; and, (b) S13 with initial impact velocity of 68m/s

5.2.4.2 Force histories

Figure 5.8 and Figure 5.10 provide the comparisons of the experimental and numerical force histories for the positively and negatively graded samples respectively. Significant fluctuations are observed in the force at the proximal end. Generally, after the initial peak and subsequent softening, two fluctuations occur close together followed by larger period of softening before another two fluctuations occur. These fluctuations correspond to the locking of the units. However, due to localisation of the response under dynamic loading, two peaks are observed for the folding of a single unit. Taking the FE results for an initial velocity of 67m/s as an example, the initial peak corresponds to the impact of the projectile with the core. As the

impacted unit begins to fold softening occurs. However, the single unit does not fold symmetrically, instead the impacted side of the unit folds faster than the side closer to the distal end, resulting in the locking of one half of the unit initially. In the force history this locking corresponds to the second force peak. The response then softens briefly until the other half of the unit locks, resulting in the full densification of the first unit. This response is observed in both experimental and FE analysis. Snap shots of this deformation at these points is provided in Figure 5.8(c) from the FE analysis.

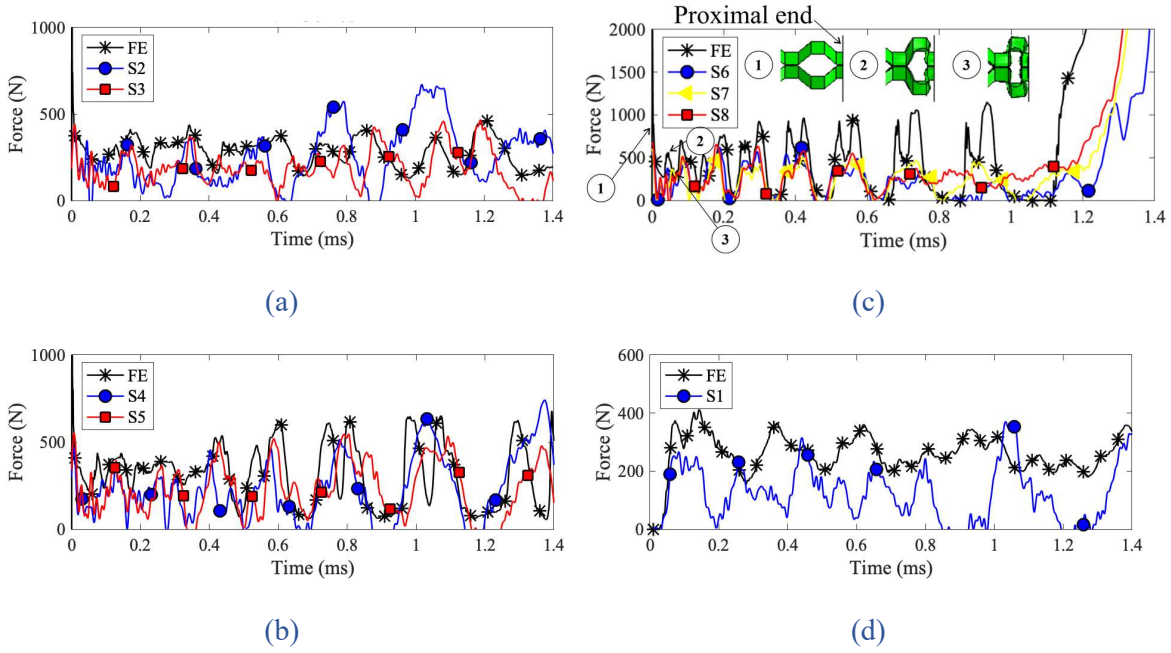


Figure 5.8 Force histories for positively graded samples with initial velocity of: (a) 36m/s; (b) 48m/s; (c) 67m/s; and, (d) 31m/s

The location of these peaks matches closely between the experimental and FE analysis for samples that are positively graded. The magnitude of these forces also matches closely for initial impact velocities of 36m/s for S3 and 47m/s for S4 and S5. In these samples, the energy absorbed in the experiments were 31%, 27% and 25% lower than the FE predictions respectively. The force fluctuations are significantly lower in magnitude after approximately 0.3ms for an initial impact velocity of 67m/s. To investigate the cause, S6 was orientated so

that the length was parallel to the cameras line of sight. Figure 5.9 shows the deformation of S6 at various time points. It can be clearly seen from these images that debonding occurs, resulting in the gradual prying open of the specimen from the proximal end. From visual inspections of the tested sample, the debonding appears to be due to adhesion failure. This is believed to have caused the reduction in the peak force magnitudes observed in experiments.

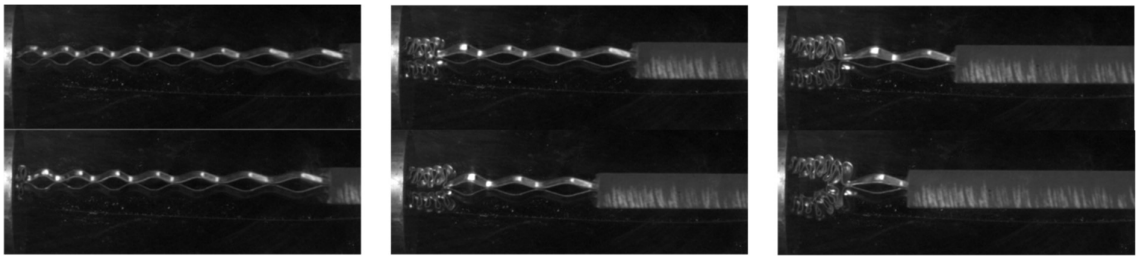


Figure 5.9 Debonding sequence of S6

Debonding is observed more widely in negatively graded specimens. This is believed to be due to the larger auxeticity of the units that are impinged. When the specimen is negatively graded, kinematically the change in length of the impacted unit should be significantly larger than when the specimen is positively graded. This is observed in Figure 5.7(b) (t = 0.18ms), where a larger length change occurs between the folded and unfolded units when compared with the positively graded specimen in Figure 5.6(b) (t = 0.07ms). This differential length results in the unit deviating further from the kinematic path prescribed by the crease pattern, resulting in larger stresses in the connection facets. The magnitude of the force oscillation's for negatively graded samples does not match as closely for this reason (Figure 5.10).

Additionally, at lower velocities, the location of the oscillations does not match closely. This is due to the difference in the failure mode observed in the experiment and FE analysis discussed in section 5.2.4.1 for negatively graded samples. As the velocity increases the location of the oscillation matches more closely as the deformation modes are alike.

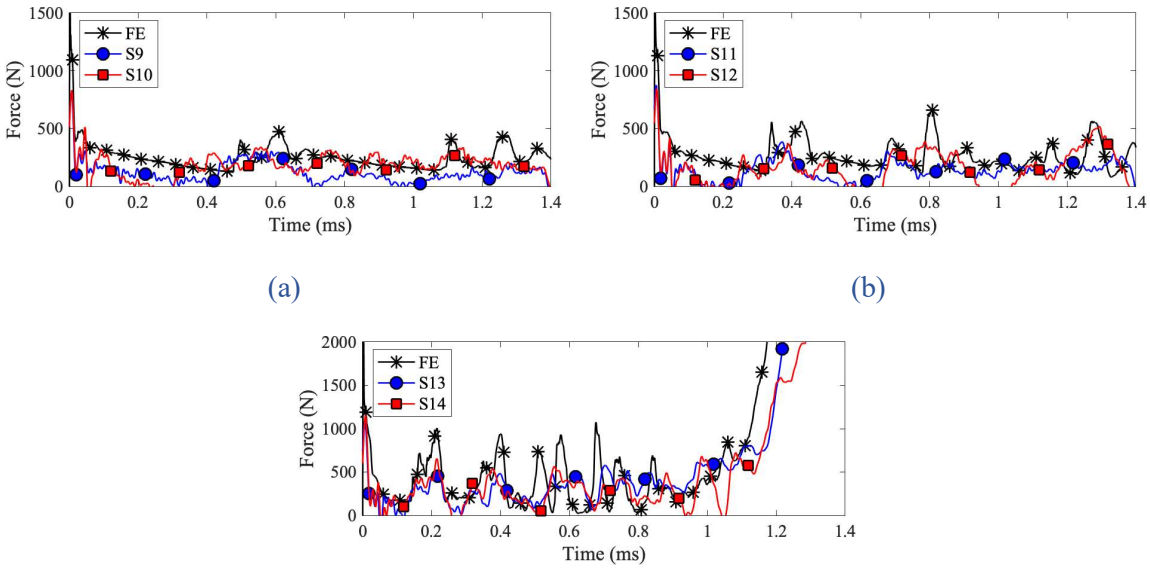


Figure 5.10 Force histories for negatively graded samples with initial velocity of: (a) 31m/s; (b) 39m/s; and, (c) 68m/s

The force history for S1, which was tested in configuration A, is shown in Figure 5.8(d). The initial slope of the curve matches well against the numerical model, however, the force recorded in the experiment is significantly lower. Again, this is most likely due to a degree of debonding between the two sheets. Difficulty aligning the specimen with the projectile and securing it to the Hopkinson bar may also play a role in this difference. This misalignment could cause an asymmetric response in the core which is only corrected after some initial deformation. Further tests in configuration A were not carried out to explore this further due to difficulty aligning the samples. Interestingly, the peak force extracted from the FE model is slightly larger than the theoretical quasi-static strength of the entire cores which is provided in Table 5.1 (note that the values in the table should be multiplied by $n = 2$ for comparison). This may be indicative of a number of phenomena and will be examined in more detail for the analysis of the core.

In this section the numerical approach is validated against experimental data. Some differences were observed due to the additional constraint added when attaching the samples to the Hopkinson bar or polycarbonate block. In spite of this, the FE model matched the experimental results closely or samples that did not exhibit debonding. Both the end restraint and debonding are somewhat caused by the restrictions imposed by the experimental setup. To ensure alignment of the samples glue was required to attach the samples to the Hopkinson bar or polycarbonate block. The small cross-sectional area of the setup resulted in small connection facets, reducing the bond area. For the purpose of the numerical study presented in section 6 the debonding and end constraints are not included as it is believed that these could be designed for without the geometric constraints imposed by the test setup.

5.2.5 Numerical simulation of core behaviour

In this section the influence of the grading on the performance of the origami honeycomb is investigated through FE analysis. The graded origami core is analysed with both positive and negative grading and compared with an ungraded core as described in section 5.2.1. These cores are labelled G1-8, G8-1 and UG respectively.

A similar modelling technique as described in section 5.2.3 was implemented for the numerical study of each 6×6 origami core. In order to reduce the number of elements, a 3×6 core was modelled with symmetry boundary conditions along the edges of the core. In contrast to section 5.2.3, a constant velocity is prescribed for the rigid loading plate. Four velocities are simulated for each core; 25m/s,50m/s,100m/s and 150m/s. This work mainly focuses on the ability to use origami techniques to introduce graded mechanical behaviour under dynamic loading. To this end, in these simulations, strain-rate effects and failure of the aluminium have not been considered. These assumptions may not be valid for larger velocities (100m/s and 150m/s), however, for the purposes of identifying the influence of the gradient on the overall behaviour, they were assumed to be reasonable.

5.2.5.1 Deformations

The deformations of the three cores when subjected to alternative velocities are provided in Figure 5.11, Figure 5.12 and Figure 5.14. For all cores the deformation modes change with velocity indicating that the modes are velocity dependent. The modes for the cores can be described in a similar manner to graded and ungraded honeycombs loaded in the in-plane direction (Ruan *et al.*, 2003; Shen *et al.*, 2013). At a velocity of 25m/s for UG, while there is initially a small amount of localisation at the distal end, the deformations quickly form into a "V" band. This is characterised by the cells at the central locations at the proximal end and cells on the edges three units in from the proximal end being relatively undeformed, whereas the cells three units in from the proximal end and cells on the edges at the proximal end fully collapse. As deformations continue, this "V" band propagates towards the distal end with minimal crushing of the central units at the proximal end. Finally, when the "V" band has propagated to the distal end, the remaining central units at the proximal end are crushed. As the velocity increases the "V" band transitions towards an "I" band, where the cells collapse sequentially from the proximal end to the distal end.

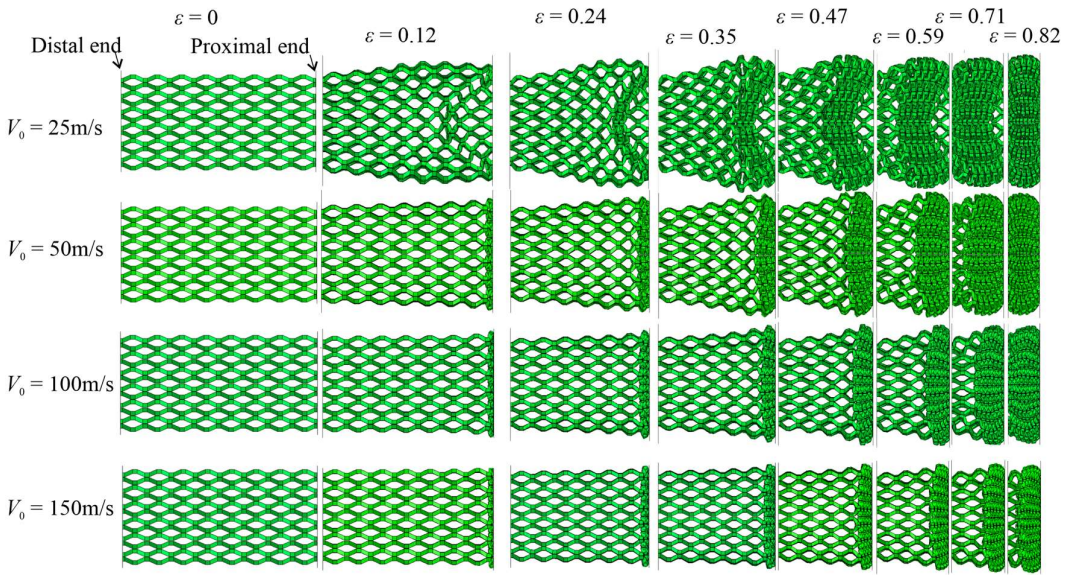


Figure 5.11 Deformation of UG core for 25m/s, 50m/s, 100m/s and 150m/s

Initially, the deformations for G1-8 appear to propagate as an "I" crushing band from the proximal end to the distal end (Figure 5.12). However, for V_0 = 25m/s, as the deformation moves towards the distal end, the cells in the centre deform a larger amount. This is observed at ε = 0.47, where the third unit from the distal end is completely crushed in the centre, whereas on the edges it is only partially deformed. This deformation takes the form of a weak "V" band. As the displacement increases to ε = 0.59 the units at the distal end along the edges begin to fold while the second unit in from the distal end on the edges deforms a smaller amount forming a weak "X" band.

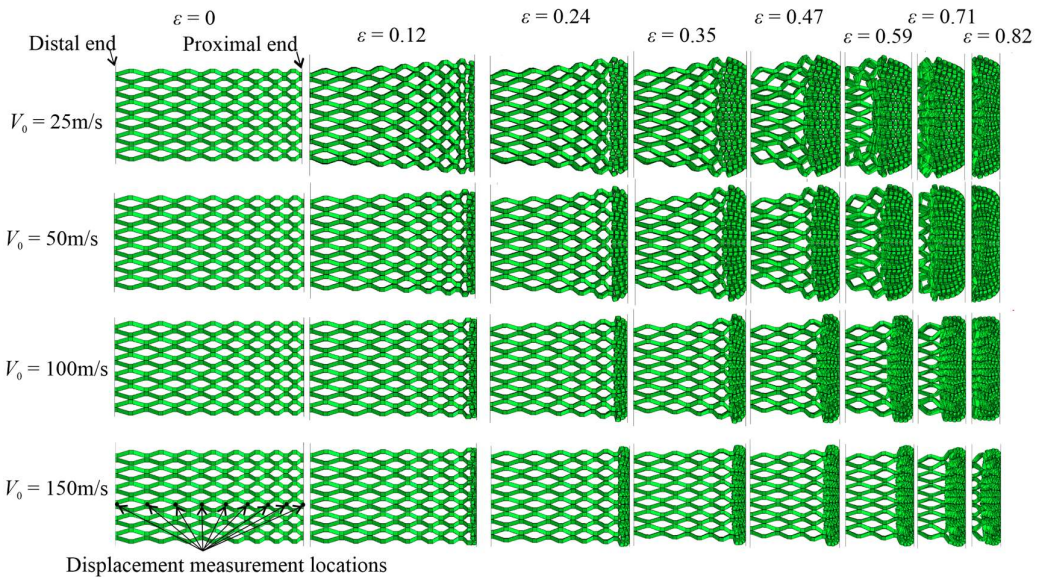
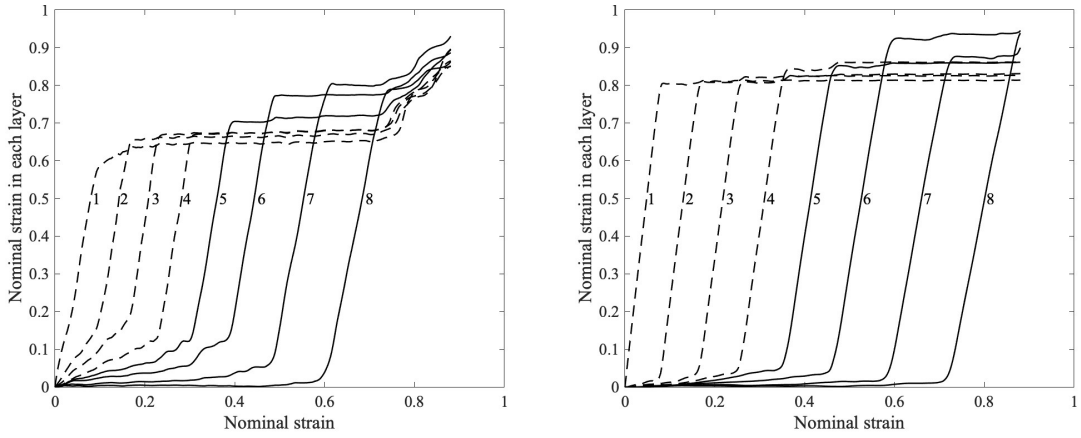


Figure 5.12 Deformation of G1-8 core for 25m/s, 50m/s, 100m/s and 150m/s

The nominal strains of each unit are determined using the equation below to further investigate the collapse of the core. The displacements are extracted from both the proximal, δ_p, and distal end, δ_d, of each unit and the change in length of the unit is then divided by the initial height, h_i. Here a positive strain is compressive. The displacement readings are extracted from the central location of the core marked at ε = 0 in Figure 5.12.

$$\varepsilon_{\mathrm{i}} = \frac{\delta_{\mathrm{p}} - \delta_{\mathrm{d}}}{h_{\mathrm{i}}} \tag{5.2}$$



(a) (b)

Figure 5.13 Nominal strain in each layer for G1-8 at: (a) 25m/s; and, (b) 150m/s

Figure 5.13 provides the strain in each unit with respect to the displacement of the loading plate for G1-8. The unit number is placed to the right of the curve it corresponds to in Figure 5.13. Additionally, the curves of the first four units from the proximal end are plotted with dashed lines for clarity. The deformation observed visually matches the trends in Figure 5.11, where the deformations progress from the proximal end to the distal end throughout the velocity range. Similar to the findings in Karagiozova *et al.* (2019), as the velocity increases the compaction of each unit increases due to the increased inertia in the loading direction. This results in a larger densification strain at higher velocities. This is also observed in Figure 5.11-13 where the units at the distal end are only partially folded for $\varepsilon = 0.82$ at 150m/s.

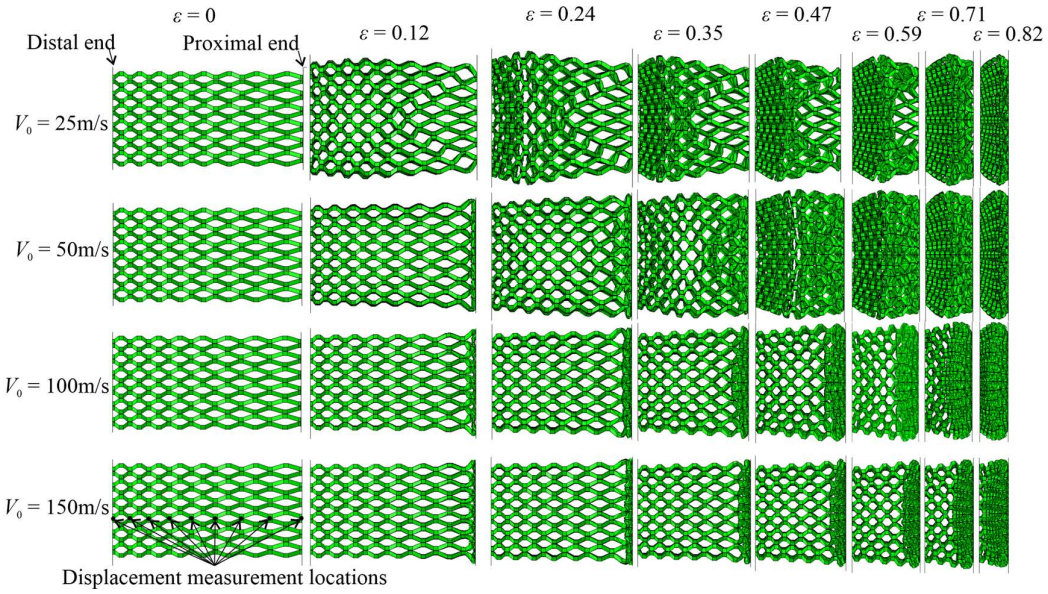


Figure 5.14 Deformation of G8-1 core for 25m/s, 50m/s, 100m/s and 150m/s

At 25m/s the deformation bands in G8-1 form a skewed "X". Similar to UG, a "V" shaped band forms from the proximal end (Figure 5.14). However, in contrast to the other cores, the deformation quickly propagates to the weaker cells at the distal end, where cells begin to collapse towards the proximal end in a weaker mirrored "V", forming the skewed "X". This is also observed for the strain in each layer (Figure 5.15(a)), where the strains in unit 8 increase rapidly after the initial impact. In Figure 5.15 the unit number is placed to the right side of the curve it is associated with. Following this, the deformation predominantly propagates from the distal end towards the proximal end, with the central units on the proximal side crushing last. The deformations become more localised at the proximal end as the velocity increases to 50m/s, however a "X" band is still observed. This is also shown in Figure 5.15(b), where initially the deformation is localised to unit 1, before larger strains are observed in the other units for the remainder of the crushing process. Similar to UG and G1-8, at 100m/s and 150m/s the "I" deformation bands appears to propagate from the proximal end to the distal end. The nominal strain in each layer, provided in Figure 5.15(c, d), indicate that although the deformation propagates in this manner, a small degree of folding occurs from the distal end,

with unit 8 experiencing larger nominal strains than units 4,5,6,7 and 5,6,7 during the majority of the crushing process for 100m/s and 150m/s respectively. In spite of this, due to the relatively small height of the core, unit 8 is still the last unit to completely crush. For cores with larger heights or gradients in strength, the unit in contact with the distal end may crush before the "I" crushing band that propagates from the proximal end reaches the distal end. This may result in larger stresses experienced at the distal end due to inertia effect.

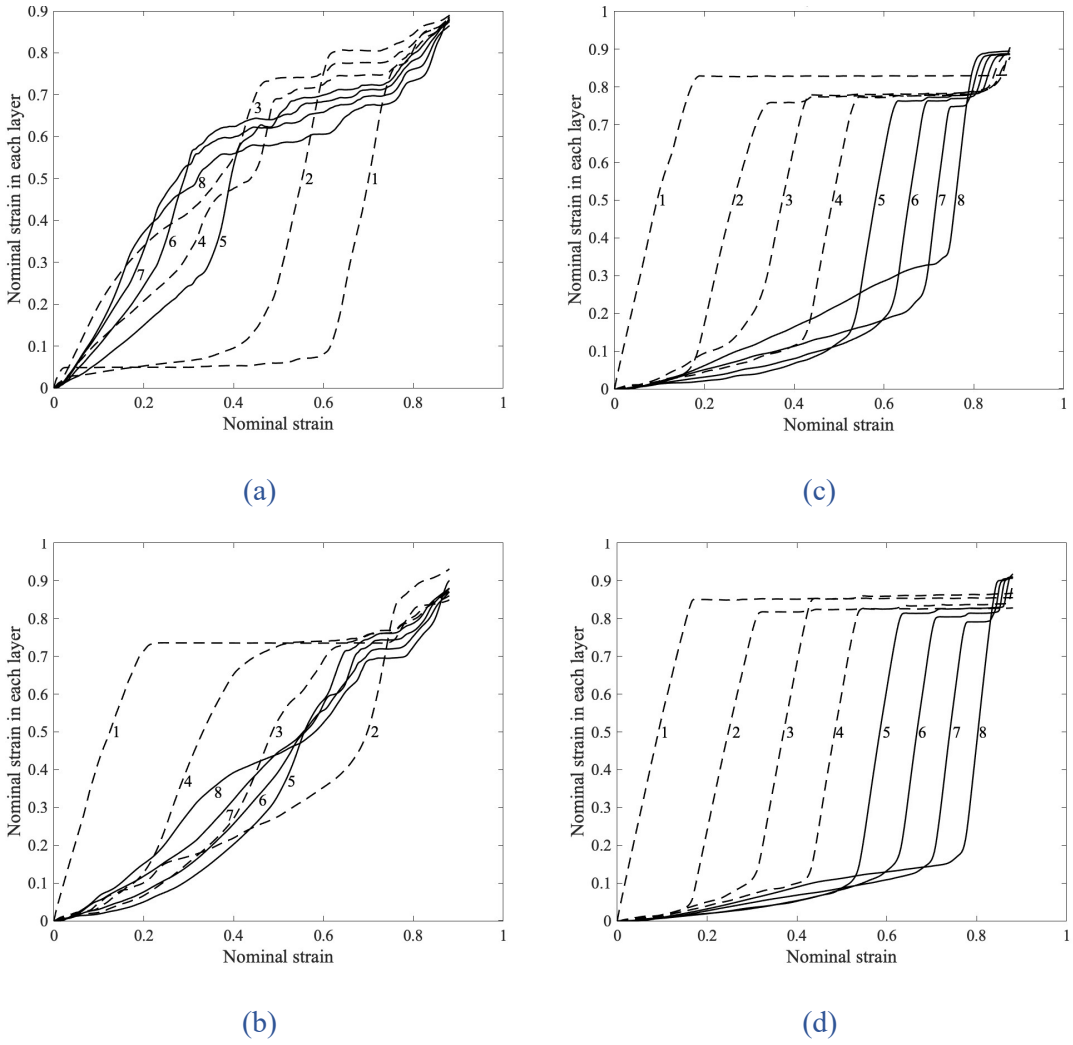


Figure 5.15 Nominal strain in each layer for G8-1 at: (a) 25m/s; (b) 50m/s; (c) 100m/s; and, (d) 150m/s

At higher velocities the "I" deformation mode is reminiscent of shock wave propagation typical of Type I structures (Calladine and English, 1984; Reid and Peng, 1997). However, shock wave propagation is characterised by a strong stress discontinuity across the shock front while the strain and velocity ahead of the front remain negligible (Tan *et al.*, 2005). Clearly, from Figure 5.15(d), for G8-1 significant strains that vary with distance from the distal end are observed in units 5-8, indicating that shock wave propagation may not be applicable. Instead the behaviour appears to be more typical of Type II structures which exhibit structural softening (Calladine and English, 1984; Karagiozova and Alves, 2017). The degree of softening of individual units is highly dependent on the initial dihedral angle. Further studies are required to determine when shock theory is applicable for the origami honeycomb and will be the focus of the next chapter.

Additionally, in all specimens the auxeticity is severely diminished for higher velocities. This is clearly seen through the lateral expansion of the core. For 150m/s the cross-sectional area of the cores before and after crushing is nearly equivalent, indicating that the crushing deviated significantly from the crease patterns prescribed kinematic motion. The disappearance of the auxeticity with increasing velocity for origami cellular structures was also reported by Harris and McShane (2021).

5.2.5.2 Force history

In order to compare the performance of the graded and ungraded core the normalised force and nominal strains are calculated with Eq. (4.2-3) respectively. The SEA is determined using Eq.(4.4), where the densification strain is based on the behaviour at the distal end.

The normalised force vs nominal strain for G8-1 at the proximal and distal end for different velocities are provided in Figure 5.16. At 25m/s, after an initial large peak, the force at the proximal end quickly reduces to the force at the distal end. The force at both ends remain

approximately equal before there is a sharp increase signifying the complete densification of the core. Throughout the majority of the deformation the core is in equilibrium, resulting in the deformation being spread across the core and the units predominately locking from the distal end (weakest unit) to the proximal end (strongest unit) (Figure 5.14).

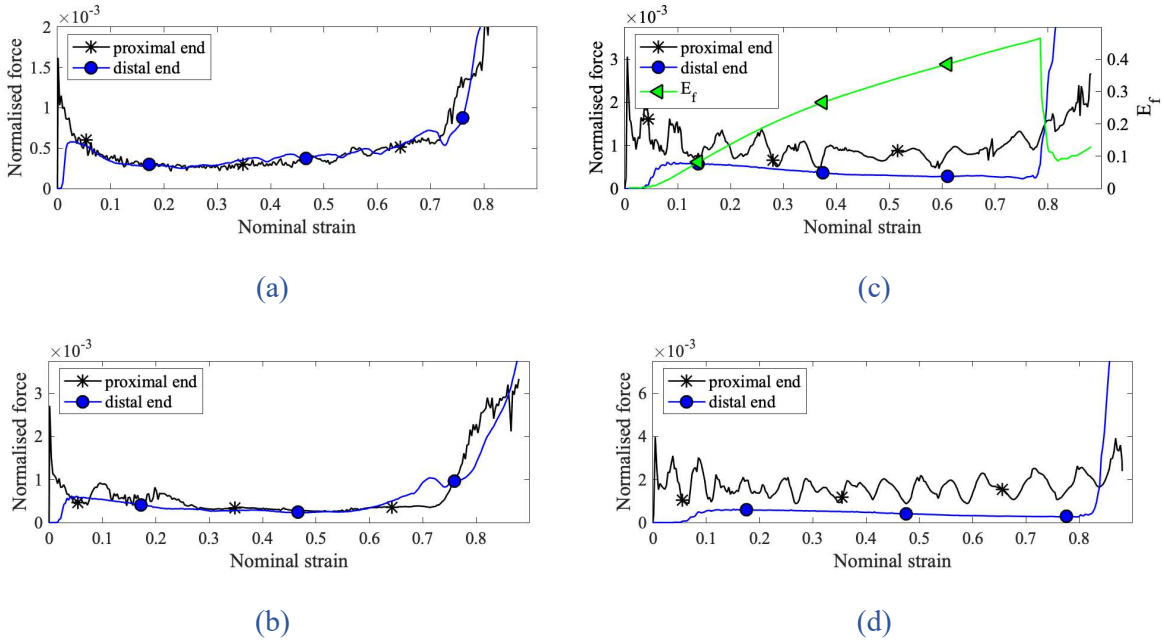


Figure 5.16 Force at proximal and distal end for G8-1 at: (a) 25m/s; (b) 50m/s; (c) 100m/s; and, (d) 150m/s

After the initial peak force, the force at the proximal end oscillates twice before reducing to the force at the distal end for 50m/s. As the velocity increases the loading plate can travel further before the stress reaches the distal end. Therefore, the first unit at the proximal end is able to completely collapse before the collapse begins to propagate from the distal end. This trend continues for 100m/s where the collapse predominately propagates from the proximal end until a nominal strain of 0.4, resulting in six distinct load oscillations at the proximal end before deformations occur at the distal end. At 150m/s the deformation occurs from the proximal end to the distal end, resulting in load oscillations at the proximal end throughout the collapse of the core. In contrast to 25m/s and 50m/s, the loads at the proximal and distal end

do not reach equilibrium. Instead, the force at the proximal end is significantly higher due to inertia effects.

Interestingly, at intermediate velocities, where the folding begins to propagate from the distal end (25m/s and 50m/s), the stress at the distal end does not increase significantly. This is in contrast with negatively graded honeycombs loaded in the in-plane direction (Shen *et al.*, 2013; Shen *et al.*, 2013; Zhang *et al.*, 2019), where the force at the distal end increases due to the axial inertia effect caused by the crushing beginning to propagate from the distal end. This is a desirable feature to minimise the risk of injury (Yang *et al.*, 2017).

At lower velocities the densification strain from the force curves at the proximal and distal ends are approximately equivalent (Figure 5.16(a, b). At higher velocities the densification appears to occur earlier at the distal end (Figure 5.16(c, d). In these cases, after the "I" front reaches the distal end, the units are compressed further from the distal end towards the proximal end. This is observed in Figure 5.15(c, d) where the strain increases after all the units have been crushed at approximately $\varepsilon = 0.8$. The strain increases layer by layer from the distal end to the proximal end after this time.

Figure 5.17 compares the normalised force at the proximal and distal ends for all three cores. The magnitude of the initial peak force at the distal end remains relatively similar throughout the velocity range for each core (Figure 5.17 (e-h)). This indicates that inertia effects are not present at the distal end. Similar observations were made for other cellular structures under dynamic loading (Fan *et al.*, 2013; Shen *et al.*, 2013; Zhang *et al.*, 2014).

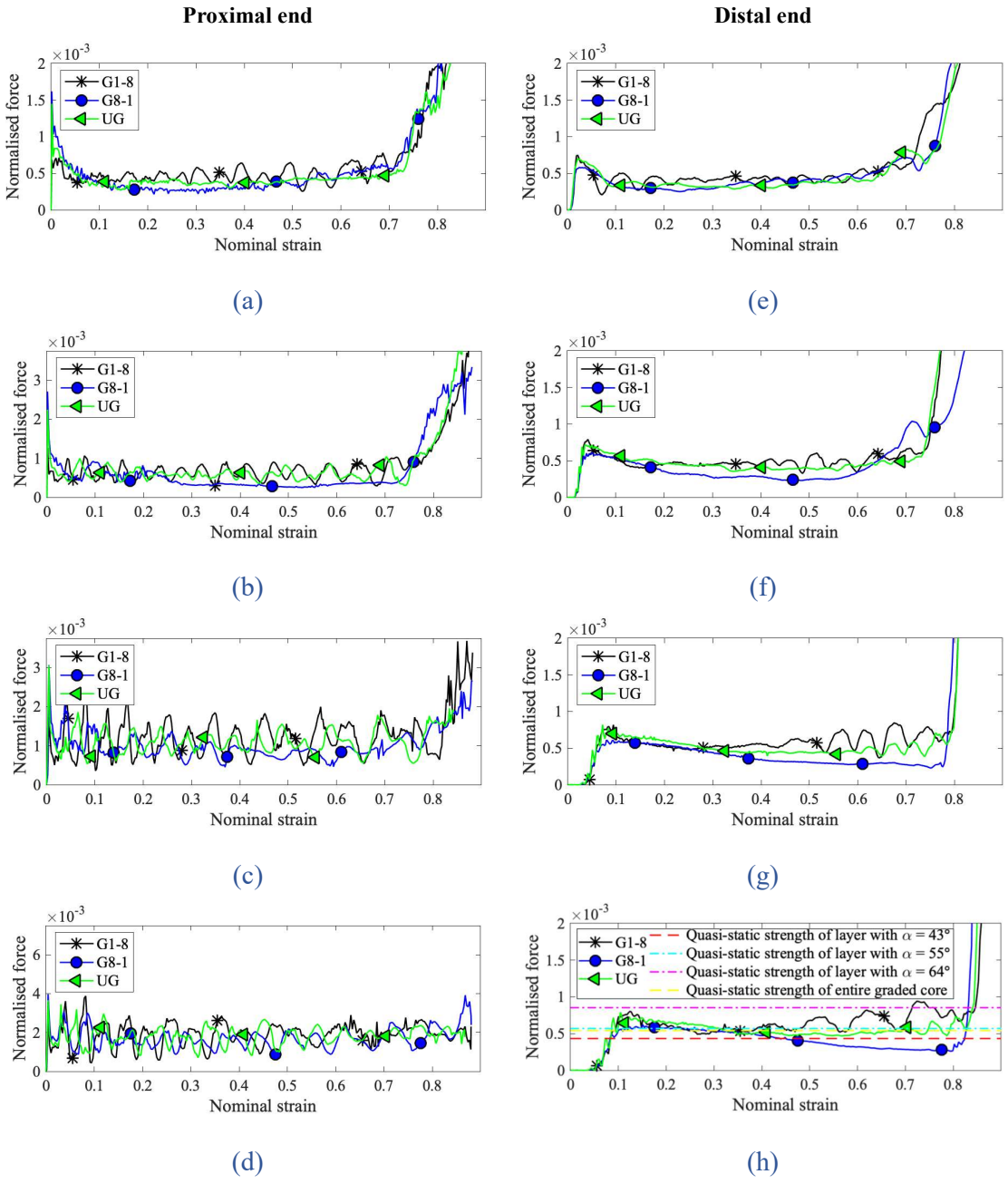


Figure 5.17 Normalised stress-strain at proximal and distal ends for (a, e) 25m/s; (b, f) 50m/s; (c, g) 100m/s; and, (d, h) 150m/s

The average initial normalised peak force at the distal end for G1-8, G8-1 and UG are 7.89e-4, 6.06e-4 and 7.56e-4 respectively. This is an indication of the gradient in the strength of the units. The gradient is also apparent by inspecting the normalised force vs nominal strain response at the distal end throughout the crushing process for 100m/s and 150m/s. At 25m/s

and 50m/s the gradient is less apparent as the stress at the proximal and distal and are approximately equivalent indicating the core is in equilibrium. However, at higher velocities the stress at the distal end for G1-8 oscillates in an increasing manner indicating the increase in quasi-static force of the layers being crushed from the proximal end. In contrast, the stress at the distal end for G8-1 predominantly exhibit softening behaviour, due to the lower quasi-static strength, resulting in the initiation of folding from the distal end. Less softening or hardening is observed in the ungraded specimen as the quasi-static strength of all units is equivalent. For the cores simulated, G8-1 provided a 21% reduction in the initial normalised peak force when compared to the UG core. By placing the weakest unit at the distal end, the stress transferred to the support can be reduced. These findings are similar to those for previously studied graded cellular structures (Zeng *et al.*, 2010; Shen *et al.*, 2014).

In Figure 5.17(h) the analytical quasi-static peak force provided in Table 5.1 for the entire core and the single layers of the core with α = 43°, 55°, 64° (refer to section 5.2.1) are provided. For G1-8 the layer in contact with the distal end has α = 64°. The analytical peak force for this layer is larger than the force observed at the distal end for most of the deformation. Only in the last load oscillation at ε = 0.82 does the magnitude of the force reach the analytical prediction for the singular layer. This suggests that the strength of the layer in contact with the support may provide a reasonable prediction of the maximum force transferred to the distal end for the positively graded specimen. In contrast, for G8-1 and UG, the analytical force prediction using the layer with α = 43° and α = 55° underpredicts the initial peak force, with the magnitude from the simulation only reaching this level at approximately ε = 0.45 and 0.32 respectively. Instead, for G8-1, the magnitude of the peak force appears to be predicted with greater accuracy by the analytical quasi-static force for the entire core.

To enable the comparison of the force at the distal end with the full range of the analytical model rather than only the initial peak, the normalised forces are provided with respect to the

nominal strain of the layer in contact with the support in Figure 5.18. From this it is quite clear that both the force prediction from the analytical model with the entire core and the single layer of α = 43° underpredict the force in the initial stages. In Chapter 4 friction was shown to influence the initial behaviour greatly, particularly for larger cross-sectional dimensions and smaller number of units along the height. To determine if the difference between the analytical prediction is due to friction, the G8-1 core was simulated with frictionless conditions for an impactor velocity of 150m/s. When comparing the FE simulations friction does not appear to influence the initial peak greatly. This indicates that the initial peak arises from an alternative phenomenon which will be explored further in Chapter 6. Following this initial peak, the force for the frictionless scenario returns to a value similar to the analytical prediction for the single layer with α = 43°, albeit the difference between the analytical prediction from the entire core is also small. In the case with friction, while the force also reduces it remains slightly larger than the analytical prediction for the single layer. Ignoring the effects due to friction, while the analytical model provides good agreement following the initial peak force, the magnitude of the initial peak maybe underpredicted. Additionally, as the difference between the analytical predictions for the entire core and the singular layer is not large, it is not clear if the maximum force transferred to the support is related to the strength of the singular layer at the support or the entire core.

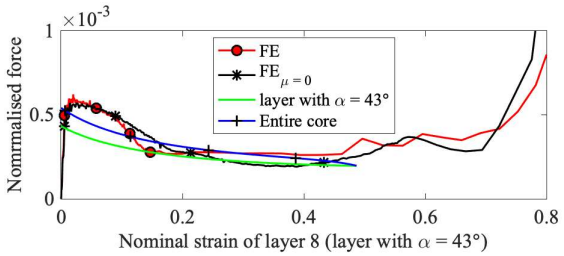


Figure 5.18 Normalised force vs nominal strain in layer in contact with support α = 43° for G8-1 V_0 = 150m/s

Load oscillations are observed at the proximal end throughout the velocity range for G1-8 (Figure 5.17(a-d)). As detailed in section 5.2.5.1, for G1-8 the cells collapse from the weakest unit, located at the proximal end, to the strongest unit, located at the distal end. The gradient in the strength of the units results in the stress that is transferred to the distal end being lower than that required for the units to collapse. The collapse of positively graded units therefore occurs from the proximal end to the distal end.

Throughout the velocity range the initial peak stress at the proximal end is largest for G8-1 and smallest for G1-8. At 25m/s the initial stress at the proximal and distal end is approximate equivalent for G1-8 (Figure 5.17(a, e)). For UG the stress is only slightly larger, whereas for G8-1 a significantly higher initial peak is observed at the proximal end when compared to the distal end. While the difference in the strength of the units placed at the proximal end contribute to this, larger lateral inertia of the units placed at the proximal end for G8-1 may also contribute. Kinematically, in order to completely fold, units with $\alpha = 64°$ undergo a larger range of motion in both directions perpendicular to the load when compared to $\alpha = 43°$. This is seen clearly in the final deformed shape of G1-8 in Figure 5.12 for 25m/s and 50m/s where the edges of the cores have a larger width for units with $\alpha = 64°$ than units with $\alpha = 43°$. As the velocity increases this becomes less pronounced and the units deform in a different manner to that prescribed by the crease pattern. This illustrates that there may not only be a gradient in the quasi-static strength of each unit, but also a gradient in the lateral inertia effect.

Table 5.3 SEA of cores

V_0 [m/s]	SEA [J/g]		
	G1-8	G8-1	UG
25	6713	6072	6543
50	9284	7110	8703
100	18054	14269	16922
150	31008	26656	29651

Table 5.3 provides the total SEA for each core with respect to the loading velocity. Although G8-1 absorbs a larger amount of energy in the initial impact, it absorbs the least throughout the crushing of the core, whereas G1-8 absorbs the largest amount. An increase of 3%, 7%, 7% and 5% in the total SEA is observed for G1-8 when compared to UG at 25-150m/s respectively. A larger reduction in the total SEA occurs in G8-1 when compared to the UG core, with 7%, 18%,16% and 10% reduction for 25-150m/s respectively. The gradient in the strength, self-locking design and lateral inertia are believed to contribute to this phenomenon, however, at this stage it is not clear to what extent each contribute. Similar trends are reported for FGM's with gradients in strength (Ali *et al.*, 2008; Zeng *et al.*, 2010; Ajdari *et al.*, 2011; Liu *et al.*, 2012, 2013; Fan *et al.*, 2013; Shen *et al.*, 2013; Shen *et al.*, 2013; Shen *et al.*, 2014; Yang *et al.*, 2017; Zhang *et al.*, 2019). This indicates that the change in strength is most probably a significant parameter. The self-locking design of the crease pattern is also believed to have some effect on the energy absorption. In G1-8, the crushing occurs from the weakest unit to the strongest unit, this is similar to the failure observed under quasi-static conditions where the cells lock layer by layer from the weakest unit to the strongest unit. As previously discussed, the kinematic range of the stronger units is larger than the weaker units. To completely collapse, the stronger unit must overcome this locking and deform further laterally than the locked unit. The constraint applied by the locked unit makes it more difficult for the stronger unit to fold, increasing the energy absorbed by the unit. Conversely, when the stronger unit folds first, stresses are introduced into the unfolded weaker unit that contribute to the folding of that unit under lower axial load. However, under higher velocity impacts, the stress at the proximal end is significantly larger than the quasi-static force due to inertia effects. In these cases, the effect of the self-locking may be insignificant when compared to inertia effects. Additionally, as the velocity increases and the origami honeycomb loses its auxeticity and deforms in a more localised manner that deviates from the path prescribed by the crease pattern. This may also

reduce the effect of the self-locking design. Further studies are required to understand the influence of each.

5.3 Dynamic behaviour of core with the face-to-face connection method

The deformation mechanism of the origami honeycomb core that implements the face-to-face connection method is significantly different to a core implementing the crease-to-crease connection method under quasi-static conditions (refer to section 4.3.2.4 of Chapter 4). This is largely due to the constraint provided by neighbouring units. Additionally, the crease-to-crease connection method requires that a_i is selected using Eq.(3.24), whereas, for the face-to-face connection method a_i can be chosen arbitrarily. Cores with the face-to-face connection method can therefore be designed with more arbitrary gradients in strength when compared to cores with the crease-to-crease connection method. For these reasons origami honeycombs with the face-to-face connection method may exhibit alternative behaviour to the core with the crease-to-crease connection method. To examine this, a numerical study of a 6×6 core utilising the face-to-face connection method is carried out in this section. The numerical method is identical to that outlined in the previous section.

5.3.1 Geometry design

The geometry is similar to the crease-to-crease connected core outlined in section 5.2.1. The variation in α is identical, ranging from α = 43° to 64°. Additionally, a for the layer where α = 52° is equivalent for the two cores. The a values for the other layers are selected so that the initial height of each layer is equal (5.93mm). The s length was set to 0 for this connection method resulting in a core with an overall height of 47.46mm. l_1^{I}, $l_2^{\mathrm{I}} = l_2^{\mathrm{II}}$, l_3^{I} where set equal to l_1, l_2, l_3 of the crease-to-crease connected core. l_1^{II}, l_3^{II} were chosen to be 4.325mm and 3.360mm respectively. The geometry of the core is shown in Figure 5.19 and summarised in Table 5.4.

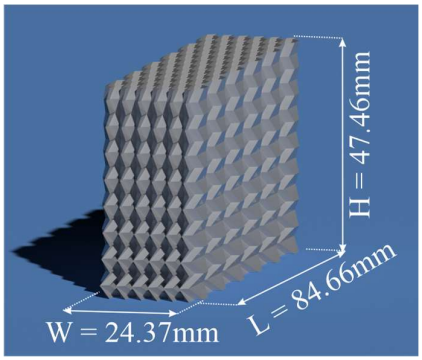


Figure 5.19 Face-to-face connected core

Table 5.4 Geometry of face-to-face connected core

α	a	l_1^I / l_1^{II}	l_2	l_3^I / l_3^{II}	$\overline{\rho}$	Normalised analytical forces		
						F_{layer}	F_{core}	$F_{avglock}$
[°]	[mm]	[mm]	[mm]	[mm]	[-]	[-]	[-]	[-]
43	3.78	1.68/4.33	2.12	8.63/3.36	0.0975	4.8e-4	7.8e-4	-
46	3.57				0.0978	6.4e-4		7.7e-4
49	3.43				0.0986	7.5e-4		9.4e-4
52	3.32				0.0997	8.7e-4		1.06e-3
55	3.24				0.1009	1.01e-3		1.15e-3
58	3.18				0.1024	1.18e-3		1.24e-3
61	3.13				0.1039	1.40e-3		1.31e-3
64	3.09				0.1056	1.47e-3		1.31e-3

Table 5.4 also provided predictions of the initial quasi-static peak force for individual layers, F_{layer}, and the entire core, F_{core}, from Eq.(4.30), in addition to predictions of the average force due to locking, $F_{avglock}$, of each layer from Eq.(4.35). The full range quasi-static prediction from these equations is provided in Figure 5.20. Little difference in the force due to locking is predicted for α = 61° and 64°. This is due to α = 64° being at the edge of the core, resulting in a reduced number of hinges that form. These forces will be compared with the force output at the distal end of the core from the FE simulations.

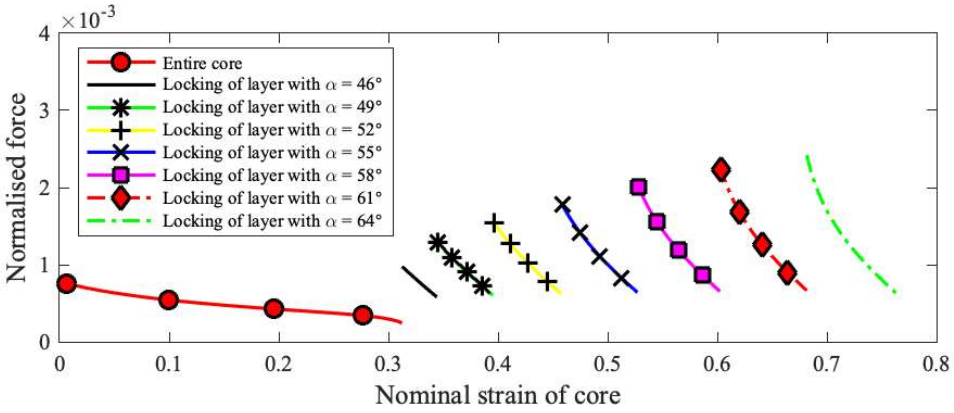


Figure 5.20 Analytical prediction of quasi-static behaviour of the core

5.3.2 Results and discussion

5.3.2.1 Deformations

The deformation process for the face-to-face connected core is generally quite similar to the crease-to-crease connected core, although, the deformation within the layer is much more uniform without the presence of the "X" and "V" deformation modes. Figure 5.21 provides the deformation for the positively graded core (TMG1-8) over the velocity range. For TMG1-8 the units almost exclusively crush in order from the proximal end to the distal end, forming the "I" deformation mode. Only for an initial impact velocity of 25m/s does the unit in contact with the support partially crush before the folding front reaches this layer ($\varepsilon = 0.63$).

Figure 5.22 provided the deformation for the negatively graded core (TMG8-1). At lower velocities (25m/s and 50m/s) the deformation predominantly propagates from the distal end to the proximal end. As the velocity increases to 100m/s the deformation initially propagates exclusively from the proximal end. However, between $\varepsilon = 0.21$ - 0.32 significant folding begins to occur at the distal end, resulting in two folding fronts propagating from either end towards one another. As the velocity increases further to 150m/s, significant folding in the unit at the distal end only develops at a larger nominal strain ($\varepsilon = 0.42$), resulting in the majority of units folding in an "I" mode from the proximal end to the distal end.

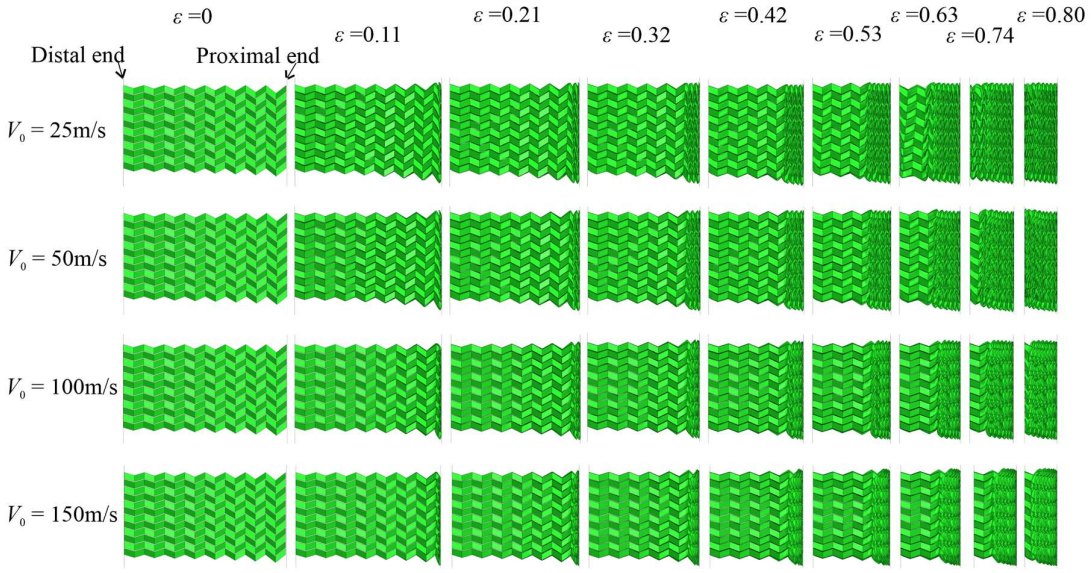


Figure 5.21 Deformation of TMG1-8 face-to-face connected core for 25m/s, 50m/s, 100m/s and 150m/s

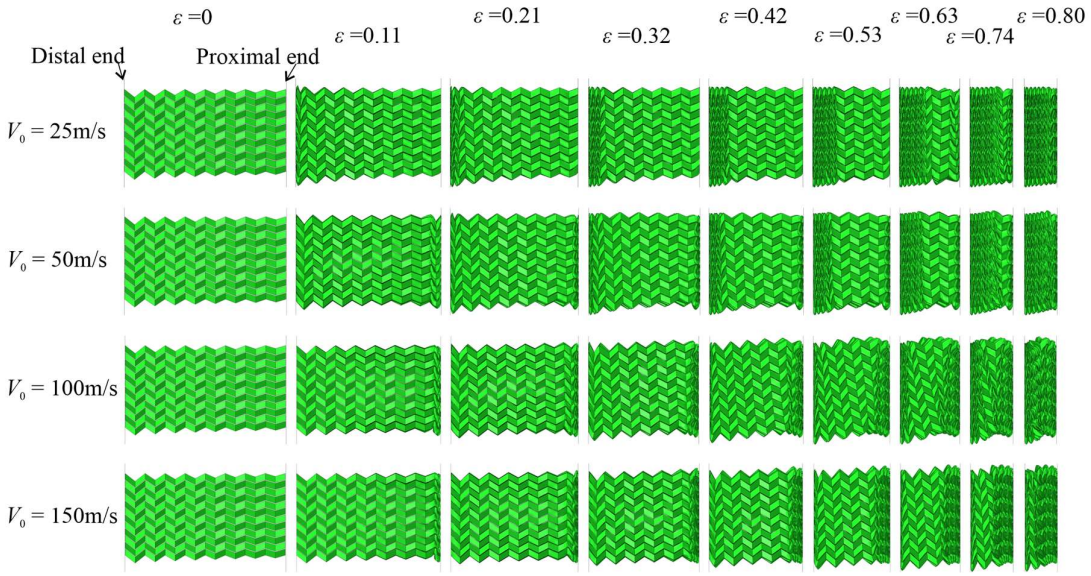


Figure 5.22 Deformation of TMG8-1 face-to-face connected core for 25m/s, 50m/s, 100m/s and 150m/s

5.3.2.2 Force histories

The normalised force vs nominal strain at the proximal and distal ends for the negatively graded face-to-face connected core (TMG8-1) are provided in Figure 5.23. At 25m/s the response at the proximal and distal ends are similar following the larger initial peak force measured at the

proximal end. This indicated that the core is approximately in equilibrium at this stage. A gradual increase in the force is also observed as crushing continues, providing an indication of the graded behaviour.

As the velocity increases the force at the proximal and distal ends begin to diverge. For 50m/s, an initial peak force, followed by a second load oscillation, is observed at the proximal end prior to the magnitude reducing to a value below that at the distal end (approximately at $\varepsilon = 0.27$). This unloading from the proximal end corresponds to the initiation of deformations propagating from the distal end (Figure 5.22). After this point, the deformation almost completely halts at the proximal end and instead propagates from the distal end. This results in the load oscillations predominantly occurring at the distal end. This trend is also observed for 100m/s, except at a more advanced stage of the deformation (ε = 0.5 - 0.6). For 150m/s the deformation almost exclusively propagated from the proximal end and therefore the force at the distal end does not exhibit major load oscillations before the densification of the entire core.

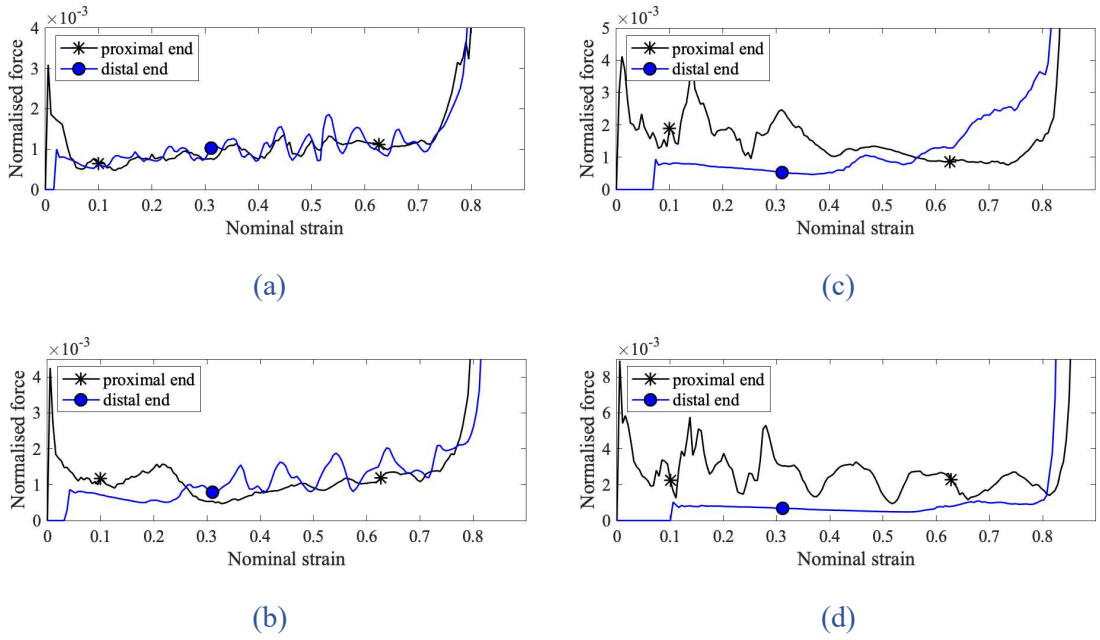


Figure 5.23 Force at proximal and distal end for the TMG8-1 face-to-face connected core at (a) 25m/s; (b) 50m/s; (c) 100m/s; and, (d) 150m/s

The normalised force at the proximal and distal end of the positively graded core (TMG1-8) and TMG8-1 are compared in Figure 5.24. Similar to the response of the cores with the crease-to-crease connection method, the initial peak force at the proximal end is largest for TMG8-1 throughout the velocity range. The reverse is observed at the distal end, indicating that placing the weakest unit at the support can reduce the force transferred to the support. The initial peak force measured at the distal end for TMG8-1 and TMG1-8 remains approximately constant throughout the velocity range indicating that inertia effects are not present here.

Aside from the initial peak, the force at the proximal end generally remains larger for TMG1-8. This is indicative of the trend observed in the SEA, where for velocities of 50m/s, 100m/s and 150m/s, TMG1-8 has 16%, 58% and 45% larger SEA when compared to TMG8-1. This is a significantly larger difference when compared to the cores with the crease-to-crease connection method (Table 5.3). This illustrates the larger gradient in strength that is possible for the face-to-face connection method.

Table 5.5 SEA comparison of face-to-face connected cores

V_0 [m/s]	SEA [J/g]	
	TMG1-8	TMG8-1
25	8355	8338
50	11424	9822
100	20723	13147
150	33479	23017

At the distal end, following the initial peak, the force for TMG1-8 and TMG8-1 remain quite similar for 25m/s and 50m/s, with both exhibiting increasing magnitude load oscillations as crushing continues. At these lower velocities the deformation predominately occurs from the weakest layer to the strongest layer, resulting in quite similar deformation modes and therefore responses. As velocity increases a larger difference is observed between TMG1-8 and TMG8-1. For these larger velocities, TMG8-1 predominately exhibiting softening behaviour,

whereas, the force for TMG1-8 continues to gradually increase. This is again associated with the deformation mode of TMG8-1 varying with velocity. As velocity increases the unit at the support only deforms a small amount before the crushing front reaches it. In contrast, at lower velocities, the unit at the support completely folds, resulting in locking and subsequent load oscillations as folding continues to propagate from the distal end.

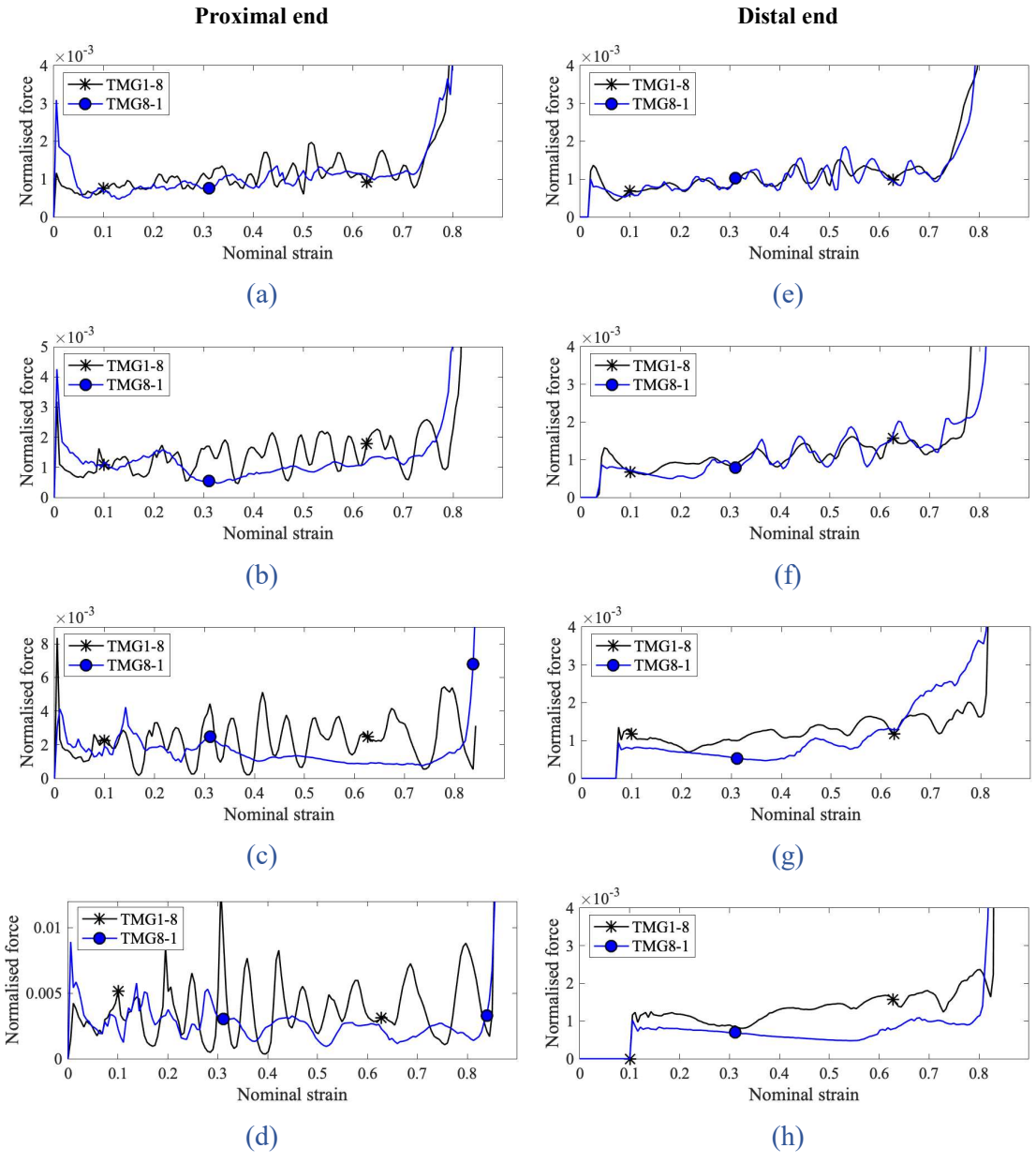


Figure 5.24 Normalised force vs nominal strain at the proximal and distal ends for the face-to-face connected core at (a, e) 25m/s; (b, f) 50m/s; (c, g) 100m/s; and, (d, h) 150m/s

Plotting the normalised force at the distal end with respect to the nominal strain of the unit at the support results in the curves over the velocity range collapsing onto one another (Figure 5.25(a)).This again shows that the response at the distal end appears to be inertia insensitive. The figure also provides the analytical predictions of the force for the entire core and an equivalent single layer. The force at the distal end is accurately predicted by the analytical model of the entire core (Eq.(4.29 - 30)). This suggests that in front of the folding front the units respond somewhat simultaneously. This calls into question the relevance of the analytical strength of the equivalent single layers for predicting the force at the support for the negatively graded core.

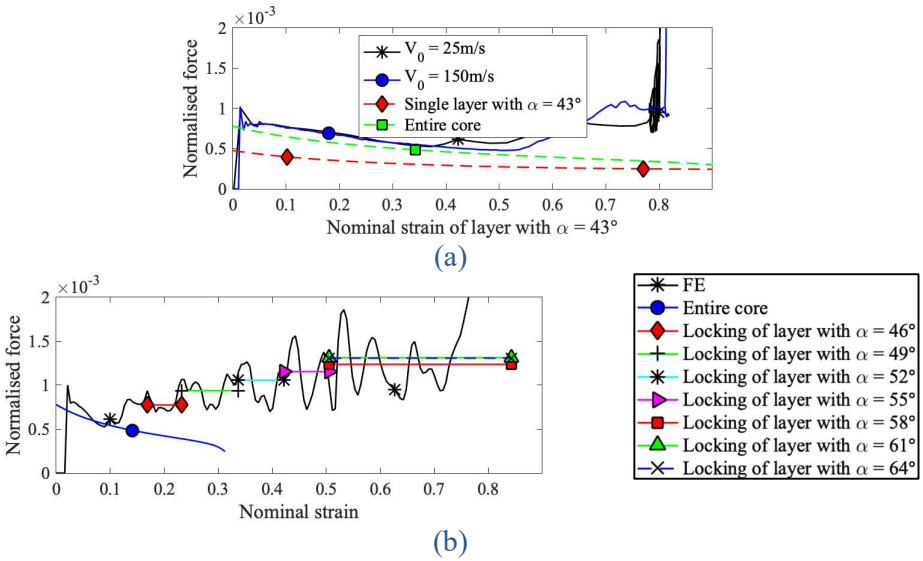


Figure 5.25 Comparison of the force at the distal end with analytical prediction for TMG8-1 for a velocity of: (a) 25m/s and 150m/s; and, (b) 25m/s

The analytical predictions of the entire core and the average force due to locking of the individual layers (Table 5.4) are provided in Figure 5.25(b). For clarity, the force due to locking of the layer is plotted only over the nominal strains where that layer is being crushed in the FE simulation. The layers with α = 58° - 64° collapse somewhat simultaneously (Figure 5.22) resulting in these being plotted over a larger range of nominal strains. As discussed above, the response of the entire core provides a reasonable prediction of the initial force. It does however

overpredict the deformation before there is a load oscillation i.e. it overpredicts the locking strain. This may be due to the degree of simultaneous folding reducing in the dynamic scenario, resulting in the analytical prediction overestimating the deformation of the other units. This may also result in the deformation deviating slightly from the crease pattern. This is observed in Figure 5.22 where the halves of the layer in contact with the support fold slightly out of sync.

The average force due to locking also provides a reasonable approximation of the force increase at the distal end as crushing continues. During the locking phase, two peaks are observed for the collapse of each layer. This is similar to the phenomena observed for the crease-to-crease core and again results from the slightly out of sync folding of each layer that is described above.

The force at the distal end for TMG1-8 (Figure 5.24(e-h)) is significantly larger than that predicted by the analytical model for the entire core. The analytical values of the average normalised forces from the single equivalent layer in contact with the support and due to locking of this layer are 1.47e-3 and 1.31e-3 respectively (Table 5.4). For 25m/s the initial peak force at the distal end for TMG1-8 is 1.37e-3 which is between the two predictions (Figure 5.24(e)). While the analytical predictions approximate this force reasonably, further analysis is required to determine the phenomena which is responsible for this force. This will be examined further in Chapter 6.

5.4 Conclusions

In this chapter the effectiveness of varying α to provide grading and influence the impact behaviour of the origami honeycomb core is investigated through numerical models. To validate the numerical method, a 2×1 core with the crease-to-crease connection method was experimentally tested using both the Direct Impact Hopkinson Pressure Bar and Taylor type impact test. The numerical model for the 2×1 core was shown to match the experimental results well for samples that did no experience debonding. While the numerical study assumes perfect

bond between the sheets used to manufacture the core, it is yet to be seen if the debonding can be negated when not subjected to the geometric constraints of the experimental setup.

The numerical model was then extrapolated to 6×6 cores to minimise edge effects. Strain-rate effects and material failure were not considered in the model. A core with positive and negative grading were compared to an ungraded core with similar relative density and height. These cores were utilised in the crease-to-crease connection method. The investigation showed that the gradient can have a significant influence on the deformation mode and thus energy absorption, with positive gradients showing the largest specific energy absorption when compared to negative and ungraded cores. This increase is believed to be due to a combination of the gradient in strength, self-locking design and lateral inertia effects. Further studies are required to investigate the influence of each.

The choice of unit placed at the proximal and distal ends provides significantly different behaviour. The initial energy absorbed by the impact at the proximal end was larger for units with larger α. This is believed to be due to a combination of the larger quasi-static strength and inertia sensitivity of units with larger α.

By placing the unit with the smallest α at the distal end the stresses at the support can be reduced. This shows great potential for applications where the design stipulates a maximum allowable force that is to be transferred to the structure.

Subsequently, 6×6 cores with the face-to-face connection method were simulated providing similar findings to the crease-to-crease connected cores. However, owing to the ability to arbitrarily select a for these cores, the graded behaviour was enhanced when compared to the crease-to-crease connection method.

At higher velocities the deformation propagates from the proximal end to the distal end. For the negatively graded core, although visually similar to the crushing of foams and honeycomb in the in-plane direction, this behaviour may not necessarily be described using a

shock front analogy as a strong discontinuity in the strain is not observed from the distal end. Depending on the initial topology, the individual units may behave similar to a Type I or Type II structure. Further investigations are required to determine when shock theory is applicable which will be the focus of Chapter 6.

CHAPTER 6

THEORETICAL MODEL

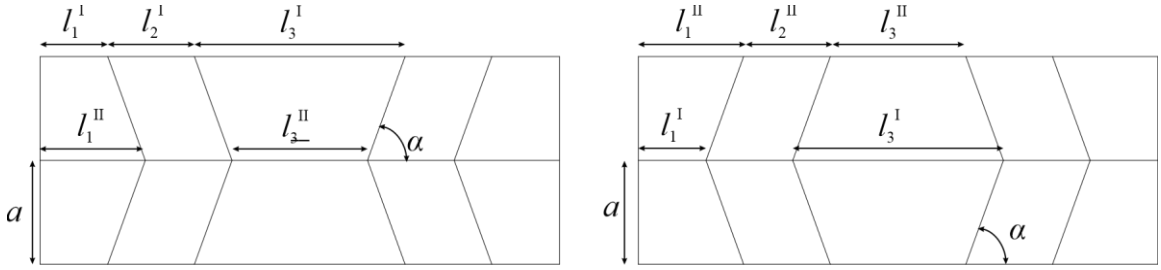
To form an analytical model for the dynamic behaviour of the origami honeycomb, the behaviour of the origami core needs to be investigated in detail to understand the response under impact. Analytical models that are applied to cellular structurers are summarised in section 2.4 of the literature review and can be broadly classified as models consisting of: continuum approaches assuming shock wave formation; continuum approaches utilising a structural approach; and, mass-spring models. In this section the dynamic behaviour of the origami honeycomb will be examined to assess the applicability of these analytical models and ultimately suggest an analytical model to capture the behaviour. As opposed to the previous chapter, which illustrated the ability to grade the stiffness of the origami honeycomb under dynamic loading, this chapter will focus on understanding the dynamic behaviour of ungraded cores with alternative geometries. This understanding of the underlying cells will hopefully enable the development of analytical models that incorporate grading in the future. Additionally, this chapter will focus exclusively on the face-to-face connection method. In chapter 4 and 5 it was shown that this connection method allowed greater versatility in the design of the grading. While it is assumed that similar findings would be applicable for the crease-to-crease connection method, no analysis has been completed to confirm this.

6.1 Geometry

In this chapter, unless stated otherwise, the understanding of the dynamic behaviour will be pursued for a cell with the underlying crease pattern dimensions provided in Table 6.1. Where superscript I and II correspond to the crease patterns for the opposite sides of the unit cell, drawn in Figure 6.1(a, b) respectively.

Table 6.1 Crease pattern variables

α [°]	t [mm]	a [mm]	l_1^{I} [mm]	$l_2^{I} = l_2^{II}$ [mm]	l_3^{I} [mm]	l_1^{II} [mm]	l_3^{II} [mm]
70°	0.2	9.5258	6.25	8	19.4342	9.7171	12.50



(a) (b)

Figure 6.1 Crease pattern for: (a) side I of the unit cell; (b) side II of the unit cell

The l_1^{I} length was selected to prevent the intersection of the vertices throughout the kinematic range using the expression provided below. l_3^{I} was selected such that the length of the neighbouring parallel crease line along the centre of the pattern is equal to $2l_1^{I}$ using the equation below. The lengths for crease pattern II were taken as the lengths of the crease lines along the centre of crease pattern I (Figure 6.1).

$$l_1^{I} \geq -l_2^{I}\cos(2\alpha) \tag{6.1}$$

$$l_3^{I} = 2l_1^{I} + \frac{2a}{\tan(\alpha)} \tag{6.2}$$

6.2 Numerical analysis

A similar approach as that detailed in section 5.2.3 of chapter 5 is applied to model the dynamic behaviour of the origami honeycomb. However, in this chapter, several changes were made to focus specifically on the behaviour imbued by the geometries rather than boundary conditions and underlying material properties. Firstly, the material model for the core was elastic perfectly-plastic, with a yield stress of 123MPa and elastic modulus of 45.6GPa. Secondly,

unless stated otherwise, a frictionless contact condition was applied to reduce the effect of the contact at the ends of the core. A convergence study found that an element size of 0.5mm provided accurate results.

6.3 Dynamic behaviour of core

Before developing an analytical model, the influence of the: initial dihedral angle, θ_0; number of units in the in-plane directions (x and y); Miura-ori angle of the underlying crease pattern, α; and, number of units along the height of the core, on the behaviour is investigated. Of particularly interest in this section is the force transferred to the support, as this provides insights into the deformation mode and lateral inertia effects.

6.3.1 Effect of the initial dihedral angle, θ_0

The effect of θ_0 was investigated for a 6×6 core with three units along the height (M = 3). To reduce the size of the model a 6×3 core (Figure 6.2) with symmetry boundary conditions applied along the edge was implemented. θ_0 of 60° and 150° were investigated. These two angles were selected as they exhibited quasi-static behaviour typical of Type I and Type II structures respectively (Figure 6.3(a)). As both cores have identical crease patterns it would be expected that they return to the same force. Clearly the core with θ_0 = 150° has a slightly larger plateau force. This difference is attributed to a slight deviation from the crease pattern observed in Figure 6.3(b), where the cells along the height fold out of sync to a small degree. Nonetheless, the overall behaviour still follows the crease pattern.

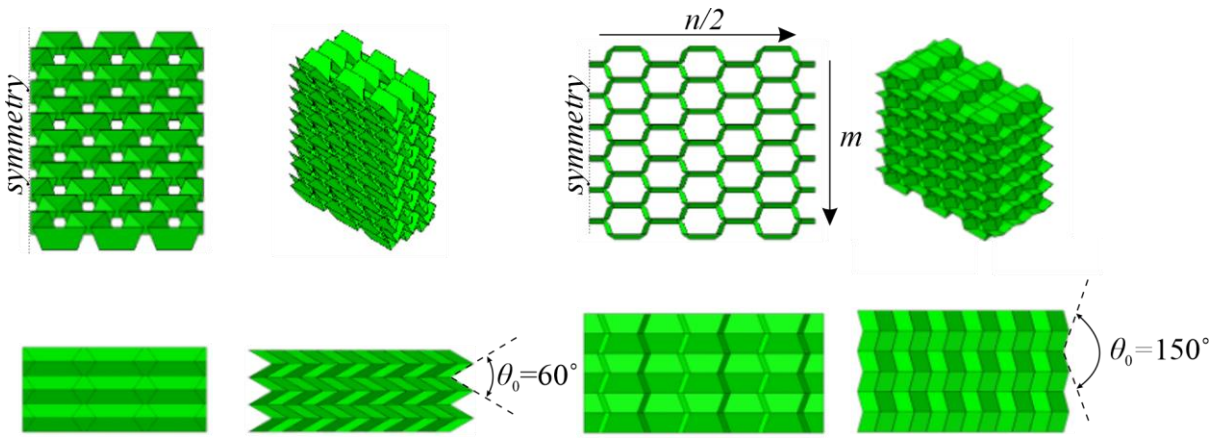
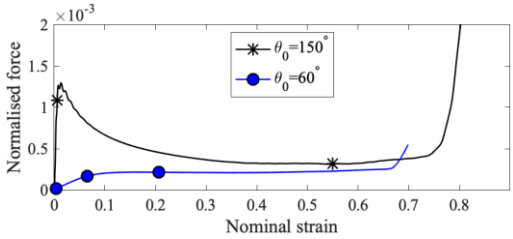
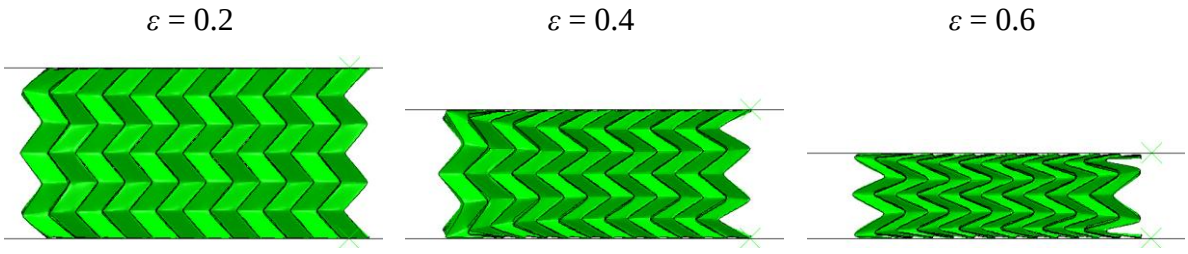


Figure 6.2 Initial configuration of cores



(a)



(b)

Figure 6.3(a) Normalised force vs nominal strain for cores with θ_0 = 60° and θ_0 = 150°; and, (b) deformation of core with θ_0 = 150°

Both cores were subjected to a dynamic impact with a rigid plate travelling at a constant velocity of 5m/s,10m/s,25m/s and 50m/s and 100m/s. The results from the FE simulations for the core with θ_0 = 60° are provided in Figure 6.4. The force is normalised using Eq.(4.2) except rather than using the entire surface area, only the surface area of one layer is used. The nominal strain is calculated following Eq.(4.3). The force under quasi-static loading conditions is also provided in the figures. For 5m/s and 10m/s, the force at the proximal end has an initial short peak before reducing to a magnitude similar to the force at the distal end. As the velocity

increases, after the initial peak, the force at the proximal end oscillates at a higher magnitude than the force at the distal end. This is most likely due to the axial inertia effect. Similar to other Type I structures, the force at the distal end remains close to or below the quasi-static value before densification occurs. The response at the distal end therefore appears to be velocity and lateral inertia insensitive for an initial dihedral angle of $\theta_0 = 60°$.

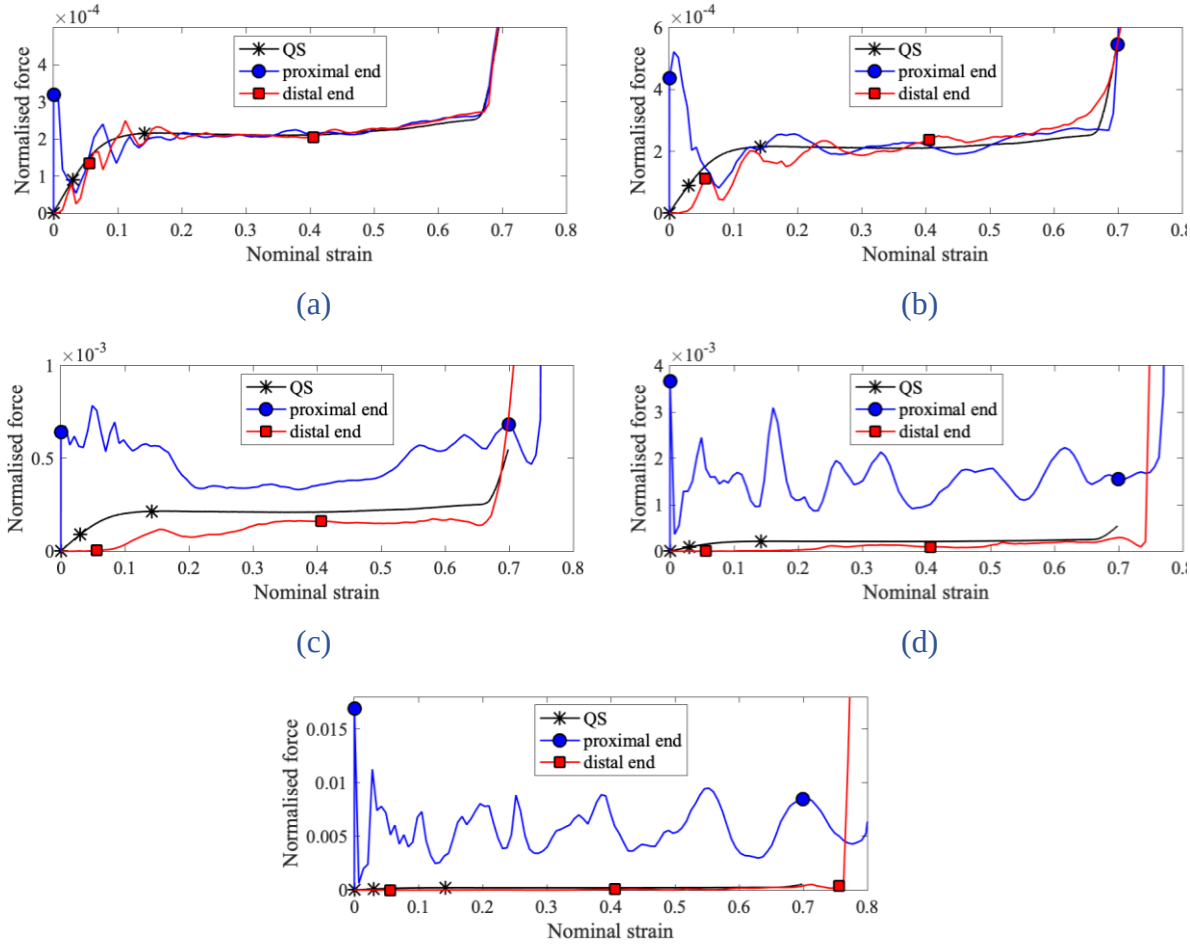


Figure 6.4 Force-displacement for 6×6×3 core with $\theta_0 = 60°$ for velocity of: (a) 5m/s; (b) 10m/s; (c) 25m/s; (d) 50m/s; and, (e) 100m/s

In contrast to the core with $\theta_0 = 60°$, even under low velocities, the force at the distal end is larger than the quasi-static value for a core with $\theta_0 = 150°$ (Figure 6.5). This is typical of Type II structures, where the lateral inertia effect can suppress the quasi-static deformation mode for a longer period, resulting in a large force transfer to the distal end. In contrast with

other Type II structures studied in literature (Tam, 1990; Tam and Calladine, 1991), this deformation mode does not seem to be associated with axial straining i.e. the full plastic squash load does not develop in the core. The theoretical squash load for the cross section of a single cell is 2.44kN (0.0109 normalised theoretical squash load), which is significantly larger than the initial peak force output at the support in Figure 6.5.

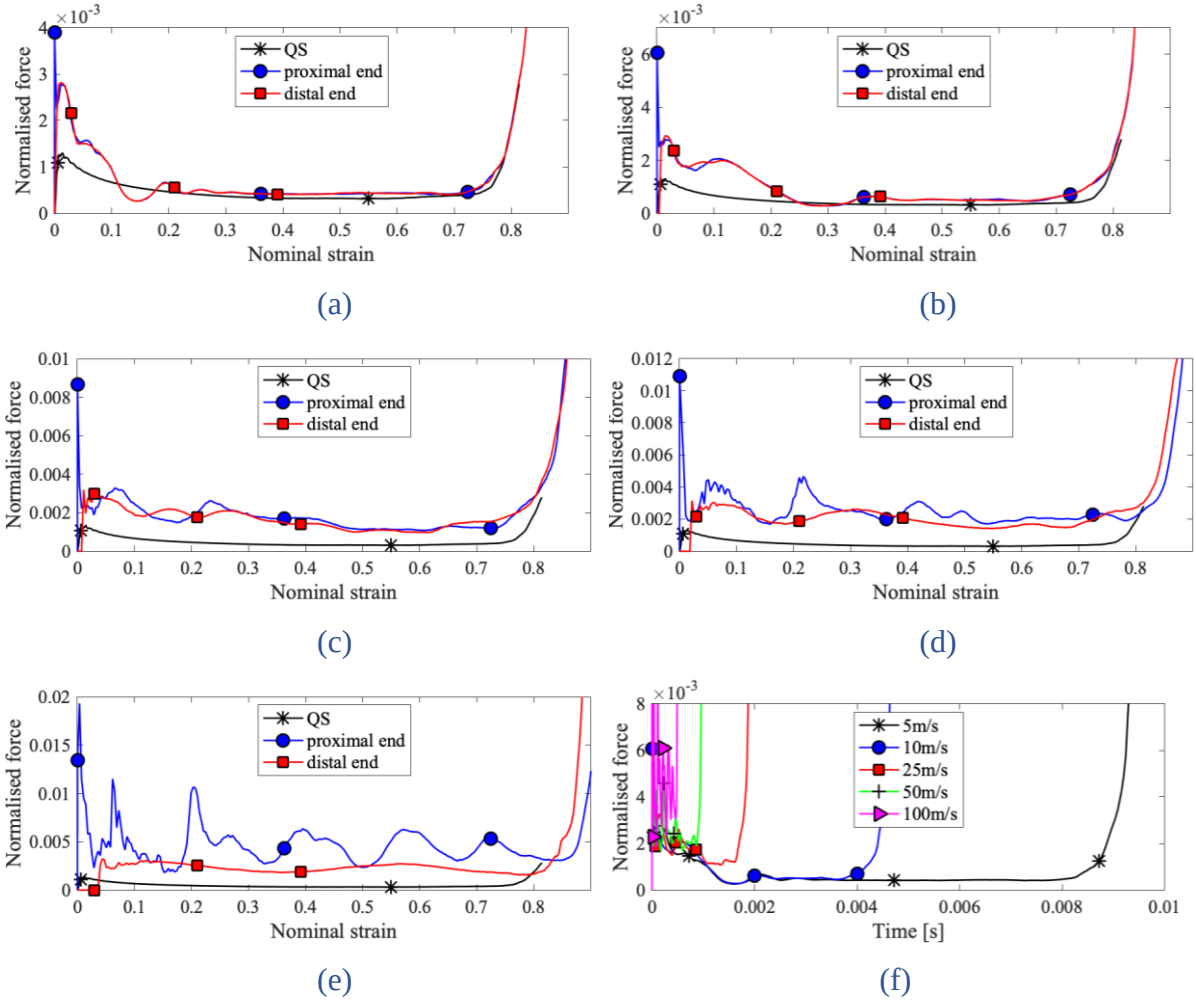


Figure 6.5 Force-displacement for 6x6x3 core with θ_0 =150° for velocity of: (a) 5m/s; (b) 10m/s; (c) 25m/s; (d) 50m/s; and, (e) 100m/s. (f) Force at distal end

The deformation of the core for 10m/s is shown in Figure 6.6. Rather than showing all units of the core, only the deformation of a representative central unit is provided for clarity. The plastic strain contours are plotted on the deformed geometry to highlight the locations where hinges form. In the initial stages, t < 9.8e-4s, the deformation is localised at the two ends

of the core and hinges form that are not in the location of the creases. Only after some initial period does the deformation become localised at the creases, resulting in the folding following the kinematics of the underling crease pattern.

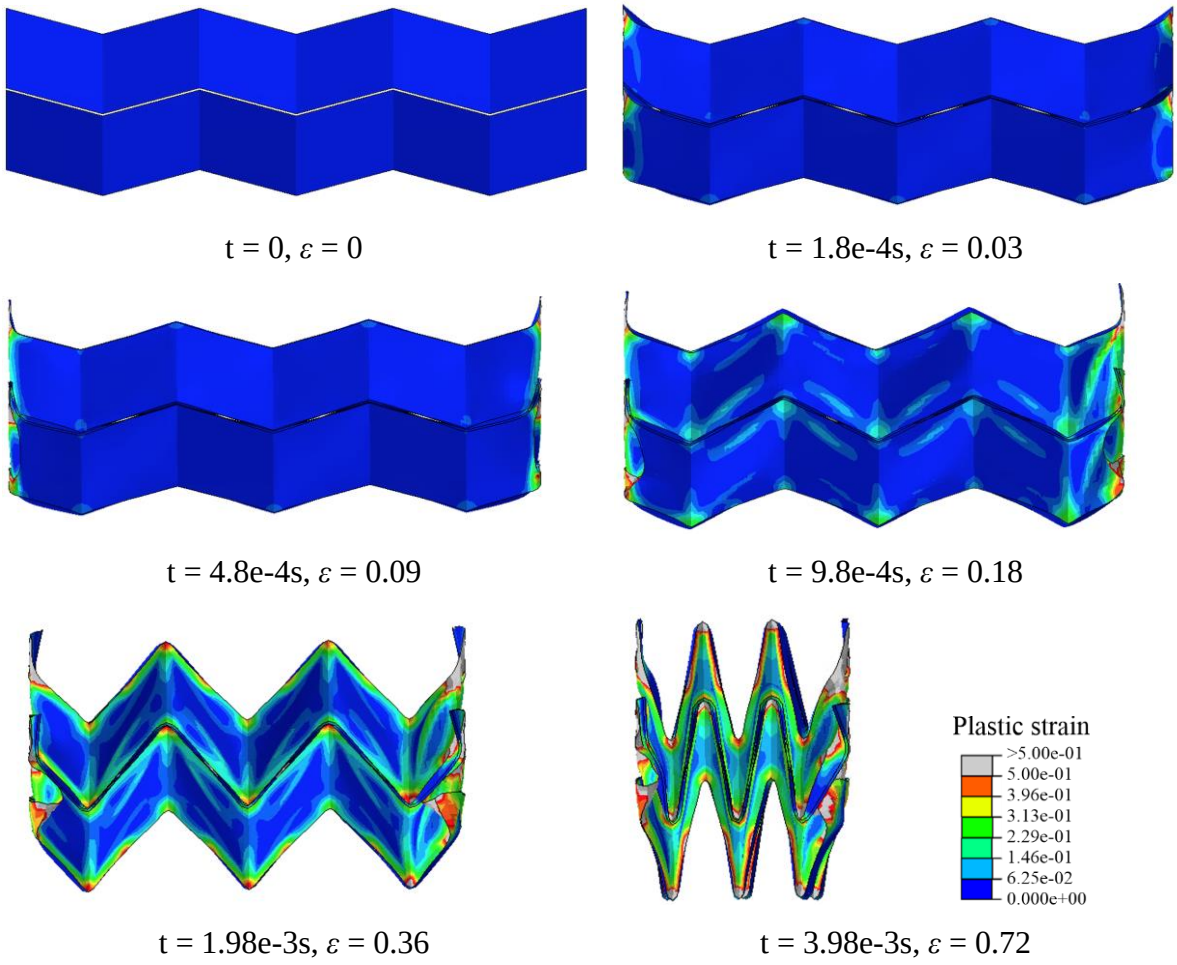


Figure 6.6 Deformation of representative central unit from the 6×6×3 core with θ_0 =150° when impacted with a rigid mass with constant velocity of 10m/s

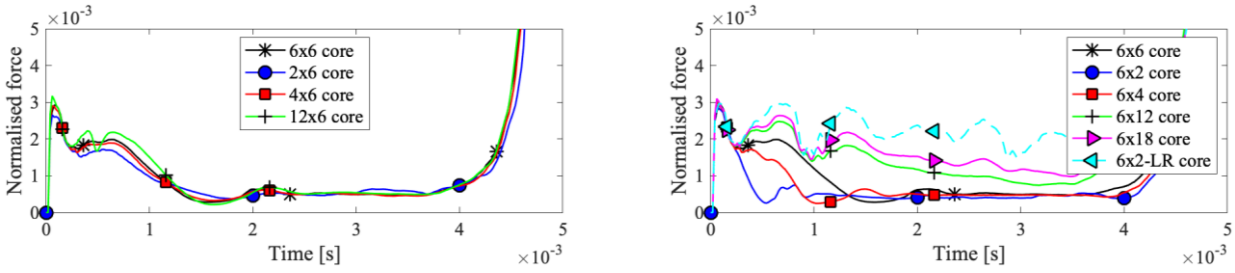
For 5m/s and 10m/s the force at the proximal and distal end are approximately equivalent. As the velocity increases the proximal force increases, again this is related to the axial inertia and will be discussed in greater detail in the following sections. At lower velocities, the force at the distal end reduces back to the quasi-static value after some initial deformation. Interestingly, when plotting the force histories at the distal end for the velocities simulated the curves collapse roughly into one curve (Figure 6.5(f)). The point at which the force at the distal end returns to the quasi-static value appears to be constant, and is most likely associated with

the time required for significant lateral acceleration to occur at the support, allowing the units in contact with the support to fold following the path prescribed by the crease pattern. This will be examined in detail in section 6.3.2. While the core with θ_0 = 150° shows lateral inertia sensitivity, again, the force at the support appears to be velocity insensitive.

6.3.2 Effect of number of units perpendicular to the loading direction (in-plane)

In the previous section the general behaviour of 6×6 cores with variable θ_0 were investigated when subjected to a range of impact velocities. In this section the effect of the number of units in the *m* and *n* direction will be investigated (Figure 6.2). Here, the force at the distal end is of primary interest as it provides an indication of the lateral inertia effects with minimal axial inertia influence. In the previous section it was shown that the response at the distal end appears to be velocity insensitive, therefore, in this section, only 10m/s will be simulated. The response of cores with θ_0 = 150° but alternative $m \times n$ for an initial impact velocity of 10m/s are provided in Figure 6.7. Figure 6.7(a) shows the influence of cores with alternative *m* values. From the figure it is seen that the time to return to the quasi-static value does not change significantly for the cores. However, the initial and secondary peak magnitudes are influenced, with larger number of units in the *m* direction resulting in larger values for both. However, the overall difference in response is not too large. This illustrates that the lateral inertia effect in the *m* direction, while influencing the behaviour, does not appear to be very significant for the geometry simulated.

The effect of the number of units in the *n* directions results in a significant change in the force transferred to the distal end (Figure 6.7(b)). In the figure, all cores appear to have similar behaviour during the first peak, however, after this initial peak, the behaviour deviates significantly. The core with smallest *n* returns to the quasi-static value in the shortest amount of time and the unit with the largest *n* never returns to the value associated with the quasi-static force.



(a) (b)

Figure 6.7 Normalised distal force histories for core with alternative number of units in the: (a) m direction; and, (b) *n* direction with θ_0 =150°

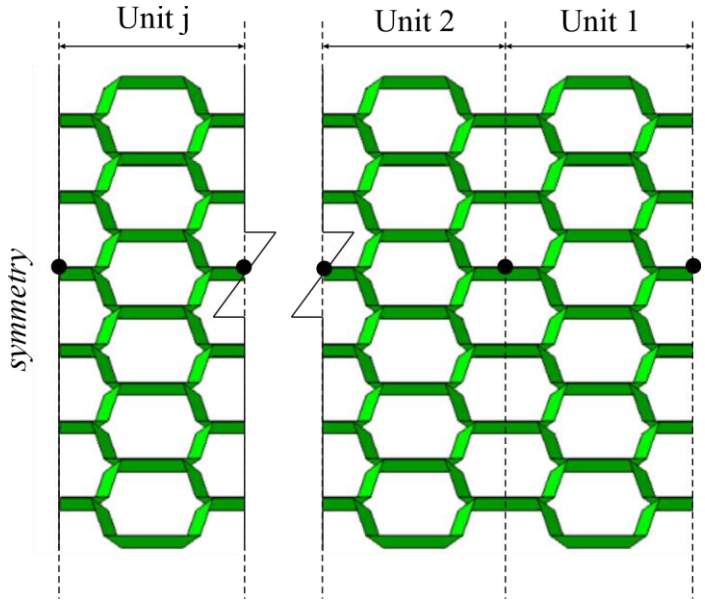


Figure 6.8 In-plane length change measurement locations of units loaded in the out-of-plane direction

To investigate the influence of the lateral inertia on the force at the distal end, the length change of each unit in the *n* direction is plotted over the force histories at the distal end in Figure 6.9. The length change of the unit is taken as the absolute value of the relative distance between either side of the unit (Figure 6.8). Unit 1 is labelled as the unit at the free edge and unit j = *n/2* is the unit where symmetry conditions are applied (i.e. the centre of the core). The measurements from the simulations are taken at *m* = 3.

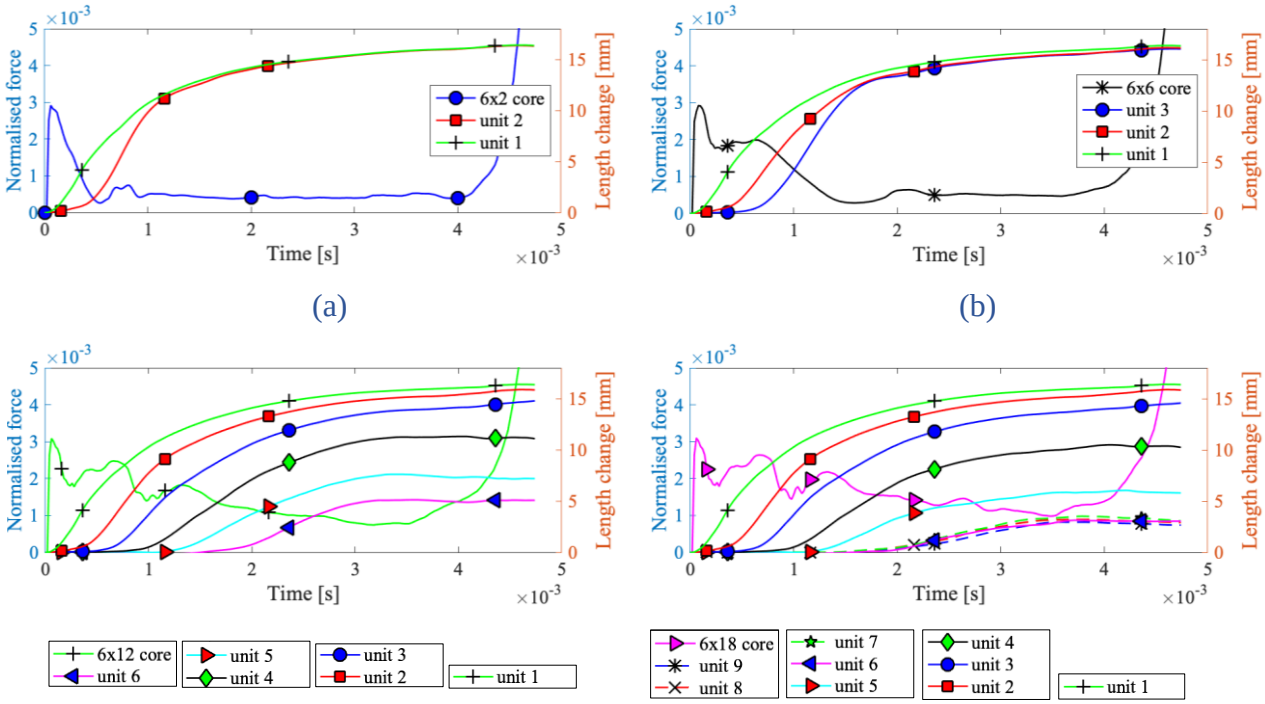


Figure 6.9 Force-histories and length change of units for: (a) 6×4 core; (b) 6×6 core; (c) 6×12 core; and, (d) 6×18 core, with $\theta_0 = 150°$

From Figure 6.9(a, b), the time at which the force at the distal end returns to the quasi-static force is approximately the time at which all the units begin to have similar length changes. For the 6x4 and 6×6 cores this is approximately 0.001s and 0.0016s respectively. Additionally, the second peak force for the 6x6 core begins to reduce when unit 3 begins to change its length significantly at 0.0006s (Figure 6.9(b)). In order to visualise this, the deformation of the units in contact with the distal end at certain times are provided in Figure 6.10 for the 6×6 core. Originally the deformation is greater for unit 1, however, after some time, the deformation propagates to the cells in the middle of the core, resulting in approximately uniform deformation.

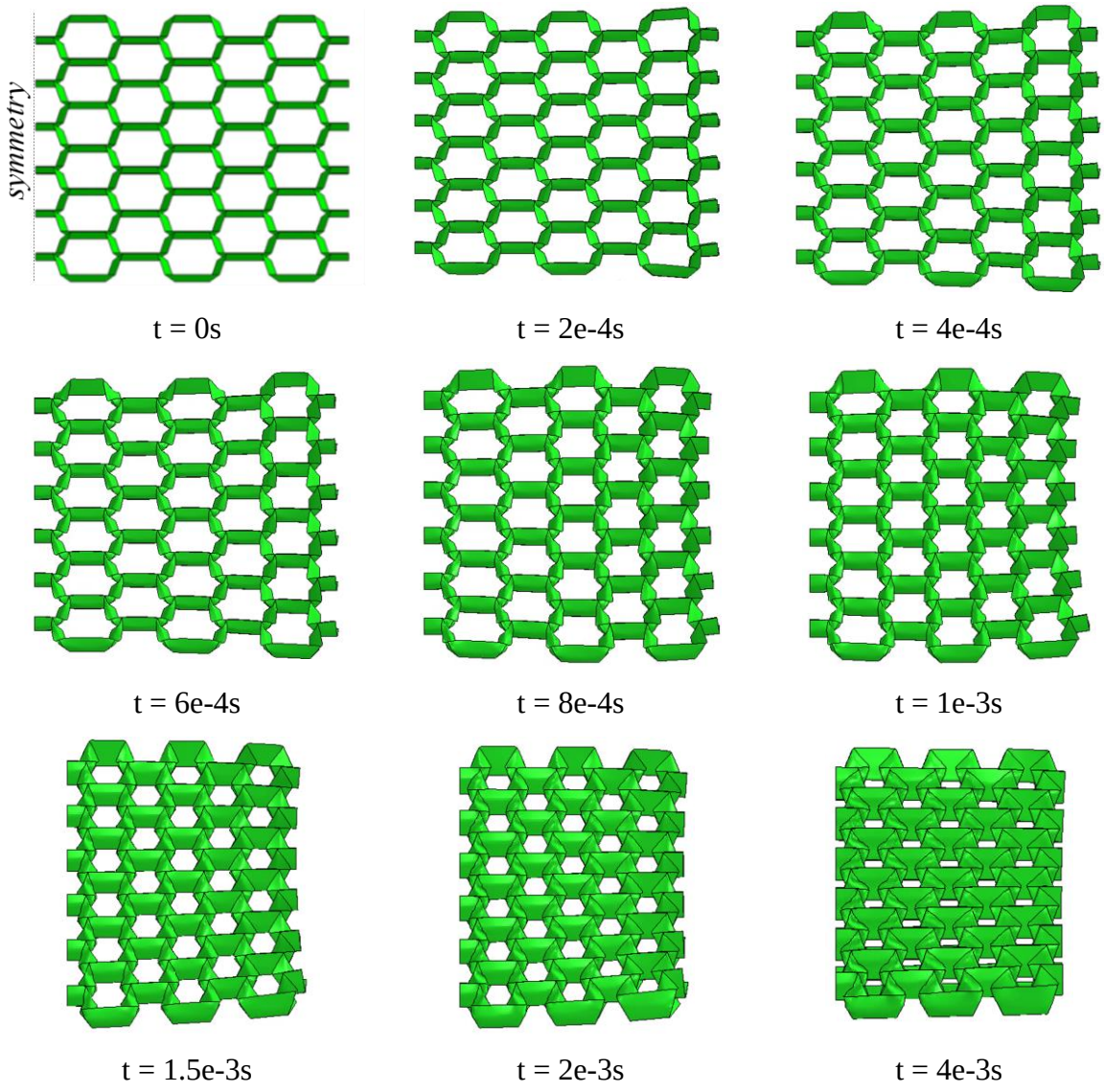


Figure 6.10 Deformation of 6x6 core with $\theta_0 = 150°$

In contrast, for the 6×12 and 6×18 cores, although some lateral displacement occurs, it reduces significantly away from unit 1. This results in a deformation mode that deviates from the one prescribed by the crease pattern. This is clear observed in Figure 6.11, where the units in the centre of the core have a smaller γ, whereas γ for units close to the free edge have increased significantly, forming re-entrant honeycomb units.

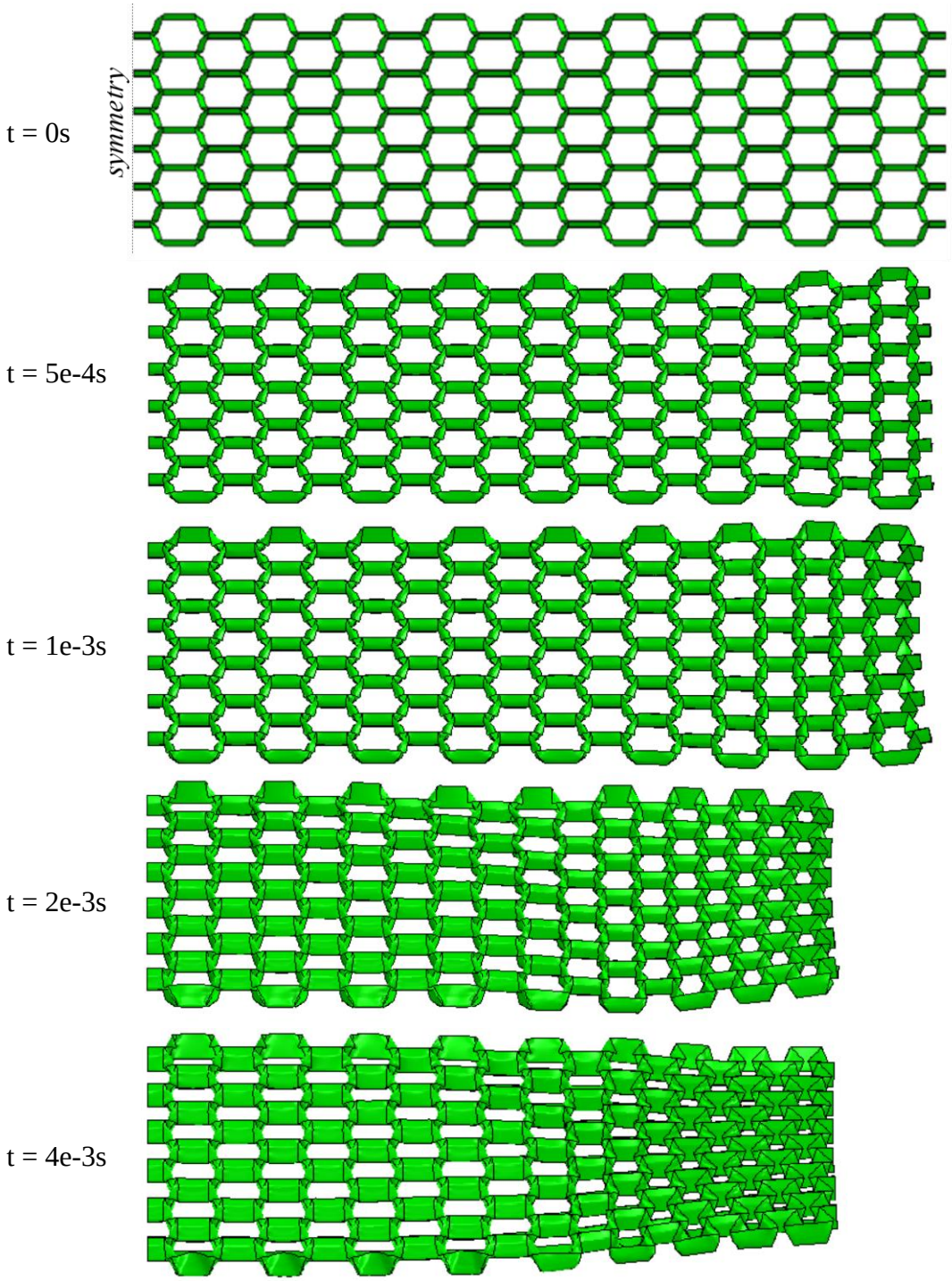


Figure 6.11 Deformation of 6×18 core with θ_0 =150°

In Figure 6.7, the second peak force at the distal of the core increases with increasing number of units in the *n* direction. As discussed above, this increase appears to be associated with the lateral restraint provided by accelerating the units in the lateral direction. The upper limit of the distal force may be approximated by simulating a 6×2 core with symmetry

conditions on one edge and lateral restraint on the other in the *n* direction. The results for these boundary conditions are provided in Figure 6.6 (6×2 LR) and show that a 6×2 core with additional lateral restraints at the free end has an equivalent initial peak to the other cores, followed by a second peak with a similar magnitude to the cores with more *n* units. It is assumed that as *n* increases the cores behaviour will tend towards this upper limit.

The analysis in the previous section showed that the force at the distal end of a 6×6 core with $\theta_0 = 60°$ did not exhibit lateral inertia sensitivity, with the force at the distal end remaining below the quasi-static value for the velocity ranges simulated. As shown above for $\theta_0 = 150°$, increasing the number of units in the *n* direction increases the lateral inertia effect. Additionally, the upper bound may be found by applying lateral restraint to a 6×2 core. Figure 6.12 provides the force at the distal end for a 6×24 core and a 6×2 laterally restrained core (6×2 LR) with $\theta_0 = 60°$. The absolute length change of selected units for the 6×24 core is also provided on a separate y-axis. Although the force at the distal end of the 6×6 core remains below the quasi-static value, increasing the number of units in the *n* direction can result in a significantly larger force transferred to the support, with the upper limit approximately resulting in an 80% increase over the quasi-static value for the geometry simulated. For the 6×24 core, the lateral displacement of the core propagates to the internal units relatively quickly, resulting in a reduction of the force back to the quasi-static value.

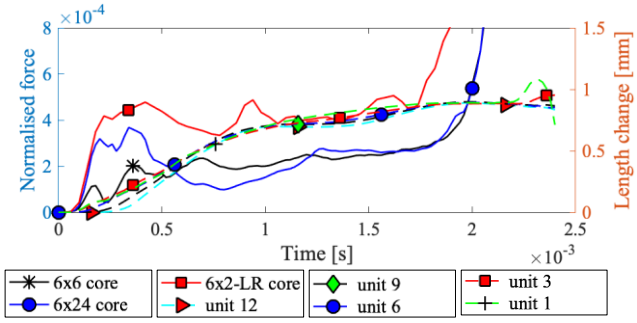


Figure 6.12 Force-histories and length change of units at the distal end for alternative *n* values when $\theta_0 = 60°$

This behaviour is different to other Type I structures, where the maximum force transferred to the distal end is limited by the quasi-static strength of the unit in contact with the support. Therefore, although when θ_0 = 60° the core exhibits a relatively flat-topped curve quasi-statically, under impact, the lateral inertia effect of the core may result in a larger force than the quasi-static force being transferred to the support. However, it should be noted that the core is less sensitive to inertia when θ_0 = 60° when compared with θ_0 = 150° as a far larger number of units must be placed along the *n* direction to increase in the force at the distal end above the quasi-static value.

6.3.3 Effect of α

In the previous sections it was observed that the time required for the response to drop back down to the force associated with the quasi-static value at the distal end appears to be dependent on lateral inertia effect. Specifically, in ordered to follow the quasi-static deformation mode, the units accelerate in the lateral directions and there appears to be a time required for this motion to become uniform and allow the units in contact with the distal end to deform following the crease pattern. Therefore, the rate-of-change of the lateral lengths in the initial configuration may influence the time required for this to occur. It should be noted that rotation of some facets also occurs, which would result in additional rotational inertia, however this is not considered in the following analysis. The equations for the length and width of a core made up of *m* x *n* units is provided with respect to the dihedral angle as follows.

$$L = n\left(2l_1 + l_3 + 2l_2\cos\gamma\right) = n\left(2l_1 + l_3 + 2l_2\frac{1-\tan^2\alpha\cos^2\frac{\theta}{2}}{1+\tan^2\alpha\cos^2\frac{\theta}{2}}\right) \tag{6.3}$$

$$W = m\left(2l_2\sin\gamma + a\cos\frac{\theta}{2}\right) = m\left(2l_2\frac{2\tan\alpha\cos\frac{\theta}{2}}{1+\tan^2\alpha\cos^2\frac{\theta}{2}} + a\cos\frac{\theta}{2}\right) \tag{6.4}$$

The rate-of-change of the length and width with respect to θ can then be found as follows.

$$\frac{dL}{d\theta} = \frac{4nl_2 \tan^2\alpha \cos\frac{\theta}{2}\sin\frac{\theta}{2}}{\left(1+\tan^2\alpha\cos^2\frac{\theta}{2}\right)^2} \tag{6.5}$$

$$\frac{dW}{d\theta} = m\left(\frac{2l_2\tan\alpha\sin\frac{\theta}{2}\left(\tan^2\alpha\cos^2\frac{\theta}{2}-1\right)}{\left(1+\tan^2\alpha\cos^2\frac{\theta}{2}\right)^2} - \frac{a\sin\frac{\theta}{2}}{2}\right) \tag{6.6}$$

Now, for an initial dihedral angle, θ_0, the rate-of-change of the lateral dimensions should be maximised with respect to α. These expressions are provided below.

$$\frac{d\left(\frac{dL}{d\theta}\right)}{d\alpha} = \frac{8nl_2\sin\frac{\theta_0}{2}\cos\frac{\theta_0}{2}\tan\alpha\sec^2\alpha\left(1-\tan^2\alpha\cos^2\frac{\theta_0}{2}\right)}{\left(1+\tan^2\alpha\cos^2\frac{\theta}{2}\right)^3} \tag{6.7}$$

$$\frac{d\left(\frac{dW}{d\theta}\right)}{d\alpha} = \frac{2ml_2\sin\frac{\theta_0}{2}\sec^2\alpha\left(6\tan^2\alpha\cos^2\frac{\theta_0}{2}-\tan^4\alpha\cos^4\frac{\theta_0}{2}-1\right)}{\left(1+\tan^2\alpha\cos^2\frac{\theta}{2}\right)^3} \tag{6.8}$$

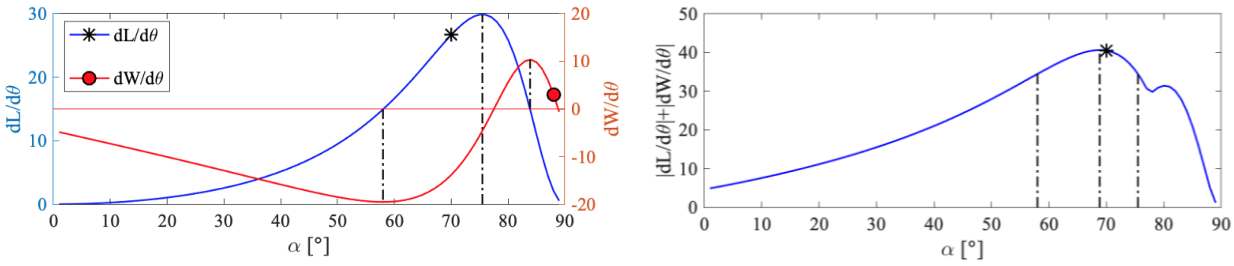
The α's that maximise the rate-of-change can be found by setting the above equations equal to 0 and solving. The below expressions provide the α solutions for the length, α_L, and width, α_W, direction respectively.

$$\tan\alpha_L = \frac{1}{\cos\frac{\theta_0}{2}} \tag{6.9}$$

$$\tan\alpha_W = \frac{\sqrt{3\pm2\sqrt{2}}}{\cos\frac{\theta_0}{2}} \tag{6.10}$$

Solving Eq.(6.9-10) when θ_0 = 150° results in one solutions for α_L, 75.5°, and two solutions for α_W, 83.9° and 58.0°. Eq.(6.5-6) are plotted with respect to α for θ_0 = 150° in Figure

6.13(a). The prediction for α_L and α_W are also provided. While $\alpha_W = 83.9°$ is a local maximum, $\alpha_W = 58.0°$ results in a larger rate-of-change globally.



(a) (b)

Figure 6.13 The influence of α on the rate-of-change of: (a) length and width; and, (b) absolute summation for $\theta_0 = 150°$

In the above analysis the rate-of-change is considered separately for the length and width directions. In reality the lateral inertia will be a combination of the rates-of-change in both lateral directions. Figure 6.13(b) provides a plot of the summation of the absolute values of Eq.(6.5-6). The α that produces absolute maximum was found to be $\alpha_{LW} = 68.8°$. It should be noted that in the previous section the lateral inertia associated with the length change was dominant, therefore the combination of the two may not be in equal parts. Additionally, the analysis is only applicable for $\alpha = 70°$. The influence of the number of units in the m and n direction may be different for alternative α values.

Three cores with the same geometry as outlined in section 6.1 but alternative α's were simulated to explore if the rate-of-change of lengths in the initial configuration alters the time at which the force at the distal end drops to the quasi-static value. θ_0 for each of the cores was set to 150°. The minimum value of α for the initial crease pattern lengths can be calculated using the equation below.

$$\alpha \geq \tan^{-1}\left(\frac{2a}{l_3^I}\right) = 44.4° \tag{6.11}$$

The α's selected were: 48.0°; 58.0°; and, 75.5°. A core with $\alpha = 68.8°$ was not simulated as it is relatively close to the original α modelled and is therefore expected to have relatively

similar behaviour. α = 48.0° was chosen to simulate a core with a lower calculated rate-of-change of lengths than the other simulated cores. Interestingly, α = 58.0° and α = 75.5° have the same absolute rate-of-change summation of the lengths, albeit the contribution of the length and width is different. The analytical predictions for the quasi-static strength of the cores from Eq.(4.17-18) are provided in Figure 6.14(e) along with the quasi-static response for α = 70° from the numerical simulation (provided previously in Figure 6.3(a)). The analytical prediction for α = 70° matches the numerical model well. Additionally, comparing the analytical predictions for the alterative α's indicates that the quasi-static response for each core is not too dissimilar. The cores simulated are shown in Figure 6.14(a-d). Again, symmetry boundary conditions are applied in the simulations, and they are therefore equivalent to a 6×6 core. The general dimensions of a single unit are provided in Table 6.2.

Table 6.2 Dimensions of a single unit

α [°]	$\bar{\rho}$ [-]	H [mm]	L [mm]	W [mm]	dL/dθ [mm]	dW/dθ [mm]
70.0	0.0152	18.4	37.2	17.6	26.6	-13.9
48.0	0.0199		45.5	11.0	8.4	-18.0
58.0	0.0167		43.2	13.8	14.9	-19.5
75.5	0.0168		31.9	18.5	29.9	-4.6

Again, in the analysis in section 6.3.1, the effect of the impact velocity was shown to have negligible effect on the force at the distal end, therefore only an initial impact velocity of 10m/s was simulated. The force at the distal end for each core is provided in Figure 6.14(f).

Figure 6.14(f) shows that the core with α =70.0° requires the longest time to return to a force similar to the quasi-static level and the core with α = 48.0° has the shortest. The core with α = 58.0° returns to the quasi-static level with a more delayed response than the core with α = 48.0° but less than the core with α = 75.5°. The core with α = 75.5° has a similar response to α = 70°, however, the second peak is somewhat flattened out and reduced for α = 75.5°.

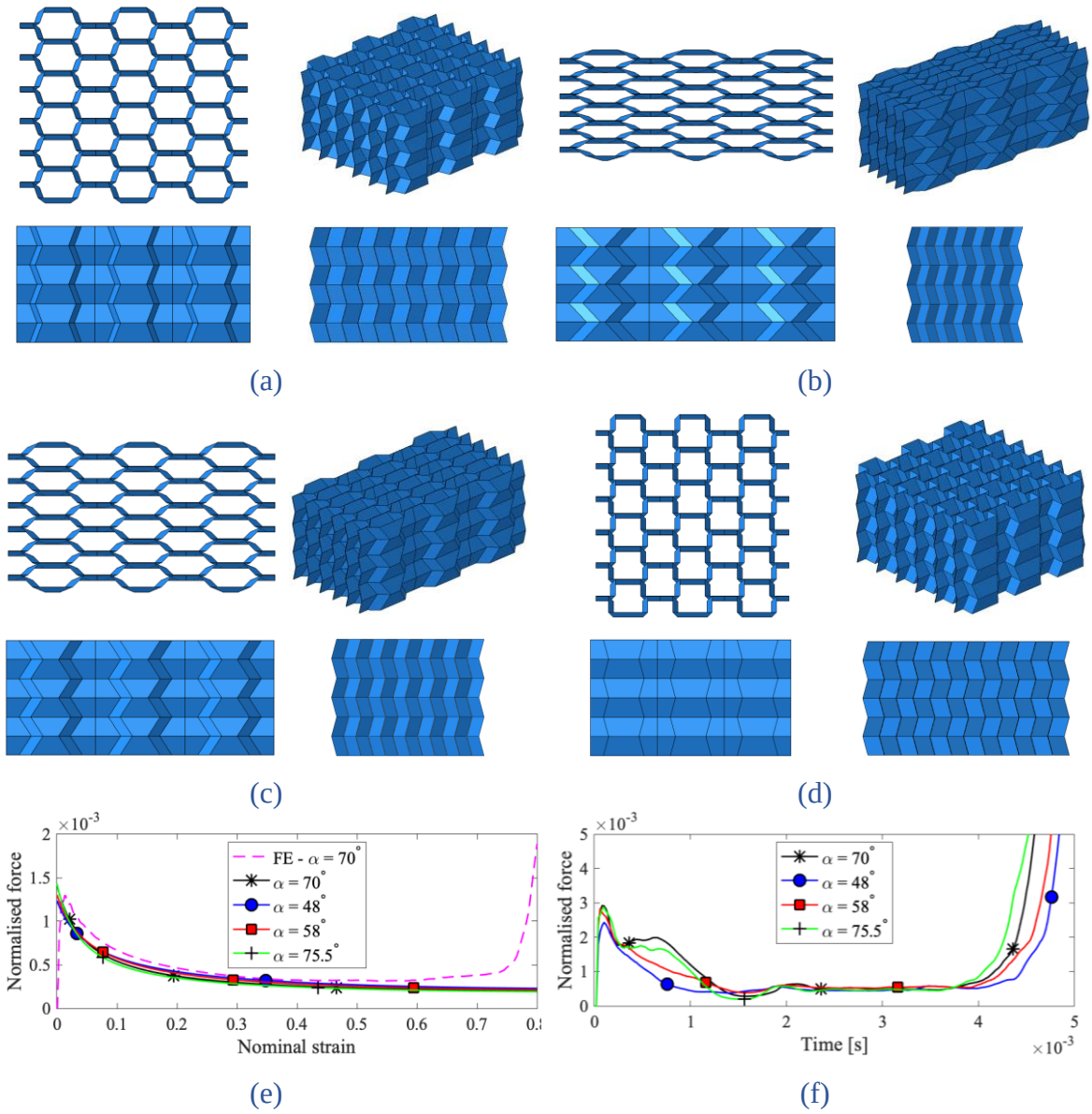


Figure 6.14 Cores with: (a) α = 70.0°;(b) α = 48.0°; (c) α = 58.0°; and (d) α = 75.5°. (e) Analytical quasi-static prediction for the cores; and, (f) force at the distal end of the cores for impact velocity of 10m/s

The cores with α = 58.0° and = 75.5° have the same absolute summation of the rate-of-change of length and width, although at different ratios (Table 6.2). α = 75.5° has a larger magnitude rate-of-change of length and α = 58.0° has a larger magnitude rate-of-change of width for their initial configuration. It therefore appears that the rate-of-change of length is more dominant, as the core with α = 75.5° response returns to the force associated with the

quasi-static level after a longer period. This agrees with the phenomena observed for the analysis of the effect that the number of units in the *m* and *n* direction have on the response.

The magnitude of the initial peak is similar for α = 70.0°, 58.0° and 75.5°, whereas the core with α = 48.0° shows a substantial reduction in the initial peak force. This additionally highlights that the lateral inertia of the core may not only affect the time at which the force drops down to the quasi-static level, but also the magnitude of the initial peak force.

Cores with approximately identical quasi-static behaviour may exhibit vastly different behaviour under dynamic impact due to the underlying kinematics of the crease pattern. The time for the response of the core to drop to the quasi-static level is quite difficult to predict as it is appears to be reliant on the topology of the core.

6.3.4 Effect of number of units along height

The effect of the number of units along the height is investigated in this section, again, with focus on the force transferred to the distal end of the core. 6×1 cores with symmetry condition (equivalent to a 6×2 core) and 3,20 and 40 units along the height were simulated subject to a constant impact velocity of 100m/s (Figure 6.15(c)). An impact velocity of 100m/s was selected to reduce the analysis time.

Figure 6.15(a, b) shows the force history for the three cores with different heights. As the height increases the time required for the stress to propagate to the distal end increases. The figure shows that the peak force at the distal end reduces with an increase in the number of units along the height.

To inspect this more closely, the force histories at different sections of the 6×2×40 core are provided in Figure 6.16. The force is taken at the distal end of several units where unit 1 corresponds to the unit that is impacted with the rigid mass and unit 40 is the unit in contact with the support. The close-up of the initial time-period shows a stepwise reduction in the peak force along the height of the core. This may be due to the effect of the stress-wave propagating

around a bend, resulting in reflection, transmission and the formation of bending waves similar to that found by Guo *et al.* (2010). While the peak force generally reduces along the height of the core, the force at the distal end of unit 35 increases when compared to the force at the distal end of unit 30. It is unclear why this occurs at this stage, although it may be a result of the reflection of the stress-wave from the support. After this initial propagation of stress, the force history at the distal end of the units tend towards the quasi-static value before the crushing front reaches the unit (Figure 6.16(a)).

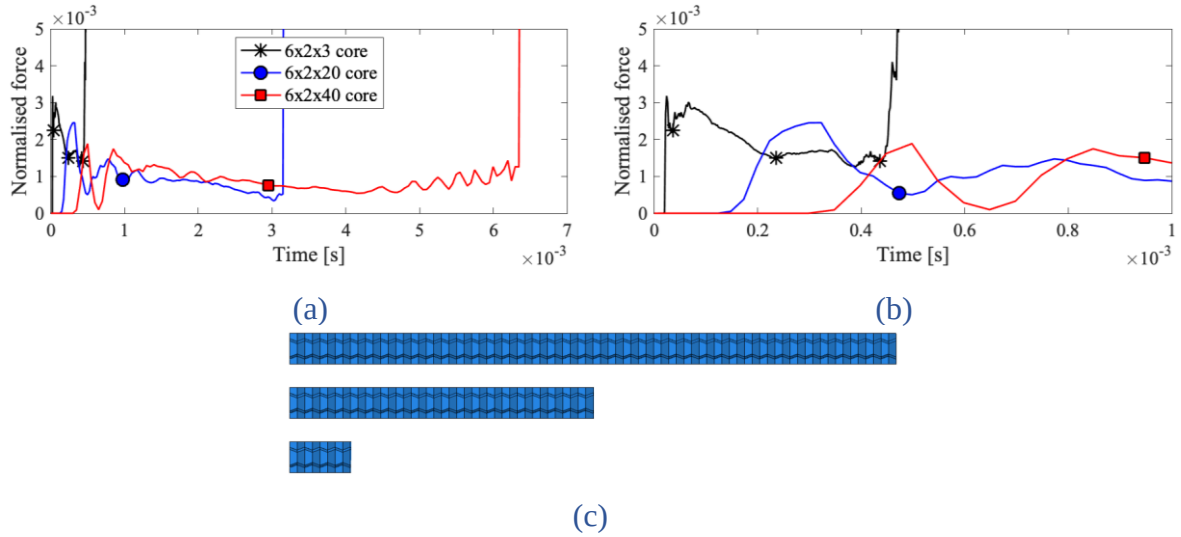


Figure 6.15 Force at distal end of a 6×2 core with alternative number of units along the height: (a) full range response; (b) zoomed in response; and (c) cores

A 6×6 core with 3, 20 and 40 units along the height was also simulated. Comparing the 6×6 core in Figure 6.17(a, b) with the 6×2 core in Figure 6.15(a, b), while the force at the support also decreases along the height for the 6x6 core, the magnitude appears to reduce. Guo *et al.* (2010) found that the flexural stiffness influenced the energy reflected and transmitted around a bend. For the origami honeycomb, the increase in lateral inertia with *n*, results in a greater lateral restraint which may result in a similar outcome as increasing the flexural stiffness. This is however outside the scope of this thesis and will not be pursued further here. Generally, increasing the number of units in the *n* direction appears to reduce the reduction in force as it travels along the height of the core.

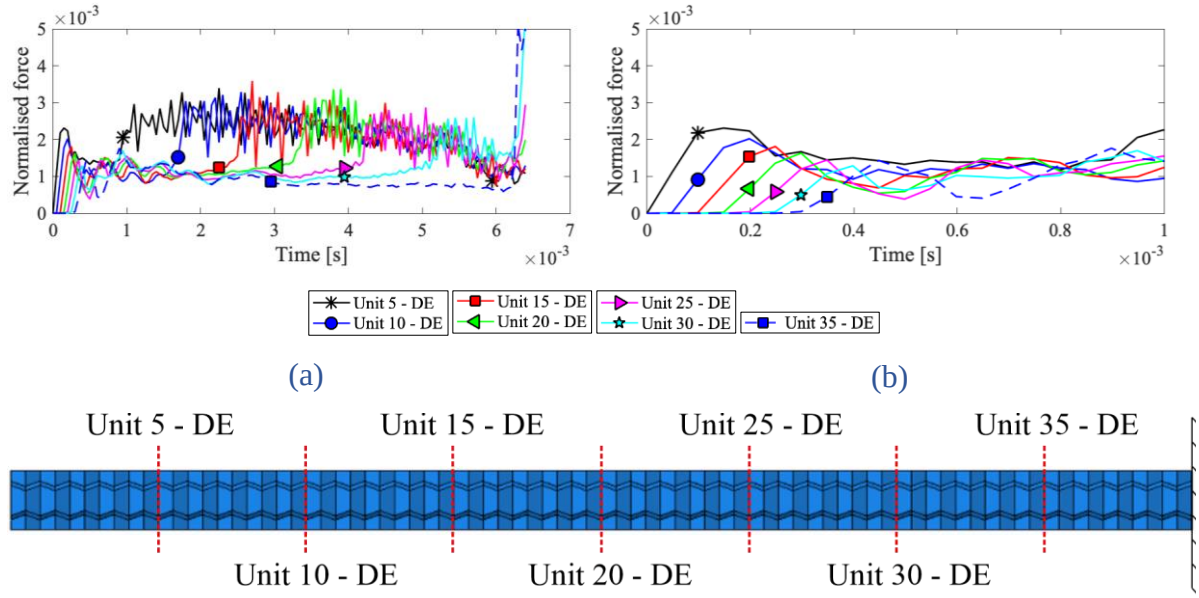


Figure 6.16 Force at different sections for the 6×2×40 core: (a) full range response; (b) zoomed in response; and (c) section locations

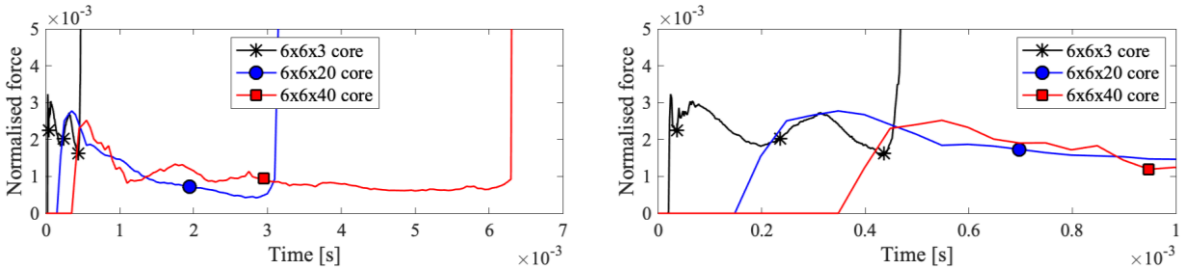


Figure 6.17 Force at distal end of a 6×6 core with alternative number of units along the height: (a) full range response; and (b) zoomed in response

The lateral deflection for the units in contact with the support is provided in Figure 6.18. Comparing this to Figure 6.9(b) for a 6×6×3 core with an impact velocity of 10m/s, the lateral deflection is more uniform in the initial stages for the core with 40 units along the height. This results in a reduction in the second peak magnitude when compared to the 6×6×3 core. Increasing the number of units along the height results in a more uniform lateral deformation in the initial stages resulting in a reduction in the lateral inertia effects.

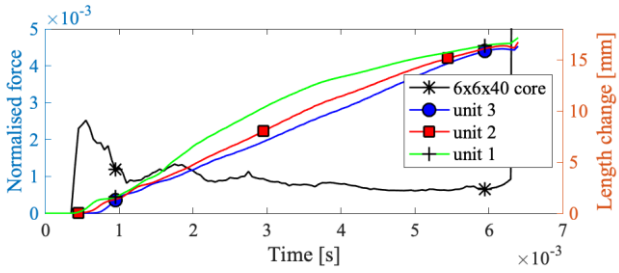


Figure 6.18 Distal force-history and length change of units of the 6×6×40 core with θ_0 = 150°

6.4 Analytical model

The dynamic behaviour of the core was found to be greatly influenced by the initial geometry, number of units in the lateral direction and the number of units along the height. The initial response of the core is sensitive to lateral inertia. In this phase, the force transferred by the units to the support may be larger than the quasi-static force due to the suppression of the quasi-static deformation mode. Following this phase, assuming the core hasn't been completely crushed by this point, the force returns to one associated with the quasi-static value.

In this section, an analytical model will initially be developed for the force transferred to the distal end. This is important for design purposes as it provides an estimation of the force that can be transferred to a supporting structure. Additionally, when developing analytical models for the force at the proximal end, the force at the distal end of the units is required. Following this, analytical models for the force at the proximal end of the core will be pursued. To simplify the problem, an analytical model will initially be developed for the core with geometry outlined in section 6.1 when θ_0 = 150°.

6.4.1 Force at distal end

Even under low velocity impact, the initial force transferred to the distal end may be larger than the quasi-static load. Figure 6.6 shows that the initial deformation mode when subjected to impactor velocity of 10m/s does not follow the crease pattern. In section 6.3.2 it was shown that this higher initial force was approximated well by a 6×2 core that was laterally restrained.

In Figure 6.6 the deformations are localised at both ends of the core. The initial portion of the force-displacement behaviour of the 6×2×3 core subjected to quasi-static loading is provided in Figure 6.19 with and without lateral restraint (LR). In the simulation for the LR core, the mesh was refined to an element size of 0.2mm at both ends. This refinement was applied to observe the hinge line formation and propagation more closely.

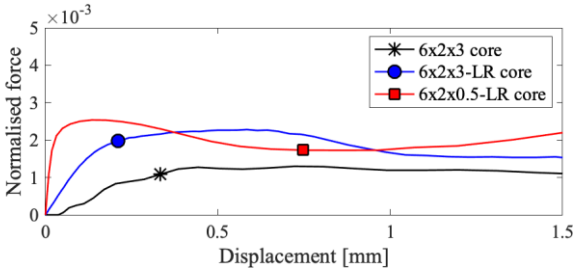


Figure 6.19 Quasi-static force-displacement for 6×2 cores with and without lateral restraint

The deformation plots with plastic strain contours at certain points are provided in Figure 6.20 for a central unit of the 6×2×3-LR core. The majority of the deformation appears to be localised at one end. Therefore, to simplify the simulation, only one half of a single unit was simulated with fixed boundary conditions (6×2×0.5-LR, Figure 6.21). The force displacement behaviour for this core is also provided in Figure 6.19. The initial peak is slightly larger when compared to 6×2×3-LR. This is most likely due to the increased stiffness caused by the fixed support. Notwithstanding, for the development of the super folding element, the deformation is similar (Figure 6.21) and therefore the 6×2×0.5-LR core simulation will be used to reduce the complexity associated with small deformations of the units along the core. For the development of the super-folding element one representative unit will be analysed, however it should be noted that the deformation is for a core where six units are attached together in the *m* direction.

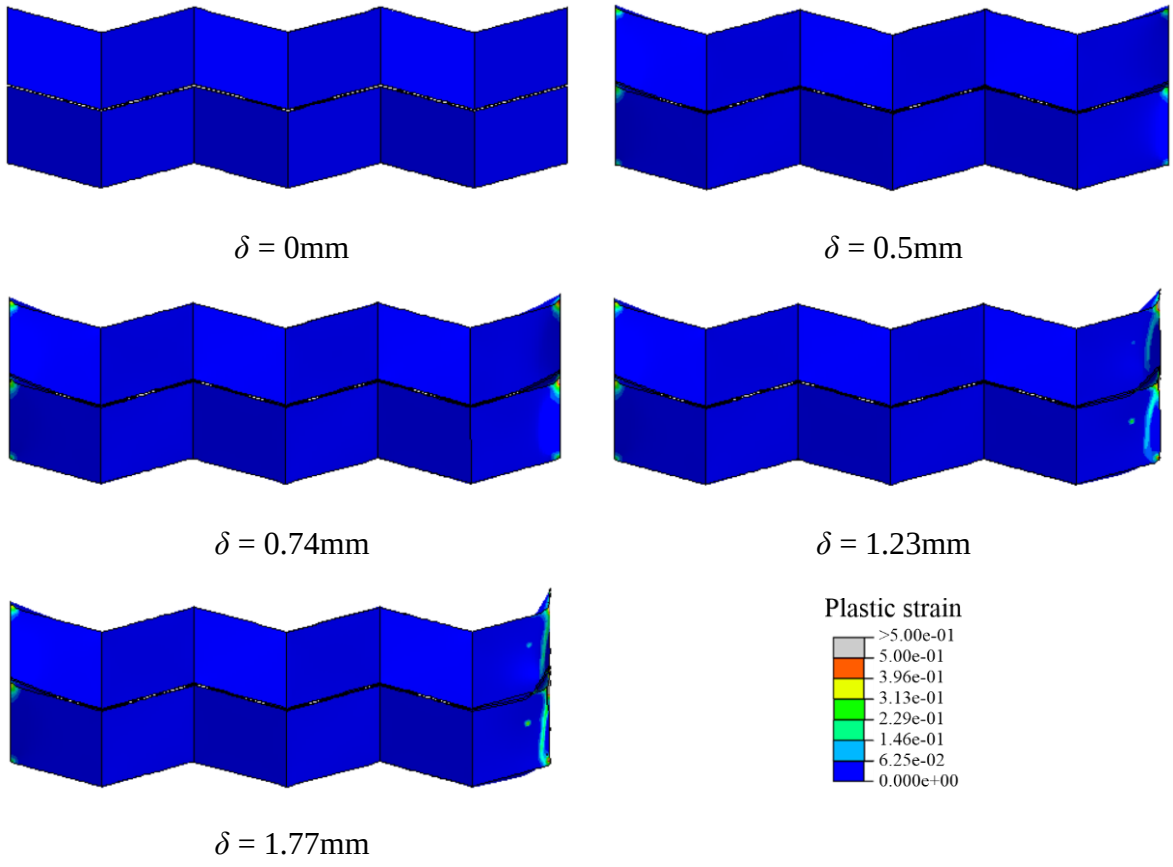


Figure 6.20: Initial deformation of a central unit of a 6×2×3-LR core under quasi-static loading

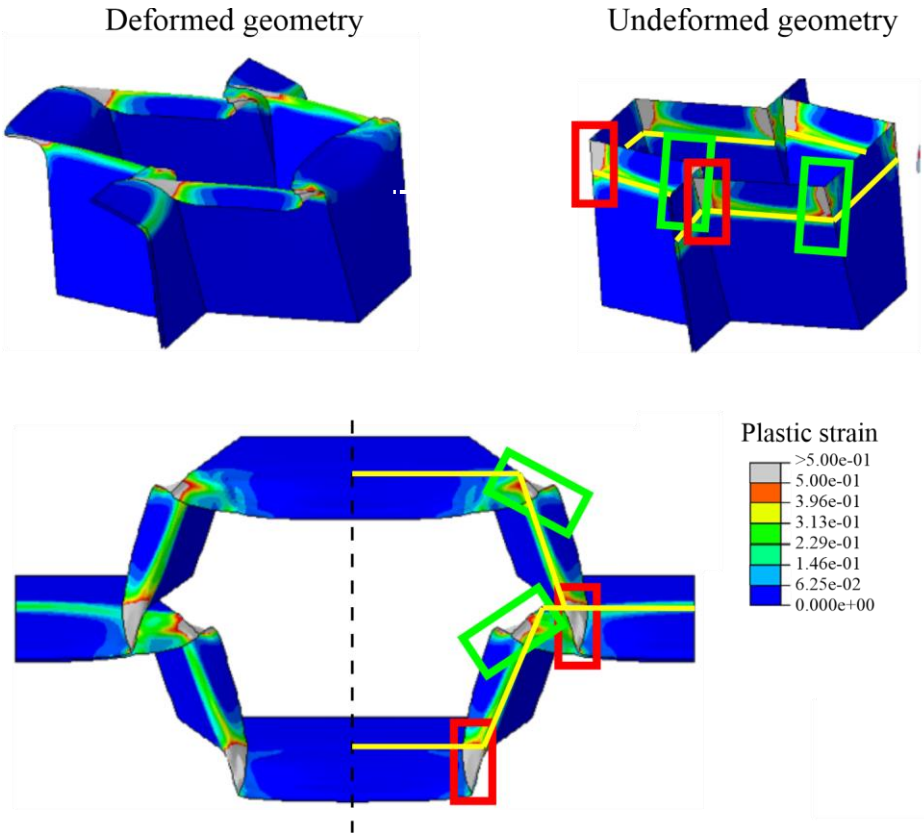


Figure 6.21 Deformation of a representative unit for the development of the super folding element

6.4.1.1 Super folding element

From the FE simulation it appears that the unit deforms through the formation of horizontal hinges some distance away from the end of the core. To accommodate the folding about these horizontal hinges, travelling hinges and facet stretching occurs in the corners where the facets of the crease pattern meet. These deformations are highlighted in Figure 6.21 with: yellow; green; and, red markers respectively. From these observations a super folding element was constructed and is shown in Figure 6.22. The energy consumed through this folding mode is described and calculated below assuming the material is rigid-perfectly plastic.

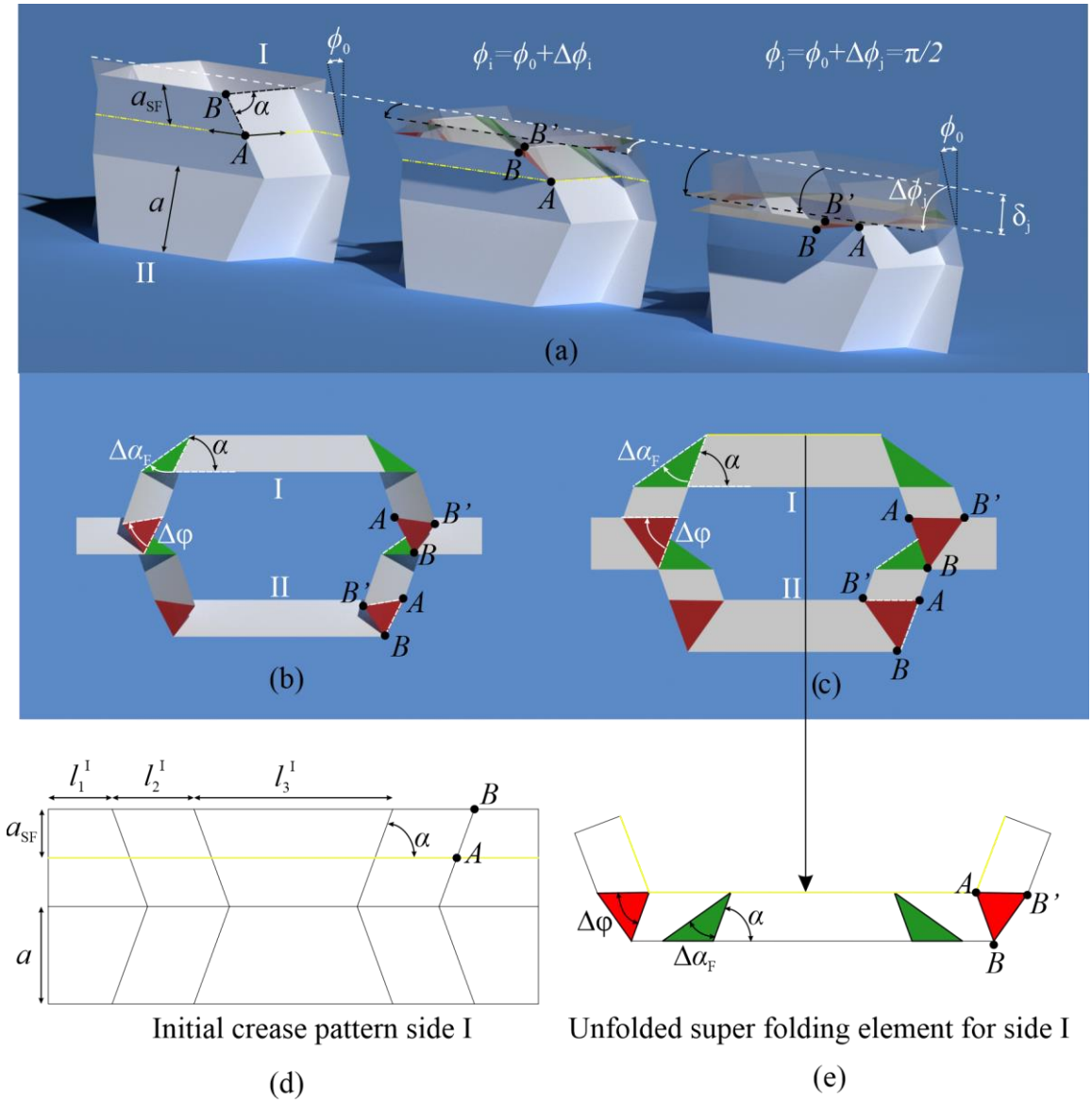


Figure 6.22: Assumed super folding element: (a) folding of super folding element; (b) top view in semi-folded state; (c) top view in locked state; (d) crease pattern of side I of a single cell; and, (e) unfolded super folding element for side I in locked state

- ***Horizontal hinge lines***

In Figure 6.23 the deformation contours are plotted on the deformed and undeformed geometry. The horizontal hinges are assumed to be stationary and form some distance a_{SF} along the crease pattern (Figure 6.22). Accounting for the double thickness at some sections (refer to chapter 4 section 4.3.2.6), the energy absorbed by rotating about the horizontal hinges, E_h, by an angle $\Delta\phi$ can be calculated as follows.

$$E_{\mathrm{h}} = 2mnM_{\mathrm{p}}\left(L_{\mathrm{s}} + 2l_{1\mathrm{c}}^{\min} + 2l_{3\mathrm{c}}^{\min} - \frac{l_{3\mathrm{c}}^{\min}}{m}\right)\Delta\phi \tag{6.12}$$

where $l_{1c}^{\min}$, $l_{3c}^{\min}$ are calculated as follows.

$$l_{1\mathrm{c}}^{\min} = \min\left(l_1^{\mathrm{I}} + \frac{a_{\mathrm{SF}}}{\tan\alpha}, l_1^{\mathrm{II}} - \frac{a_{\mathrm{SF}}}{\tan\alpha}\right) \tag{6.13}$$

$$l_{3\mathrm{c}}^{\min} = \min\left(l_3^{\mathrm{I}} - \frac{2a_{\mathrm{SF}}}{\tan\alpha}, l_3^{\mathrm{II}} + \frac{2a_{\mathrm{SF}}}{\tan\alpha}\right) \tag{6.14}$$

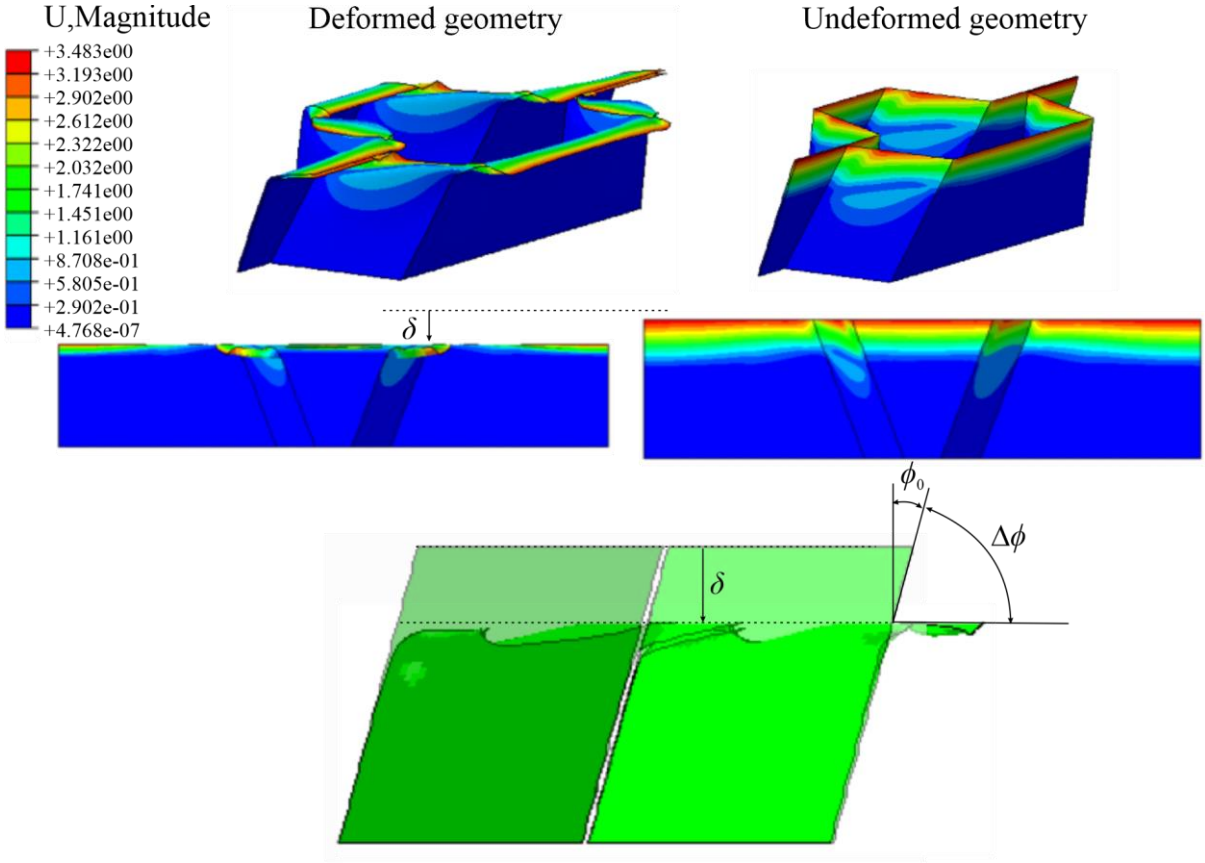


Figure 6.23 Horizontal hinge line definition for the super folding element

One thing to note here is that the lengths l_1, l_2, l_3 appear to have a strong influence on the location a_{SF} where the horizontal hinges form. Ignoring the components of energy absorbed at the corners for a moment, if we equate the energy consumed by the rotation of the horizontal hinges with the work done by the force F, we can find an equation for the average force which is provided below. Where ϕ_0 is defined from the initial geometry using Eq.(4.10).

$$F_{avg} = \frac{2mnM_p\left(L_s + 2l_{1c}^{min} + 2l_{3c}^{min} - \frac{l_{3c}^{min}}{m}\right)\Delta\phi}{a_{SF}\left(\cos\left(\phi_0 + \Delta\phi\right) - \cos\left(\phi_0\right)\right)} \tag{6.15}$$

The average force is inversely proportional to the distance a_{SF} where the horizontal hinges form. Therefore, the minimum force occurs at the maximum a_{SF} value, which is equal to half the height of the cell ($a_{SF} = a$). For the cell geometry above, the hinge lines form at a smaller value of a_{SF}. This is due to the energy consumed at the corners being proportional to $a_{SF}{}^2$, which is shown later in this section. However, in the scenario where the l_1, l_2, l_3 lengths are much larger, rather than horizontal stationary hinges forming in the facets, the hinges form at some angle, where near the corner the a_{SF} length, $a_{SF,c}$, is much smaller than in the middle of the facet, where, the a_{SF} length, $a_{SF,f}$, is at a maximum. Figure 6.24 shows the deformation for a core that has the l_1, l_3 length set to five times that of the dimensions outlined in section 6.1. For the purposes of the analysis it is assumed that the length are such that the stationary lines are horizontal and at only one height a_{SF}.

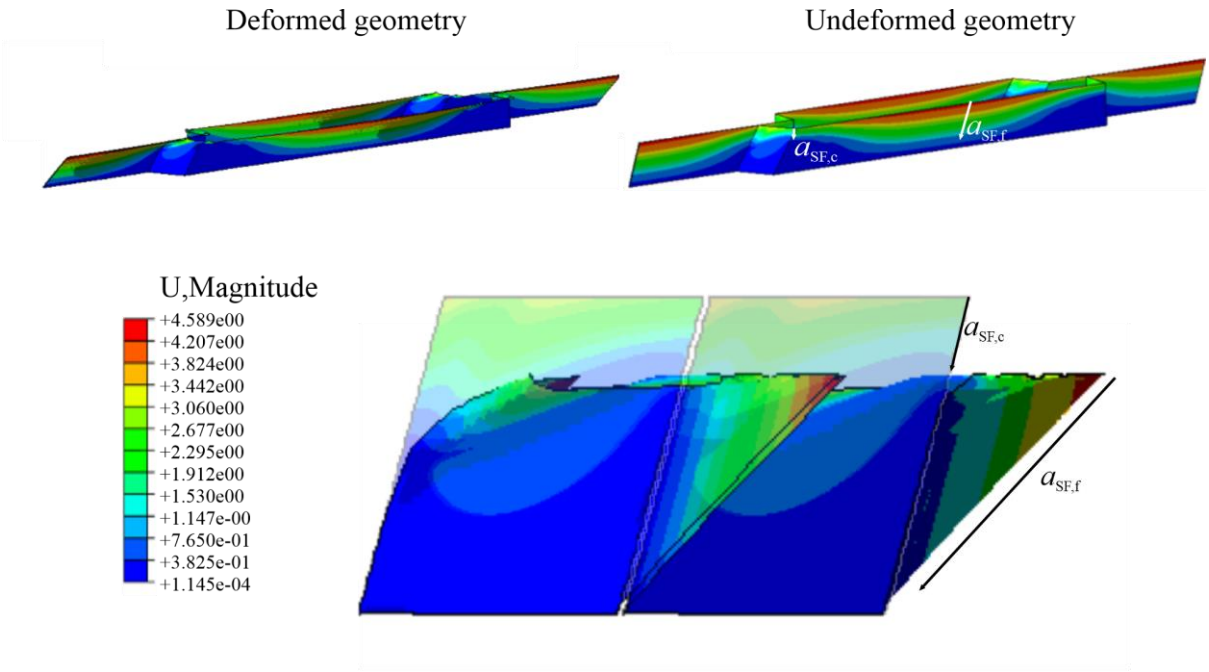


Figure 6.24 Effect of increasing l_1, l_3 on the location of the hinges

- ***Travelling hinge lines***

The progression of the travelling hinges is shown in Figure 6.25. In these figures the corner associated with the travelling hinges are shown in the green boxes.

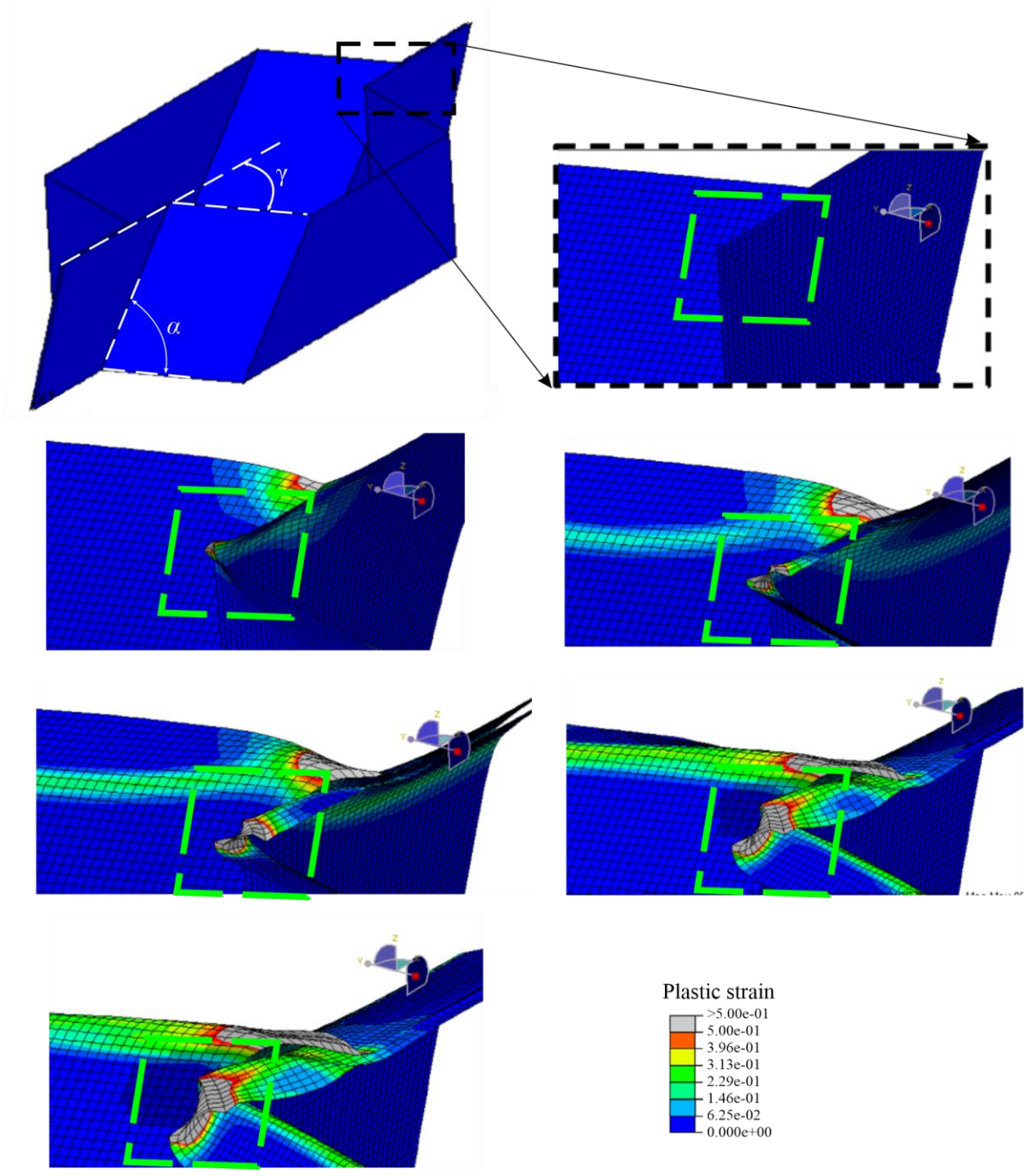


Figure 6.25 Travelling hinge formation and propagation

Kinematically, for this model to fold flat, the travelling hinge should sweep an angle $\Delta\alpha$ (Figure 6.22). This theorical value can be found by assuming that the γ remains constant during

the folding process with Eq.(4.11). The initial values for ϕ, α and γ are 15°, 70° and 70.83° respectively. To fold flat (ϕ = 90°) when the cell angle remains constant ($\gamma = \gamma_0$) the theoretical value for $\Delta\alpha$ is 34.48°. When measuring the angle from the simulation the angle is approximately 36° (Figure 6.26). It should be noted that there is some variation depending on how the angle is measured, however, generally it appears to be approaching this value.

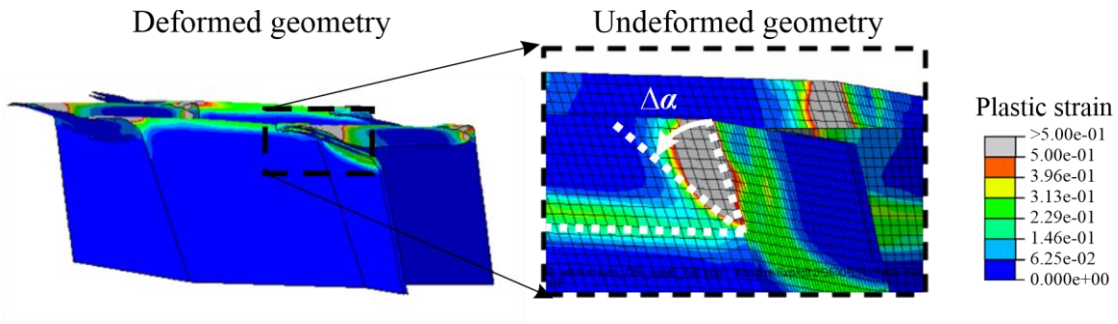


Figure 6.26 Angle swept by travelling hinge

The energy absorbed by the travelling hinge can be calculated with the below equation, where r is the radius the travelling hinge is bent and unbent around (refer to section 4.3.4.2 in chapter 4).

$$E_t = \frac{2mnM_p}{r}\frac{a_{SF}{}^2}{\tan\frac{\gamma}{2}}\sin\frac{\Delta\phi}{2}\cos\left(\phi_0 + \frac{\Delta\phi}{2}\right) \tag{6.16}$$

- ***Stretching***

At the other corners, rather than travelling hinges forming, it appears that stretching occurs. This is likely due to the attachment of two units resulting in parts of the facets having double thickness (Figure 6.27), which would increase the energy that is consumed by the travelling hinge by four.

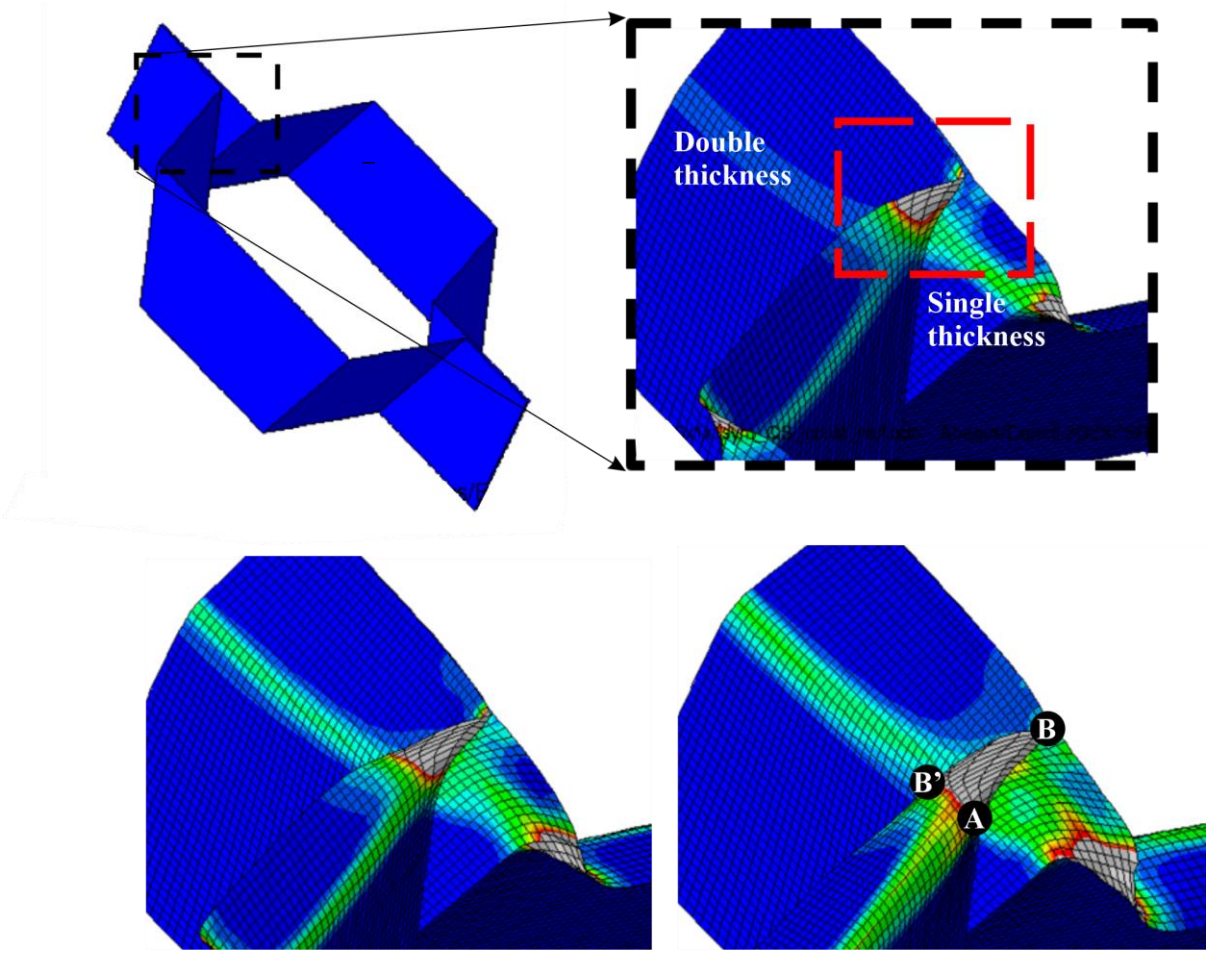


Figure 6.27 Stretching deformation for super folding element

The material is assumed to stretch by rotating an angle $\Delta\varphi$ about a central point (A), such that a point on the line that is originally at B moves to B' (Figure 6.22, Figure 6.27). The yield stress of the material is σ_y and is assumed to be perfectly plastic. The energy consumed by this stretching, E_s, can be found as follows.

$$E_s = \sigma_y t \int_{r=0}^{r=\overline{|AB|}=\frac{a_{SF}}{\sin\alpha}} r\Delta\varphi dr = \sigma_y t \Delta\varphi \left(\frac{r^2}{2}\right)_0^{\frac{a_{SF}}{\sin\alpha}} = \frac{\sigma_y t \Delta\varphi a_{SF}^2}{2\sin^2\alpha} \tag{6.17}$$

$\Delta\varphi$ can be found in terms of $\Delta\phi$ by tracking point B when it rotates by $\Delta\phi$ about two separate axis which are aligned with the l_2 and l_3 facets lengths (Figure 6.22).

In addition to stretching, there will be a stationary hinge between AB that rotates to allow the facets to fold flat (Figure 6.22). When the core is folding following the crease pattern, the relationship between β, ϕ and α is provided in Eq.(4.12). However, in this case the core is

essentially locked, and, to accommodate the collapse, the deformation occurs following the assumed super folding element. To find $\Delta\beta = \beta - \beta_0$, rather than using α of the crease pattern, it is set equal to the value, α_{SF}, associated with the current ϕ and γ_0 This is equivalent to the α associated with the traveling hinge and is found as follows.

$$\tan\alpha_{SF} = \frac{\tan\left(\frac{\gamma_0}{2}\right)}{\sin\left(\phi_0 + \Delta\phi\right)} \tag{6.18}$$

$$\tan\left(\frac{\beta}{2}\right) = \frac{\tan\left(\phi_0 + \Delta\phi\right)}{\cos\alpha_{SF}} \tag{6.19}$$

The energy consumed by rotating the hinge by this angle is then found using the equation below.

$$E_A = \frac{mna_{SF}M_p\Delta\beta}{\sin\alpha_0} \tag{6.20}$$

- ***Average force***

The below expression is formed by equating the internal energy to external work for a single unit.

$$\begin{aligned} F\times\delta &= E_h + 4E_t + 4E_s + 4E_A \\ &= 2mnM_p\left(L_s + 2l_{1c}^{\min} + 2l_{3c}^{\min} - \frac{l_{3c}^{\min}}{m}\right)\Delta\phi + \frac{8mnM_p}{r}\frac{{a_{SF}}^2}{\tan\frac{\gamma}{2}}\sin\frac{\Delta\phi}{2}\cos\left(\phi_0 + \frac{\Delta\phi}{2}\right) \\ &+ \frac{2mn\sigma_y t\Delta\varphi a_{SF}^2}{\sin^2\alpha} + \frac{4mna_{SF}M_p\Delta\beta}{\sin\alpha_0} \end{aligned} \tag{6.21}$$

where:

$$\delta = a_{SF}\left(\cos\left(\phi_0 + \Delta\phi\right) - \cos\left(\phi_0\right)\right) \tag{6.22}$$

Substituting Eq.(6.22) into Eq.(6.21) and rearranging.

$$F = \frac{mn\left[\frac{2M_p}{a_{SF}}\left(L_s + 2l_{1c}^{min} + 2l_{3c}^{min} - \frac{l_{3c}^{min}}{m}\right)\Delta\phi + \frac{8M_p}{r}\frac{a_{SF}}{\tan\frac{\gamma}{2}}\sin\frac{\Delta\phi}{2}\cos\left(\phi_0 + \frac{\Delta\phi}{2}\right) + \frac{2\sigma_y t\Delta\varphi a_{SF}}{\sin^2\alpha} + \frac{4M_p\Delta\beta}{\sin\alpha_0}\right]}{\cos(\phi_0 + \Delta\phi) - \cos(\phi_0)} \quad (6.23)$$

This provides the average force when folding from ϕ_0 to $\phi_0 + \Delta\phi$. The unknowns in this equation are: a_{SF} - the location where the hinge forms; and, r - the radius around which the travelling hinge bends and unbends the material. To find r the wall thickness is ignored. It is then assumed that the maximum distance that the unit is able to fold, δ_{max}, is equal to the initial height minus two time the radius around which the material folds (Meng *et al.*, 1983)

$$\delta_{max} = a_{SF}\cos\phi_0 - 2r \quad (6.24)$$

When the super folding element folds flat the maximum values of $\Delta\phi$, $\Delta\varphi$ and $\Delta\beta$ can be found as follows.

$$\Delta\phi = \frac{\pi}{2} - \phi_0$$

$$\Delta\varphi = 2\left(\alpha_0 - \frac{\gamma_0}{2}\right) \quad (6.25)$$

$$\Delta\beta = \pi - \beta_0$$

Substituting Eq.(6.24) and Eq.(6.25) into Eq.(6.21) and rearranging.

$$F = \frac{mn\left[\frac{2M_p}{a_{SF}}\left(L_s + 2l_{1c}^{min} + 2l_{3c}^{min} - \frac{l_{3c}^{min}}{m}\right)\left(\frac{\pi}{2} - \phi_0\right) + \frac{8M_p}{r}\frac{a_{SF}}{\tan\frac{\gamma}{2}}\sin\left(\frac{\pi}{4} - \frac{\phi_0}{2}\right)\cos\left(\frac{\pi}{4} + \frac{\phi_0}{2}\right) + \frac{4\sigma_y t\left(\alpha_0 - \frac{\gamma_0}{2}\right)a_{SF}}{\sin^2\alpha} + \frac{4M_p(\pi - \beta_0)}{\sin\alpha_0}\right]}{a_{SF}\cos(\phi_0) - 2r} \quad (6.26)$$

For a given a_{SF}, it is then possible to differentiate the average force with respect to r and find the r at which the force is a minimum. To find a_{SF}, *fminbnd* was applied in MATLAB to solve for a a_{SF} that results in the minimum average force between the bounds of $0 \leq a_{SF} \leq a$. In each iteration, r is found for the specific a_{SF}. M_p is calculated using Eq.(4.7).

From the FE simulation, two measurements were taken for a_{SF}, one at the location of the corners and the other in the centre of the facets (Figure 6.28). These a_{SF} values are compared

to the analytical prediction in Table 6.3. The prediction from the analytical model is within the range found from the FE simulation.

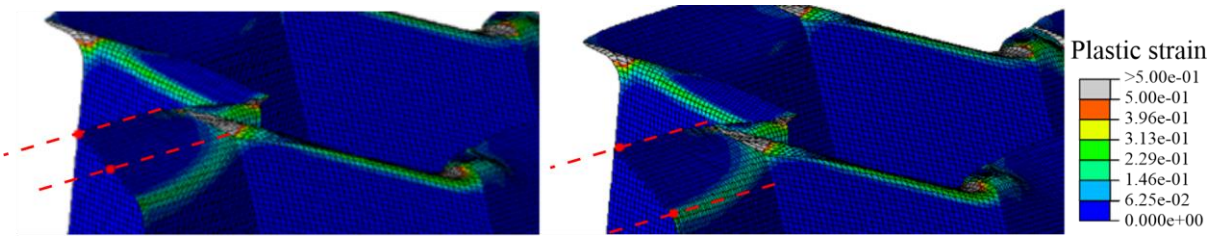


Figure 6.28 Location where hinges form

Table 6.3 Comparison of hinge location

	r [mm]	a_{SF} [mm]
FE		1.56 (at corners) 2.88 (at middle of facet)
Theoretical	0.1	1.65

Using this a_{SF} value, the average force is calculated using Eq.(6.26) and is compared with the FE results in Figure 6.29. Eq.(6.26) appears to provide a reasonable approximation of the average normalised force (0.0021).

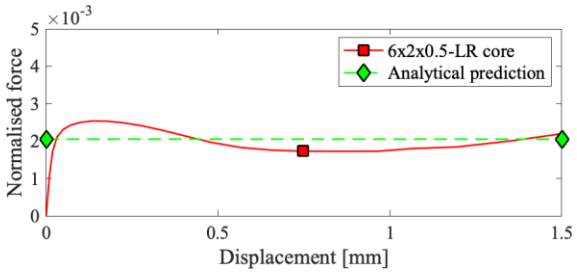


Figure 6.29 Super folding element average force comparison with FE simulation

- ***Limitations***

As discussed previously, the super folding element assumes that the hinge lines that form in the facets are horizonal. This is geometry specific and it was shown earlier in this section an increase in the l_1, l_2, l_3 lengths may result in this assumption becoming invalid.

The design of the double thickness location also appears to have a significant impact on the deformation mode. A FE simulation for a cell with equivalent cross-sectional area and

quasi-static strength but different double thickness locations was simulated. The location of double thickness was adjusted through the selection of l_1^{II} and l_3^{II} values, resulting in the double thickness swapping for the corners at either side of the l_2 lengths (Figure 6.30). This results in the corners folding in an alternative manner to the one described by the super folding element. Instead of stretching occurring, all corners appear to have travelling hinges. The super folding element for this deformation mode is not pursued further.

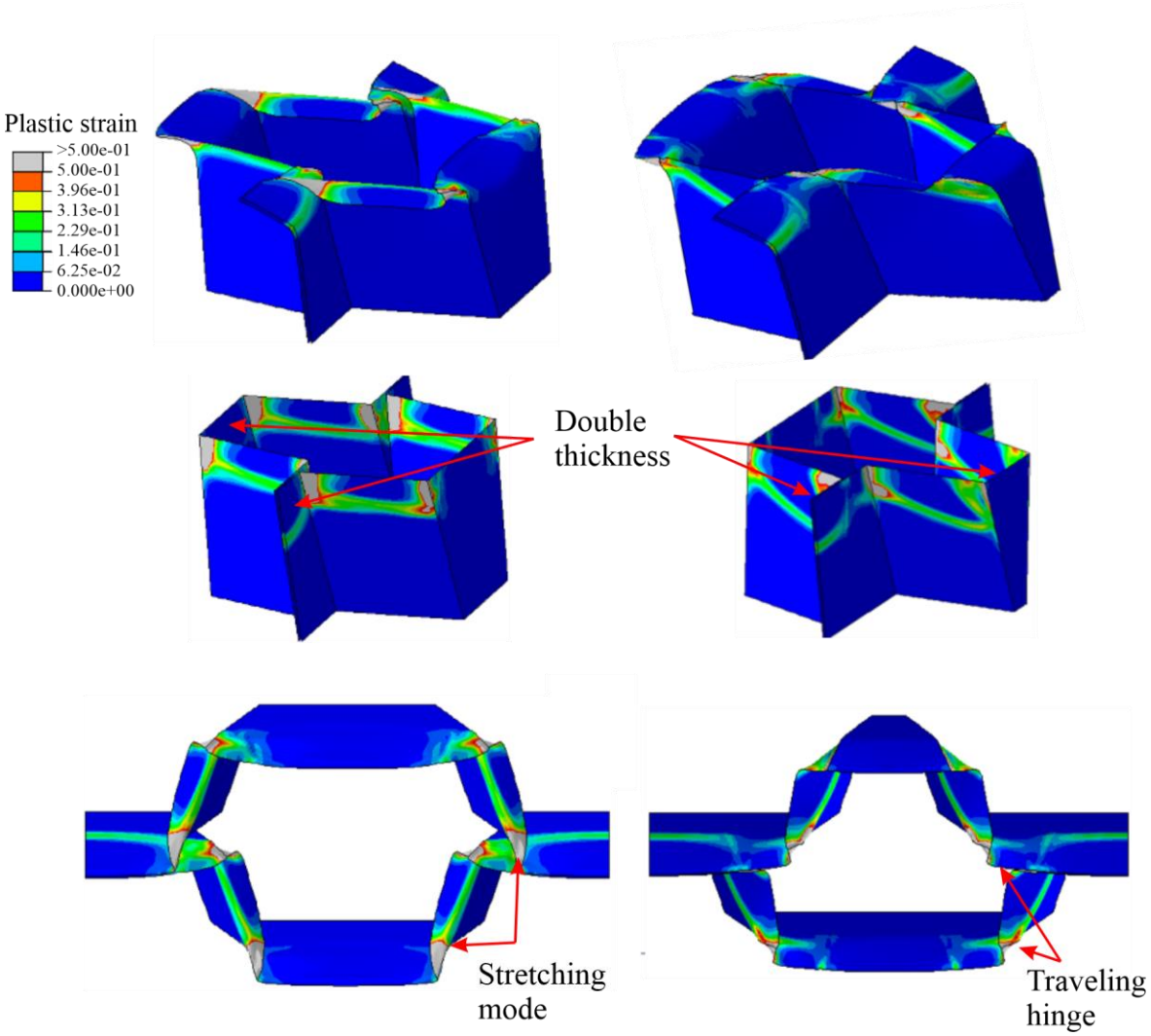


Figure 6.30 Alternative deformation mode depending on location of double thickness

The super folding element was only derived for $\theta_0 = 150°$ and has not been validated for cores with alternative θ_0. Further analysis is required to determine its applicability for these alternative geometries.

- ***Design of cell to limit force transferred at distal end***

The initial geometry defines the quasi-static force. This is the lower bound for the force transferred to the support. Under dynamic impact the force felt at the support may be orders of magnitude larger than the quasi-static force of the unit due to the development of higher energy deformation modes. This magnitude was found to approach the quasi-static force of a core which is restrained from lateral movement in the in-plane *n* direction. This provides an estimate for the upper bound. The difference between the lower and upper bound can be controlled by an appropriate selection of the *a* length. The average force in Eq.(6.26), derived with the super folding element, is independent of *a*. In contrast, the quasi-static behaviour is inversely proportional to *a* (Eq.(4.18)). Then, provided that $a_{SF} \neq a$, by reducing the *a* towards a_{SF}, the difference in magnitudes should theoretically reduce. To examine this, a 6×2×3 core with identical geometry as outline in section 6.1, except the *a* length was set equal to 3mm, was simulated. 3mm was selected as this is larger than the observed location where horizontal hinges form in the FE simulation (refer to a_{SF} values in Table 6.3) and therefore should not affect the restrained deformation mode. Three simulations were completed, quasi-static simulations of the core with and without lateral restraint (LR) and a dynamic simulation with an impact velocity of 10m/s. The results are provided in Figure 6.31.

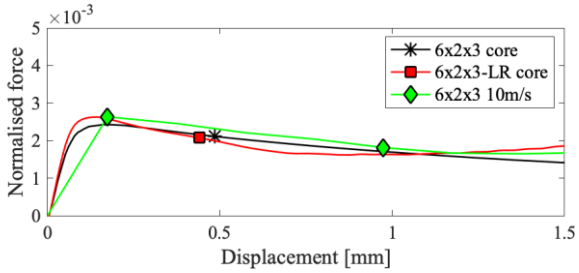


Figure 6.31 6×2×3 core with *a* = 3mm

The figure shows that the magnitude of the initial quasi-static peak for the unrestrained core (6×2×3) is far closer to the laterally restrained core (6×2×3-LR) when compared to the core with the original dimensions (Figure 6.29). Additionally, the initial peak force at the distal

end under an impact of 10m/s is close to the peak quasi-static force of the restrained core. The difference in the peak force of the lower and upper bound can therefore be reduced by adjusting the *a* value to be a similar to the location of the horizontal plastic hinge formation when laterally restrained.

6.4.2 Force at proximal end

The force at the proximal end of the core will be investigated for a 6×2×40 core with $\theta_0 = 150°$ and initial dimensions detailed in section 6.1 subject to a constant impact velocity of 75m/s, 100m/s, 150m/s and 200m/s. Figure 6.32 provides the normalised force history at the proximal and distal end of the core and the nominal strain history for selected units along the height of the core for an impact velocity of 100m/s. The nominal strain for a unit is taken as the change in relative displacement between the proximal and distal end of a central unit divided by the initial height of the unit (Eq.(5.2)), where unit 1 is impacted and unit 40 is at the support. Only selected units are provided for clarity.

The general trend for the force at the proximal end can be described by an initial peak followed by a degree of softening, an approximate plateau between 0.002s to 0.003s and finally further by softening until full densification. When comparing the nominal strain in each cell with the force at the proximal end it appears that the initial peak is associated with a larger densification strain of unit 1. The end of this initial peak at the proximal end appears to coincide with the initial peak at the distal end. As previously discussed, the initial peak at the distal end is related to the time required for the units to accelerate laterally to accommodate crushing following the path prescribed by the crease pattern. The larger densification strain of unit 1 may therefore be associated with the alternative deformation mode that would result in a larger force supported at the distal end of the unit. As crushing continues, the nominal strain reduces to an approximately constant value, around 0.85, which appears to be associated with the plateau phase. During this phase, the force at the distal end returns to the quasi-static value.

This suggests that the units have accelerated laterally to a sufficient degree for the quasi-static deformation mode to develop, resulting in the force at the distal end of the unit returning to the quasi-static value.

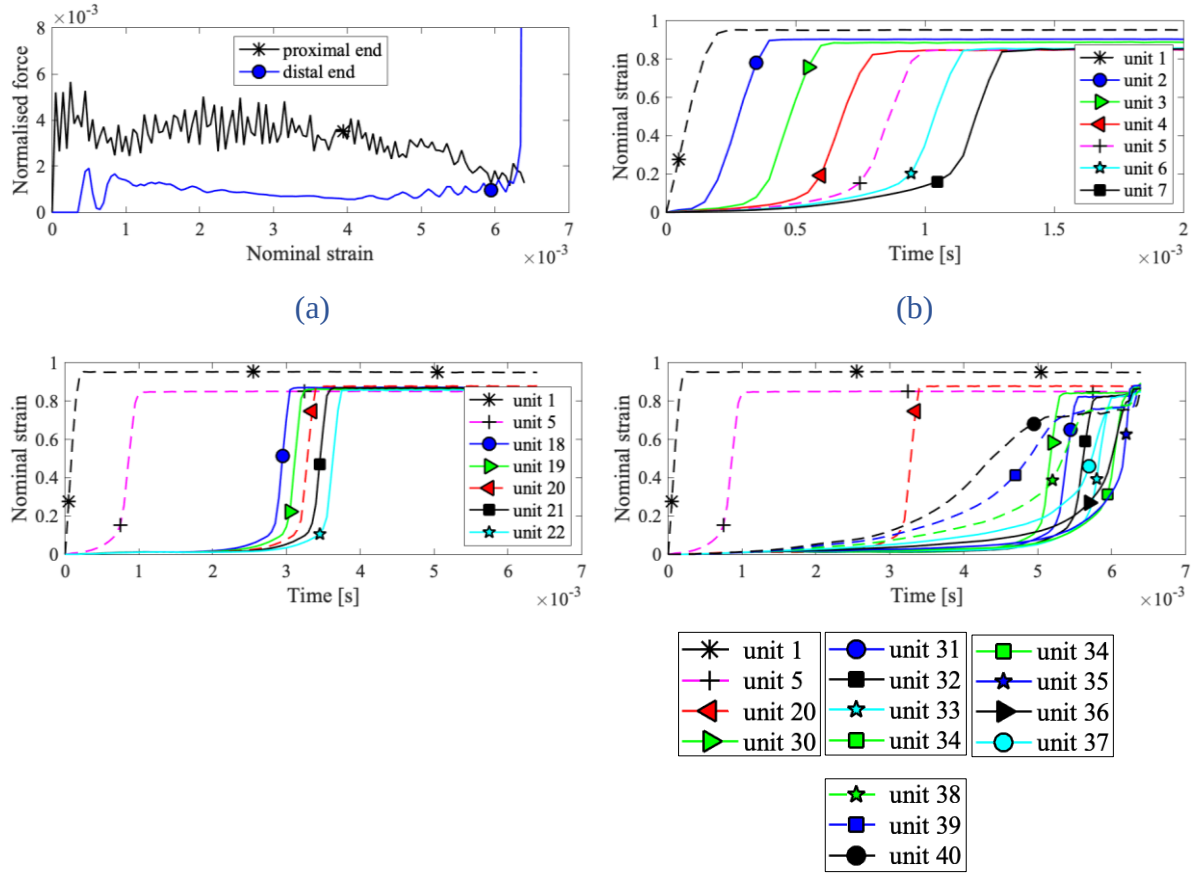


Figure 6.32 (a) Force; and, (b-d) nominal strain history for a 6×2×40 core with impactor velocity of 100m/s

The final softening phase appears to be related to the onset of significant deformation at the distal end (Figure 6.32). In the initial phases the units collapse in a sequential manner from the proximal end towards the distal end. However, at approximately 0.003s, significant deformations begin to develop in unit 40, followed by the collapse of several other units from the distal end toward the proximal end (Figure 6.32(d)). This behaviour shows that a part of the origami honeycomb experienced unloading due to the fold formation near the distal end. Subsequent folds develop from the distal end towards to the proximal end. The deformation

shown at t = 6e-3s in Figure 6.33 resembles the propagation of a dispersive wave from the distal end. The force at the proximal end is expected to decrease due to the propagation of this wave.

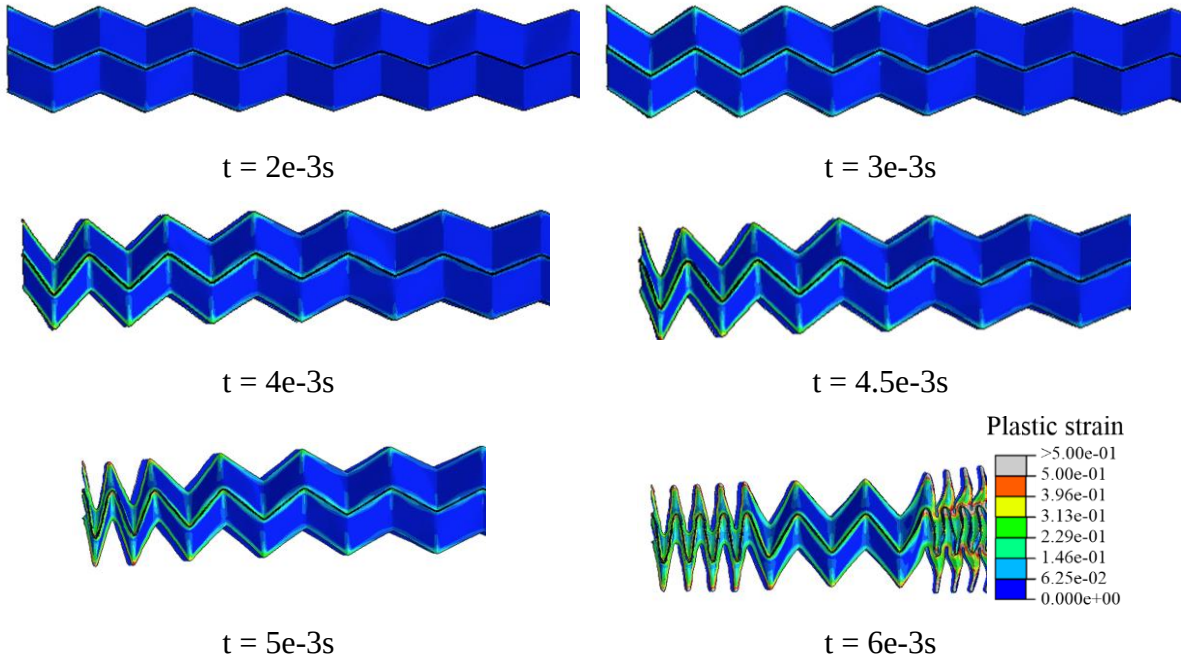


Figure 6.33 Displacement of units close to the support for 100m/s

A degree of simultaneous folding appears to occur for units at the distal end. In the initial phase, while the units are sequentially crushing from the proximal end to the distal end, there is some initial deformation in the neighbouring unit before the unit at the crushing front reaches the densification strain. In Figure 6.32(b) when unit 6 densifies the nominal strain in unit 7 is close to 30%.

The force at the distal end of selected units is provided in Figure 6.34. The entire history is provided in Figure 6.34(a) and close ups are provided in Figure 6.34(b-d). In the figures guide lines are provided at the time where the densification of the unit is reached. The densification of the units is taken from Figure 6.32. While only the force at the distal end of units is provided, the force at the distal end of unit i is representative of the force at the proximal end of unit i+1.

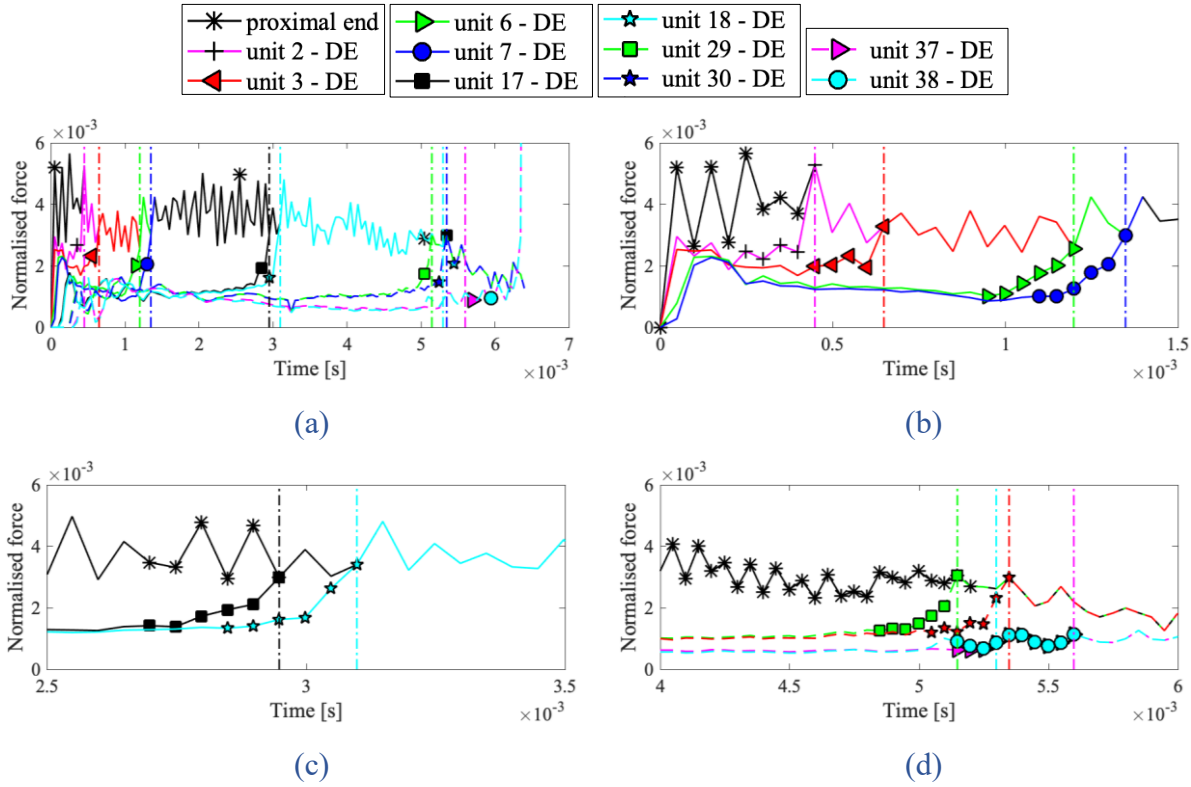


Figure 6.34 Force history at distal end of selected units for 100m/s

Firstly, looking at the force at the proximal (unit 2 -DE) and distal end (unit 3 -DE) of unit 3 provided in in Figure 6.34(b). During the phase the force at the distal end remains approximately constant with a magnitude in the range of the initial peak that is associated with a deformation that does not follow the quasi-static deformation mode. The average force found with the super folding element provides a reasonable prediction of the force at the distal end of unit 3 while it is crushing. Figure 6.35 provides deformation plots with plastic strain contours during the collapse of unit 3. The figure clearly shows that unit 3 does not deform following the crease pattern, with significant plastic deformations occurring in the facets.

In contrast, for unit 7, 18 and 30, the force at the distal end increases during the collapse of the unit rather than remaining approximately constant. Figure 6.36 provides the deformation of unit 7 with plastic strain contours. Compared to Figure 6.35 for unit 3, unit 7 and 8 have plastic strains localised at the crease locations before the densification of unit 7 begins (t = 0.0011s). However, as unit 7 is crushed plastic strains develop in the facets of the unit and

it does not crush following the path prescribed by the crease pattern. If the unit is not deforming in a manner prescribed by the crease pattern it could be expected that the force at the distal end would increase, as the unit is no longer following the quasi-static deformation mode. This may be the reason why the force at the distal end of these units appears to rise from the quasi-static level before full densification of the cell occurs. Notwithstanding, before this alternative deformation mode develops during the crushing of the unit and if the core has accelerated laterally a sufficient amount that the force at the distal end of each unit is approximated well by the quasi-static force.

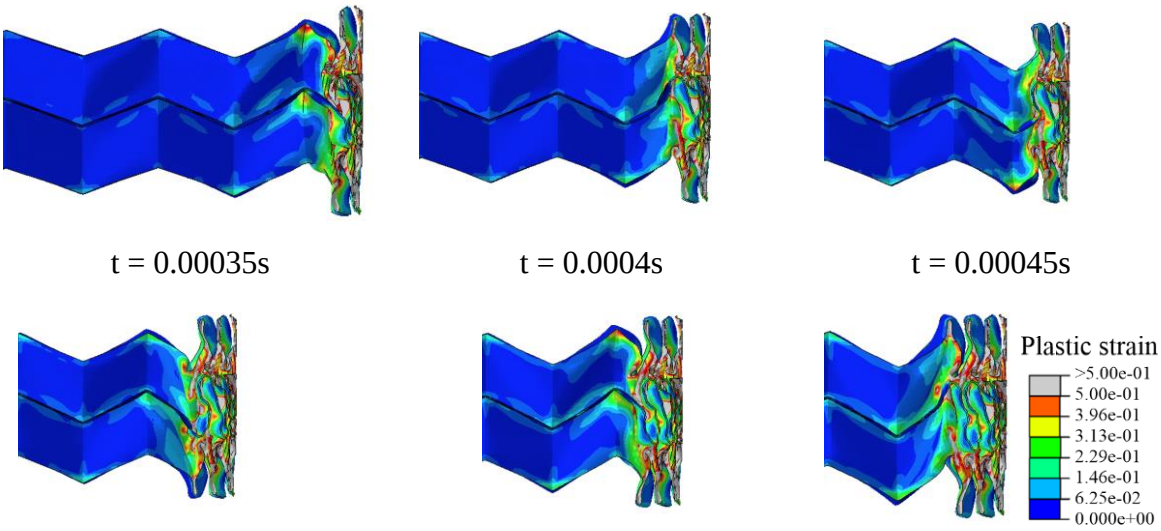


Figure 6.35 Unit 3 deformation for 100m/s

The force at the proximal and distal end of unit 38 remain almost equivalent and at a magnitude close to the quasi-static value during the densification of this cell (Figure 6.34(d)). This illustrated that unit 38 is deforming under approximately quasi-static conditions.

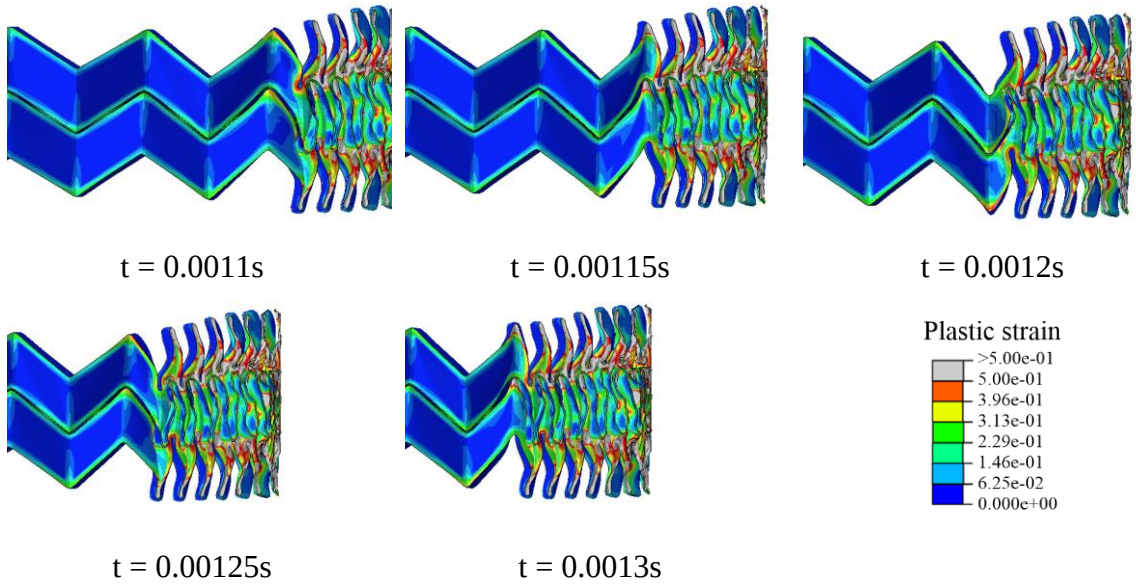


Figure 6.36 Unit 7 deformation for 100m/s

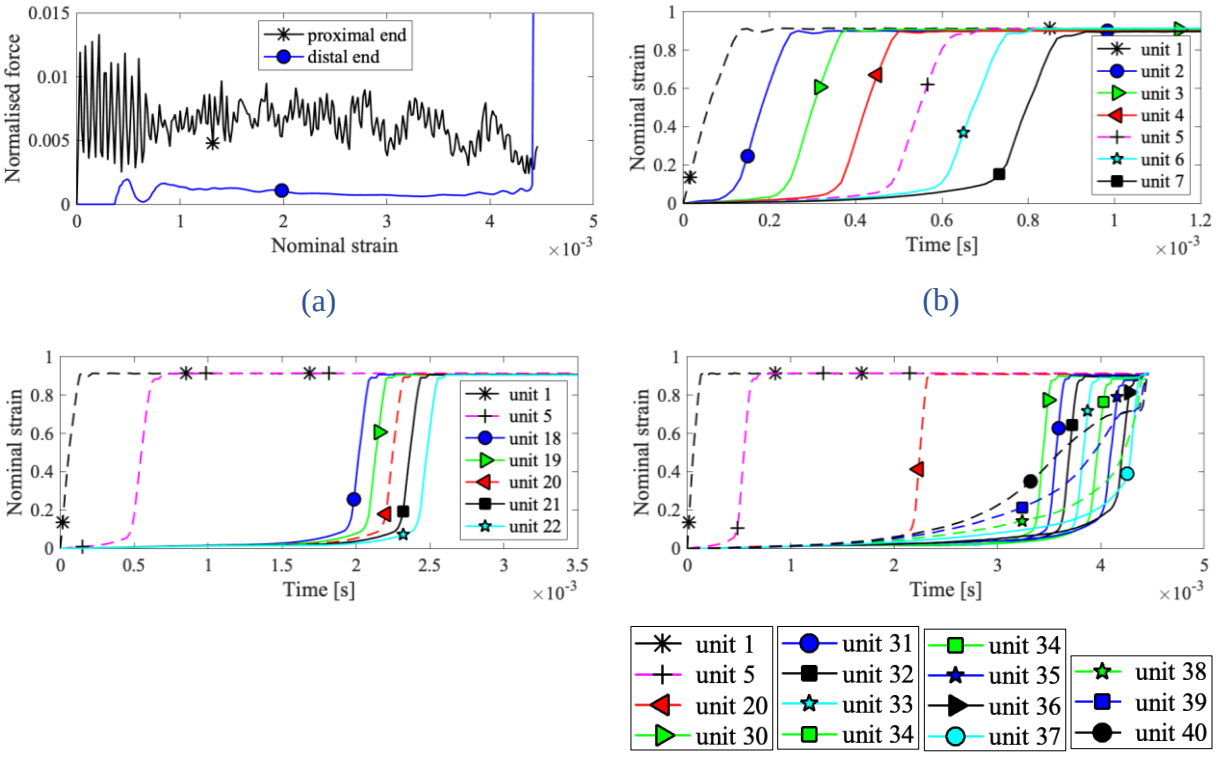
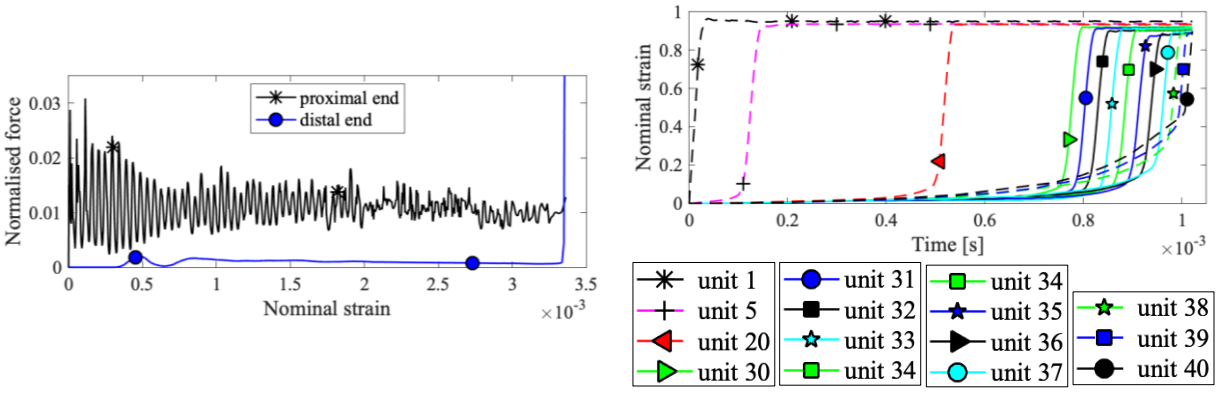


Figure 6.37 Force and nominal strain history for a 6x2x40 core with impactor velocity of 150m/s

As the velocity increases, the amount of deformation that occurs at the distal end of the core before the primary compaction wave travelling from the proximal end reaches the unit

reduces. This is due to the reduction in time required for the compaction front to reach the distal end (Figure 6.32, Figure 6.37 and Figure 6.38). Additionally, the average nominal densification strain of the core appears to increase with velocity. Where the densification strain for 150m/s is approximately 90% and for 200m/s > 90%. The cores average nominal densification strain is found using the method described in section 4.3.2.2 of Chapter 4.



(a) (b)

Figure 6.38 Force and nominal strain history for a 6×2×40 core with impactor velocity of 200m/s

The force at the proximal and distal ends of selected units are provided in Figure 6.39 for an impactor velocity of 150m/s. Similar to a 100m/s, the force at the distal end of unit 3 remains approximately constant during its collapse with a magnitude approximated by the super folding element. Additionally, for 150m/s, the force at the distal end of units 7 and 18 rises to a value that is also close to this magnitude before full densification.

While unit 3 also has a similar response for an initial impactor velocity of 75m/s, a jump (discontinuity) in the force at the distal end of unit 7 is not readily observed (Figure 6.40). Instead, the force at the distal end gradually increases to the force at the proximal end of the unit. This suggests that the application of shock wave theory may not be applicable for this velocity.

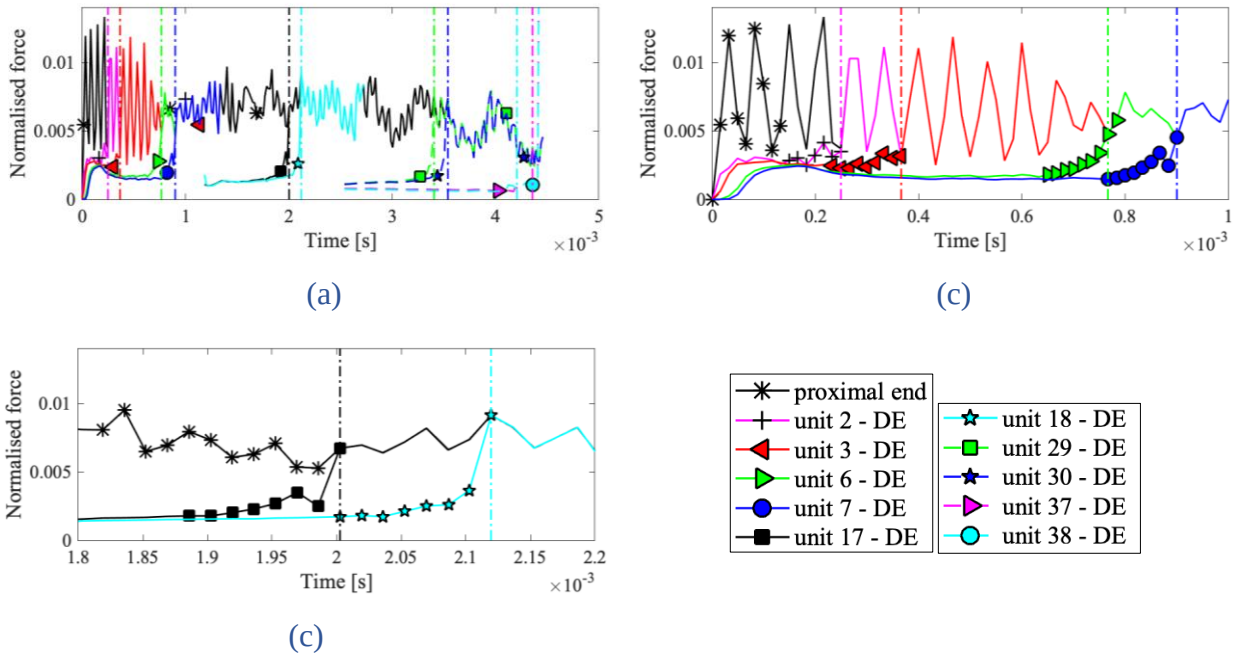


Figure 6.39 Force history at distal end of selected units for 150m/s

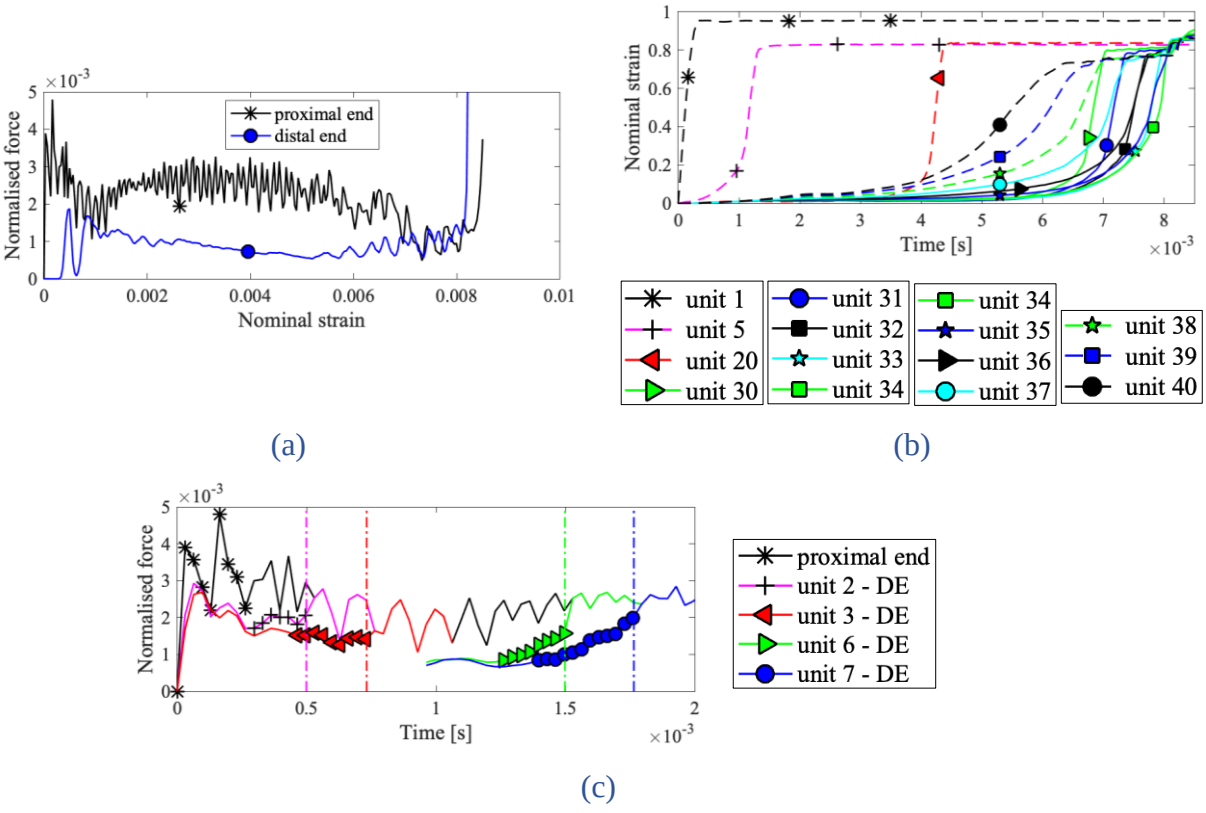


Figure 6.40 Force and nominal strain history for a 6x2x40 core with impactor velocity of 75m/s

The thickness of the band of cells that are at the crushing front is an important consideration for the application of the analytical model. In Figure 6.41 the nominal strain in the unit is provided at the time when unit 21 and 31 have reached the densification strain. For 100m/s to 200m/s the nominal strain in the units jumps from a value between 0.1 - 0.2 to the densification strain across the length of approximately one unit. As the velocity reduces to 75m/s the thickness of the crushing front becomes slightly more diffuse, with unit 22 having a nominal strain of slightly larger than 0.2. For the densification of unit 31, the thickness of the crushing front also increases, especially for 75m/s and 100m/s, where the thickness of the wave crushing front appears to be over the height of two units. This also coincides with the dispersive wave traveling from the distal end. This highlights that shock wave theory may not be applicable for impact velocity of 75m/s and 100m/s.

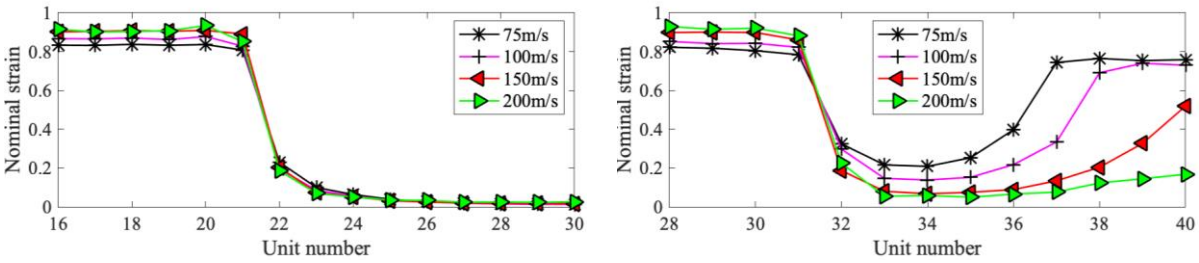


Figure 6.41 Nominal strain in units when unit 21 has densified (b) unit 31 has densified

6.4.2.1 Analytical model for the force at the proximal end

Several salient features for the development of an analytical model for the origami honeycomb under dynamic impact are summarised below:

1. At higher velocities, the deformation appears similar to one associated with shock wave propagation, the cells collapse sequentially from the proximal end to the distal end. The thickness of the crushing band was found to be approximately equivalent to the height of one unit for impactor velocities over 100m/s. For 75m/s and 100m/s the thickness of the crushing band increases closer to two units in the later stages of crushing.

2. There appears to be two quite distinct phases in relation to the force transferred to the support. Initially a larger force, associated with lateral inertia effects is felt. Then, once significant lateral acceleration has occurred, the force at the distal end returns to one associated with the quasi-static level. As the height of the core increases, and/or the number of units in the lateral directions reduces, much of the response occurs under phase 2.
3. In phase 2, although the deformation of the cell resembles the quasi-static deformation, the walls are not rigid and plastic deformations in the facets do occur. This behaviour leads to an increase in the force observed at the distal end of the unit during its collapse.

While under quasi-static loading the origami honeycomb may exhibit softening behaviour, the velocity-dependent deformation mode makes it challenging to apply a structural approach or a mass spring model. Instead, an analytical model assuming the propagation of a shock wave will be pursued. The model is derived assuming a constant impact velocity and sequential cell collapse from the proximal end to the distal end.

Applying the conservation of momentum over a single unit collapsing with initial velocity of zero and a final velocity equal to the impactor mass, an equation for the force at the proximal end, F_d, can be derived. Where: F_0 is the force at the distal end of the unit; and, A_0 is the area enclosed by the cross section of the core.

$$F_d = F_0 + \frac{\rho A_0}{\varepsilon_D} V^2 \tag{6.27}$$

As described above, the force at the distal end of the unit depends on the phase of the deformation. In the initial phase it was found it was equal to the force related to the deformation of a laterally restrained core. The average force found from the super folding element is therefore applicable ($F_{0,I}$ = 461N). The force at the distal end of the unit is more complicated during the second phase. In phase 2, initially the force at the distal end begins at the quasi-

static value, however, once the crushing front reaches the unit, the force at the distal end increases to a value similar to phase 1. In this analysis, the force variation at the distal end of the unit will not be considered and will instead be set equal to the value associated with the initial quasi-static peak force ($F_{0,II}$ = 280N) (Figure 6.3(a)).

As discussed above, ε_D is velocity dependent. For other Type I cellular structures rather than using the quasi-static densification strain a velocity dependent densification strain is required. The densification strains are found using the method described in section 4.3.2.2 of chapter 4 and are provided for a range of velocities in Figure 6.42. These values are found from the FE simulations of the 6×2×40 core and therefore represent the average nominal densification strain of the core. The densification strain of individual units using this method is not pursued.

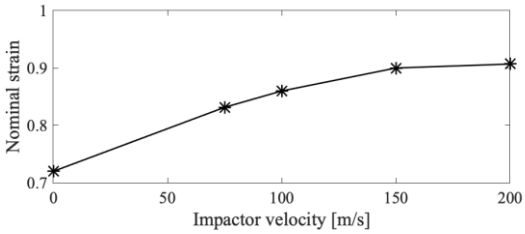


Figure 6.42 Densification strain vs impactor velocity

Comparisons of Eq.(6.27) for cores impacted at 75m/s, 100m/s, 150m/s and 200m/s are provided in Figure 6.43. Setting $F_0 = F_{0,I,}$ results in a reasonable prediction for the initial peak for 75m/s and 100m/s. Additionally, for 100m/s and 150m/s the analytical model predicts the peak load oscillations during phase 2 relatively well. For these velocities, the force at the distal end of the units were shown to increase to a value close to $F_{0,I}$ close to densification (Figure 6.34 and Figure 6.39 respectively).

For cores impacted at 100m/s to 200m/s, setting $F_0 = F_{0,II}$ appears to provide a reasonable prediction of the mean load at the proximal end during the deformation. However, towards the end of the crushing a reduction in the force is observed, especially for 75m/s and 100m/s. This is believed to be associated with the significant deformation forming at the distal end. The

analytical equations are derived assuming deformation occurs in a sequential manner from the proximal end to the distal end and therefore cannot capture this behaviour.

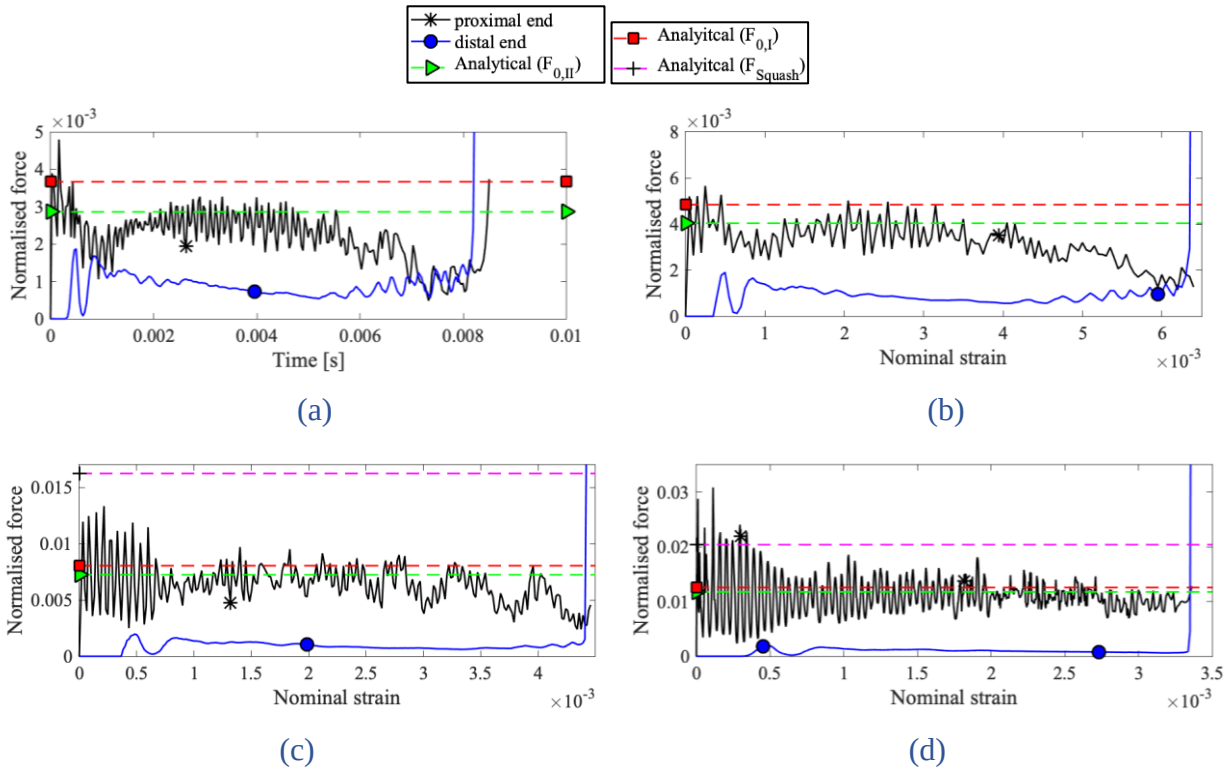


Figure 6.43 Comparison of analytical mode with FE simulation for: (a) 75m/s; (b) 100m/s; (c) 150m/s; and (d) 200m/s

The mean force at the distal end is overpredicted by the analytical model for 75m/s. As noted earlier, for this velocity the crushing band is larger than the height of a single unit and therefore the sequential cell collapse associated with shock wave formation is not applicable. To predict the minimum velocity where shock wave propagation can be expected, Tan *et al.* (2005) proposed an expression for aluminium foam Eq.(2.7). The inputs for the origami honeycomb with θ_0 = 150° and impact velocity of 75m/s are provided below.

$$\rho = 74.0\text{kg/m}^3$$

$$\varepsilon_D = 0.83 \tag{6.28}$$

$$\sigma_p = \frac{F_{0,I}}{A_0} = \frac{461}{724.4} = 0.636\text{MPa}$$

Inputting these values into Eq.(2.7) the velocity is calculated as 120m/s. This agrees well with the numerical model as both 75m/s and 100m/s exhibited features which suggested that shock wave propagation may not be applicable. This is also highlighted by the analytical model through the overestimation of the dynamic force for these velocities.

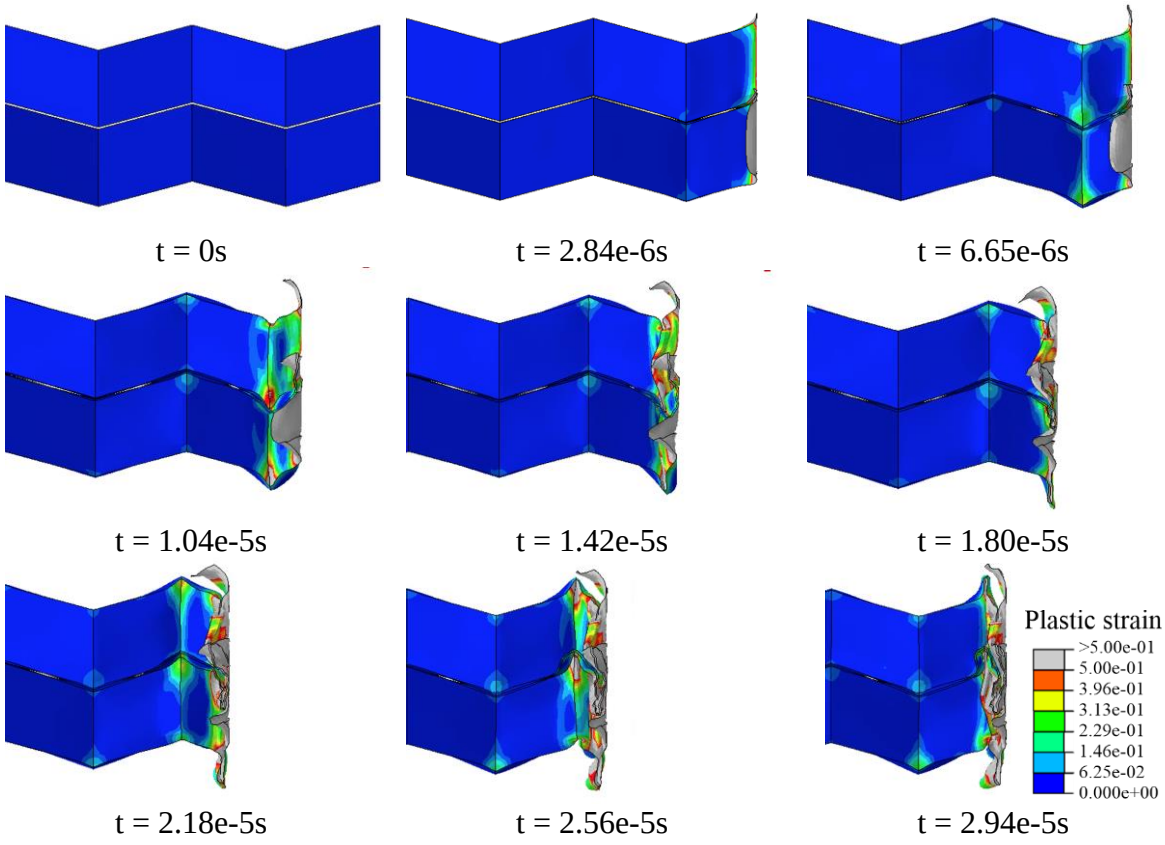


Figure 6.44 Deformation of unit 1 for a 200m/s

The initial peak for 150m/s and 200m/s is significantly larger than that predicted using Eq.(6.27). This may be due to the increase in velocity resulting in a more localised deformation mode. Looking closely at the deformation at the impacted end for 200m/s (Figure 6.44), the initial deformation appears is similar to the 'stubbing' deformation mode described by McShane *et al.* (2012) for the dynamic buckling of an inclined strut. For this mode, McShane *et al.* (2012) applied a conservation of momentum approach where the force supported was equal to the squash load of the inclined strut. To check if the squash load develops in the unit, the force at a section 2.76mm from the top of the core for an impact velocity of 100m/s and

200m/s was output from the FE analysis and is provided in Figure 6.45. The squash load, F_{squash}, accounting for the initial angle of the wall, was calculated as 2.44kN (0.0109 normalised) and is also provided.

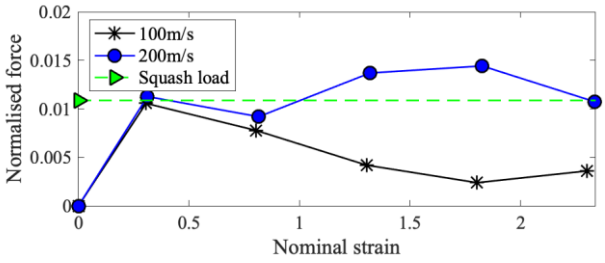


Figure 6.45 Force at a cross section 2.76mm below the top of the core.

Figure 6.45 shows that the squash load is supported by the core for larger crushing distances as the velocity increases. To predict the initial peak force for the core at 200m/s, the conservation of momentum is applied for a localised deformation mode, shown in Figure 6.46 which is comparable to the 'stubbing' of inclined struts (McShane *et al.*, 2012), resulting in the below equation. Where: m_e is the mass of the material within the bounded box shown in Figure 6.46 that is accelerated from 0 to V_0; and, ρ_s is the density of the sheet material.

$$F_d = F_{squash} + \frac{m_e V_0^2}{\delta} = F_{squash} + \frac{2\rho_s t\left(2l_1 + 2l_2 + l_3\right)V_0^2}{\sin\frac{\theta_0}{2}} \tag{6.29}$$

The predictions from Eq.(6.29) are provided for 150m/s and 200m/s in Figure 6.43(c, d). For 200m/s the initial peak oscillations magnitudes (t < 0.0005s) are captured reasonably by Eq.(6.29). However, for 150m/s the peak oscillations are significantly lower. The calculations according to Eq.(6.29), where F_{squash} is taken as a load of the distal end of the deformed part, assumes that the entire wall of the deformed portion is plastic. This happens at sufficiently high velocity, which is observed at 200 m/s. The response of the honeycomb block at 150m/s is, perhaps, a transition between the response by the super folding element (when the deformations are localized along the crease lines) and deformation with entirely plastic walls. A larger velocity range should be simulated to determine the critical velocity at which the squash load

develops. Notwithstanding, this provides an estimate of the maximum initial peak force for the origami honeycomb core.

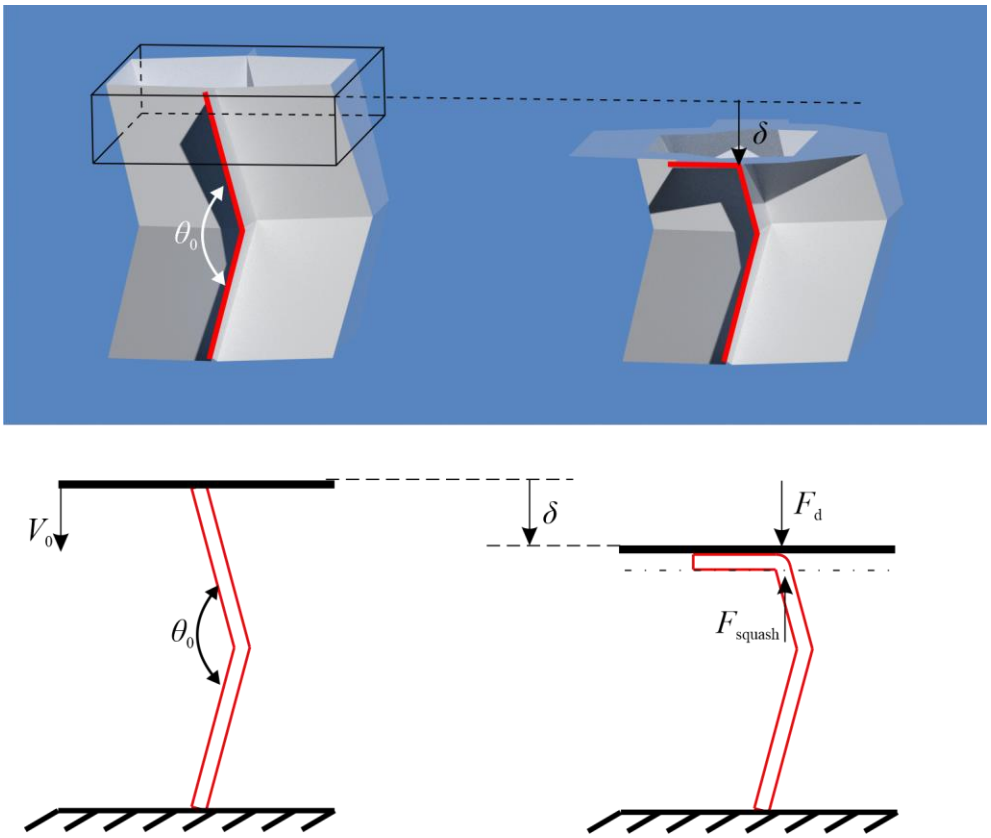


Figure 6.46 Assumed stubbing deformation mode for core at high velocities

6.4.2.2 Comments

The analytical models provide an estimation of the force at the proximal end by assuming three separate stress states and deformation modes. For the purpose of calculating the energy absorption of the origami honeycomb, using Eq.(6.27) with $F_0 = F_{0,II}$ provides a reasonable approximation of the average force for the core simulated when the velocity is above 100m/s.

It should be noted that the applicability of the analytical model appears to also be dependent on the number of units along the height of the core. For larger θ_0, where the core exhibits Type II behaviour, a sufficiently large force can be transmitted to the distal end before the shock wave has reached it. This results in large plastic deformations due to folding at the support. Partial unloading at the proximal end also occurs due to the deformation at the distal

end (refer to 75m/s and 100m/s in Figure 6.43(c, d)). While minimal deformation is observed at the support for 150m/s and 200m/s, it is not negligible (refer to Figure 6.41(b)). If a larger number of units were simulated along the height of the core it would be expected that the unloading would also be more readily observed for these velocities.

The analytical model can therefore not be applied in a universal manner. Care should be taken when applying the analytical model as shock wave theory is only applicable for certain combinations of the core height and impact velocity. Nevertheless, a reasonable estimate of the average force is achieved by applying the shock wave theory, which would allow evaluating the energy absorption at high velocity impacts. For the geometry simulated the analytical model can be applied for velocities above 120m/s (refer to analysis in section 6.4.2.1 using Eq.(2.7)).

For smaller θ_0 it is expected that the shock wave theory can be applied more successfully as the force transmitted to the distal end will be smaller and will therefore not cause large cell deformation at the distal end. This however has not been validated at this stage.

6.5 Conclusion

The origami honeycomb has a complex topology and kinematics which translates to a complex response under dynamic impact. Initially in this chapter the response of an ungraded origami honeycomb was examined closely for two θ_0's and varying α's. The two θ_0's were selected as 150° and 60° which exhibit Type II and Type I behaviour respectively. This analysis highlighted that the lateral inertia of the cell/core influences the behaviour at both the proximal and distal end greatly.

At the distal end, the force transferred to the support may be orders of magnitude larger than the quasi-static prediction due to lateral inertia effects for both θ_0's. To follow the kinematics of the crease pattern the cells must accelerate laterally to accommodate a change in height (Poisson's effect). Depending on the underlying kinematics and the number of $m \times n$ units in the core, the mass that is required to accelerate laterally to accommodate this height

change may become significant, resulting in a degree of lateral restraint. Due to this restraint the cells deformation will deviate from the crease pattern, which results in a larger force than the quasi-static prediction being transferred to the support.

For the geometry simulated, the lateral inertia in the *n* direction was found to be dominant. An upper bound for this increased force was approximated well by assuming that a single row of *m* cells is restrained laterally in the *n* direction at both edges. Subsequently a super folding element was defined for the observed deformation mode and provided an analytical prediction of the upper bound force that is transferred to the support. In the analytical model, the energy associated with the assumed deformation mode was minimised to approximate the location where the super folding element materialises, a_{SF}. One method of reducing the difference in the lower bound (quasi-static) and the upper bound (super folding element) force prediction is to reduce the *a* length of the underlying crease pattern towards a_{SF}. This increases the quasi-static strength of the cell. Alternatively, rather than reducing the difference between the lower and upper bound force predictions, increasing the number of units along the height of the core and/or reducing the lateral inertia of the underlying crease pattern, can result in the force transferred to the support tending towards the lower bound approximation. The lateral inertia of the cell can be varied through the selection of the lengths, α and θ_0.

To approximate the force at the proximal end, a continuum approach was applied assuming shock wave formation. This approach assumes that the deformation occurs exclusively from the proximal end to the distal end, layer by layer, and the crushing front is of a comparable width to the cell size. The analytical model was compared to results from a numerical study of a 6×2×40 core with θ_0 = 150° subject to constant impact velocities of 75m/s,100m/s,150m/s and 200m/s. Above 100m/s the analytical model provided a reasonable approximation of the average force. Below this velocity significant deformation occurs at the

distal end of the core resulting in unloading at the proximal end which cannot be captured by the analytical model. This results in an overestimation of the average force and therefore the energy absorption. Shock wave theory is only applicable for certain combinations of height and impact velocities for the origami honeycomb and therefore the analytical model cannot be applied universally. It can however provide a reasonable estimate of the average force for certain scenarios which would allow the evaluation of energy absorption at high velocities.

CHAPTER 7

CONCLUSIONS

This dissertation explores the use of origami techniques to imbue cellular structures with programable characteristics under both quasi-static and dynamic loading scenarios for energy absorbing applications. Understanding the behaviour of these origami inspired structures is required to functionally design them in a manner that increases their structurally efficiency. This inherently leads to improvements in sustainability within the field. In this chapter a summary of the achievements as well as future research directions are outlined.

7.1 Summary and main achievements

Through a rigorous kinematic study, a range of origami honeycomb derivatives were uncovered and defined in chapter 3. These derivatives were formed for two connection methods: one which preserved symmetry about both in-plane axis (crease-to-crease connection method); and, one which did not (face-to-face connection method). Through the variation of the underlying crease pattern, it was then shown that self-locking could be designed in both the in-plane and out-of-plane directions. The self-locking restricts the kinematical range of adjacent cells and is realised through the variation of the Miura-ori angle, α, in the underlying crease pattern. This chapter provides an understanding of the underlying kinematics of the crease pattern as well as self-locking methodologies, which are essential for the development of the subsequent chapters. In addition, a variety of novel origami honeycomb cores are formed that exhibit unique behaviour that may be of interest for other applications.

Chapter 4 presents the quasi-static response of the origami honeycomb graded in the out-of-pane direction for both connection methods. Initially, an experimental study of an ungraded 1x1 core was conducted to validate the numerical method. In the out-of-plane direction the

origami honeycomb was found to be insensitive to initial imperfections and stress states arising from the manufacturing method. However, the behaviour was found to be sensitive to friction. With larger number of units along the height or smaller lengths the friction sensitivity was found to reduce. Following this, a parametric study was undertaken for ungraded cores with both connection methods to determine the influence of the underlying crease pattern variables and initial fold angle. An analytical model was then derived which matched the numerical results well when the cores were friction insensitive. From this study it was shown that force is inversely proportional to the offset eccentricity ($a\cos\theta_0$). Therefore, the initial peak force can be increased by reducing a or increasing θ_0. Additionally, when all other variables are equivalent, α can be varied to increase the peak force and/or energy absorbed. Generally, for smaller θ_0 values, smaller α's were shown to increase both, whereas, at larger values of θ_0, larger α's increased the initial peaks.

Subsequently, the out-of-plane behaviour of graded cores utilising both connection methods was explored through numerical and analytical models. In order to tesselate the crease-to-crease connected core, the a length of the units must be selected to allow the connection facets to meet. For a 1×1 core this resulted in minimal increase in force due to locking. However, when implemented as a core, the restraint provided by adjacent cells drastically alter the deformation mode, resulting in a graded stiffness. For the face-to-face connection method, a could be chosen arbitrarily. The deformation was also relatively similar for both the 1×1 core and $m \times n$ cores. However, it was shown that the locations of double thickness could be selected to control the deformation mode.

Due to the alternative complex deformation mode observed for the crease-to-crease connected core, a super folding element could not be defined. However, for the face-to-face connection method, a super folding element was defined and an analytical model to predict the force increase due to locking was derived from this. The analytical model provided a reasonable

approximation of the force increase with some sensitivity related to the cell angle, γ, that the unit is locked at. Larger value of θ_0 within the locking phase increased the force. Additionally, while an increase in a does result in a larger energy absorption associated with the travelling hinges, it also results in a reduction in the energy associated with the stationary horizontal hinges. Interestingly, the energy associated with the travelling hinges reduces with increasing α when all other variables are held constant.

Chapter 4 showed that origami techniques can be applied to provide a programable response through the variation of the underlying crease pattern. Furthermore, the analytical model provides the means to estimate the response of the origami honeycomb. This can facilitate the efficient design of cellular structures under quasi-static loading.

Few studies have explored the dynamic behaviour of origami inspired structures, especially the ability of these structures to provide a functionally graded response. To this end, chapter 5 explored the effectiveness of varying α to provide grading and therefore influence the impact behaviour of the cores for both connection methods through a numerical study. The numerical method was validated against an experimental program of a 2×1 core experimentally tested using the Direct Impact Hopkinson Bar and Taylor Type Impact test set ups. When debonding did not occur, the numerical model matched the experiments reasonably well. The validated numerical model was then applied to compare the behaviour of positively, negatively and ungraded 6×6 crease-to-crease connected cores with similar relative density and height under constant velocity impact. The variation in α was shown to greatly affect the deformation mode and therefore the energy absorption, with positive gradients showing the largest specific energy absorption when compared to negative and ungraded cores. Additionally, the unit placed at the support can limit the force transferred. This shows great potential for applications where the design stipulates a maximum allowable force that is to be transferred to the structure. Subsequently, 6×6 face-to-face connected cores were simulated and provided similar findings

to the crease-to-crease connected cores. However, owing to the ability to arbitrarily select a for these cores, the graded behaviour was enhanced when compared to the crease-to-crease connection method.

Chapter 5 highlighted that origami techniques can be implemented to design structures that exhibit similar behaviour to typical functionally graded structures under dynamic loading. Compared with these standard structures, origami techniques alleviate many issues related to the manufacturing of these structures and therefore provide an attractive alternative.

Chapter 6 explored the dynamic behaviour of the ungraded face-to-face connected core to determine a suitable analytical mode. The force transferred to the distal end of the units was shown to be influenced greatly by the lateral inertia of the cell/core. To collapse in the manner prescribed by the crease pattern, the cells must accelerate laterally to accommodate the change in height. This provides a varying degree of lateral restraint, depending on the underlying crease pattern and the number units within the core ($m \times n$), and may result in the force at the distal end of the core being orders of magnitude larger than the quasi-static prediction. An analytical model for this increase in force was derived using a super folding element which captured the deformation mode for laterally restrained cells. The analytical mode also predicted the location at which the super folding element materialised, a_{SF}. Through the analytical model it was then shown that the difference between the quasi-static force and the force associated with the laterally restrained cell can be reduced by selecting a to be of a similar length to a_{SF}. Alternatively, it was also shown that increasing the number of units along the height of the core and/or reducing the lateral inertia of the underlying crease pattern results in the force at the distal end tending towards the quasi-static prediction.

A continuum approach assuming shock wave formation was applied to predict the force at the proximal end of the core. The model assumed sequential layer collapse from the proximal end to the distal end. The analytical mode was compared to the numerical results of a 6×2×40

core with $\theta_0 = 150°$ subject to constant impact velocities of 75m/s,100m/s,150m/s and 200m/s. The analytical mode provided a reasonable approximation of the average force for velocities greater than 100m/s. For the lower velocities, unloading is observed at the proximal end due to significant deformations developing at the distal end. The analytical model was therefore shown to only be applicable for certain combinations of height and impact velocities. Notwithstanding, in these scenarios a reasonable approximation of the average force can be achieved and therefore the evaluation of the energy absorption.

7.2 Future work

The ability of origami techniques to functionally grade cellular structures under quasi-static and dynamic loading has been shown in this dissertation. To facilitate the use of the structures widely in industry further understanding of their response is required. To this end several future research directions are outline in this section.

In chapter 3 a variety of derivatives were outlined. These derivatives showed quite unique kinematic behaviour. For instance, class 2 responds to a length change in the in-plane direction with rotations of the facets. This is in contrast with the standard origami honeycomb where the Poisson's effect is well defined in both directions. The behaviour of these cores under quasi-static and dynamic loading is therefore of interest. For instance, under dynamic loading the effect of this rotation may result in increased inertia effects. Further analysis to understand the behaviour of these structures is beneficial as it provides greater versatility in the design of these structures. Furthermore, the behaviour of grading only in the out-of-plane directing was pursued. There is further opportunity to examine the behaviour of the derivatives and in-plane grading under the various loading scenarios.

Secondly in chapter 4, an analytical model was not derived for the graded crease-to-crease connected core. To facilitate the application of the crease-to-crease connected cores, an analytical model is required to enable the design of a crease pattern for a prescribed response.

In addition, the analytical model for the face-to-face connection method has not been validated against a variety of alternative geometries. This should be completed to determine if it can be applied universally.

The behaviour of the origami honeycombs was also exclusively sought for loading directly in the out-of-plane direction. In practise, the angle of impact is variable. Further analysis of the origami honeycomb under oblique loading should be completed to determine if a similar stable collapse can be expected.

Finally, an analytical model for the dynamic impact was only provided for a 6×2×40 ungraded core with θ_0 = 150°. The analytical mode should be compared to cores with alternative: initial θ_0; number of units along the height; and, alternative crease patterns to determine when it is applicable. Furthermore, the analytical model should be expanded to predict the behaviour of graded cores.

REFERENCES

ABAQUS (2004) ‘ABAQUS Documentation’. Providence, RI, USA.: Dassault Systèmes.

Ajdari, A., Nayeb-Hashemi, H. and Vaziri, A. (2011) ‘Dynamic crushing and energy absorption of regular, irregular and functionally graded cellular structures’, *International Journal of Solids and Structures*, 48(3–4), pp. 506–516.

Alexander, J. M. (1960) ‘An approximate analysis of the collapse of thin cylindrical shells under axial loading’, *Quarterly Journal of Mechanics and Applied Mathematics*, 13(1), pp. 10–15.

Ali, M., Qamhiyah, A., Flugrad, D. and Shakoor, M. (2008) ‘Theoretical and finite element study of a compact energy absorber’, *Advances in Engineering Software*, 39(2), pp. 95–106.

ASTM International (2016) *Standard Test Methods of Tension Testing of Metallic Materials E345*.

Calladine, C. R. and English, R. W. (1984) ‘Strain-rate and inertia effects in the collapse of two types of energy-absorbing structure’, *International Journal of Mechanical Sciences*, 26(11–12), pp. 689–701.

Chen, L. and Goto, T. (2003) ‘Functionally Graded Materials’, in Sōmiya, S. et al. (eds) *Handbook of Advanced Ceramics: Materials, Applications, Processing and Properties*, pp. 445–464.

Cullen, J. M. and Allwood, J. M. (2010) ‘The efficient use of energy: Tracing the global flow of energy from fuel to service’, *Energy Policy*, 38(1), pp. 75–81.

Fan, J., Zhang, J., Wang, Z., Li, Z. and Zhao, L. (2013) ‘Dynamic crushing behavior of random and functionally graded metal hollow sphere foams’, *Materials Science and Engineering A*, 561, pp. 352–361.

Fang, H., Li, S. and Wang, K. W. (2016) ‘Self-locking degree-4 vertex origami structures’, *Proceedings of the Royal Society A*, 472(2195).

Ferri, E., Antinucci, E., He, M. Y., Hutchinson, J. W., Zok, F. W. and Evans, A. G. (2006) 'Dynamic Buckling of impulsively loaded prismatic cores', *Journal of Mechanics of Materials and Structures*, 1(8), pp. 1345-1365.

Ferri, E., Deshpande, V. S. and Evans, A. G. (2010) 'The dynamic strength of a representative double layer prismatic core: A combined experimental, numerical, and analytical assessment', *Journal of Applied Mechanics*,77(6), pp. 1–7.

Fu, M. W. and Chan, W. L. (2011) 'Geometry and grain size effects on the fracture behavior of sheet metal in micro-scale plastic deformation', *Materials and Design*, 32(10), pp. 4738–4746.

Gao, Z. Y. and Yu, T. X. (2006) 'One-dimensional analysis on the dynamic response of cellular chains to pulse loading', *Proceedings of the Institution of Mechanical Engineers, Part C: Journal of Mechanical Engineering Science*, 220(5), pp. 679–689.

Gao, Z. Y., Yu, T. X. and Lu, G. (2005a) 'A study on type II structures. Part I: A modified one-dimensional mass-spring model', *International Journal of Impact Engineering*, 31(7), pp. 895–910.

Gao, Z. Y., Yu, T. X. and Lu, G. (2005b) 'A study on type II structures. Part II: Dynamic behavior of a chain of pre-bent plates', *International Journal of Impact Engineering*, 31(7), pp. 911–926.

Gattas, J. M. and You, Z. (2015) 'The behaviour of curved-crease foldcores under low-velocity impact loads', *International Journal of Solids and Structures*, 53, pp. 80–91.

Gibson, L. J. and Ashby, M. F. (1997) *Cellular solids: Structure and properties*. 2nd edn. Cambridge: Cambridge University Press.

Guo, Y. B., Shim, V. P. W. and Yeo, A. Y. L. (2010) 'Elastic wave and energy propagation in angled beams', *Acta Mechanica*, 214(1), pp. 79–94.

Harrigan, J. J., Reid, S. R., Tan, P. J. and Reddy, T. Y. (2005) 'High rate crushing of wood along the grain', *International Journal of Mechanical Sciences*, 47(4–5), pp. 521–544.

Harrigan, J. J., Reid, S. R. and Seyed Yaghoubi, A. (2010) 'The correct analysis of shocks in a cellular material', *International Journal of Impact Engineering*, 37(8), pp. 918–927.

Harris, J. A. and McShane, G. J. (2021) 'Impact response of metallic stacked origami cellular materials', *International Journal of Impact Engineering*, 147, p. 103730.

Harris, J. A., Winter, R. E. and McShane, G. J. (2017) 'Impact response of additively manufactured metallic hybrid lattice materials', *International Journal of Impact Engineering*, 104, pp. 177–191.

Heimbs, S. (2013) 'Foldcore Sandwich Structures and Their Impact Behaviour: An Overview', in Abrate, S., Castanié, B., and Rajapakse, Y. D. S. (eds) *Dynamic Failure of Composite and Sandwich Structures*. Springer, pp. 491–544.

Hu, L. L. and Yu, T. X. (2010) 'Dynamic crushing strength of hexagonal honeycombs', *International Journal of Impact Engineering*., 37(5), pp. 467–474.

Hu, L. L., Zhou, M. Z. and Deng, H. (2018) 'Dynamic crushing response of auxetic honeycombs under large deformation: Theoretical analysis and numerical simulation', *Thin-Walled Structures*, 131, pp. 373–384.

Hull, T. (1994) 'On the Mathematics of Flat Origamis', *Congressus Numerantium*, 100, pp. 215–224.

IEA (2009) *Energy Technology Transitions for Industry*, International Energy Agency, Paris.

Johnson, W. (1972) *Impact Strength of Materials*. London: Edward Arnold Publishers Ltd.

Johnson, W., Soden, P. D. and Al-Hassani, S. T. S. (1977) 'INEXTENSIONAL COLLAPSE OF THIN- WALLED TUBES UNDER AXIAL COMPRESSION', *Journal of Strain Analysis*, 12(4).

Karagiozova, D., Zhang, J., Lu, G. and You, Z. (2019) 'Dynamic in-plane compression of Miura-ori patterned metamaterials', *International Journal of Impact Engineering*, 129, pp. 80–100.

Karagiozova, D. and Alves, M. (2017) ‘On the dynamic compression of cellular materials with local structural softening’, *International Journal of Impact Engineering*, 108, pp. 153–170.

Kindervater, C. M. and Georgi, H. (1993) ‘Composite strength and energy absorption as an aspect of structural crash resistance’, in Jones, N. and Wierzbicki, T. (eds) *Structural Crashworthiness and Failure*. Elsevier, pp. 189–236.

Li, G., Xu, F., Sun, G. and Li, Q. (2015) ‘A comparative study on thin-walled structures with functionally graded thickness (FGT) and tapered tubes withstanding oblique impact loading’, *International Journal of Impact Engineering*, 77, pp. 68–83.

Li, L., Zhao, Z., Zhang, R., Han, B., Zhang, Q. and Lu, T.J. (2019) ‘Dual-level stress plateaus in honeycombs subjected to impact loading: perspectives from bucklewaves, buckling and cell-wall progressive folding’, *Acta Mechanica Sinica*, 35(1), pp. 70–77.

Li, Q. M. and Meng, H. (2002) ‘Attenuation or enhancement - A one-dimensional analysis on shock transmission in the solid phase of a cellular material’, *International Journal of Impact Engineering*, 27(10), pp. 1049–1065.

Liu, Y., Wu, H.-X., Lu, G. and Wang, B. (2013) ‘Dynamic Properties of Density Graded Thin-Walled Metal Hollow Sphere Arrays’, *Mechanics of Advanced Materials and Structures*. Taylor & Francis Group, 20(6), pp. 478–488.

Liu, Y., Wu, H.-X. and Wang, B. (2012) ‘Gradient design of metal hollow sphere (MHS) foams with density gradients’, *Composites Part B: Engineering*, 43, pp. 1346–1352.

Lu, G. and Yu, T. (2003) *Energy absorption of structures and materials*. Cambridge, England: Woodhead Publishing Limited.

Ma, J., Hou, D., Chen, Y. and You, Z. (2016) ‘Quasi-static axial crushing of thin-walled tubes with a kite-shape rigid origami pattern: Numerical simulation’, *Thin-Walled Structures*, 100, pp. 38–47.

Ma, J., Song, J. and Chen, Y. (2018) ‘An origami-inspired structure with graded stiffness’, *International Journal of Mechanical Sciences*, 136, pp. 134–142.

Ma, J. and You, Z. (2014) ‘Energy Absorption of Thin-Walled Square Tubes With a Prefolded Origami Pattern-Part I: Geometry and Numerical Simulation’, *Journal of Applied Mechanics*, 81(1), pp. 011003.

McShane, G. J., Pingle, S. M., Deshpande, V. S. and Fleck, N. A. (2012) ‘Dynamic buckling of an inclined strut’, *International Journal of Solids and Structures*, 49(19–20), pp. 2830–2838.

Meng, Q., Al-Hassani, S. T. S. and Soden, P. D. (1983) ‘Axial Crushing of Square Tubes’, *International Journal of Mechanical Sciences*, 25(9-10), pp. 747–773.

Miura, K. and Tachi, T. (2010) ‘Synthesis of rigid-foldable cylindrical polyhedra’, in *Symmetry: Art and Science, International Society for the Interdisciplinary Study of Symmetry*. Gmuend, pp. 204–213.

Papka, S. D. and Kyriakides, S. (1994) ‘In-plane compressive response and crushing of honeycomb’, *Journal of the Mechanics and Physics of Solids*, 42(10), pp. 1499–1532.

Radford, D. D., Mcshane, G. J., Deshpande, V. S. and Fleck, N. A. (2007) ‘Dynamic Compressive Response of Stainless-Steel Square Honeycombs’, *Journal of Applied Mechanics*, 74(4), pp. 658-667

Reid, S. R., Bell, W. W. and Barr, R. A. (1983) ‘Structural plastic shock model for one-dimensional ring systems’, *International Journal of Impact Engineering*, 1(2), pp. 175–191.

Reid, S. R. and Peng, C. (1997) ‘Dynamic Uniaxial Crushing of Wood’, *International Journal of Impact Engineering*, 19, pp. 531–570.

Ruan, D., Lu, G., Wang, B. and Yu, T. X. (2003) ‘In-plane dynamic crushing of honeycombs—a finite element study’, *International Journal of Impact Engineering*. 28(2), pp. 161–182.

Schenk, M., Guest, S. D. and McShane, G. J. (2014) ‘Novel stacked folded cores for blast-resistant sandwich beams’, *International Journal of Solids and Structures*, 51, pp. 4196–4214.

Shen, C. J., Lu, G., Ruan, D. and Yu, T.X. (2016) 'Propagation of the compaction waves in a cellular block with varying cross-section', *International Journal of Solids and Structures*, 88–89, pp. 319–336.

Shen, C. J., Lu, G. and Yu, T. X. (2013) 'Dynamic behavior of graded honeycombs - A finite element study', *Composite Structures*, 98, pp. 282–293.

Shen, C. J., Lu, G. and Yu, T. X. (2014) 'Investigation into the behavior of a graded cellular rod under impact', *International Journal of Impact Engineering*, 74, pp. 92–106.

Shen, C. J, Yu, T. X. and Lu, G. (2013) 'Double shock mode in graded cellular rod under impact', *International Journal of Solids and Structures*, 50, pp. 217–233.

Song, J., Chen, Y. and Lu, G. (2012) 'Axial crushing of thin-walled structures with origami patterns', *Thin-Walled Structures*, 54, pp. 65–71.

Su, X. Y., Yu, T. X. and Reid, S. R. (1995) 'Inertia-sensitive impact energy-absorbing structures part I: Effects of inertia and elasticity', *International Journal of Impact Engineering*, 16(4), pp. 651–672.

Tachi, T. (2009) 'Generalization of Rigid Foldable Quadrilateral Mesh Origami', *Journal Of The International Association For Shell And Spatial Structures*, 50, pp. 2287–2294.

Tam, L. L. (1990) *Strain-rate and inertia effects in the collapse of energy-absorbing structures, Thesis*. Cambridge.

Tam, L. L. and Calladine, C. R. (1991) 'Inertia and strain-rate effects in a simple plate-structure under impact loading', *International Journal of Impact Engineering*, 11(3), pp. 349–377.

Tan, P. J., Reid, S. R., Harrigan, J. J., Zou, Z. and Li, S. (2005) 'Dynamic compressive strength properties of aluminium foams. Part II—"shock" theory and comparison with experimental data and numerical models', *Journal of the Mechanics and Physics of Solids*, 53(10), pp. 2206–2230.

Tan, P. J., Harrigan, J. J. and Reid, S. R. (2002) 'Inertia effects in uniaxial dynamic compression of a closed cell aluminium alloy foam', *Materials Science and Technology*, 18(5), pp. 480–488.

Vaughn, D. G. and Hutchinson, J. W. (2006) 'Bucklewaves', *European Journal of Mechanics A/Solids*, 25, pp. 1–12.

Wang, H., Zhao, D., Jin, Y., Wang, M., Mukhopadhyay, T. and You, Z. (2020) 'Modulation of multi-directional auxeticity in hybrid origami metamaterials', *Applied Materials Today*. Elsevier Ltd, 20, p. 100715.

Wierzbicki, T. (1983) 'Crushing analysis of metal honeycombs', *International Journal of Impact Engineering*, 1(2), pp. 157–174.

Wierzbicki, T. and Abramowicz, W. (1983) 'On the Crushing Mechanics of Thin-Walled Structures', *Journal of Applied Mechanics*, 50, pp. 727–734.

Xiang, X. M., Lu, G. and You, Z. (2020) 'Energy absorption of origami inspired structures and materials', *Thin-Walled Structures*, 157, pp. 1071301.

Xu, F., Tian, X. and Li, G. (2015) 'Experimental Study on Crashworthiness of Functionally Graded Thickness Thin-Walled Tubular Structures', *Experimental Mechanics*, 55(7), pp. 1339–1352.

Xu, F., Zhang, X. and Zhang, H. (2018) 'A review on functionally graded structures and materials for energy absorption', *Engineering Structures*, 171, pp. 309–325.

Xu, S., Ruan, D., Lu, G. and Yu, T. X. (2015) 'Collision and rebounding of circular rings on rigid target', *International Journal of Impact Engineering*, 79, pp. 14–21.

Yang, J., Wang, S., Ding, Y., Zheng, Z. and Yu, J. (2017) 'Crashworthiness of graded cellular materials: A design strategy based on a nonlinear plastic shock model', *Materials Science and Engineering A*, 680, pp. 411–420.

Yang, Y., Nara, C. and Hagiwara, I. (2016) 'Energy absorbing characteristics of pairing origami structures', in *Proceedings of the Dynamics and Design Conference*, Yamaguchi-ken, Japan.

Yu, H., Tieu, K., Lu, C., Lou, Y., Liu, X., Godbole, A. and Kong, C. (2014) 'Tensile fracture of ultrafine grained aluminum 6061 sheets by asymmetric cryorolling for microforming', *International Journal of Damage Mechanics*, 23(8), pp. 1077–1095.

Yu, T. X. and Qiu, X. (2018) *Introduction to impact dynamics*. 1st ed. New Jersey: Hoboken.

Zeng, H. B., Pattofatto, S., Zhao, H., Girard, Y. and Fascio, V. (2010) 'Impact behaviour of hollow sphere agglomerates with density gradient', *International Journal of Mechanical Sciences*. Pergamon, 52(5), pp. 680–688.

Zhang, J., Wei, H., Wang, Z. and Zhao, L. (2014) 'Dynamic crushing of uniform and density graded cellular structures based on the circle arc model', *Latin American Journal of Solids and Structures*, 12(6), pp. 1102–1125.

Zhang, J., Lu, G., Ruan, D. and Huang, X. (2019) 'Experimental observations of the double shock deformation mode in density graded honeycombs', *International Journal of Impact Engineering*, 134, p. 103386.

Zhang, T. G. and Yu, T. X. (1989) 'A note on a "velocity sensitive" energy-absorbing structure', *International Journal of Impact Engineering*, 8(1), pp. 43–51.

Zhao, H. and Gary, G. (1998) 'Crushing behaviour of aluminium honeycombs under impact loading', *International Journal of Impact Engineering*, 21(10), pp. 827–836.

Zou, Z., Tan, P. J., Reid, S. R., Li, S. and Harrigan, J. J. (2007) 'Dynamic crushing of a one-dimensional chain of type II structures', *International Journal of Impact Engineering*. Pergamon, 34(2), pp. 303–328.

Zou, Z., Reid, S. R., Tan, P. J., Li, S. and Harrigan, J. J. (2009) 'Dynamic crushing of honeycombs and features of shock fronts', *International Journal of Impact Engineering*, 36(1), pp. 165–176.